Copper Creek, Arizona: Laramide Early Halo Style Porphyry, Breccia and Massive Sulphide Mineralization

Thomas Bissig[1], **Dante Padilla**[1], **Matias Sanchez**[2], **Paul Harbidge**[1]
[1]*Faraday Copper Corp. 250-200 Burrard St. Vancouver, BC, Canada*
[2]*Faultrocks Inc. Victoria, BC, Canada*

Abstract. Copper Creek is an unusual porphyry Cu-Mo district characterized by early halo style veining and magmatic cupola style mineralization overprinted by abundant hydrothermal breccias. The latter commonly contain high-grade mineralization. Massive sulphide bodies interpreted as silica-replacive intermediate sulphidation mineralization occur locally as well. Breccias are dominantly crackle or jigsaw fit breccias with sulphide cement and sericite +/- kaolinite alteration. They probably didn't breach the surface during emplacement.

The mineralization is largely hosted by the 62 Ma Copper Creek batholith and 63 Ma Glory Hole volcanics emplaced in a NW trending Laramide thrust fault system, later reactivated during Basin and Range extension. While breccias and porphyry intrusions followed this principal NW orientation, a prominent array of steeply dipping E to ENE oriented as well as shallowly west dipping extensional veins controlled early halo style porphyry mineralization.

Mineralization styles and cross-cutting relationships suggest that early halo-style porphyry mineralization took place at approximately 5-6 km crustal depth followed by rapid exhumation which facilitated the emplacement of hydrothermal breccias. Thus, the mineral system was emplaced at a time of an important tectonic transition.

1 Introduction

Copper Creek in Arizona is one of the largest undeveloped copper deposits in the prolific Laramide copper province of Southwestern US and northern Mexico, with 422 million tons of 0.48% Cu equivalent measured and indicated resource (Fig. 1: Faraday Copper news release May 3rd 2022).

Mineralization styles differ from those in other deposits in the region and from the classic porphyry model. Early halo style porphyry veins (e.g., Proffett, 2009), are dominant whereas A and B-type veins are comparatively rare. In addition, the district is known for widespread breccia hosted mineralization, with recently identified massive sulphide mineralized zones consisting of chalcopyrite, bornite and pyrite. This paper summarizes the current understanding of the geology and mineralization of this district.

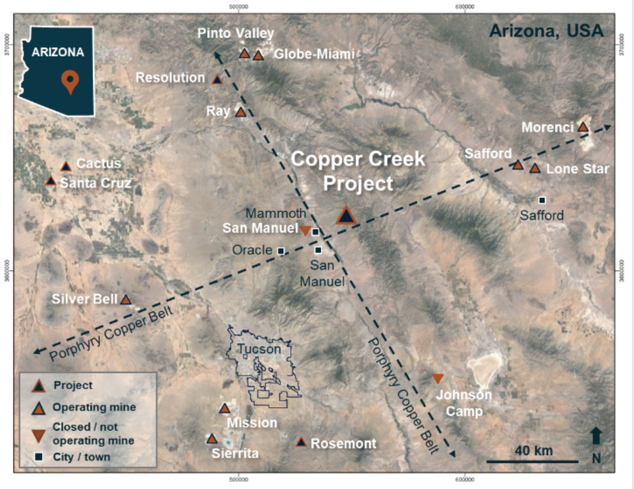

Figure 1. Location of Copper Creek, relative to other major porphyry copper deposits and prospects in southern Arizona.

1.1. Exploration and Mining History

Small scale mining in the district occurred intermittently between 1861 and 1982 with approximately 300,000 t of ore produced from the Old Reliable and Childs-Aldwinkle mines in the early 20th century.

More than 200 km of drilling was carried out in the district, the bulk of it between the mid-1990s and 2015. Exploration including drilling resumed after 7 years of minimal activity in late 2021 when the new Management of Faraday Copper Corp. took over the project.

2. Geology of Copper Creek

The Copper Creek deposit is in the Galiuro mountains in southern Arizona, approximately 20 km NE of the historic San Manuel mine at the intersection of two major trends of porphyry copper deposits (Fig. 1).

Mineralization at Copper Creek is largely hosted by the Palaeocene (~62 Ma) Copper Creek batholith which intruded Palaeocene Glory Hole volcanics (~63 Ma) and Proterozoic to Palaeozoic sedimentary rocks (Fig. 2). The Copper Creek batholith is compositionally zoned and contains a shallowly west dipping monzogranite domain at depth and a dioritic border phase (Fig. 3), with the bulk being of granodioritic composition. Four main types of granodiorite to quartz diorite porphyry dykes and plugs have been recognized; these largely intruded before and during mineralisation (cf., Riedell et al. 2013).

Hydrothermal breccias crosscut both the batholith and Glory Hole volcanics. The Oligocene Galiuro volcanics cover the Copper Creek batholith and Glory Hole volcanics.

The Copper Creek batholith, porphyries and breccias were emplaced in the hanging wall of the NW trending Holy Joe thrust fault (Favorito and Seedorff, 2018) and parallel, related structures.

Over 400 mapped breccias form two prominent NW-aligned trends: the Western and Eastern breccia trends, the latter containing the bulk of the resource (Fig. 2) but only 17 of the mapped breccias have been sufficiently drilled to be included in the current mineral resource estimate.

The Western breccia trend is characterized by widespread argillic and locally advanced argillic alteration and widespread occurrence of tourmaline, whereas alteration in the Eastern breccia trend is more confined and dominated by quartz-sericite +/- kaolinite.

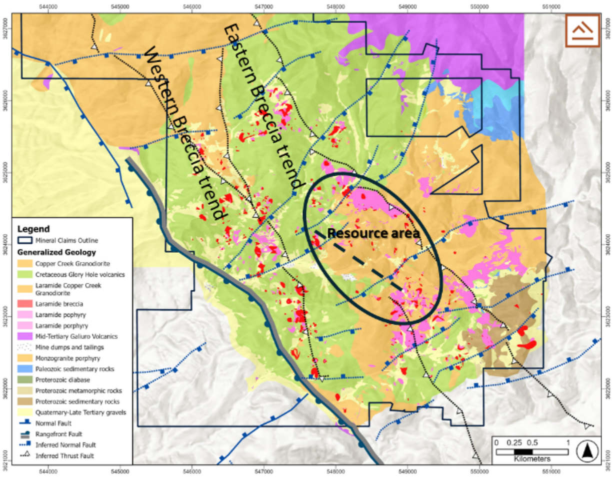

Figure 2: Geology, structural architecture, and distribution of breccias in the copper Creek district. Dashed line in the resource area indicates approximate section trace for Figure 3.

The thrust faults were variably reactivated as extensional faults during Miocene Basin and Range extension leading to more exhumation in the Eastern, compared to the Western breccia trend, which also explains the more mature stage of exploration in the eastern trend with ~90% of the historic drilling focused there.

3. Alteration and Mineralization

The mineralization can be subdivided into an early porphyry stage overprinted by breccia-hosted mineralization. Supergene oxidation and secondary sulphide enrichment are relatively minor but occurred within the uppermost 10-40 m.

The bulk of the porphyry stage mineralization is hosted by early halo veins in the American Eagle zone (Fig. 3, 4) above the monzogranite domain, i.e., 500 to 1100 m below present surface. Two dominant vein orientations are recognized: steeply dipping E to NE striking extensional veins crosscut shallowly west to southwest dipping extensional veins. Sulphides are vertically zoned from pyrite>chalcopyrite to chalcopyrite to bornite-chalcopyrite. Mineralization hosted by miarolitic cavities and coarse quartz +/- K-feldspar veins, interpreted as a variation of unidirectional solidification textures (UST's) is important in some areas such as in the Keel zone.

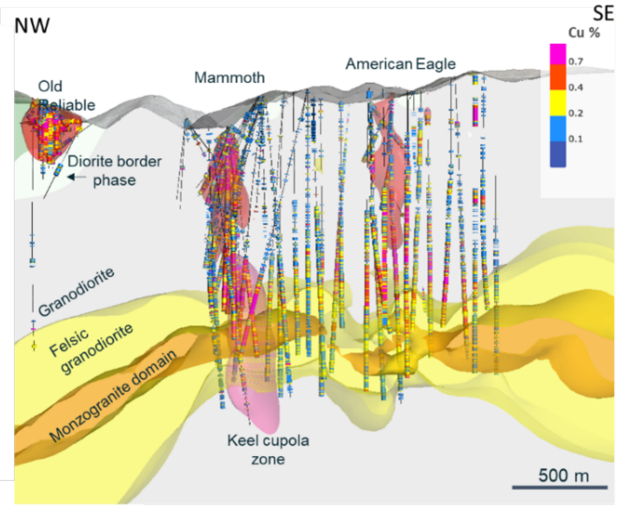

Figure 3: Long section through the American Eagle and Keel zone, showing the batholith zonation and copper mineralization concentrated above the monzogranite domain.

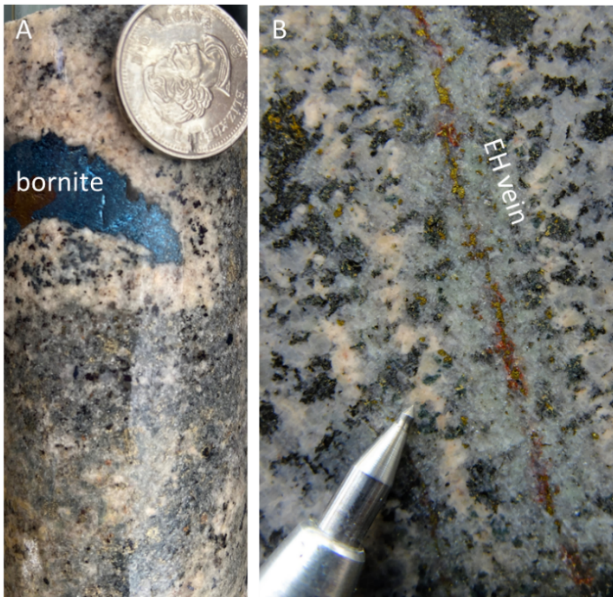

Figure 4: Examples of early-stage mineralization styles: A) miarolitic cavity with central bornite infill surrounded by K-feldspar: Keel cupola zone; B) Early halo vein cutting granodiorite with finely disseminated chalcopyrite with muscovite-biotite and K-feldspar alteration in halo: American Eagle zone.

Alteration is overall subtle during the first stage of mineralization and is characterized by biotite, muscovite and K-feldspar in the early halo veins with localized zones of K-feldspar flooding as well as secondary biotite.

Breccia-hosted mineralization occurs dominantly as sulphide cement to crackle and jigsaw fit breccias without appreciable clastic matrix (Fig. 5). The breccias have not experienced significant clast rounding or milling and are not thought to have breached the surface at the time of formation.

Figure 5: Examples of late-stage mineralization styles: A) Glory Hole breccia with pyrite-chalcopyrite cementing angular, sericite-kaolinite altered clasts. B) Massive chalcopyrite-bornite-pyrite mineralization from Copper Prince. The overall zone has 10.83% Cu over 15 m.

Alteration associated with mineralized breccias is quartz-sericite +/- kaolinite. Breccias can be vertically extensive with up to 1430 m of known vertical extent in the Keel-Mammoth zone (see also Andersson et al. 2009) but are only few 100 m across. The Mammoth breccia is the largest known breccia body. It reaches within 30 m of present-day surface but does not crop out (Andersson et al. 2009) and recent drilling suggests that it overprints earlier cupola style mineralization in the Keel zone over 1000 m below surface.

During Faraday’s phase II drilling program, a zone of massive sulphide mineralization (15 m @ 10.83% Cu, 55.6 g/t Ag and 1.65 g/t Au; Fig. 5) was discovered approximately 200 m below surface near the Copper Prince breccia. Sulphides in this zone are dominantly chalcopyrite with variable amounts of pyrite and bornite and are spatially associated with highly crystalline kaolinite and sericite alteration. This zone contains the highest gold grades known from the Copper Creek district.

3.1 Mine plan

Approximately one third of the measured and indicated resource is hosted in high-grade breccias and occurs near the surface, whereas the remainder occurs as porphyry style and magmatic cupola style mineralization 500-1100 m below surface. This distribution of the mineralized resource lends itself to an initial open pit mine plan followed by the development of an underground block caving operation.

4. Discussion and Conclusions

Mineralization at Copper Creek was emplaced immediately after Laramide orogeny and was controlled by a significant NW striking thrust fault. This setting is consistent with porphyry deposits elsewhere, including the Central Andes (e.g., Mpodozis and Cornejo, 2012). Both, the distribution of breccias and vein orientations can be explained by this setting, with early subhorizontal veining forming during thrusting and E to NE oriented steeply dipping extensional veins explained by extension normal to the orogen following compressional deformation. Breccias were emplaced in the hanging wall of the orogen parallel thrust faults.

Reactivation of thrust faults as normal faults during Neogene basin and range extension led to the preservation of shallow portions of the mineral system, including epithermal alteration assemblages in the Western- compared to the Eastern Breccia trend.

Early halo vein hosted mineralization is interpreted to reflect relatively deep crustal emplacement of porphyry mineralization at approximately 5-6 km crustal depth (e.g., Proffett, 2009). Conversely, hydrothermal brecciation occurs above magmatic cupolas where fluid pressure is sufficient to overcome confining lithostatic pressure which would be facilitated at shallower crustal depths. However, there is no evidence that any of these breccias breached the surface at the time of emplacement. Nevertheless, the cross-cutting relationships suggest that the Copper Creek mineral system experienced a period of rapid exhumation accompanied by breccia emplacement following the emplacement of Early Halo vein hosted mineralization. This interpretation is also consistent with the structural observations from the district which suggest that mineralization was emplaced following Laramide orogeny during a time of tectonic relaxation.

The processes forming massive sulphide zones at Copper Prince are interpreted to be somewhat similar to some of those described from Bor, Serbia (Klimentyeva et al. 2021). There, they have been explained as silicate-replacive orebodies resulting from a high-sulphidation overprint on earlier porphyry Cu-Au mineralization. Due to their limited size, such massive sulphide zones can be challenging to explore for, but the exceptional grades make them a worthwhile exploration objective at Copper Creek.

Acknowledgements

This paper is the outcome of exploration by Faraday Copper since Nov. 2021. It builds on a wealth of data and knowledge from preceding companies (see also Riedell et al. 2013). The contributions of the entire geology team at San Manuel Arizona are acknowledged.

References

Anderson ED, Atkinson WW, Marsh T, Iriondo A (2009) Geology and geochemistry of the Mammoth breccia pipe, Copper Creek mining district, southeastern Arizona: evidence for a magmatic–hydrothermal origin. Mineralium Deposita 44:151-170.

Favorito DA, Seedorff E (2018) Discovery of major basement-cored uplifts in the northern Galiuro Mountains, Southeastern Arizona: Implications for regional Laramide deformation style and structural evolution. Tectonics 37:3916-3940.

Klimentyeva D, Driesner T, von Quadt A, Tončić T, and Heinrich C (2021) Silicate-replacive high sulfidation massive sulfide orebodies in a porphyry Cu-Au system: Bor, Serbia. Mineralium Deposita 56:1423-1448.

Mpodozis C, Cornejo P (2012) Cenozoic tectonics and porphyry copper systems of the Chilean Andes. Society of Economic Geologists Special Publication Number 16:329-360.

Proffett JM (2009) High Cu grades in porphyry Cu deposits and their relationship to emplacement depth of magmatic sources. Geology 37:675-678.

Riedell KB, Sandberg RJ, Guthrie JO, Gorecki AD, Lambiotte MJ, Reynolds SJ, Proffett JM, Ybarra SJ, Poulter JE (2013) Early Halo Type Porphyry and Breccia Cu-Mo Mineralization at Copper Creek, Pinal County, Arizona. Extended Abstract SEG 2013 conference, Whistler, BC, Canada, 9 p.

The role of magmatic sulphide saturation in the formation of the supergiant porphyry copper deposits from Central Chile

Yamila Cajal[1,2], **Ian H. Campbell**[1], **Carlos I. Carrasco-Godoy**[1]
[1]*Research School of Earth Sciences, The Australian National University*
[2]*Centre for Ore Deposit and Earth Sciences, University of Tasmania*

Abstract. Porphyry copper deposits have been widely studied; however, it is still unclear why some systems are fertile while others are not. This work explores this question by studying igneous rocks associated with the world's largest and third largest copper deposits, the Rio Blanco and El Teniente Cu deposits, located in Central Chile, with special emphasis on the role that sulphide saturation plays in magma fertility. We provide new whole-rock, major and trace elements data, including platinum group elements from intrusions related to these deposits. The results show that the Rio Blanco and El Teniente magmatic systems reached sulphide saturation early in their evolution. This depleted the magma in Au, relative to Cu, leading to the formation of Cu-dominated deposits. It is concluded that the timing of sulphide saturation did not play a key role in the formation of these deposits because early sulphide saturation did not prevent their formation. Instead, we argue that other factors such as the small amount of sulphide melt to precipitate from the magma and the enormous size of the magma chamber, were responsible for the formation of these supergiant deposits.

1 Introduction

There are several factors that affect the ability of magmas to form a porphyry deposit, such as: the tectonic setting; the depth of magma emplacement; the duration of the magmatic activity; the metal and water content and oxidation state of the magma; among others (e.g. Richards 2003, 2013; Cooke et al. 2005; Audétat and Simon 2012; Wilkinson 2013). Although it is usually the combination and optimization of all these processes that lead to the formation of economic porphyries (Richards, 2003, 2013), this study focuses on the role that the timing of sulphide saturation plays in magma fertility.

Previous studies (e.g. Park et al. 2013, 2019; Cocker et al. 2015; Hao et al. 2017; Lowczak et al. 2018) have shown that the Platinum Group Elements (PGE) can be used to identify the onset of sulphide saturation because they have a strong affinity for immiscible sulphide melts during magmatic differentiation. It has been suggested that if sulphide saturation occurs early in the magmatic evolution, chalcophile elements, including Cu and Au, will be trapped in the magma chamber and, therefore, will not be available to enter the fluid phase when volatile exsolution occurs, which will prevent the formation of an economic deposit (Hamlyn et al. 1985; Park et al. 2013; Cocker et al. 2015; Hao et al. 2017).

This study evaluates the role that the timing of sulphide saturation plays in copper-gold magma fertility in the Andes of Central Chile, where the world's largest copper reserves are found. For this, we have studied igneous rocks associated with the Rio Blanco and El Teniente porphyry copper deposits. We present new whole-rock geochemistry for the intrusions from these deposits, including whole-rock major and trace elements concentrations, with an emphasis on the PGE.

2 Geological setting

The Rio Blanco and El Teniente porphyry copper deposits are located in the Main Cordillera of the Andes of central Chile (Fig. 1). They contain the largest and third largest known concentration of copper in the world, each of them containing more than 100 Mt of this metal (Mudd and Jowitt 2018). Molybdenum is an important by-product.

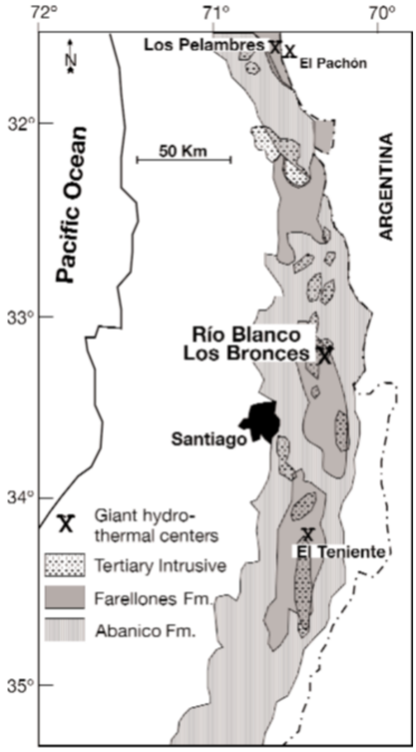

Figure 1. Simplified regional geologic map of the Late Tertiary magmatic belt of Central Chile (Serrano et al. 1996 in Deckart et al. 2005).

These deposits are part of the Miocene-Pliocene metallogenic belt of Central Chile (Maksaev et al. 2004). This belt coincides with the position of the Miocene volcanic centres (Fig. 1), which comprises volcanic and volcaniclastic rocks of the Farellones and Abanico formations (Maksaev et al. 2004). Both units are intruded by late Miocene to early Pliocene plutons (Fig. 1), the late stages of which are temporally and spatially related to the Cu-Mo mineralization (Cannell et al. 2005; Stern et al. 2011; Mpodozis and Cornejo 2012).

At the Rio Blanco-Los Bronces District, the San Francisco Batholith was emplaced between 16.4 ± 0.2 and 8.16 ± 0.45 Ma (Warnaars et al. 1985; Deckart et al. 2005; Toro et al. 2012). The Cu-Mo endowment is hosted in porphyry stocks and breccia pipes that formed between 8.36 ± 0.06 Ma and 4.87 ± 0.02 Ma (Toro et al. 2012; Deckart et al. 2014). The magmatic activity ended with the emplacement of the post-mineralization La Copa Volcanic Complex at 4.92 ± 0.1 to 4.31 ± 0.05 Ma (Warnaars et al. 1985; Deckart et al. 2005; Toro et al. 2012).

The magmatism at El Teniente includes a large pre-mineral intrusive complex that includes the El Teniente Mafic Complex, emplaced at 8.9 ± 1.4 Ma (Stern et al. 2011), and the Sewell Tonalite, which formed between 7.4 ± 1.5 Ma and 6.15 ± 0.08 Ma (Cuadra 1986; Maksaev et al. 2004). Several felsic intrusions, linked to the mineralization were emplaced between 6.46 and 4.82 Ma (Mpodozis and Cornejo 2012). The formation of post-mineralization lamprophyre dikes at 3.85 ± 0.18 Ma (Maksaev et al. 2004) mark the last magmatic pulse in the district (Cuadra 1986).

This long magmatic history and wide range of compositions make these deposits ideal cases to study the role of the timing of sulphide saturation in the formation of porphyry copper deposits.

3 Samples and methods

A total of fifty-eight drill-core samples from both deposits were collected with the support of the Andina and El Teniente divisions of CODELCO, and Exploraciones Mineras Andinas (EMSA). The samples were selected to cover the widest possible range of compositions and to avoid areas with strong hydrothermal alteration. They include the different lithologies recognized in the pre-mineralization and ore-related porphyritic intrusions. In addition, three samples of hydrothermal veins from Rio Blanco were also studied.

The samples were prepared for chemical analyses at the Research School of Earth Sciences (RSES) of the Australian National University (ANU). Approximately 1 kg of sample was crushed and ~200g was milled to the consistency of flour. Major elements were measured by XRF with sample digestion by lithium tetraborate fusion at Intertek Laboratories (Perth, Australia). Trace elements were analysed on lithium tetraborate fused samples and quantified by Laser Ablation Inductively Coupled Plasma Mass Spectrometry (LA-ICP-MS) at RSES-ANU.

The concentrations of PGE, Re and Au were determined using the Ni-sulphide fire assay, isotope dilution method (NiS-FA-ID) described by Park et al. (2012), which allows the determination of PGE at ultra-low concentrations (pg/g levels). For the measurements, two quadrupole ICP-MS systems were used: An Agilent 7700x and a ThermoFisher iCap RQ, both at RSES-ANU. Duplicate analyses, procedural blanks and the reference material TDB-1 (CANMET diabase) were analysed in each analytical session to assess heterogeneity, contamination, accuracy and precision. The method detection limits (MDL) were calculated as half the difference between the highest and lowest values of the laboratory historical procedural blanks.

4 Results and discussions

4.1 Major and trace element geochemistry

The samples have different degrees of differentiation with compositions that range from basalt to rhyolite. The MgO contents in the samples range from 2.83 to 0.42 wt.% for Rio Blanco and from 5.63 to 0.62 wt.% for El Teniente.

The general coherence between the geochemical data and particularly, the sub-parallel rare earth elements (REE) and multi-incompatible elements patterns, indicate that the pre-mineralization and the porphyritic intrusions are co-genetic for each deposit. Although there is considerable scatter in the data, the concentrations of most of the major and trace elements vary continuously with decreasing MgO wt.%, which suggests that fractional crystallization dominated the observed variations.

4.2 PGE, Re and Au geochemistry

Most of the Ir, Rh and Ru contents of the samples are close to or below detection limits (b.d.l.) and for this reason, will not be discussed further. The Pd and Pt abundances in the Rio Blanco samples do not show any clear trend with decreasing MgO until ~1.4 wt.%, when the Pd and Pt values fall with decreasing MgO. Rhenium and Au concentrations in these samples are scattered, and they do not exhibit a clear trend. Although some scatter, at El Teniente District there is an overall decrease in the concentrations of Pt, Pd, Re and Au with decreasing MgO in the high MgO pre-mineralization intrusions, which suggests that sulphide saturation occurred early in the El Teniente magmatic system.

Figure 2 compares the variations in Pd and Pt in the Rio Blanco and El Teniente samples as a function of MgO with samples from Pual-Ridge and Niuatahi-Motutahi oceanic arc lavas (Park et al. 2013, 2015); the intrusions related to El Abra (Cocker et al. 2015) and Escondida (Hao et al. 2019) porphyry copper deposits and the Sanim and Sanyo-Ryoke barren suites (Park et al. 2019). The Rio Blanco and El Teniente intrusions show Pd and Pt concentrations that are about one order of magnitude lower than pre-sulphide saturation samples from Pual-Ridge and Niuatahi-Motutahi lavas but are similar to the post-sulphide saturation samples from the same locations. We interpret this to indicate that sulphide saturation occurred early in the Rio Blanco and El

Teniente magmatic systems, which caused an overall decrease in the PGE content of the magma.

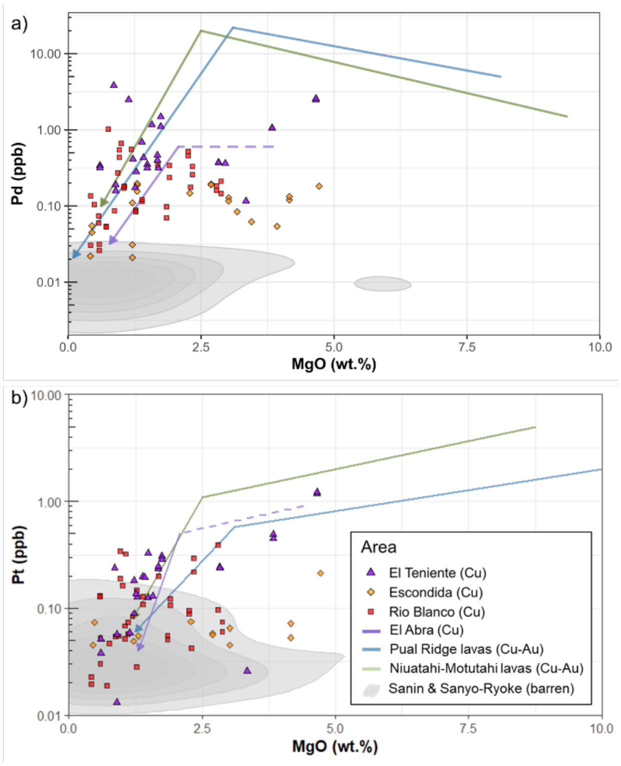

Figure 2. (a) Pd and (b) Pt versus MgO for the Rio Blanco and El Teniente intrusions (this study) compared to Escondida, (Hao et al. 2019) and El Abra (Cocker et al. 2015) porphyry copper deposits; the Pual Ridge and Niuatahi-Motutahi (Park et al. 2013, 2015) Cu-Au lavas; and the Sanin and Sanyo-Ryoke barren suites (Park et al. 2019). The Pd-Pt line trends are from the cited authors.

Sulphides cumulates also sequester Au and Cu, but their partition coefficients into sulphide melts are about one and two orders of magnitude lower than Pd and Pt (Mungall and Brenan 2014), respectively. Elements with lower partition coefficients will enter the immiscible sulphide melt at a lower rate. We suggest that the low Au content of the Rio Blanco and El Teniente ores are due to this element being sequestered by cumulus sulphides in a putative lower magma chamber. Here, Au remains trapped, and inaccessible to the ore-fluids that exsolve from upper crustal magma systems.

4.3 Implications for ore-forming processes

Previous studies have suggested that the timing of sulphide saturation relative to volatile exsolution, together with the amount of sulphide that separates from the melt, can play a critical role in determining the fertility of felsic magma systems (Park et al. 2015, 2019; Cocker et al. 2015; Hao et al. 2017; Lowczak et al. 2018). Here we have interpreted the Rio Blanco and El Teniente magmatic systems to have reached early sulphide saturation, before the MgO content of the magma had fallen to 3 and 6 wt.% MgO, respectively, in a deep, unexposed lower magma chamber. Although the Rio Blanco and El Teniente magmatic system experienced early sulphide saturation, which must have resulted in a large fraction of the Cu being locked in the cumulates of the lower crustal magma chamber, this has not prevented the formation of two of world's largest copper deposits.

One possibility is that the amount of sulphide to precipitate from the melt was small, so it had little effect on the concentration of copper in the melt, due to its low partition coefficient in sulphide melts compared to Pd and Au. We suggest that early sulphide saturation caused an important depletion in the Pd and Au content of the residual melt, but it did not cause an important decrease in the Cu content due to its lower partition coefficient into immiscible sulphide melts compared to Pd and Au (Mungall and Brenan 2014; Cocker et al. 2015). Then, by the time that the evolving melt reached volatile exsolution, the magma still contained enough Cu to form a porphyry deposit. Furthermore, the significant decrease in the Au content of the magma compared to Cu is likely to have been responsible for the formation of a Cu-dominated porphyry deposit, rather than a Cu-Au one.

Although several factors may have contributed to the formation of these supergiant porphyry copper deposits, we suggest that the size of the magma chamber and its long duration were the most important. Assuming a magma that contains 50 ppm of Cu, a minimum of 1,400 km^3 and 761 km^3 are required to produce the ~184 and 100 Mt of Cu in the Rio Blanco and El Teniente deposits, respectively. However, this back-of-the-envelope calculation assumes that Cu was extracted with 100% efficiency, which is highly unlikely. A more realistic minimum volume is ten times this or 14,000 and 7,610 km^3 respectively for each of the ore systems. Although we cannot calculate the exact size of the magma chamber that produced these deposits, it is clear that it was enormous.

5 Conclusions

The results from this study show that the magmas that produced the pre-mineralization and ore-related porphyries at the Rio Blanco and El Teniente deposits are co-magmatic. The overall low concentrations of PGE show that the Rio Blanco and El Teniente magmatic systems reached sulphide saturation at an early stage of their evolution, before their MgO content fell to 2.8 and 5.7 wt.% MgO, respectively. We interpret this to have occurred in a deep and unexposed lower magma chamber, where the sulphide cumulates trapped a significant proportion of the PGE, Au and Cu content in the magma. Gold was more affected than Cu due to its higher partition coefficient in sulphide melts, which explains why the Rio Blanco and El Teniente are Cu-dominant deposits with little Au.

The results from our study show that early sulphide saturation did not prevent the formation of the Rio Blanco and El Teniente deposits and therefore, we conclude that the timing of sulphide saturation did not play a key role in the formation of the supergiant porphyry copper deposits in Central Chile. We propose that there are other factors controlled the formation of these deposits, including the small amount of sulphide melt that formed, the large size of the magma chamber and the long duration of the magmatic activity.

Acknowledgements

This study was financed by Australian Research Council Discovery Project [DP170103140] to Ian Campbell and Andrew Berry and by the 2020 SEG Student Research Grant from the Hugh McKinstry Fund to Yamila Cajal. The authors would like to acknowledge the Andina and El Teniente divisions of CODELCO and the Exploraciones Mineras Andinas for providing the samples for this study.

References

Audétat A, Simon AC (2012) Magmatic controls on porphyry copper genesis. In: Hedenquist JW, Harris M, Camus F (eds) Geology and genesis of major copper deposits and districts of the world: a tribute to Richard H. Sillitoe. Society of Economic Geologists, Special Publication, pp 553–572

Cannell J, Cooke DR, Walshe JL (2005) Geology, Mineralization, Alteration, and Structural Evolution of the El Teniente Porphyry Cu-Mo Deposit. Economic Geology 100:979–1003

Cocker HA, Valente DL, Park J-W, Campbell IH (2015) Using platinum group elements to identify sulfide saturation in a porphyry Cu system: the El Abra porphyry Cu deposit, Northern Chile. J Petrology 56:2491–2514. https://doi.org/10.1093/petrology/egv076

Cooke DR, Hollings P, Walshe JL (2005) Giant porphyry deposits: characteristics, distribution, and tectonic controls. Economic Geology 100:801–818

Cuadra P (1986) Geocronología K-Ar del Yacimiento El Teniente y áreas adyacentes. Revista Geologica de Chile 27:3–26

Deckart K, Clark AH, Aguilar CA, et al (2005) Magmatic and hydrothermal chronology of the giant Río Blanco porphyry copper deposit, Central Chile: implications of an integrated U-Pb and 40Ar/39Ar database. Economic Geology 905–934

Deckart K, Silva W, Spröhnle C, Vela I (2014) Timing and duration of hydrothermal activity at the Los Bronces porphyry cluster: an update. Miner Deposita 49:535–546. https://doi.org/10.1007/s00126-014-0512-9

Hamlyn PR, Keays RR, Cameron WE, et al (1985) Precious metals in magnesian low-Ti lavas: implications for metallogenesis and sulfur saturation in primary magmas. Geochimica et Cosmochimica Acta 49:1797–1811. https://doi.org/10.1016/0016-7037(85)90150-4

Hao H, Campbell IH, Park J-W, Cooke DR (2017) Platinum-group element geochemistry used to determine Cu and Au fertility in the Northparkes igneous suites, New South Wales, Australia. Geochimica et Cosmochimica Acta 216:372–392. https://doi.org/10.1016/j.gca.2017.05.009

Hao H, Campbell IH, Richards JP, et al (2019) Platinum-group element geochemistry of the Escondida Igneous Suites, Northern Chile: implications for ore formation. J Petrology 60:487–514. https://doi.org/10.1093/petrology/egz004

Lowczak JN, Campbell IH, Cocker H, et al (2018) Platinum-group element geochemistry of the Forest Reef Volcanics, southeastern Australia: Implications for porphyry Au-Cu mineralisation. Geochimica et Cosmochimica Acta 220:385–406. https://doi.org/10.1016/j.gca.2017.09.052

Maksaev V, Munizaga F, Mcwilliams M, et al (2004) New Chronology for El Teniente, Chilean Andes, from U-Pb, 40Ar/39Ar, Re-Os, and Fission-Track Dating: Implications for the Evolution of a Supergiant Porphyry Cu-Mo Deposit. In: Economic Geology. Society of Economic Geologists, Special Publication, pp 15–54

Mpodozis C, Cornejo P (2012) Cenozoic tectonics and porphyry copper systems of the Chilean Andes. In: Hedenquist JW, Harris M, Camus F (eds) Geology and genesis of major copper deposits and districts of the world: a tribute to Richard H. Sillitoe. Society of Economic Geologists, Special Publication, p 32

Mudd GM, Jowitt SM (2018) Growing Global Copper Resources, Reserves and Production: Discovery Is Not the Only Control on Supply. Economic Geology 113:1235–1267. https://doi.org/10.5382/econgeo.2018.4590

Mungall JE, Brenan JM (2014) Partitioning of platinum-group elements and Au between sulfide liquid and basalt and the origins of mantle-crust fractionation of the chalcophile elements. Geochimica et Cosmochimica Acta 125:265–289. https://doi.org/10.1016/j.gca.2013.10.002

Park J-W, Campbell IH, Arculus RJ (2013) Platinum-alloy and sulfur saturation in an arc-related basalt to rhyolite suite: Evidence from the Pual Ridge lavas, the Eastern Manus Basin. Geochimica et Cosmochimica Acta 101:76–95. https://doi.org/10.1016/j.gca.2012.10.001

Park J-W, Campbell IH, Kim J, Moon J-W (2015) The role of late sulfide saturation in the formation of a Cu- and Au-rich magma: insights from the platinum group element geochemistry of Niuatahi-Motutahi Lavas, Tonga Rear Arc. Journal of Petrology 56:59–81. https://doi.org/10.1093/petrology/egu071

Park J-W, Campbell IH, Malaviarachchi SPK, et al (2019) Chalcophile element fertility and the formation of porphyry Cu ± Au deposits. Miner Deposita 54:657–670. https://doi.org/10.1007/s00126-018-0834-0

Richards JP (2003) Tectono-magmatic precursors for porphyry Cu-(Mo-Au) deposit formation. Economic Geology 98:1515–1533

Richards JP (2013) Giant ore deposits formed by optimal alignments and combinations of geological processes. Nature Geosci 6:911–916. https://doi.org/10.1038/ngeo1920

Serrano L, Vargas R, Stambuk V, et al (1996) The late Miocene to early Pliocene Rio Blanco-Los Bronces Cu Deposit, Central Chilean Andes. In: Camus F, Sillitoe RH, Petersen R (eds) Andean copper deposits: new discoveries, mineralization, styles and metallogeny. Society of Economic Geology Special Publication

Stern CR, Skewes MA, Arévalo A (2011) Magmatic Evolution of the Giant El Teniente Cu–Mo Deposit, Central Chile. Journal of Petrology 52:1591–1617. https://doi.org/10.1093/petrology/egq029

Toro JC, Ortúzar J, Zamorano J, et al (2012) Protracted magmatic-hydrothermal history of the Río Blanco-Los Bronces District, Central Chile: development of world's greatest known concentration of copper. In: Geology and genesis of major copper deposits and districts of the world: a tribute to Richard H. Sillitoe. Society of Economic Geologists, Special Publication, pp 105–126

Warnaars FW, Holmgren D. C, Barassi F. S (1985) Porphyry copper and tourmaline breccias at Los Bronces-Rio Blanco, Chile. Economic Geology 80:1544–1565. https://doi.org/10.2113/gsecongeo.80.6.1544

Wilkinson JJ (2013) Triggers for the formation of porphyry ore deposits in magmatic arcs. Nature Geosci 6:917–925. https://doi.org/10.1038/ngeo1940

Metallogenic model of the Eocene Zn-Pb(-Ag) Santa María and Antares bodies of the Velardeña skarn district (Durango, Mexico)

Néstor Cano[1], Antoni Camprubí[2], Eduardo González-Partida[3], Pura Alfonso[4], Daniel P. Miggins[5], Edith Fuentes-Guzmán[1,2,6], Edith Cienfuegos-Alvarado[2,6], Ana K. González-Ambrocio[1], and Vanessa Colas[1]
[1]*Posgrado en Ciencias de la Tierra, Universidad Nacional Autónoma de México. Mexico City, Mexico.*
[2]*Instituto de Geología, Universidad Nacional Autónoma de México. Juriquilla, Mexico.*
[3]*Centro de Geociencias, Universidad Nacional Autónoma de México. Mexico City, Mexico.*
[4]*Departament d'Enginyeria Minera, Industrial i TIC, Universitat Politècnica de Catalunya. Manresa, Catalonia, Spain.*
[5]*College of Earth, Ocean, and Atmospheric Sciences, Oregon State University. Corvallis, United States.*
[6]*Laboratorio Nacional de Geoquímica y Mineralogía. Mexico City, Mexico.*

Abstract. The Santa María and Antares Zn-Pb skarn deposits from the Velardeña mining district are located in central-NW Mexico. They lie 470 m apart from each other along the contact between Oligocene felsic bodies and Cretaceous limestones. The prograde stage in these systems was promoted by fluids at ~600 °C and 15 wt. % NaCl equiv., and was dominated by garnet-wollastonite±vesuvianite±clinopyroxene and biotite±K-feldspar±magnetite assemblages. The retrograde stage formed by fluids around 400 °C and ~20-50 wt. % NaCl equiv., is characterized by chlorite-amphibole-epidote-calcite-quartz-sericite-adularia-fluorite-muscovite along with sphalerite-pyrite-galena-pyrrhotite-arsenopyrite-chalcopyrite±fahlore±Bi-Sb-sulfosalts assemblages. $\delta^{18}O_{calcite}$ data between 15 and 20 ‰ in Santa María, and between 10 and 15 ‰ in Antares show a less-modified magmatic affinity for the latter. $\delta^{13}C_{calcite}$ values between 0 and -9 ‰ register recycling processes of sedimentary C. Moreover, $\delta^{34}S_{VCDT}$ values between -3 and 2 ‰ revealed a magmatic source for S. Altogether, these data suggest that, in Santa María, magmatic-derived fluids actively interacted with the wall rocks, which did not occur at Antares. In both bodies, ore deposition was triggered by cooling and neutralization of the magmatic derived fluids. The $^{40}Ar/^{39}Ar$ ages for adularia at ~37.5 Ma place the deposits within the Eocene-early Miocene metallogenetic epoch of central-NW Mexico.

1 Introduction

Skarn deposits are governed by diverse variables that control the evolution and type of mineralization —i.e., temperature and depth of formation, nature of wall rocks, $fO_2 – fS_2$ of involved fluids, and proximity to the heat/fluids source (Meinert et al. 2005). Sulfide-rich skarn deposits are common in central-NW Mexico, where silicic flare-ups during the Eocene-Oligocene intercepted carbonates units of the "*Sector Transversal de Parras*" (STP; Camprubí 2013).

The Zn-Pb±Ag Velardeña Mining District is located in Durango state and encompasses the Santa María and San Lorenzo ranges (Figure 1A). Skarn systems in the Santa María range are present along the contact between Cretaceous limestones (Cuesta del Cura Formation) and felsic intrusions from the Velardeña Intrusive Complex (Figure 1B). The combined resource of the Santa María and Antares deposits is 8 Mt, grading at 25 g/t Ag, 0.3-0.6 wt. % Pb, and 5-6 wt. % Zn.

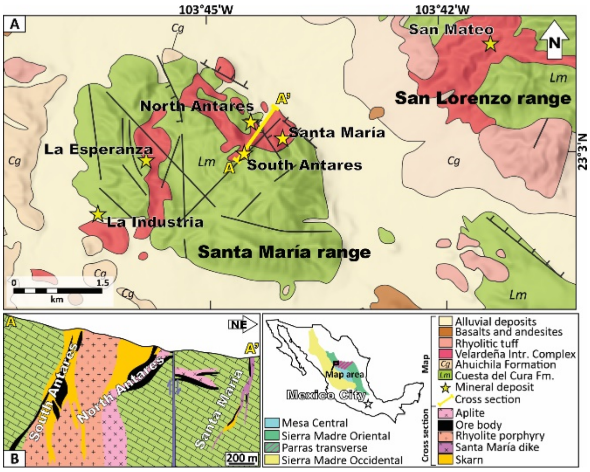

Figure 1. Geological map (A) and cross section (B) depicting the Antares and Santa María skarn deposits.

In the present study, we analyzed drill-core sample suites from the Antares and Santa María bodies through petrography, fluid inclusion studies, EPMA mineral chemistries, stable isotope analyses, and $^{40}Ar/^{39}Ar$ geochronology. Our results underpin the first comprehensive genetic model for the deposits. In addition, these data shed new light on the processes involved into the development of a Zn-Pb skarn system consisting of orebodies with distinct features. The orebodies at Antares are associated with a "typical" stock, whereas those at Santa María are the result of a smaller "satellite" intrusive (Figure 1B). This allows to assess, by comparison, two mineralization endmembers whose mineralizing fluids show variably modified magmatic signals due to interaction with the host limestones. Additionally, detailed studies on fluid evolution and mineral assemblages revealed peculiarities regarding physicochemical conditions of the fluids during ore precipitation (*e.g.*, moderate-high temperature and salinity) —when compared to "traditional" Zn-Pb skarns (Chang et al. 2019).

2 Methodology

A total of 15 drill holes across the Santa María and Antares orebodies were provided by Industrias Peñoles. Quantitative mineral chemistry analyses were performed with a JEOL JXA-8900R electron probe micro-analyzer at the Laboratorio de Geoquímica y Mineralogía (LANGEM) with as analytical condition: 20KeV, 20nA beam current, and 40s acquisition time.

Carbon and oxygen stable isotopes were analyzed in 82 samples of calcite from the wall-rocks and skarn system. Measurements were carried out at the LANGEM using a Thermo Finnigan MAT 253 mass spectrometer coupled with a Gas Bench II.

Sulfur isotopes were carried out in 61 pure sulfide separates from massive ores and mineralized veins. Analyses were performed at the Centres Científics i Tecnològics (Universitat de Barcelona) with a Delta Plus XP Thermo Fisher mass spectrometer coupled with a TC-EA pyrolizer and a Carlo Erba 1108 elemental analyzer.

Fluid inclusion studies were carried out in 23 samples using a microscope coupled with a Linkam THMSG 600 stage, available at the LANGEM. Salinities were calculated using ice melting temperature or, when present, halite dissolution temperature following Bodnar (1993).

Two samples of adularia from the ore stage at Santa María were collected for $^{40}Ar/^{39}Ar$ dating. The analyses were performed at the Geochronology Laboratory of Oregon State University (OSU) on samples that had been previously irradiated at a TRIGA CLICIT nuclear reactor available at the Radiation Center of the OSU. A FCT-NM (28.201 ± 0.023 Ma) neutron fluence monitor was employed. The ages were obtained using an ARGUS-VI multi-collector mass spectrometer. Irradiated samples were placed in a high-vacuum sample chamber and incrementally heated by a 25 W Synrad CO_2 laser.

3 Results and discussion

3.1 Ore and gangue assemblages

Santa María

-Exoskarn: The prograde mineralogy consists of grossular-andradite, wollastonite, and vesuvianite, plus lesser calcite and quartz (Figure 2). The retrograde stage obliterates prograde minerals in most cases and consist of the following mineral assemblages: 1) garnet, tremolite, and calcite; 2) sericite, chlorite, calcite, quartz, tremolite, and lesser biotite, epidote, and muscovite; 3) actinolite, sphalerite, quartz, and pyrite; and 4) sulfides and sulfosalts accompanied by chlorite, fluorite, quartz, calcite, epidote, tremolite, and muscovite.

-Endoskarn: The prograde stage consists only of local biotitic alteration. In contrast, the retrograde stage consists of 1) actinolite, quartz, pyrite, and lesser scapolite, followed by 2) pseudorhombohedral adularia, fluorite, quartz, muscovite, and calcite. The latter assemblage is conspicuous and tightly related to ore deposition.

-Mineralization: Sulfides and sulfosalts formed massive replacement zones that obliterate any remaining sedimentary or igneous textures. Pyrite and sphalerite dominate the ore assemblages and coexist with variable amounts of galena, arsenopyrite, pyrrhotite, chalcopyrite, tetrahedrite-hakite-freibergite, lillianite-gustavite, and heyrovskýite-eskimoite (Figure 3B-C, E). Fahlore and arsenopyrite geothermometry yielded 170-300 °C and 350-490 °C, respectively (Figure 3D, F).

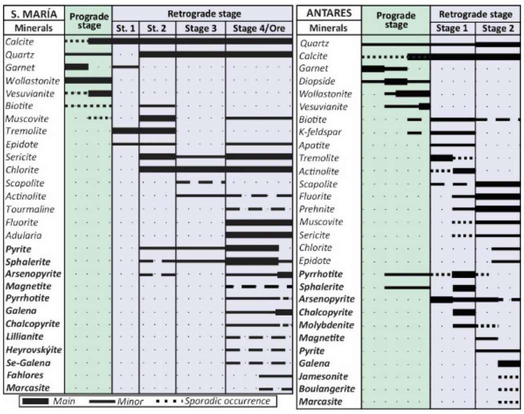

Figure 2. Paragenetic sequences for both orebodies.

Antares

-Exoskarn: Prograde assemblages are dominated by garnet, clinopyroxene, wollastonite, and vesuvianite. In some cases, pyrrhotite and sphalerite crystallized during garnet formation, and are observed as tiny solid inclusions, rims, or intercrystalline fillings. The retrograde event consists of actinolite, tremolite, quartz, calcite, epidote, and chlorite that accompany the most economically important mineralization in the orebody.

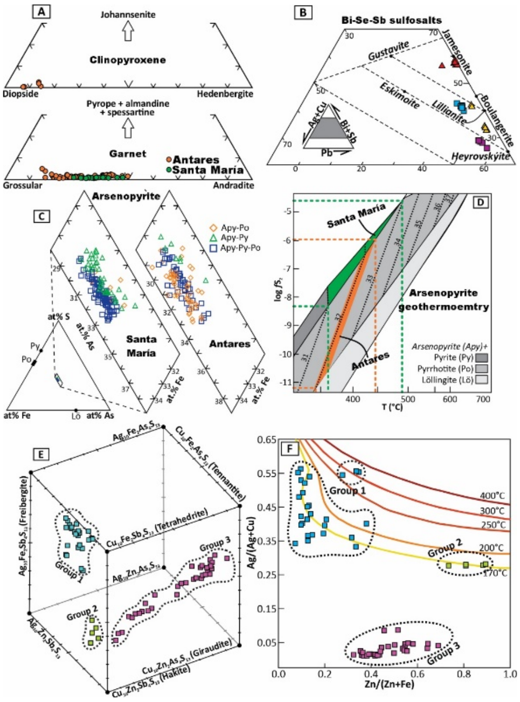

Figure 3. Diagrams for garnet-clinopyroxene (A), Bi-Se-Sb sulfosalts (B), arsenopyrite (C), and fahlores (E). Arsenopyrite (D) and fahlore (F) geothermometry.

-Endoskarn: Prograde minerals are grossular-andradite and diopside with locally pyrrhotite, arsenopyrite, and Fe-rich sphalerite. Further, biotite and K-feldspar alteration was produced at the end of the prograde stage and became more widespread during the retrograde stage, which is marked by 1) tremolite-actinolite, fluorite, and apatite, and 2) muscovite, sericite, prehnite, scapolite, and pyrite assemblages.

-Mineralization: Massive sulfides and minor sulfosalts crystallized during two substages: 1) pyrrhotite, arsenopyrite, Fe-rich sphalerite, chalcopyrite, molybdenite, and 2) arsenopyrite, pyrite, galena, and minor pyrrhotite, molybdenite, jamesonite, boulangerite, and marcasite (Figure 1B-C). Arsenopyrite geothermometry yielded 350-450 °C (Figure 1D).

3.2 Fluid inclusion studies

Santa María

-Prograde stage: Secondary L + V fluid inclusions hosted in garnet exhibit ice melting temperatures (*Tmi*) averaging -28.9 °C (28.1 wt.% NaCl equiv.). The average homogenization temperature (*Th*) to liquid is 437 °C (Figure 4A).

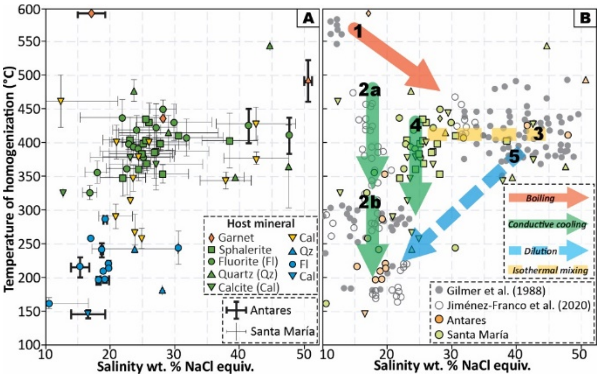

Figure 4. *Th vs.* salinity plots with evolutionary trends (B).

-Ore stage: primary and pseudosecondary L + V fluid inclusion assemblages (FIAs) hosted in sphalerite, calcite, quartz, and fluorite from the ore stage have eutectic temperatures (*Te*) between -120 and -90 °C, suggesting the occurrence of methane (confirmed through FT-IR spectroscopy analyses). The average *Tmi* are -19.2 ± 9.4 °C (1σ) in FIAs hosted in calcite, -26.5 ± 5.3 °C in sphalerite, -22,8 ± 5.8 °C in fluorite, and -38.1 ± 11.9 °C in quartz, equivalent to salinities of 21.0 ± 7.5, 26.6 ± 3.7, 24.0 ± 4.1, and 36.8 ± 10.2 wt. % NaCl equiv., respectively. The very low *Tmi* suggests abundant $CaCl_2$ in the salt assemblage, which is also revealed by hydrohalite melting temperatures around -50 °C approaching the H_2O-NaCl-$CaCl_2$ eutectic point (-51.0 °C). This could also explain the obtained high salinities in the absence of daughter halite crystals. Homogenization to liquid occurred at 374 ± 7 °C in FIAs hosted in calcite, 392 ± 23 °C in sphalerite, 399 ± 36 °C in fluorite, and 431 ± 81 °C in quartz.

Antares

-Prograde stage: FIAs enclosed in garnet display *Te* around -40.0 °C, thus indicating the occurrence of bivalent cation chlorides (i.e., $FeCl_2$ or $MgCl_2$). The *Tmi* range between -16.7 and -11.4 °C (15.4 and 20.0 wt. % NaCl equiv.), and *Th* varies between 595 and 598 °C. However, several fluid inclusions remained biphasic at 600 °C.

-Ore stage: Primary and pseudosecondary FIAs in fluorite from the massive ores contain daughter halite, sylvite, and two unidentified solids. The *Te* at ~-38.4 °C and -100.0 °C suggest the presence of $MgCl_2$ or $FeCl_2$ plus NaCl, KCl, and, perhaps, CH_4. The average *Tmi* and *Th* are -16.3 ± 0.2 °C and 416 ± 10 °C, respectively. Halite dissolution occurs at ~379 °C and sylvite between 195 and 299 °C, equivalent to salinities of 45.5 wt. % NaCl equiv.

3.3 C, O, and S stable isotopes

Santa María

Limestones display $\delta^{18}O_{VSMOW}$ from 18.5 to 19.5 ‰, and $\delta^{13}C_{VPDB}$ from -3.4 to 0.7 ‰. Calcite from the exoskarns has $\delta^{18}O_{VSMOW}$ between 14.8 and 18.1 ‰, and $\delta^{13}C_{VPDB}$ between -6.9 and -3.3 ‰, plotting near or within the magmatic fluids box. Marbles show $\delta^{18}O_{VSMOW}$ between 14.6 and 21.3 ‰, and $\delta^{13}C_{VPDB}$ between -8.0 and -0.5 ‰ —i.e., mixed signatures between limestones and magmatic fluids— similar to calcite from massive sulfides ($\delta^{18}O_{VSMOW}$ from 14.6 to 21.1 ‰, and $\delta^{13}C_{VPDB}$ from -2.6 to -0.2 ‰).

$\delta^{34}S_{VCDT}$ values range between -3.2 and 1.7 ‰, matching those of magmatic S (~0‰; Hoefs, 2009). The $\delta^{34}S_{VCDT}$ values in arsenopyrite range between -2.6 and -0.3 ‰, between -2.8 and 0.5 ‰ in pyrite, between -0.7 and -0.2 ‰ in pyrrhotite, between -3.2 and 1.2 ‰ in sphalerite, at -1.4 ‰ in galena, and at -0.4 ‰ in marcasite.

Antares

Limestones display average $\delta^{13}C_{VPDB}$ values at 14.1 ‰ and $\delta^{18}O_{VSMOW}$ at -0.3 ‰. Calcite from prograde skarns yielded $\delta^{18}O_{VSMOW}$ between 9.4 and 15.4 ‰, and $\delta^{13}C_{VPDB}$ between -7.0 and -0.6 ‰ —that is, within the fields of magmatic fluids. Similarly, calcite from marble yielded consistent $\delta^{18}O_{VSMOW}$ at ~13.1 ‰ and $\delta^{13}C_{VPDB}$ between -5.6 and -0.1 ‰, partly overlapping the magmatic fluids box. Moreover, calcite from massive sulfides yielded $\delta^{18}O_{VSMOW}$ between 12.2 and 20.1 ‰, and $\delta^{13}C_{VPDB}$ between -8.1 and 0.4 ‰, similar to magmatic fluid signatures. Overall, calcites from Antares show lower isotopic values than at Santa María, revealing less modified magmatic signals.

$\delta^{34}S_{VCDT}$ data range between -2.8 and 1.7 ‰ (magmatic S; Hoefs, 2009). $\delta^{34}S_{VCDT}$ values in arsenopyrite range between -1.5 and -0.6 ‰, between -1.4 and 1.2 ‰ in chalcopyrite, between -0.9 and 1.7 ‰ in galena, between -2.8 and 0.4 ‰ in pyrrhotite, between 0.0 and 0.4 ‰ in pyrite, between -1.9 and 1.5 ‰ in sphalerite, at -0.4 ‰ in marcasite, and at 0.8 ‰ in molybdenite.

3.4 $^{39}Ar/^{40}Ar$ geochronology

Two samples of pseudorhombohedral adularia from the ore stage at Santa María yielded plateau ages at 37.48 ± 0.09, 37.62 ± 0.09 and 37.58 ± 0.09 Ma, and inverse isochron ages at 37.47 ± 0.13 and 37.64 ± 0.1 Ma. This reveals that the ore event at Santa María occurred during the latest Eocene.

4 Evolution of the skarn deposits

The Santa María and Antares Zn-Pb±Ag skarn deposits developed during the intrusion of felsic subalkaline-alkaline magmas into hypabyssal Cretaceous carbonates of the Sector Transversal de Parras (STP) during the Eocene-Oligocene. The age dates presented in this study are similar to other polymetallic skarn deposits along the STP (*e.g.*, Concepción del Oro, Mazapil, and Mapimí; see references in Camprubí 2013).

The intrusion of igneous bodies into carbonate rocks generated extensive marble aureoles and was followed by metasomatism. Metasomatic pulses were produced by deep magmatic-exsolved fluids that flowed upwards along lithological contacts and reacted with limestones and, to a lesser extent, felsic rocks, producing high-temperature calcsilicate assemblages (Figures 2, 5). This process was promoted by single-phase fluids with moderate salinities. Albeit sulfides are normally scarce during the prograde stage in skarns, early pyrrhotite and sphalerite were partly coeval with garnet at Antares.

The ore event occurred during the retrograde stage, as is usually observed in skarn deposits elsewhere (Meinert et al. 2005). Ore stages at Antares and Santa María were produced by cyclic fluid pulses at intermediate temperatures (360-430 °C). These temperatures for the ore-stage are atypically high compared to what have been found in many Zn-Pb skarn deposits worldwide (*e.g.*, Shu et al. 2021). Nevertheless, other relatively “high”-temperature deposits have been documented (*e.g.*, El Mochito, Honduras; Samson et al. 2008).

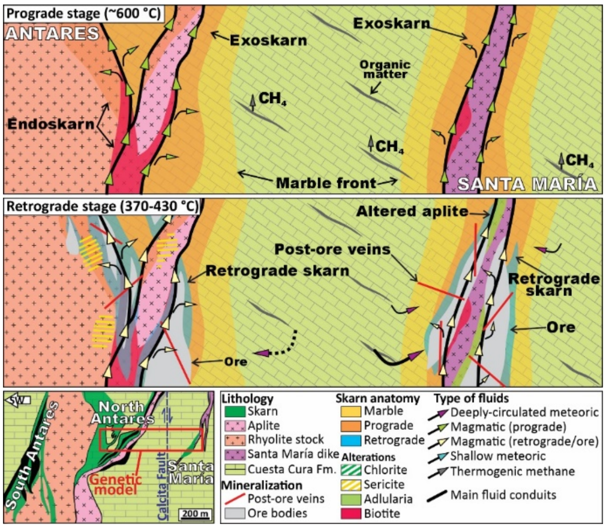

Figure 5. Genetic model for Antares and Santa María.

Hypogene ores consisting of sphalerite (either Fe-rich or Fe-poor) – pyrite – arsenopyrite ± fahlores at Santa María and pyrrhotite – Fe-rich sphalerite – arsenopyrite at Antares, suggest that, during the ore stage, the Antares body evolved along a low sulfidation trend, whereas Santa María records a transition from low- to intermediate-sulfidation as the system cooled (Einaudi et al. 2003).

The evolution of the fluids in each ore body behaved differently. At Antares, magmatic-derived fluids evolved along deep boiling (arrow 1 in Figure 4B) and cooling paths (arrow 2a-2b). Later, boiled-off fluids experienced dilution with meteoric waters (arrow 5 in Figure 4B). Magmatic waters at Santa María followed a boiling path (arrow 1) that led to isothermal mixing with deeply-circulated meteoric fluids (arrow 3). Afterwards, cooling processes became dominant (arrow 4). In both ore bodies, ore deposition was mostly triggered by cooling and neutralization of the mineralizing fluids.

5 Conclusions

The Santa María and Antares ore bodies are Zn-Pb±Ag skarn deposits spatially linked to aplite dikes and rhyolitic stocks related to the initial silicic flare-ups of the Sierra Madre Occidental. Both deposits were formed in two major stages: prograde and retrograde/ore. The prograde stage was promoted by magmatic fluids that generated high-temperature alterations, which later evolved into cooler fluids that produced the retrograde and ore stages. Carbon-O isotopic data denote a magmatic signature in calcite from Antares, contrasting with trends at Santa María that are greatly influenced by the host limestones. Sulfur isotopes indicate a magmatic source for S.

Acknowledgements

CONACyT supported N.C. with a grant during his M.Sc. research, which was focused on this investigation. The study was supported by means of personal allocations to UNAM academicians. UNAM academics: María Colín, Alexander Iriondo, Carlos Linares, and Juan Vázquez are acknowledged for their kind assistance in sample preparation and laboratory analyses. We thank Industrias Peñoles for their help during the visit at mine’s facilities.

References

Bodnar R (1993) Revised equation and table for determining the freezing point depression of H_2O-NaCl solutions. Geochim Cosmochim Ac, 57(3):683–684.

Camprubí A (2013) Tectonic and metallogenic history of Mexico. Soc Econ Geol Spec Pub, 17:201–243.

Chang Z, Shu Q, Meinert, L (2019) Skarn deposits of China; Soc Econ Geol Spec Pub, 22:189–234.

Einaudi M, Hedenquist J, Inan E (2003) Sulfidation state of fluids in active and extinct hydrothermal systems: transitions from porphyry to epithermal environments. Soc Econ Geol Spec Pub, 10: 1–51.

Hoefs J (2009) Stable isotope geochemistry Sixth edition. Springer, Berlin Heidelberg.

Meinert L, Dipple G, Nicolescu S (2005) World skarn deposits. Econ Geol, 100th Anniversary Volume:299–336.

Samson I, Williams-Jones A, Ault K, Gagnon J, Fryer, B (2008) Source of fluids forming distal Zn-Pb-Ag skarns: Evidence from laser ablation-inductively coupled plasma-mass spectrometry analysis of fluid inclusions from El Mochito, Honduras. Geology, 36:947–950.

Shu Q, Chang Z, Mavrogenes J (2021) Fluid compositions reveal fluid nature, metal deposition mechanisms, and mineralization potential: An example at the Haobugao Zn-Pb skarn, China. Geology, 49:473–477.

Tracking deep crustal evolution in porphyry copper systems: preliminary results from whole rock geochemistry and zircon trace elements in the Tres Cerrillos Cu-Mo prospect, Western Cordillera of Ecuador.

Hugo Carrasco[1], Massimo Chiaradia[1], Francesca del Rio[1], Angelo Aguilar[2], Sergio Cubelli[2], Carolina Rodríguez[2], Carlos Urrutia[2].
[1]Department of Earth Sciences, University of Geneva, rue des Maraîchers 13, 1205, Geneva, Switzerland.
[2]Corporación Nacional del Cobre de Chile (CODELCO), Huérfanos 1270, Santiago, Chile.

Abstract. The Tres Cerrillos prospect is a Miocene porphyry copper system located in the Western Cordillera of Ecuador, which is under an exploration program by EMSAEC (Codelco). Preliminary results from whole rock geochemistry and zircon trace elements of this magmatic-hydrothermal system show that porphyritic and precursor intrusions underwent a deep crustal evolution with suppression of plagioclase, and possibly involving some garnet fractionation in addition to amphibole. Whole rock geochemical proxies (Sr/Y, La/Y, V/Sc and Sr/Zr) and zircon trace elements suggest a fertile magmatic suite for this prospect. Future work will consist of placing mineral chemistry (e.g., zircon and apatite) within the frame of high precision CA-ID-TIMS U-Pb zircon geochronology to refine fertility indicators that can potentially be used as a proxy for metal endowments.

1 Introduction

Magmatism in thick convergent margins is a major process in the development of porphyry copper deposits (PCD) and large eruptions. Both require large magma volumes accumulated at upper crustal levels from magmas that have previously evolved in mid- to lower crustal zones (Chiaradia and Caricchi 2022). From the economic point of view, understanding the temporal evolution of fertile magmatic systems associated with supergiant PCD (>10 Mt Cu), from precursor intrusions (barren batholiths) to pre-, syn-, and post- mineralization porphyritic events, is crucial for developing toolkits for exploration and understanding what controls the different orders of magnitude of PCD. Here, we present preliminary results from whole rock geochemistry and zircon trace elements from precursor and syn-mineral porphyritic intrusions of the Tres Cerrillos prospect of the Western Cordillera of Ecuador assessing magma fertility for PCD and an early deep crustal evolution of their magmas.

The Tres Cerrillos prospect is a Cu-Mo porphyry system that is being explored by geologists of the EMSAEC team (Codelco) in the northernmost part of the Western Cordillera of Ecuador, approximately 120 km northeast from Quito (Figure 1). The basement rocks of the prospect mainly consist of allochthonous oceanic and island arc terranes (and associated sedimentary units), part of the Caribbean Large Igneous Province that collided and accreted to the continental margin of South America during the Late Cretaceous (Vallejo et al. 2019). Subsequently, intermittent subduction has produced Cenozoic plutonic and volcanic arc units that intrude and overlie the basement rocks and are sites of ongoing exploration for porphyry copper systems (Figure 1). In fact, the northernmost part of the Western Cordillera is of high economic interest due to the recent discovery of the Cascabel porphyry Cu-Au deposit which is associated with Eocene rocks and the Llurimagua porphyry Cu-Mo of Miocene age, both defining two different metallogenic belts.

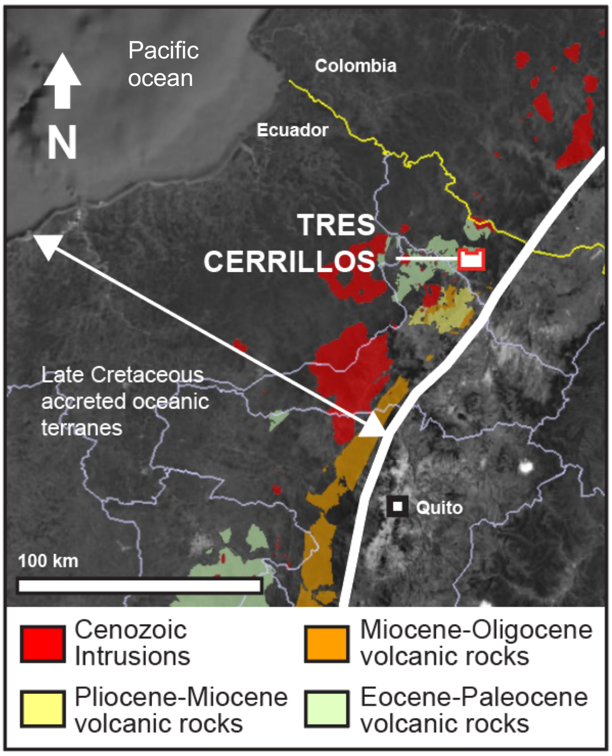

Figure 1. Location of the Tres Cerrillos prospect and simplified geology of the northwestern Ecuador.

The Tres Cerrillos project is centered on Miocene multiphase porphyritic intrusions of dacitic, quartzdioritic and dioritic compositions (Figure 2a), which are emplaced either into equigranular, granodioritic to dioritic intrusions (precursor intrusions that can be as old as Eocene, Figure 2b), or into the local basement. Various degrees of potassic (biotite-K-feldspar) and sericitic (quartz-sericite) alteration develop extensively throughout the porphyry intrusions, where pyrite ± chalcopyrite

± molybdenite occur in stockwork veinlets. U-Pb zircon crystallization ages of the porphyritic intrusions reveals they are syn-mineralization, overlapping the range of Re-Os molybdenite dates that bracket the duration of the ore deposition (dates from CODELCO). The youngest mineralization age from Tres Cerrillos is similar to previous Re-Os molybdenite dates from the Chaucha Cu-Mo porphyry district located further south (i.e., 9.54±0.05 Ma; Schütte 2012). Late andesitic dykes crosscut the system.

Future work will consist of placing mineral chemistry (e.g., zircon and apatite) within the frame of high precision CA-ID-TIMS U-Pb zircon geochronology to refine fertility indicators that can potentially be used as a proxy for metal endowments.

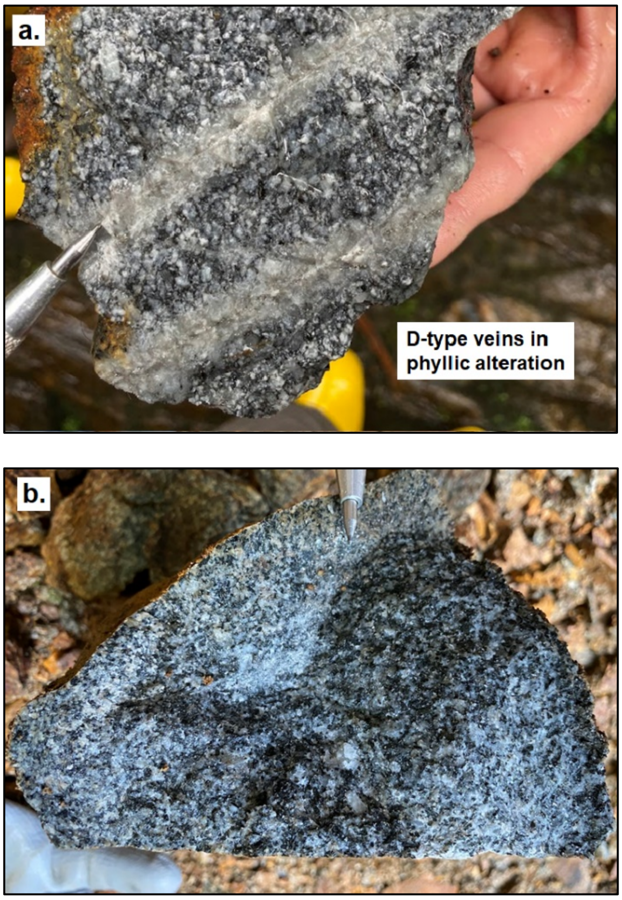

Figure 2. Main intrusions in the Tres Cerrillos prospect. **a.** Syn-mineralization, quartzdioritic porphyritic intrusion, showing sericitic alteration with D-type veins. **b.** Unaltered, equigranular, phaneritic granodiorite (precursor intrusion).

2 Whole rock geochemistry

The SiO_2 content from precursor and porphyry intrusions ranges between 57.8–72 wt%, while MgO content spans between 0.71–5.88 wt%. The volatile content (LOI) ranges mainly between 0.38-6.43 wt% which is high for igneous rocks in arc settings and indicates alteration. These intrusive rocks have a broad calc-alkaline signature that show intermediate andesitic compositions when compared with incompatible elements (Nb/Y versus Zr/TiO_2 classification diagram, Figure 3a). The investigated rocks are the least altered ones as seen in the alteration box plot that compare major oxides (Figure 3b). However, they can be misleadingly classified as more felsic, due to the presence of quartz veinlets (Figure 2a).

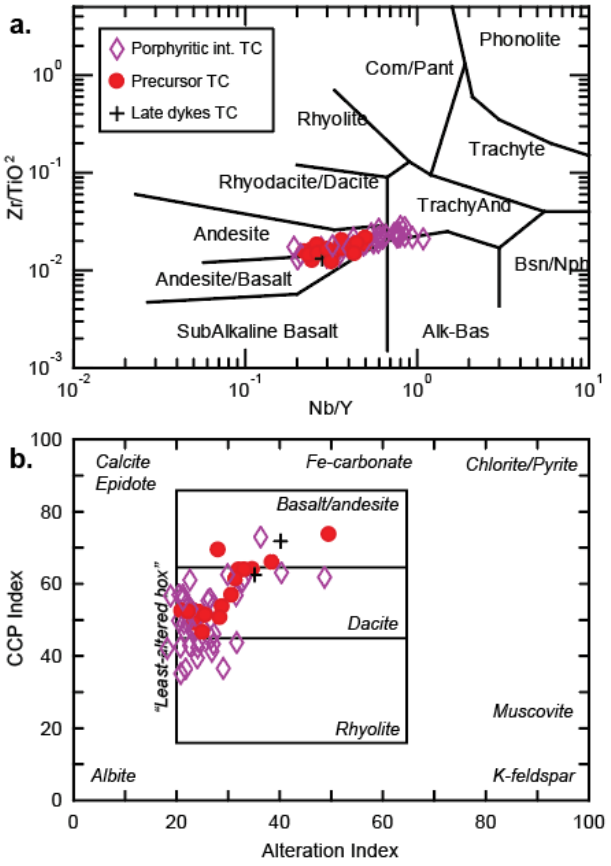

Figure 3. a. Nb/Y versus Zr/TiO_2 plot (Winchester and Floyd 1977). **b.** Alteration Box Plot (Large et al. 2001) that compares the Ishikawa Alteration Index versus Chlorite-carbonate-Pyrite index (CCPI).

Precursor intrusions, intra-mineral porphyries and late dykes (Figure 4a), show a strong enrichment of LREE compared to MREE and HREE, and a common lack of Eu anomaly in chondrite-normalized plots. Additionally, intra-mineral porphyritic intrusions display a clear depletion of MREE and HREE compared with precursor intrusions and late andesitic dykes. This MREE and HREE depletion could be due to amphibole ± garnet ± titanite fractionation. The systematic increase of Dy/Yb and $Sm_{(N)}/Yb_{(N)}$ with differentiation proxies (i.e., MgO and SiO_2; Figure 4b, c) also support garnet ± zircon fractionation, and therefore a possible deep crustal evolution of these magmas prior reaching shallow levels in the thick crust of the Western Cordillera of Ecuador (>35 km).

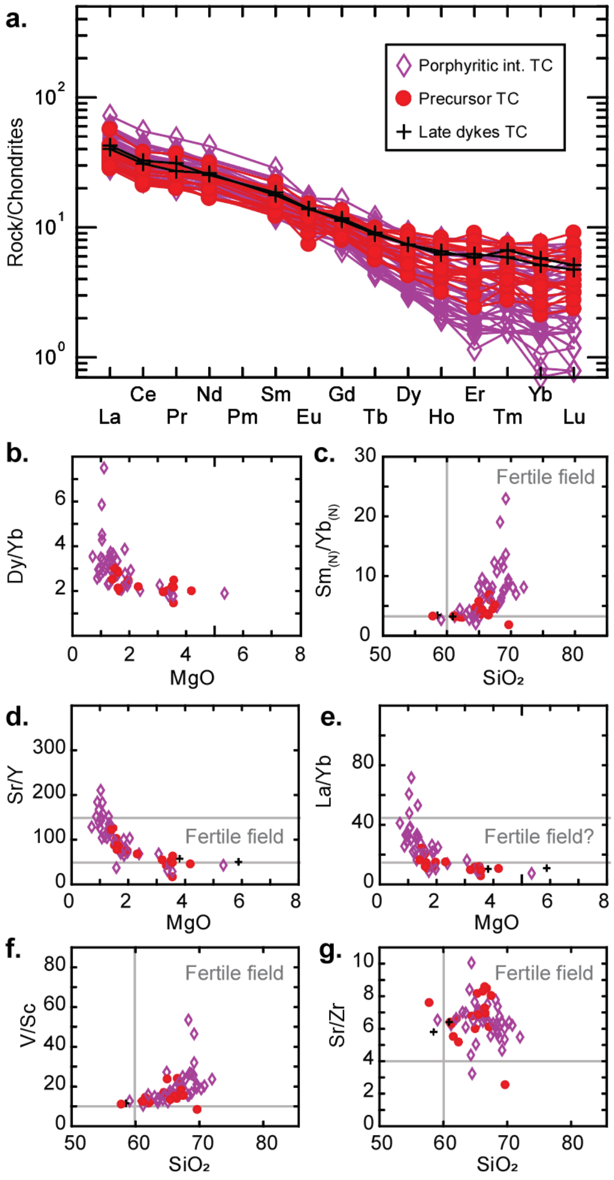

Figure 4. Whole rock geochemistry plots **a.** REE concentrations normalized to Chondrites. **b-g.** Geochemical proxies of magma fertility for porphyry copper systems.

Protracted magma storage at deep crustal level suppresses plagioclase fractionation (where Sr and Eu are compatible), whereas high pressure and H_2O content stabilize amphibole ± garnet (where Y, MREE and HREE are compatible) (Richards 2011; Chiaradia and Caricchi 2017). Therefore, assessing Sr/Y is of high importance as a magma fertility proxy. In the Tres Cerrillos prospect, Sr/Y ratios from the intra-mineral porphyritic intrusions have values that overlap the range of fertility (50-150), whereas precursor bodies and late dykes have lower values (Figure 4d). This probably reflects a different magmatic evolution for the two series. Likewise, the Sr/Y ratio decreases as the chemical composition of the magma is more primitive. This pattern is also shown by the La/Yb proxy when compared with MgO (Figure 4e). Other magma fertility proxies such as V/Sc and Sr/Zr also define a fertile behavior for the Tres Cerrillos magmatic suite (Figure 4f, g).

3 Zircon trace elements

Zircon trace elements proxies based on plots of Eu/Eu* (and also (Eu/Eu*)/Y) against Ce/Nd, Dy/Yb and (Ce/Nd)/Y (Lu et al. 2016) do not clearly discriminate between pre- and syn-mineralization samples from the same mineralized system. However, when comparing Dy/Yb versus Eu/Eu*, a distinction between the intra-mineral porphyritic intrusions of Tres Cerrillos and Eocene to Oligocene intrusion (old intrusions) becomes evident (Figure 5a), with the intra-mineral rocks presenting higher Dy/Yb values (~>0.3).

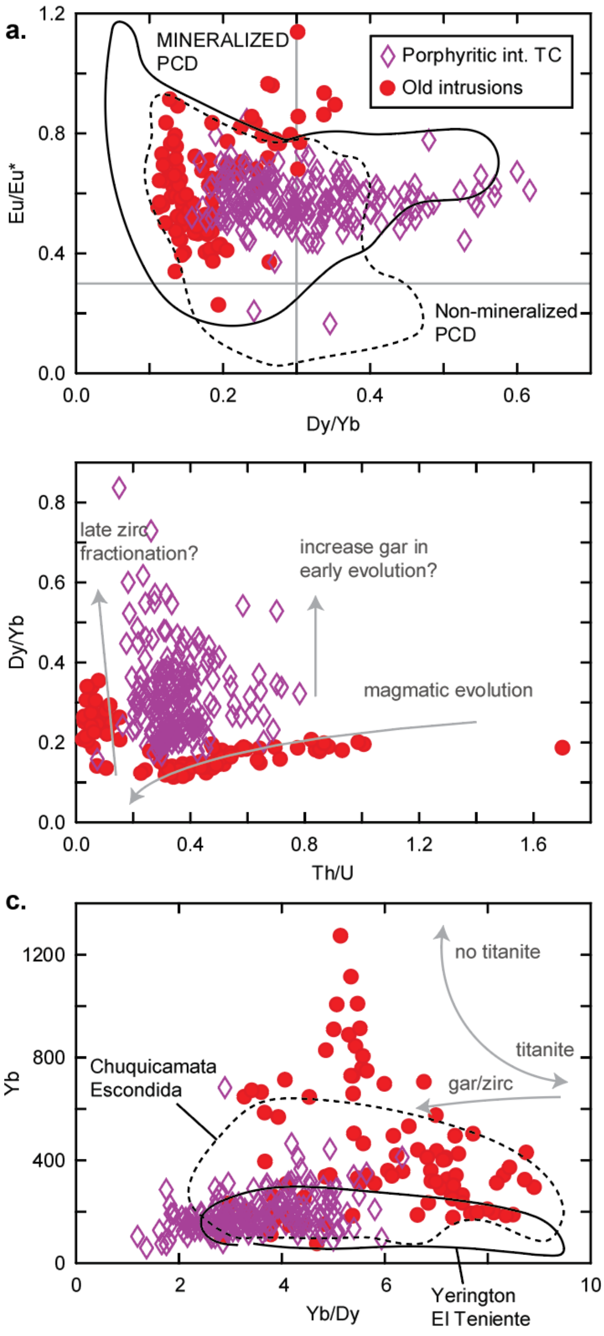

Figure 5. Zircon trace element plots **a.** Dy/Yb against Eu/Eu* (Lu et al. 2016), **b.** Th/U against Yb/Gd. **c.** Yb/Dy against Yb.

On the other hand, zircon trace elements can be used to assess the magmatic evolution of the fertile/barren rocks. Th/U is a ratio commonly used to track the crystallization from increasingly evolved magmas, with zircons having lower Th/U values being crystallized from more differentiated magmas. In the Th/U versus Dy/Yb plot (Figure 5b), the intra-mineral intrusions of the Tres Cerrillos prospect show higher Dy/Yb ratio at similar Th/U values, suggesting garnet fractionation at similar degrees of relatively early evolution, consistent with whole rock geochemistry results. In contrast, the old intrusion suite seems to have evolved at shallower levels following a differentiation trend with decreasing Dy/Yb as Th/U decreases, and a late zircon fractionation explaining the drastic increase in Dy/Yb values. These different magmatic evolution of barren versus fertile suites may provide regional geochemical tools to discriminate and fertile systems. In Figure 5c, a comparison between Yb/Dy versus Yb, where garnet fractionation is addressed with by low Yb and Yb/Dy ratio, shows that the Tres Cerrillos intra-mineral porphyritic intrusions possibly underwent a magmatic evolution similar to that of giant copper porphyry systems such as Chuquicamata, Escondida and El Teniente.

4 Conclusions

Syn-mineralization porphyritic intrusion of the Tres Cerrillos Cu-Mo prospect show evidence for a deeper crustal evolution compared with their precursor intrusions. In fact, both whole rock geochemistry and zircon trace elements suggest that these magmas could have experienced early garnet fractionation in addition to amphibole at lower crustal levels, a typical feature of fertile magmatic suites associated with PCD. Zircon geochemistry of Tres Cerrillos rocks shares similar geochemical characteristics as those of supergiant porphyry copper systems, making this prospect potentially important in terms of Cu endowment.

Acknowledgements

We are grateful with CODELCO for funding this project. Fieldwork benefited from the assistance of Hugo Narvaez and Yorki Patiño, exploration geologist of EMSAEC.

References

Chiaradia M, Caricchi L (2017) Stochastic modelling of deep magmatic controls on porphyry copper deposit endowment. Sci Rep 7, 44523. https://doi.org/10.1038/srep44523

Chiaradia M, Caricchi L (2022) Supergiant porphyry copper deposits are failed large eruptions. Commun Earth Environ 3, 107. https://doi.org/10.1038/s43247-022-00440-7

Large RR, Gemmell JB, Paulick H, Huston DL (2001) The alteration box plot: A simple approach to understanding the relationship between alteration mineralogy and lithogeochemistry associated with volcanic-hosted massive sulfide deposits. Economic geology, 96(5), 957-971. https://doi.org/10.2113/gsecongeo.96.5.957

Lu YJ, Loucks RR, Fiorentini M, McCuaig TC, Evans NJ, Yang ZM, et al (2016) Zircon Compositions as a pathfinder for Porphyry Cu±Mo±Au Deposits. Soc. Econ. Geologists. Special Publ. Series 19, 329–347. https://doi.org/10.5382/SP.19.13

Richards JP (2011) High Sr/Y arc magmas and porphyry Cu±Mo±Au deposits: Just add water. Economic Geology, 106(7), 1075-1081. https://doi.org/10.2113/econgeo.106.7.1075

Schütte P, Chiaradia M, Barra F, Villagómez D, & Beate B (2012) Metallogenic features of Miocene porphyry Cu and porphyry-related mineral deposits in Ecuador revealed by Re-Os, 40 Ar/39 Ar, and U-Pb geochronology. Mineralium Deposita, 47, 383-410. https://doi.org/10.1007/s00126-011-0378-z

Vallejo C, Spikings RA, Horton BK, Luzieux L, Romero C, Winkler W, Thomsen TB (2019) Late Cretaceous to Miocene stratigraphy and provenance of the coastal forearc and Western Cordillera of Ecuador: Evidence for accretion of a single oceanic plateau fragment. In Andean tectonics (pp. 209-236). Elsevier. https://doi.org/10.1016/B978-0-12-816009-1.00010-1

Winchester JA, Floyd PA (1977) Geochemical discrimination of different magma series and their differentiation products using immobile elements. Chemical geology, 20, 325-343. https://doi.org/10.1016/0009-2541(77)90057-2

State-of-the-art garnet petrochronology in the Yerington district: What does it tell us about Cu skarn formation?

Maria Paula Castellanos Melendez[1]; Daniela Rubatto[2]; Francesca Piccoli[2]; Julien Allaz[1]; Marcel Guillong[1] and Olivier Bachmann[1]
[1]ETH Zürich, Institute of Geochemistry and Petrology, Zürich, Switzerland
[2]University of Bern, Institute of Geological Sciences, Bern, Switzerland

Abstract. The interaction between magmatic-hydrothermal fluids sourced from the Jurassic Yerington batholith and the carbonate-rich middle Triassic – early Jurassic basement produced several generations of metasomatic garnet-pyroxene skarn that locally contain Cu mineralization (Einaudi, 1977). The Cu-skarn is assumed to be genetically linked to the porphyry Cu deposits found in the Yerington district (Einaudi, 1977; Harris and Einaudi, 1982). However, state-of-the-art petrographic, geochemical, and geochronological evidence for a genetic link between porphyry-style and skarn mineralization is still lacking. Four different garnet textures have been identified throughout the Yerington skarn: (a) cm-sized coarse-grained oscillatory zoned garnet, (b) fine-grained matrix garnet associated with pyroxene, carbonate, and oxides, (c) breccia-filling garnet, and (d) vein garnet in non-brecciated settings. In this study we provide the first in-situ geochemical characterization of the different garnet textures that constitute the garnet-pyroxene Cu-skarn. Geochemical differences between garnet generations possibly document the origin and evolution of the metasomatizing fluids. Moreover, preliminary in situ LA-ICP-MS U-Pb dating of garnet further helps constraining a 4D skarn evolution and indicate at least two main events of garnet formation.

1 The Yerington Cu-Skarn

Skarn horizons or lenses are common within porphyry systems and economically important as they can host high-grade Cu (proximal) or base metal (distal) mineralization (e.g., Ok Tedi, Van Dongen et al. 2013; Bingham Canyon, Schlöglova, 2018). At Yerington, at least two skarn generations formed by sequential magmatic activity: a skarnoid stage followed by a metasomatic stage (Harris and Einaudi, 1982). Several garnet generations have been petrographically and geochemically distinguished (Einaudi, 1977; Harris and Einaudi, 1982). Grossular-andradite garnet is characteristic of the skarnoid stage while the later metasomatic event produced more andraditic garnet. A later stage veined the skarn types with grossular-andradite garnet (Harris and Einaudi, 1982). Copper mineralization has been linked to coarse-grained andraditic garnet and is assumed to be genetically linked to the ore-forming fluids of the porphyry environment (Einaudi, 1977), although no clear evidence for this association exists. In this study we provide preliminary results of in situ petrochronology analyses on different garnet types throughout the Yerington skarn and aim at providing important insights into its formation and the so far assumed genetic link between the porphyry and the skarn environment in the district.

2 Materials and methods

Samples were collected in a field campaign in the vicinities of the Casting Copper Skarn and the Douglas Hill Mine in the Yerington district, Nevada, USA. Polished thin sections were studied by conventional transmitted light petrography and back-scattered electron (BSE) imaging with a JEOL JSM-6390LA scanning electron microscope.

Representative ca. 1x1 mm areas of the different garnet textural variations were selected for quantitative elemental mapping using a JEOL JXA 8230 electron microprobe at ETH Zurich. Major oxide maps were quantified and exported as wt% SiO_2, Al_2O_3, FeO_{total}, MgO, CaO, MnO and TiO_2 (Donovan et al., 2021). Trace element mapping was performed over areas for which major element maps were obtained using a Resonetics RESOlutionSE 193nm excimer laser system coupled to an Agilent 7900 quadrupole ICP-MS instrument at the University of Bern. Additionally, U-Pb in-situ garnet dating was done using an ASI RESOlution excimer ArF (193 nm) laser ablation system coupled to a Thermo Fisher Element XR sector field ICP-MS at ETH Zurich.

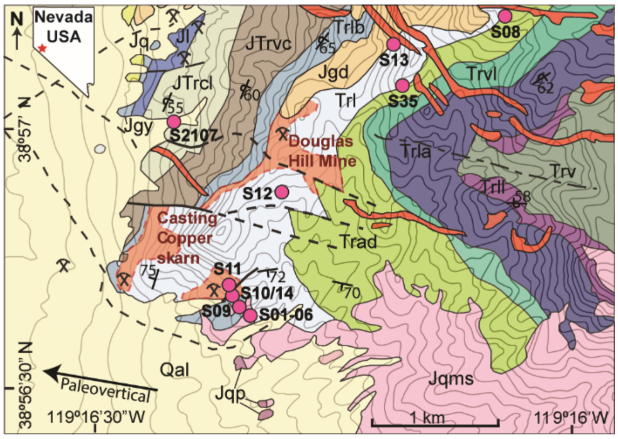

Figure 1. Geological map of the garnet-pyroxene Cu-skarn exposures in the Yerington district, Nevada, USA. Sample locations in fuchsia circles. Geological units: Jqms-quartz monzonite; Jqp-granite porphyry; Jq-quartzite; Jgy-gypsum; Jl-Ludwig limestone; JTrcl-argillite limestone felsite; JTrvc-rhyolitic siltstone; Trlb-argillaceous limestone; Trl-massive limestone; Trad-andesitic-dacitic tuff and sandstone; Trvl-rhyolitic sandstone and limestone; Trla-black calcareous argillite; Trll-dolomitic limestone; Trv-volcanic rocks; Qal-Quaternary alluvium. Modified after Barkoff et al. (2017).

3 Results and Discussion

3.1 Garnet textures

Throughout the skarn exposures garnet occurs in various textural positions as (a) cm-size coarse-grained oscillatory zoned crystals in garnetite, (b) fine-grained zoned or unzoned crystals in fine-grained domains associated with pyroxene, calcite, oxides and ± apatite, (c) cement of brecciated coarse-grained crystals in hornfels, (d) overgrowths with or without oscillatory zoning that crosscut the coarse-grained zoned crystals, and (e) vein fillings (Fig. 2). BSE images reveal compositional differences between the different textural occurrences of garnet. Generally, crosscutting overgrowths, breccia cement and vein fillings show distinctive darker BSE images matching Fe-poor domains. Similarly darker rims and intermediate bands are found in the brighter crystals and correlate with anisotropic domains under cross-polarized light microscopy. Such anisotropy, typical of grossular-andradite garnet (Cesare et al. 2019) could be the result of the incorporation of OH- in the garnet structure (Antao et al. 2017), lattice strains after garnet growth (Allen and Buseck, 1988) or initial growth with tetragonal symmetry (Cesare et al. 2019).

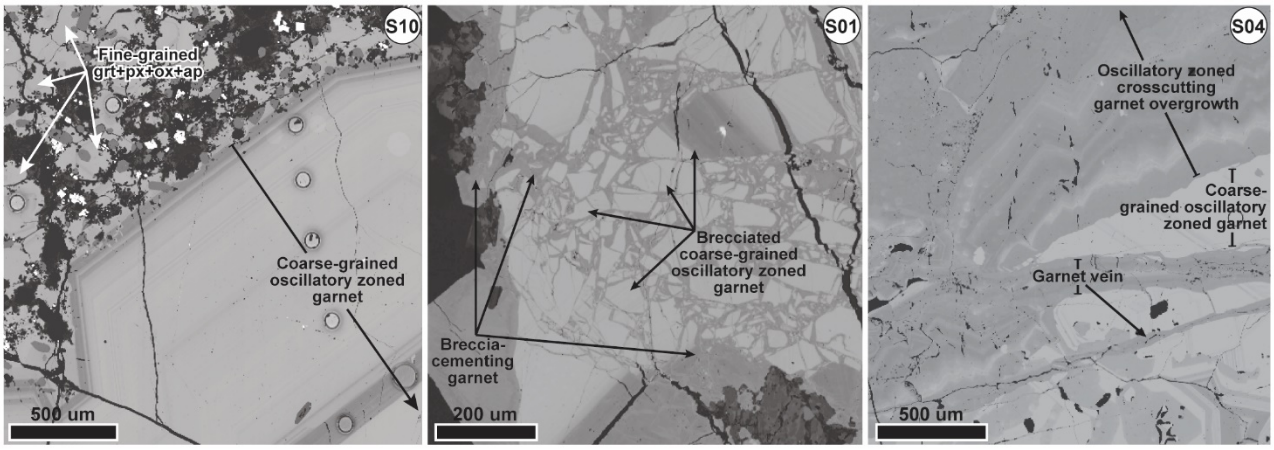

Figure 2. BSE images of the different textures of garnet in the Yerington skarn. Sample number is indicated at the top-right corner. Garnet occurs as coarse-grained oscillatory zoned crystals and fine-grained crystals in association with pyroxene, oxides, apatite, and carbonates (S10). Oscillatory zoned overgrowths and garnet veins also occur crosscutting the coarse-grained garnet (S04). Additionally, coarse garnet blobs occur with brecciated margins within hornfels where garnet cements the brecciated particles (S01).

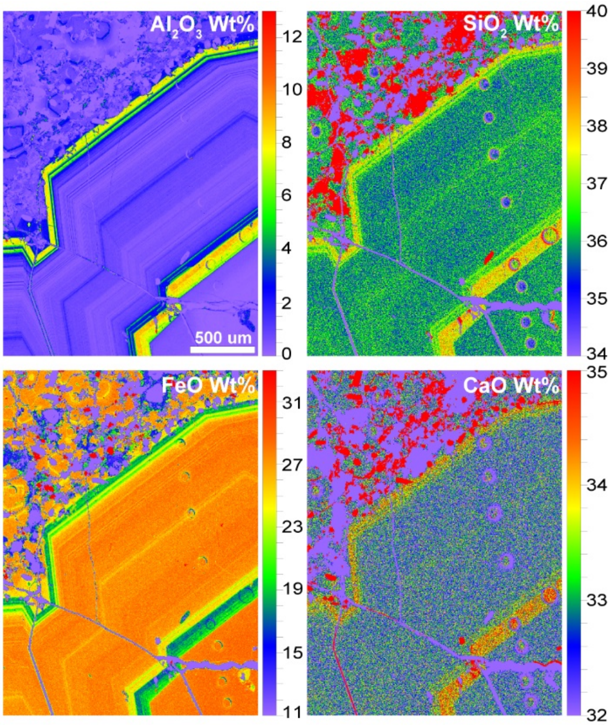

Figure 3. Quantitative element mapping of Al_2O_3, SiO_2, $FeO_{(total)}$ and CaO wt% in garnet from sample S10. The maps highlight the coarse-grained oscillatory zoned garnet in association with a fine-grained garnet + pyroxene + apatite + calcite domain.

3.2 Garnet geochemistry

Chemical variations suggested by BSE images are documented by quantitative electron microprobe mapping. Two main garnet compositions represent all textural variations throughout the district. Coarse-grained garnet in generally Fe-rich (And_{93-96}), with no MgO or MnO components. Narrow anisotropic intermediate bands and rims in this garnet type are Fe-poor and Al-rich ($Gross_{24-36}$, And_{58-69}) with SiO_2 and CaO enrichment (Fig. 3), and low MnO contents (up to 0.2 wt%). MgO is absent in all garnet types, while TiO_2 occurs sporadically in low contents (up to 1 wt%) correlated with Al-rich domains. Fine-grained garnet is generally Fe-rich (And_{91}) with or without Al-rich rims. Conversely, garnet overgrowths, breccia cement and vein fillings are generally Al-rich Fe-poor ($Gros_{36-41}$, And_{52-61}), except for S12 in the vicinities of the Douglas Hill mine, where coarse-grained garnet is generally Al-rich ($Gros_{56}$, And_{36}) with Fe-rich overgrowths and crosscutting veins ($And_{77,}$ $Gros_{19}$).

Preliminary trace element mapping in S10 indicates that Fe-rich domains host variable but generally high U contents (up to 20 ppm), while U is depleted in the Al-rich zones. Other traces such as

Sc, V, Cr, Y and the HREE (from Gd to Lu) are also positively correlated with Al contents in the garnet rim while La, Ce, Pr and Nd are enriched in the Fe-rich core. These variable trace element compositions could be the result of significant variations in fluid chemistry during garnet formation. However, the scale and rate at which such variations occur is yet to be defined with further geochemical analyses on other samples throughout the district.

3.3 Garnet in-situ geochronology

Skarn garnet in situ U-Pb dating has been successfully achieved due to their variable U contents (e.g., Seman et al. 2017; Gevedon et al. 2018). High U contents in the studied garnet allowed for preliminary U-Pb in situ dating by LA-ICP-MS and we provide here the first garnet ages for the Yerington skarn. In general, Fe-rich garnet domains yield concordant Middle Jurassic U-Pb dates with negligible initial Pb contents. On the contrary, U-Pb dates in Al-rich rims are discordant with variable amounts of common Pb allowing for the construction of a well-defined Discordia line with Upper Jurassic lower intercept.

The definition of at least two resolvable ages, with no overlapping analytical uncertainties, of garnet formation in the Yerington skarn questions the genetic link between at least one of these events and the Middle Jurassic porphyry Cu formation (ca. 167.4 Ma; Carter et al. 2022). Additionally, the correlation between age and different garnet geochemical signatures might provide important insights into the characteristics of fertile fluids for Cu deposition. Undergoing further in-situ dating of the geochemically and texturally different garnet types will allow for a robust definition of a 4D garnet evolution in the Yerington skarn and the role of fluid chemistry in ore formation.

Acknowledgements

The authors would like to express their gratitude towards John Dilles and Richard Tosdal for their guidance in the field and insightful views on the formation of the Yerington Cu skarn.

References

Allen, F. M., & Buseck, P. R. (1988). XRD, FTIR, and TEM studies of optically anisotropic grossular garnets. American Mineralogist, 73(5-6), 568-584.

Antao, S. M., & Cruickshank, L. A. (2018). Crystal structure refinements of tetragonal (OH, F)-rich spessartine and henritermierite garnets. Acta Crystallographica Section B: Structural Science, Crystal Engineering and Materials, 74(1), 104-114.

Barkoff, D. W., Ashley, K. T., & Steele-MacInnis, M. (2017). Pressures of skarn mineralization at Casting Copper, Nevada, USA, based on apatite inclusions in garnet. Geology, 45(10), 947-950.

Carter, L. C., Tapster, S. R., Williamson, B. J., Buret, Y., Selby, D., Rollinson, G. K., ... & Parvaz, D. B. (2022). A rapid change in magma plumbing taps porphyry copper deposit-forming magmas. Scientific Reports, 12(1), 17272.

Cesare, B., Nestola, F., Johnson, T., Mugnaioli, E., Della Ventura, G., Peruzzo, L., ... & Erickson, T. (2019). Garnet, the archetypal cubic mineral, grows tetragonal. Scientific reports, 9(1), 1-13.

Donovan, J. J., Allaz, J. M., von der Handt, A., Seward, G. G. E., Neill, O., Goemann, K., Chouinard, J. & Carpenter, P. K. (2021). Quantitative WDS compositional mapping using the electron microprobe. American Mineralogist 106, 1717–1735.

Einaudi, M. T. (1977). Petrogenesis of the copper-bearing skarn at the Mason Valley Mine, Yerington District, Nevada. Economic Geology, 72(5), 769-795.

Gevedon, M., Seman, S., Barnes, J. D., Lackey, J. S., & Stockli, D. F. (2018). Unraveling histories of hydrothermal systems via U–Pb laser ablation dating of skarn garnet. Earth and Planetary Science Letters, 498, 237-246.

Harris, N. B., & Einaudi, M. T. (1982). Skarn deposits in the Yerington District, Nevada; metasomatic skarn evolution near Ludwig. Economic Geology, 77(4), 877-898.

Schlöglova, K. (2018). Fluid Inclusion Analysis of other Host Minerals besides Quartz: Application to Granite-Related Quartz-Topaz Veins and Garnet Skarns in Porphyry Copper-Gold Ore Systems (Doctoral dissertation, ETH Zurich).

Seman, S., Stockli, D. F., & McLean, N. M. (2017). U-Pb geochronology of grossular-andradite garnet. Chemical Geology, 460, 106-116.

Van Dongen, M., Weinberg, R. F., & Tomkins, A. G. (2013). Grade distribution of the giant Ok Tedi Cu-Au deposit, Papua New Guinea. Economic Geology, 108(7), 1773-1781.

Hydrothermal alteration chemistry and mineralogy of the Maricunga-style Vendaval Central Cu-Au porphyry

Federico Cernuschi [1,2], Santiago Gigola [3,2], William Brownscombe [4], Tim Ireland [2], James Banyard [2], David Arribasplata [2], Jaime Schorr [2], Paula Gonnet [2], Paula Sosa [2], Mauricio Duran [2]
[1]Eclectic Rock, Punta del Este, Uruguay
[2]First Quantum Minerals, Salta, Argentina
[3]Independent Consultant, Mendoza, Argentina
[4]Natural History Museum, London, UK

Abstract. The hydrothermal alteration at the Vendaval Central Cu-Au Middle Miocene porphyry project (Salta, Argentina) was studied using drill-hole core logging, whole-rock compositions, and mineral phase maps acquired using a Tescan Integrated Mineral Analyser (TIMA) system. The central part of the prospect experienced four alteration stages: 1) calcic alteration with pyroxene and garnet, 2) K-silicate alteration with K-feldspar, biotite, magnetite, A quartz veins, and banded Maricunga quartz veins, 3) albitization and 4) intermediate argillic alteration overprint with smectites, hydrobiotite, calcite, and less chlorite. Shallow peripheral illitic alteration with pyrite and shallower remnants of advanced argillic alteration with deep and narrow breccias are also observed. The superimposition of these alteration stages results in whole rock compositions with high Na/Al and low K/Al. Nonetheless, Cu-Au mineralization is associated with K-silicate alteration, A veins, and banded Maricunga veins. Hydrothermal alteration at Maricunga porphyries like Vendaval is somewhat reminiscent of silica-saturated alkaline porphyry deposits elsewhere: early calcic alteration and late albitization with respect to K-silicate alteration and absent sericitic alteration. Similarly, the hypogene intermediate argillic overprint may be a common feature of Au-rich porphyries. The calcic alteration and albitization are not associated with a sedimentary wall-rock composition and are likely magmatic-hydrothermal in origin.

1 Introduction

Vendaval Central is a porphyry copper-gold project of Middle Miocene age located in Argentina next to the border with Chile at least 200 km N-NE of the northernmost gold–rich porphyry in the Maricunga Belt (Vila and Sillitoe 1991). The gold-bearing copper mineralization, type of quartz veinlets, age, and interpreted shallow emplacement depth suggest that Vendaval Central is part of the northern extension of this belt.

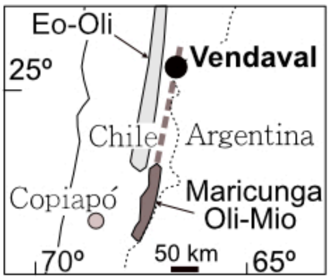

Figure 1. Schematic location map of Vendaval Central showing the Maricunga belt and its possible northern extension (modified from Muntean and Einaudi 2000).

The copper-gold mineralization (~1:1) is hosted by a series of at least five different quartz dioritic to dacitic porphyries (early to late-mineral) and the immediately adjacent andesitic volcanic flows and volcanic breccia. K-Ar dating indicates that the age of the volcanic host rocks is early to middle Miocene (Ramirez *et al.* 1991). The successive porphyry phases control quartz vein density and hypogene grades, as is normally found in A-vein-type porphyries (Proffett 2009).

The central parts of the system are characterized by a high density of sheeted quartz veinlets (>20-30 veins/meter) hosted in early mineral porphyry and immediately adjacent andesitic wall rock with strong K-silicate alteration (~850 x 350 m). These quartz veins display a banded Maricunga-style texture over the highest parts of the deposit and transition at depth into typical, granular A-type quartz-chalcopyrite-magnetite veinlets. Quartz vein truncations, quartz vein xenoliths, and sharp changes in hypogene grades are common at contacts between different porphyry phases.

2 Methodology

Two-meter-long split core samples (n=12.300) were obtained throughout the drill holes and assayed by inductively coupled plasma-atomic emission spectroscopy (ICP-AES) and inductively coupled plasma-mass spectroscopy (ICP-MS) following four-acid digestion (MEMS61 at ALS). Short wave infrared (SWIR) spot data was obtained on coarse rejects for each compositional sample (ALS) and processed using The Spectral Geologist. Compositional and spectral data were integrated and studied using ioGAS^{TM} in reference to geologic observations and cross-sections. Lithogeochemical units were inferred using immobile trace elements (*e.g.* Th, Zr, Nb, Sc). Hydrothermal alteration types were inferred by studying major element gains and losses (Ca, Na, K, Mg) and supported by SWIR mineralogy (see Halley 2020).

Twenty hand samples of key hydrothermal alteration types were obtained to produce polished thin sections and 25 mm polished blocks. Mineral phase maps were obtained on these samples using a Tescan Integrated Mineral Analyser (TIMA) system at the Natural History Museum, London. The analytical conditions were 25 kV accelerating voltage, 14 nA current, and a working distance of 15 mm. Standard instrument calibration was performed prior to analysis. A pixel size of 5 microns was used for both backscatter electron imaging (BSE) and energy dispersive spectroscopy (EDS) modal analysis, and phase classifications were based on spectra chosen and identified from these analyses.

3 Hydrothermal alteration

Elemental gains and losses were studied independently for each magmatic lithogeochemical unit. Pre-alteration major element compositions were estimated from immobile trace elements concentrations. Some magmatic units are mildly alkaline, have slightly elevated Nb (>10 ppm) compared to sub-alkaline units, and may have more magmatic pyroxene than amphibole. The original magmatic compositions were likely slightly elevated in alkalis. The expected least altered compositions may be shifted to higher K/Al and/or Na/Al than typical sub-alkaline Andean magmas (Figure 2).

Most samples experienced multiple intense and overprinting alteration events that caused opposing effects on the gains and losses of major elements (Figures 2 & 3). Therefore, apparent least altered compositions may be, in reality, very altered samples. For this interpretation, we assumed that there are no completely preserved magmatic compositions and color-coded the samples according to the dominant alteration type inferred. Core logging observations, SWIR mineralogy, and TIMA mineral phase maps informed this interpretation.

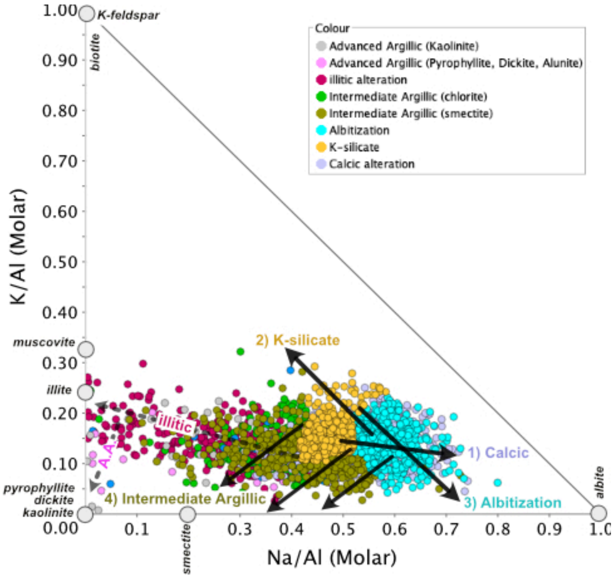

Figure 2. K/Al vs Na/Al gains and losses diagram showing a subset of samples of andesitic composition (wall-rock) and mineral compositions of relevant alteration minerals. Timing of illitic and advanced argillic alteration (A.A.) is not resolved.

Large areas within the central part of the system experienced four overlapping alteration stages (Figures 2 & 3) that in temporal order are: 1) calcic alteration, 2) K-silicate alteration, 3) albitization, and 4) intermediate argillic alteration.

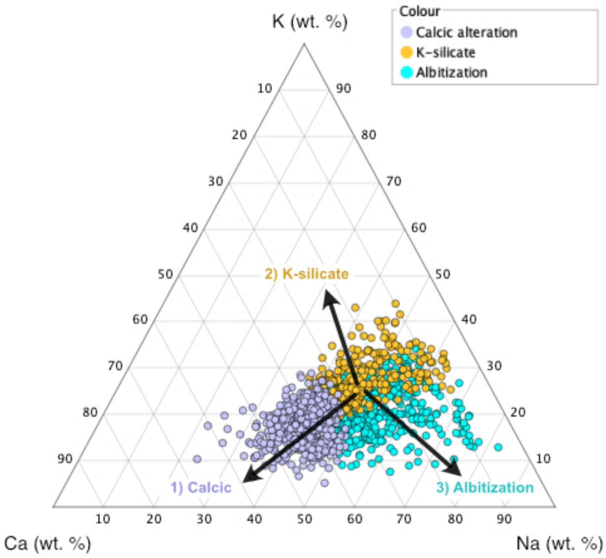

Figure 3. K-Ca-Na gains and losses diagram showing a subset of the samples from Figure 2 that are inferred as dominantly altered to K-silicate, calcic, or albitization.

3.1 Calcic alteration

The volcanic wall-rock and associated sub-volcanic units experienced an early stage of calcic alteration at the intermediate and deep zones of the system. This alteration gained Ca at the expense of K and Na (Figures 2 & 3), predates the bulk of Fe-Cu-sulfides and the intrusion of porphyry dikes. However, the calcic alteration is most intense near the dikes. It is observed as thin and irregular pyroxene veinlets of up to 2 mm thick and locally abundant garnet-pyroxene patches. The thin pyroxene veinlets are challenging to recognize in hand samples but are readily observed in TIMA images, where pyroxene is identified as augite (Figure 4 & 5). The patches are identified during logging, and the TIMA mineralogy indicates that pyroxene composition is hedenbergite, garnet is andradite, and both replace magmatic plagioclase (Anorthite 40, Figure 4).

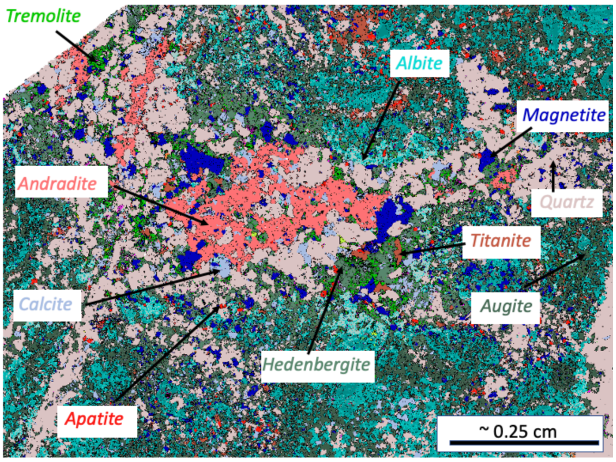

Figure 4. Garnet-pyroxene patches, pyroxene veinlets, and quartz veinlets with magnetite.

Pyroxene rims are commonly replaced by tremolite and other amphiboles (Figures 4 & 5). This hydration (uralitization) event may have started at the end of the Ca-alteration and continued during later stages of hydrothermal alteration.

3.2 K-silicate alteration

Within the Calcic alteration zone, a central area experienced K-silicate alteration where K was gained at the expense of Ca and Na. Therefore, in some cases, K-gains are overprinted to older Ca-gains (Figures 2 & 3). K-silicate alteration comprises hydrothermal K-feldspar, shreddy biotite, and magnetite that replaces magmatic plagioclase, pyroxene, and amphibole (Figure 5).

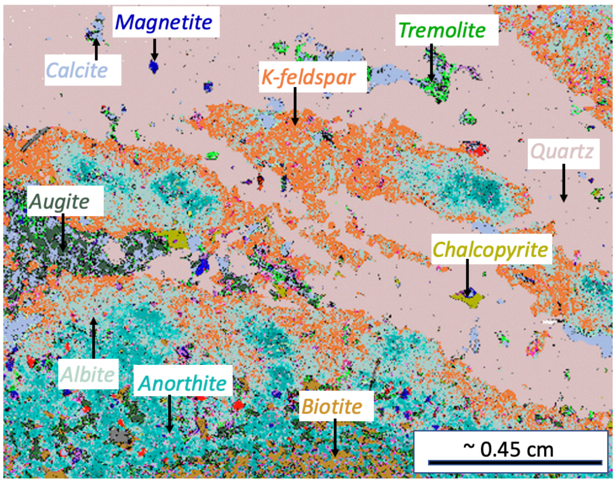

Figure 5. Quartz A veins with chalcopyrite and K-feldspar halos truncate augite veinlets. Albite rims magmatic anorthite and replaces hydrothermal K-feldspar. Thin biotite veinlets and shreddy biotite after pyroxene are also present.

Cross-cutting observations indicate that hydrothermal K-feldspar and biotite post-date pyroxene and garnet. Albite is observed in some cases in contact with K-feldspar, but not always. Some hydrothermal albite may have formed during K-silicate alteration by leftover Na after K-feldspar replaces magmatic anorthite. However, cross-cutting relationships in TIMA images suggest that most of the observed albite post-dates K-silicate alteration (see section 3.3).

K-feldspar and biotite form narrow but continuous selvages to A veins, banded Maricunga veins, and thin alkali seams with little quartz (Figure 5). Both quartz vein types crosscut the older pyroxene veins. K-feldspar is, in some cases, observed as younger outer selvages to the older pyroxene veins (Figure 5). To a lesser degree, K-feldspar and biotite are also observed as pervasive replacements of phenocrysts and groundmass.

A veins and banded Maricunga veins and associated K-feldspar and biotite outer selvages and patches contain chalcopyrite, pyrite, traces of bornite, and magnetite. Cu-Au bearing intercepts are rich in these vein types (Figure 5).

3.3 Albitization

The system's central part and periphery has hydrothermal albite that resulted from the gain of Na at the expense of Ca and K (Figure 2 & 3). This alteration is difficult to observe in a hand sample due to the minimal change in texture and color where magmatic anorthite is replaced by albite. Nonetheless, albite is readily observed in TIMA imaging (Figure 4 & 5) and inferred through gains and losses (Figure 2 & 3).

In TIMA images, albite can be observed in contact with older pyroxene veins, garnet patches, and K-feldspar/biotite (Figure 4 & 5). It is also observed as a pervasive replacement where magmatic anorthite and older hydrothermal K-feldspar are only locally preserved. At the system's periphery, albite is observed as the only hydrothermal mineral in samples that do not have evidence of previous calcic and K-silicate alteration. Therefore, albitization is considered younger than Calcic and K-silicate alteration and has been superimposed on both alteration types in some of the central areas of the system (Figures 2 & 3). Here, we choose the name albitization to avoid confusion with other types of Na- and Na-Ca-gains, where albite is also formed (see discussion).

Albitization does not remobilize older Fe-Cu sulfides, as its presence does not affect the Cu-Au grade. In heavily overprinted samples, albite can be observed containing Fe-Cu-sulphides and pyrite. However, traces of preserved hydrothermal K-feldspar, biotite, and A-veins indicate that albite overprints older K-silicate alteration. In these cases, the whole rock composition of a sample will plot at high Na/Al and low K/Al ratio despite having experienced an older stage of K-silicate alteration (Figure 2 & 3).

3.4 Intermediate argillic alteration

The central part of the system has experienced hypogene intermediate argillic alteration except on the very deep parts. This alteration particularly overprints K-silicate alteration, in some cases pervasively, and results in the loss of K and Na. The intermediate argillic alteration gives the rock a pale, light brown to orange color in hand sample. Different types of smectites and calcite are observed replacing magmatic anorthite, pyroxene, amphibole and hydrothermal pyroxene, K-feldspar, albite, magnetite, and biotite. Chlorite is also present; however, smectites are much more abundant (Figure 6). Hydrothermal and magmatic biotite are partially replaced by vermiculite, resulting in hydrobiotite (interlayered vermiculite-biotite, Cornejo 2021). The intense replacement of "shreddy" biotite by hydrobiotite, smectite and calcite results in samples with low K/Al and Na/Al (Figures 2 & 6).
The intermediate argillic alteration has no associated pyrite and does not remobilize older Cu-Fe-sulphides nor introduce Au.

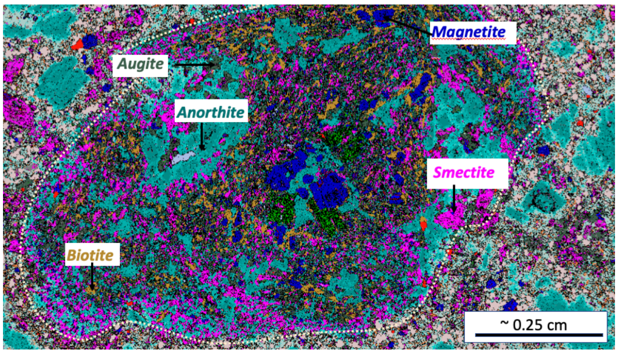

Figure 6. A pyroxene-anorthite oikocryst was replaced by biotite-magnetite (K-silicate alteration). Biotite and anorthite were then replaced by smectites (I.A.A.).

3.5 Illitic alteration and advanced argillic alteration

Advanced argillic (kaolinite, alunite, pyrophyllite, and dickite; Figure 2) in narrow polymictic phreatic breccias penetrate deeply (~500 m) on the south side of the deposit but are volumetrically restricted. Erosional remnants of the advanced argillic altered lithocap are preserved around Vendaval Central's higher ridges.

Sericitic alteration (muscovite) and D-type veins are absent. However, the barren shallow periphery surrounding Vendaval is altered to illite and has hair-like pyrite veinlets (lower K/Al than muscovite, Figure 2). We name this alteration “illitic” to differentiate it from intermediate argillic and sericitic alteration.

4 Discussion

At Vendaval Central, the K-silicate alteration is associated with Cu-Au bearing Fe-sulfide in quartz A veins, as in A-vein-type porphyries elsewhere (Proffett 2009). A-veins transition to banded Maricunga quartz veins with shallowing depth, as in other Maricunga deposits. This is likely a feature of the very shallow emplacement and rapid cooling (Muntean and Einaudi, 2000).

Other hydrothermal features at Vendaval Central may be comparable to those observed in silica-saturated alkaline deposits elsewhere. This may be related to the mildly alkaline nature of some of Vendaval’s magmatic units. The early calcic alteration occurs at similar timing in other Maricunga deposits, and it is not related to Ca-rich wall-rock as in skarns associated with porphyry deposits elsewhere (Muntean and Einaudi 2000). Calcic alteration in Maricunga deposits appears to be magmatic-hydrothermal in origin, as proposed for some alkaline porphyries in BC, Canada (Lang *et al.* 1995). Similarly, albitization, as previously proposed by Muntean and Einaudi (2000), is not comparable to heating basin fluid-related sodic-calcic (*e.g.* Yerington, Nevada, Dilles and Einaudi 1992). Similar albitization that post-dates K-silicate alteration has also been observed in some alkaline porphyry deposits in the Lachlan fold belt in SE Australia (Wilson *et al.* 2003), and also appears to be magmatic-hydrothermal in nature.

In both Maricunga and alkaline porphyries, typical sericitic alteration, as observed in calc-alkaline porphyries, is virtually absent. At Vendaval, the shallow peripheral illitic alteration with pyrite veins may be a temporal and spatial equivalent.

The widespread hypogene intermediate argillic alteration overprint of K-silicate alteration is a characteristic of Au-rich porphyries in the Maricunga belt. This overprint has also been described in other Andean Au-rich porphyries (Esperanza, Perelló *et al.* 2004) and is likely comparable to sericite-chlorite-clay (SCC) alteration in Au-rich porphyries in the SW Pacific (Sillitoe and Gappe, 1984), where chlorite-clay may overlap in space with older muscovite.

Acknowledgments

We thank First Quantum Minerals, Markku Lappalainen, and Steve Andersson for supporting this research and encouraging this publication.

References

Cornejo, P (2021) Petrographic report of Vendaval samples. Internal to FQM.

Dilles, J H and Einaudi, M T (1992) Wall-rock alteration and hydrothermal flow paths about the Ann-Mason porphyry copper deposit, Nevada: A 6-km vertical reconstruction: Economic Geology, v. 87, p. 1963–2001.

Halley, S (2020) Mapping Magmatic and Hydrothermal Processes from Routine Exploration Geochemical Analyses. Economic Geology. 115 (3): 489–503. doi: https://doi.org/10.5382/econgeo.4722

Lang, J R, Stanley, C R, Thompson, J F H and Dunne, K P E (1995) Na-K-Ca magmatic-hydrothermal alteration in alkalic porphyry Cu-Au deposits, British Columbia: Mineralogical Association of Canada Short Course, v. 23, p. 339–366.

Muntean, J L and Einaudi, M T (2000) Porphyry Gold Deposits of the Refugio District, MaricungaBelt, Northern Chile. Economic Geology, 95(7), 1445.

Perelló, J, Brockway, H, and Martini, R (2004) Discovery and geology of the Esperanza porphyry copper-gold deposit, Antofagasta Region, northern Chile: Society of Economic Geologists Special Publication 11, p. 167−186.

Proffett, J M (2009) High Cu grades in porphyry Cu deposits and their relationship to emplacement depth of magmatic sources: Geology, v. 37, p. 675–678, doi:10.1130/G30072A.1

Ramirez, C A, Gardeweg, M, Davidson, J and Pino, H (1991) Mapa Geológico del área de los volcanes Socompa y Pular: Región Antofagasta. Servicio Nacional de Geología y Minería, Chile.

Sillitoe, R H, and Gappe, I M (1984) Philippine porphyry copper deposits Geologic setting and characteristics: United Nations Development Program, Coordinating Committee for Geosciences Programmes in East and Southeast Asia, Technical Publication 14, 89 p.

Vila, T, Sillitoe, R H (1991) Gold-rich porphyry systems in the Maricunga Belt, northern Chile. *Economic Geology*. 86 (6): 1238–1260. doi: https://doi.org/10.2113/gsecongeo.86.6.1238

Wilson, A J, Cooke, D R and Harper, B L (2003) The Ridgeway Gold-Copper Deposit: A High-Grade Alkalic Porphyry Deposit in the Lachlan Fold Belt, New South Wales, Australia. *Economic Geology* 2003; 98 (8): 1637–1666. doi: https://doi.org/10.2113/gsecongeo.98.8.1637

Magmatic evolution of the Archean Upper Beaver Intrusive Complex and its implications for Au-Cu mineralization

Michael Cloutier[1,2], Bertrand Rottier[1,2], Ross Sherlock[3], Georges Beaudoin[1,2], Jonathan Sutton[3,4], Olivier Côté-Mantha[4], Joshua Davies[5], Morgann Perrot[5]
[1]*Département de Géologie et Génie Géologique, Université Laval, Québec, Canada*
[2]*Centre de recherche sur la géologie et l'ingénierie des ressources minérales (E4m), Québec, Canada*
[3]*Harquail School of Earth Sciences, Mineral Exploration Research Center, Laurentian University, Canada*
[4]*Agnico Eagle Mines Ltd, Exploration Canada*
[5]*Département des sciences de la Terre et de l'atmosphère/GEOTOP, Université du Québec à Montréal*

Abstract. The Upper Beaver intrusion-related Au-Cu deposit is associated with the Archean Upper Beaver Intrusive Complex (UBIC). The UBIC is a polyphase intrusive complex with pre-, syn-, and post-mineralization phases. Whole-rock geochemistry is consistent with the UBIC having formed through magma mixing between a mafic to intermediate mantle-derived sanukitoid magma and an intermediate to felsic, basaltic-crust derived TTG magma. Phases of the UBIC that are associated with Au-Cu (+/- Mo) mineralization have a TTG magmatic affinity. LA-ICP-MS zircon geochronology shows that all phases of the UBIC were emplaced within error of ca. 2680 Ma which is consistent with previous Re-Os and U-Pb geochronology of molybdenite and zircon, respectively. Amphibole oxybarometry indicates that the UBIC was oxidized with fO_2 values between ΔNNO 0 and +1.6 which are similar to values from Phanerozoic arc magmas. Apatite geochemistry reveals a bimodal distribution in S content of the UBIC with the more felsic, mineralization-associated, TTG phases having lower S content than the more mafic sanukitoid phases. Additionally, negative Eu anomalies and low Sr content in apatite from the TTG phases are indicative of early plagioclase crystallization. This suggest that high magmatic H_2O content may not be a key factor for magmatic-hydrothermal Au-Cu mineralization in Archean systems.

1 Introduction

Magmatic-hydrothermal deposits are rare in the Archean compared to the Phanerozoic (Groves et al. 2005). This relative scarcity has been variably attributed to poor preservation, differences in geodynamic setting, and/or differences in physiochemical conditions (e.g., pressure, temperature, fO_2, fS_2, duration of the magmatic system) (Groves et al. 2005; Richards and Mumin 2013). In addition, the relative scarcity of these deposits in the Archean has resulted in a poor understanding on the processes controlling their fertility.

This study examines the magmatic evolution of the Archean Upper Beaver intrusive complex (UBIC) and its possible controls on mineralization in the related Au-Cu intrusion-related deposit.

2 The Upper Beaver Au-Cu Deposit

The Upper Beaver Au-Cu deposit (probable mineral reserves of ~1.4 Moz Au at 5.43 g/t and 20.0 kt Cu at 0.25%; indicated resources of ~0.4 Moz Au at 3.45 g/t and ~5.1 kt Cu at 0.14%; inferred resources of ~1.4 Moz Au at 5.07 g/t and ~17.3 kt Cu at 0.20%; Agnico Eagle Mines Ltd. 2023) comprises two temporally and mineralogically distinct Au-Cu(±Mo) intrusion-related mineralization events including 1) an early Ep+Adr skarnoid with replacement style Cp+Py+Mag+Au mineralization that is concordant to Blake River group mafic volcanics and volcaniclastics, and 2) later discordant Qz+Mag+Cc+Cp+Py+Hem+Au+Mol veins. Both mineralization events are spatially and temporally related to the UBIC which is subdivided into seven phases that are pre- syn- and post-mineralization (Figs. 1, 2). The earliest phase of the UBIC is a hypabyssal Amp-phyric diorite porphyry. The second phase of the UBIC is a Pl-Hbl glomerophyric diorite porphyry (GP). The GP is pre- to syn- the first Au-Cu mineralization event and is affected by the skarnoid alteration. The phases that post-date the first mineralization event are divided into two distinct groups (Fig. 2). The earlier of the two groups comprises three distinct dioritic to quartz-diorite phases that are defined by the presence of Amp±Pl phenocrysts. The latter of the two groups consists of Pl±Amp±Qz phyric monzodiorite to quartz-monzonite dykes (Fsp-porphyry) that crosscut all earlier phases. The Fsp-porphyry dykes have been divided based on their quartz content. However, it is not clear if they represent two distinct phases or a slight variation of mineralogy of the Pl+Amp±Qz porphyry. Finally, a post-mineralization Pl+Hbl phyric diorite dyke has been dated at 2678.7 ± 0.7 Ma (McNicoll, unpublished) marking the end of the magmatic-hydrothermal system.

The first Au-Cu skarnoid mineralization event is spatially associated with and hosted within the early GP as well as being concordant to the host mafic Blake River volcanic and volcaniclastic rocks. The skarnoid and its host rocks are crosscut by the diorite to quartz diorite phases.

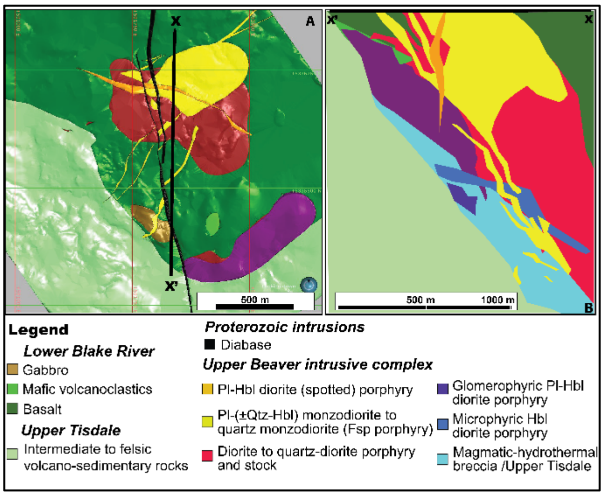

Figure 1. A) Simplified geological map of the Upper Beaver deposit. B) Cross section of the Upper Beaver deposit looking west (modified from Sutton and Côté-Mantha 2022)

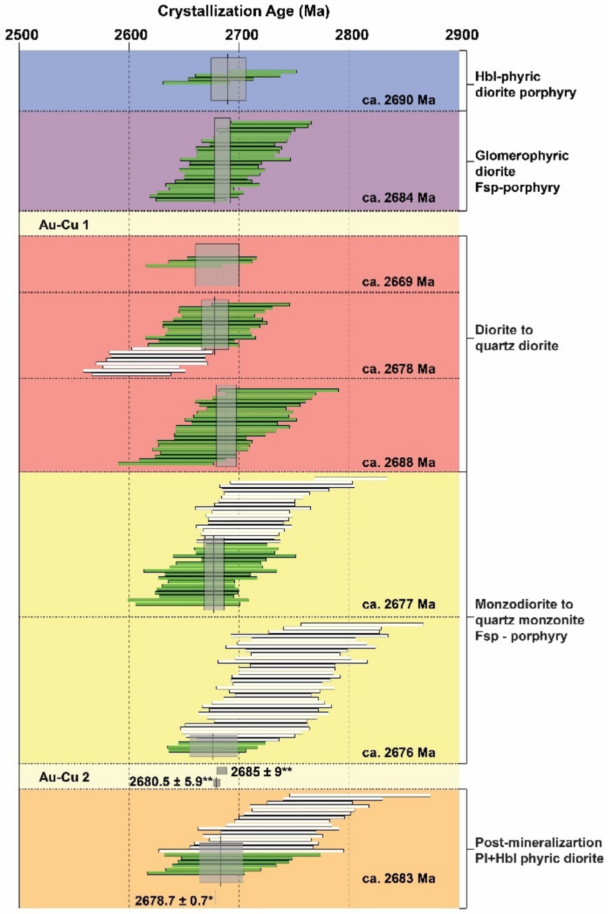

Figure 2. Relative timing and weighted mean zircon ^{207}Pb/^{206}Pb crystallization ages of the individual phases of the UBIC with the top being the earliest and bottom being the latest based on cross-cutting relationships. *Zircon U-Pb upper intercept crystallization age of 2678.7 ± 0.7 Ma (McNicoll, Unpublished). **Molybdenite Re-Os ages of 2685 ± 9 Ma and 2680.5 ± 5.9 Ma (Kontak et al. 2013; Mercier-Langevin et al. 2021, respectively).

The second mineralization event is responsible for most of the Au-Cu endowment of the Upper Beaver deposit and displays a spatio-temporal relationship with the Fsp-porphyry dykes. This event has been previously dated by Re-Os geochronology in molybdenite with ages of 2685 ± 9 Ma and 2680.5 ± 5.9 Ma (Fig. 2; Kontak et al. 2013; Mercier-Langevin et al. 2021 respectively) which are consistent with the crystallization age for the late post-mineralization Pl+Hbl phyric dyke.

3 U-Pb geochronology

New crystallization ages for each of the individual intrusive phases of the UBIC were determined using U-Pb methods in zircon by laser-ablation inductively coupled mass-spectrometry (LA-ICP-MS). Cathodoluminescence (CL) imaging of the zircons from the UBIC shows oscillatory and sector zoning with no evidence of inherited cores. Ages were calculated as a weighted mean of the ^{207}Pb/^{206}Pb ages for the youngest zircons in the samples. The number of zircons used for each age calculation was constrained using the maximum number of analyses for which the MSWD is consistent with a single population (Spencer et al. 2016). The second diorite to quartz diorite phase (Fig. 2) is an exception to this as the ^{207}Pb/^{206}Pb zircon ages for this sample form two populations with the younger population yielding a weighted mean ^{207}Pb/^{206}Pb age of ca. 2619 Ma. This age is significantly younger than the calculated ages for the Fsp-porphyry phases that crosscut this unit. Because this younger age is incompatible with observed field relationships, the older population was used in the age calculation.

All phases of the UBIC have crystallization ages within error of ca. 2680 Ma which is consistent with the previous U-Pb and Re-Os ages (Fig. 2; Kontak et al. 2013; Mercier-Langevin et al. 2021). A distinct difference is noted in the spread of ^{207}Pb/^{206}Pb ages in zircon from the UBIC, as the later Fsp-porphyry phases and post-mineralization Pl+Hbl phyric diorite dyke have an abundance of inherited zircon, in contrast to the earlier phases that have minimal inheritance.

4 Geochemistry

Whole-rock geochemistry of the UBIC, using only the least altered samples based on optical petrography, micro-XRF maps, and geochemistry, shows that the intrusive complex is calc-alkaline to slightly alkaline and metaluminous. Compositionally the samples range from monzodiorite to quartz monzonite when plotted on a TAS diagram (Middlemost 1994). While the total alkali content (K_2O + Na_2O) of the UBIC is elevated across the range of SiO_2, K_2O shows a negative correlation whereas Na_2O shows a positive correlation. General trace-elements signatures for the UBIC exhibit moderately to strongly fractionated REE patterns with minor Eu anomalies, elevated Sr/Y values, negative correlation between Dy/Yb and SiO_2, and primitive mantle normalized patterns (enriched LILE and depleted Nb and Ta). These signatures are consistent with a hydrated source for the UBIC with fractionation being driven by amphibole and minimal plagioclase. The GP phase is an exception to these patterns having a less fractionated REE signature (due to both relatively low La and high Yb concentrations) with an unfractionated HREE signature which suggests that amphibole and/or garnet were not fractionating phases for this unit (Fig. 3). On the A/CNK, Na_2O, FMSB discriminant diagram of Laurent et al. (2014), samples from the more mafic diorite to quartz-diorite phases plot within the sanukitoid-type field while the more felsic monzonite to quartz monzonite GP and Fsp-porphyry phases plot within the TTG-type field (Fig. 3).

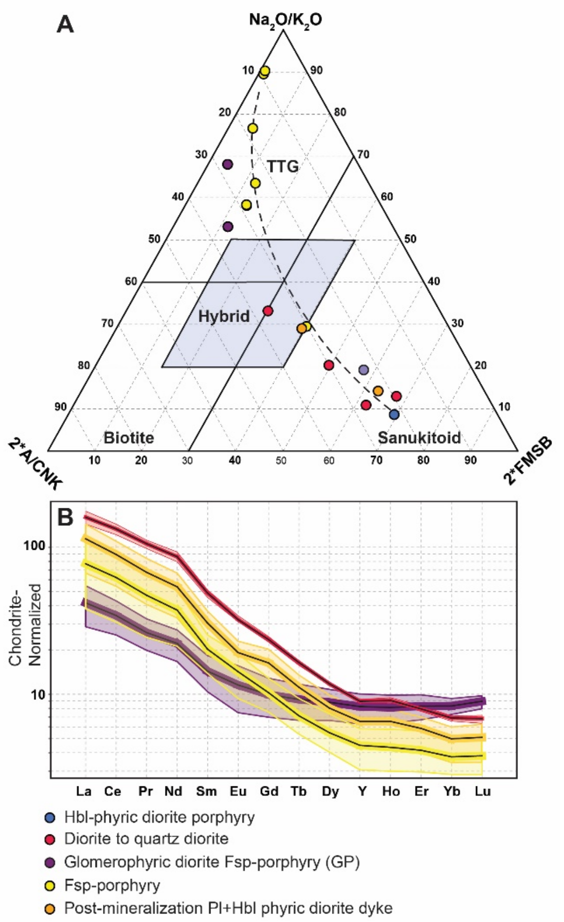

Figure 3. A) *A/CNK (molar Al/[Ca+Na+K]) vs Na_2O/K_2O vs 2*FMSB ([FeOt + MgO]wt.% * [Sr + Ba]wt.%) ternary plot of Laurent et al. (2014) showing magmatic affinity of the UBIC. The dashed line is the calculated mixing line between the sanukitoid and TTG end-members. B) Chondrite normalized (Sun and McDonough, 1989) REE+Y spider diagram. Coloured outlines show the range of concentrations for the respective intrusive phases. Coloured lines with black centers are the average values for the intrusive phases.

5 Mineral Chemistry

Physiochemical conditions of the UBIC were constrained through the use of amphibole and apatite chemistry.

The Al-in-amphibole geothermometer (Putirka 2016) for the earlier diorite to quartz diorite phase indicates an emplacement temperature of 885°C - 935°C (±30°C). Amphibole from the later Fsp-porphyry indicates a lower emplacement temperature of 770°C - 840°C (±30°C). Amphibole oxybarometry (Ridolfi et al. 2010) for the dioritic to quartz dioritic phase indicates fO_2 values between ΔNNO 0 and +1. The Fsp-porphyry are more oxidized with fO_2 values ΔNNO +0.5 and +1.6.

Apatite was analysed for major and trace elements for each of the phases of the UBIC. Sulfur content of apatite from the UBIC has a bimodal distribution and is comparable to the S content of apatite from Phanerozoic arc magmas (Meng et al. 2021a). Apatite from the main diorite to quartz diorite phases have the highest S content ranging from 0.15 – 0.35 wt.% while all other phases, including those associated with mineralization, typically have lower S content (0 – 0.175 wt.%). Manganese concentrations in apatite, which have been shown track melt evolution (Bromiley 2021), are positively correlated with Cl. This may suggest that the apatite crystalized prior to fluid exsolution and that S concentrations are reflective of the magma content. Apatite from the phases associated with mineralization (GP and Fsp-porphyry) have lower Sr concentrations and negative Eu anomalies compared to the other phases which is indicative of early plagioclase crystallization for these phases.

6 Discussion

6.1 Formation of the UBIC by magma mixing

The whole rock geochemical signatures are consistent with the UBIC having been derived from a hydrated source (Laurent et al. 2014). The sanukitoid-type signature of the more mafic dioritic and dioritic phases are suggestive of a predominately metasomatized mantle source. The TTG signature of the more felsic GP and Fsp-porphyry phases are suggestive of derivation from a hydrated low-K basaltic crust (Laurent et al. 2014). The negative K_2O vs SiO_2 correlation supports the UBIC having formed through mixing between melts derived from these two sources instead of fractional crystallization. The LA-ICP-MS U-Pb data from zircon are also consistent with two distinct sources as the phases that have a more “TTG-like” geochemical signature also have an abundance of inherited zircons. This abundance of inherited zircons is consistent with derivation from a crustal source.

6.2 Mineralization associated with low S, low H_2O magmas

Mineralization at the Upper Beaver deposit is spatially and temporally related to both GP and Fsp-porphyry phases. The relatively low S content of these phases as recorded by apatite indicates that high S content may not be a requirement for mineralization. Apatite from both the GP and Fsp-porphyry have negative Eu anomalies and low Sr concentrations consistent with plagioclase crystallization pre- to syn- apatite crystallization. Apatite is typically a near-liquidus phase in magmatic systems (Webster and Piccoli 2015), in agreement with our petrographic observations, which suggests that plagioclase was also a near-liquidus phase. The early crystallization of plagioclase in turn suggests a relative low H_2O

content for the GP and Fsp-porphyry phases as high H_2O has been shown to delay plagioclase crystallization (Loucks, 2014). This is in contrast to the causative magmas in Phanerozoic magmatic-hydrothermal systems which are typically more hydrous (Sillitoe, 2010; Richards, 2011; Loucks 2014). Relatively dry conditions are also reported for the other Archean mineralization-associated intrusions at the Archean (e.g., the Côté Gold Au±Cu deposit; Meng et al. 2021b). Evidence for these mineralization-associated magmas being relatively dry suggests that high magmatic H_2O content may not be a key factor in magmatic-hydrothermal Au±Cu mineralization for Archean systems.

7 Conclusions

The UBIC formed through mixing of at least two distinct magma derived from metasomatized mantle and basaltic crustal sources. U-Pb geochronology demonstrates that all phases of the intrusive complex were emplaced at ca. 2680 Ma and within the resolution of the LA-ICP-MS analysis. Amphibole and apatite chemistry shows that the physiochemical conditions (temperature, fO_2, S content) for emplacement of the UBIC are similar to conditions observed in Phanerozoic arc magmas. However, evidence of early plagioclase crystallization in the intrusive phases associated with mineralization suggest that they were relatively dry.

LASS-ICP-MS trace element and Lu-Hf isotopic analysis of previously analysed zircons to better constrain the physiochemical conditions and the degree of crustal contamination of the UBIC is in progress. High-precision dating of previously analysed zircons is currently in progress using CA-ID-TIMS to accurately constrain the total duration of the Upper Beaver magmatic-hydrothermal system.

Acknowledgements

This research is funded through a NSERC-Agnico Eagle Industrial Research Chair. The authors are grateful to Agnico Eagle Mines Ltd. for logistical support.

References

Agnico Eagle Mines Limited (2023) Kirkland Lake Regional. https://www.agnicoeagle.com/English/exploration/exploration-projects/Kirkland-Lake-project/default.aspx

Bromiley GD (2021) Do concentrations of Mn, Eu and Ce in apatite reliably record oxygen fugacity in magmas? Lithos 384–385:105900. https://doi.org/10.1016/j.lithos.2020.105900

Groves DI, Vielreicher RM, Goldfarb RJ, Condie KC (2005) Controls on the heterogeneous distribution of mineral deposits through time. SP 248:71–101. https://doi.org/10.1144/GSL.SP.2005.248.01.04

Kontak DJ, Dubé B, McNicoll V, et al (2013) The Upper Beaver Au-Cu deposit, Kirkland Lake, Ontario, Canada: An Archean IOCG analogue or just an intrusion-related iron oxide copper-gold deposit? Geol. Assoc. Canada - Mineral. Assoc. Canada Conf, May 21-24, Winnipeg, MB, Abstr. Vol. 36, p. 122

Laurent O, Martin H, Moyen JF, Doucelance R (2014) The diversity and evolution of late-Archean granitoids: Evidence for the onset of “modern-style” plate tectonics between 3.0 and 2.5Ga. Lithos 205:208–235. https://doi.org/10.1016/j.lithos.2014.06.012

Meng X, Kleinsasser JM, Richards JP, et al (2021a) Oxidized sulfur-rich arc magmas formed porphyry Cu deposits by 1.88 Ga. Nat Commun 12:2189. https://doi.org/10.1038/s41467-021-22349-z

Meng X, Richards JP, Kontak DJ, et al (2021b) Variable Modes of Formation for Tonalite–Trondhjemite–Granodiorite–Diorite (TTG)-related Porphyry-type Cu ± Au Deposits in the Neoarchean Southern Abitibi Subprovince (Canada): Evidence from Petrochronology and Oxybarometry. Journal of Petrology 62: egab079. https://doi.org/10.1093/petrology/egab079

Mercier-Langevin P, Creaser R, Dube B, et al (2021) Molybdenite Re-Os ages of a gold-rich vein, Porphyry zone, Upper Beaver deposit, Abitibi greenstone belt, Ontario. Geological Survey of Canada Open File 8789:13

Middlemost EAK (1994) Naming materials in the magma/igneous rock system. Earth-Science Reviews 37:215–224. https://doi.org/10.1016/0012-8252(94)90029-9

Putirka K (2016) Amphibole thermometers and barometers for igneous systems and some implications for eruption mechanisms of felsic magmas at arc volcanoes. American Mineralogist 101:841–858. https://doi.org/10.2138/am-2016-5506

Richards JP, Mumin AH (2013) Magmatic-hydrothermal processes within an evolving Earth: Iron oxide-copper-gold and porphyry Cu Mo Au deposits. Geology 41:767–770. https://doi.org/10.1130/G34275.1

Ridolfi F, Renzulli A, Puerini M (2010) Stability and chemical equilibrium of amphibole in calc-alkaline magmas: an overview, new thermobarometric formulations and application to subduction-related volcanoes. Contrib Mineral Petrol 160:45–66. https://doi.org/10.1007/s00410-009-0465-7

Spencer CJ, Kirkland CL, Taylor RJM (2016) Strategies towards statistically robust interpretations of in situ U–Pb zircon geochronology. Geoscience Frontiers 7:581–589. https://doi.org/10.1016/j.gsf.2015.11.006

Sutton J, Côté-Mantha O (2022) Geology of the Archean Upper Beaver oxidised intrusion-related Au-Cu deposit (Kirkland Lake, Ontario). Quebec Mineral Exploration Association XPLOR, Oct 3-6, Montreal QC.

Webster JD, Piccoli PM (2015) Magmatic Apatite: A Powerful, Yet Deceptive, Mineral. Elements 11:177–182. https://doi.org/10.2113/gselements.11.3.177

Volatiles in zircon-hosted apatite from the Escondida porphyry copper district, northern Chile

Giulia Consuma[1], Anthony I. S[1]. Kemp, Laure Martin[2], Steffen Hagemann[1], Marco L. Fiorentini[1], Brian Tattitch[1]
[1] Centre for Exploration Targeting, The University of Western Australia, Perth, Western Australia, Australia.
[2] Centre for Microscopy, Characterisation and Analysis, The University of Western Australia, Perth, WA 6009, Australia

Abstract. Apatite inclusions armoured in zircon are ideal candidates to fingerprint the original volatile component (S, Cl, F, OH) of ore-forming magmas. A thorough investigation of such inclusions, together with matrix apatite, is hereby used to elucidate the volatiles sources and pathways throughout the magmatic-hydrothermal stages of individual porphyry Cu deposits at Escondida, northern Chile. We selected a suit of least-altered samples, mineralised and barren, to resolve the physico-chemical conditions of the melt/fluid responsible for the Cu-Mo±Au mineralisation in Escondida during the long-lasting late Eocene-Oligocene (44-33 Ma) arc magmatic activity. SEM-BSE-CL imaging, together with measurements of halogens and sulfur concentrations with electron micropobe allowed us to build a comprehensive insight into the volatile content and geochemical signature of apatite. We also measured high precision $\delta^{34}S$ values in apatite via SIMS to elucidate the S isotope signature of apatite inclusions and matrix apatite. Our preliminary data show that detailed mineral chemistry, microtextural studies, and sulfur isotope measurements applied to apatite inclusions in zircon and matrix apatite provide a unique insight into the geochemical behaviour of sulfur and halogens in ore-forming magmas.

1 Introduction

Different volatile-rich species exsolve from silicate magmas at variable P-T conditions. In addition to water, chlorine (as a metal complexing agent) and sulfur (to sequester metals as sulfide minerals) are essential components for the generation of ore-porphyry magmas (i.e., Grondahl and Zajacz 2022; Tattitch et al. 2021). However, direct studies of the magmatic volatile components are hindered by degassing processes and by the limited suitability of inclusions for analyses. For this reason, the volatile budget and isotopic signature of the initial melt, together with constraints on the volatile sources in porphyry copper environments remain unresolved. To address this, we examine the budget of S, Cl, and other volatile species from the Escondida porphyry Cu-Mo±Au district by investigating apatite enclosed in zircon.

Apatite, $Ca_5(PO_4)_3(F,Cl,OH)$, is a well-known repository of volatile species (H_2O, CO_2, S, halogens) in addition to numerous trace elements, making it an excellent mineral to study the volatile budget of a magma (Piccoli and Candela 2002). Once encapsulated in zircon, apatite inclusions are able to preserve a unique record of the abundance of volatile ore-forming constituents, eliminating diffusion effects associated with late-stage melts and/or fluids (Kendall-Langley et al. 2021).

We use a multi-microanalytical approach (petrography, cathodoluminescence imaging, SEM-BSE, EPMA and SIMS) in apatite enclosed in zircon and zoned matrix apatite to ultimately understand the role volatiles into the formation of high-grade copper deposits at Escondida.

2 Escondida porphyry Cu-Mo±Au district

The Escondida porphyry copper district is developed along the regional Domeyko Faut system in the Atacama Desert of Chile, ca. 170 km southeast of the port city of Antofagasta at an elevation of 3,050m above the sea level. The entire district comprises the Escondida cluster (namely, Escondida-Escondida-Este, Pampa Escondida, Baker, Pinta Verde, Escondida Norte-Zaldívar) and 15km north-west, the Chimborazo deposit (Figure 1). The ore-forming magmatism took place in the framework of the long-lasting late Eocene-Oligocene (44-33 Ma) arc magmatic activity (Hervé et al 2012 and references therein), favouring the emplacement of multiphase porphyry stocks (early, inter-, late). The Escondida stock intrudes a series of Paleocene andesites, corresponding to the *Augusta Victoria Formation*, which are interbedded by sedimentary units and are mostly exposed in the western and southern part of the district (Quiroz 2003 Unpubl MSc thesis). Magmatic-hydrothermal breccias of intermineral timing formed in all the deposits of the Escondida district, including Chimborazo, and host significant hypogene mineralisation (Hervé et al. 2012).

For this study, we sampled a suit of mineralised porphyries from the Escondida cluster and unmineralized volcanic and intrusive rocks that are spatially and temporally related to the Cu-Mo±Au mineralisation.

3 Analytical methods

3.1 SEM-CL analyses

The mineralogical and textural characterisation of apatite and zircon was carried out with an optical microscope and a Tescan VEGA3 scanning electron microscopy-energy dispersive spectroscopy (SEM–EDS) system. Mineral inclusions within the zircon crystals were analysed by EDS, allowing the identification of apatite inclusions. High contrast back scattered electron (BSE) and cathodoluminescence (CL) imaging was carried out on epoxy mounted zircon and apatite crystals to identify crystal growth structures and the presence of core domains that may represent older (pre-magmatic) components. Further apatite crystals were characterised in thin sections, allowing a detailed microtextural investigation.

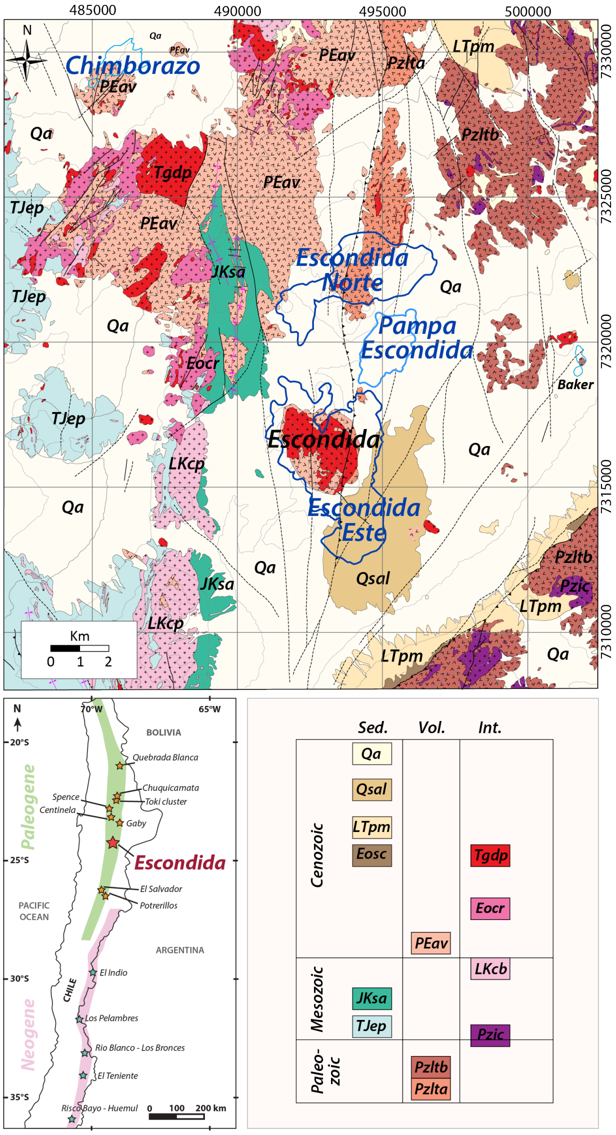

Figure 1. Geology of the Escondida district adapted and slightly modified from Gibbson 2018 (published PhD Thesis) whose figure was originally based on mapping by Hervé et al. (2012) and Urzúa (2009). Map of the central and northern Chile showing the Paleogene and Neogene metallogenic belts is modified after Piquer et al. (2021).

3.2 EPMA – Apatite volatile contents

Major and minor elements of targeted groundmass apatite and apatite inclusions were measured with a JEOL 8350F field emission electron micro-analyser (EPMA) at the Centre for Microscopy, Characterisation, and analyses (CMCA) of the University of Western Australia. Elements F, Cl, Ca, P, Sr, S, Mn, Mg, Si, Na, La, Ce, and Nd were measured in apatite inclusions in zircon using a 15nA electron beam current, 15 kV accelerating voltage and a spot size of 5 µm. The EPMA spots were set to be perpendicular to the *c*-axis of apatite to avoid the disturbance from the orientation of apatite grains. The accuracy of the analyses relative to standards was the following: major elements (Ca and P) < 1%; F and Cl < 2-3%; minor elements (S, Si, Ce, Na, Mn, Fe, Nd) <10%.

The F, Cl, OH concentrations of apatite inclusions were determined stoichiometrically following the approach of Ketcham (2015), assuming a full X-site.

3.3 SIMS – S isotope of apatite

In situ sulfur isotope (^{32}S and ^{34}S) analyses of apatite inclusions and matrix apatite were conducted using a CAMECA IMS1280 at the Centre for Microscopy, Characterisation, and analyses (CMCA) of the University of Western Australia. Zircon and apatite grains were mounted in epoxy resin and carefully polished. Epoxy resin mounts were therefore coated with 20nm-thick gold. Big1 grains were used as standard material, and the reader is referred to the work of Hammerli et al. (2021) for the analytical procedure. For matrix apatite, the sample surface was sputtered over a 15 x 15 µm area with a 10 kb, Gaussian Cs+ beam with intensity of ca. 1-3 nA and total impact energy of 20 keV. For apatite inclusions, the beam size was reduced to a 5 x 5 µm area.

4 Zircon and apatite microstructure

Zircon grains containing apatite inclusions were retrieved from mineral separation procedures and handpicked under a binocular microscope, mounted into epoxy mounts with zircon and apatite reference materials and polished to expose the mid-sections. BSE and CL imaging of zircon was carried out to detect zircon growth textures and zoning, in addition to identifying the mineral inclusion cargoes. Zircon grains in the mineralised samples range between 100 – 300 µm in length, with the majority around 200 µm in length and aspect ratios of 1:2 to 1:4. Most zircon grains contain mineral inclusions, with apatite as the most abundant followed by k-feldspar and quartz. Zircon grains from the barren intrusions show a larger size compared to those found in the mineralised samples, ranging between 100 to 500 µm in length and with the majority of the crystals around 300 µm. Spherical and lobate inclusions identified as melt inclusions are common in zircon from the unmineralized andesite host rock and other barren rocks. Zircon crystals display a range of internal textures revealed by CL (Figure 2). Secondary dissolution/reabsorption features are present in some grains and are most visible where they interrupt zoning. The reabsorption may just affect one CL band or affect a whole section of the zircon. The most common texture is oscillatory zoning, which exhibits bands ranging in CL intensity from a bright CL response to near black.

Apatite inclusions have a grain size ranging between 5 to 20 µm in the mineralised samples and reaching up to 40 µm in size in the associated unmineralized igneous rocks. The inclusions occur at the proximity of the zircon rims, with a few examples observed close to the zircon core. Thin sections observations show apatite crystals interstitial to silicates and inclusions of apatite within other primary igneous minerals, such as plagioclase phenocrysts and amphibole. In the mineralised samples, anhedral apatite locally forms veins and veinlets in equilibrium with anhydrite. Euhedral crystals of apatite are also commonly found as inclusions in anhydrite. Matrix apatite often intergrows with hydrothermal minerals, such as rutile, ilmenite, anhydrite, pyrite, and chalcopyrite. Apatite crystals elongated on the c-axis commonly show inclusions of monazite, carbonates, anhydrite, K-feldspar, quartz, and zircon.

CL imaging reveals that the majority of apatite crystals parallel to the c-axis are chemically zoned. These apatite crystals usually show gradational zoning from near black cores to lighter rims under CL. However, irregular CL patches and homogenous CL colors are also observed in matrix apatite.

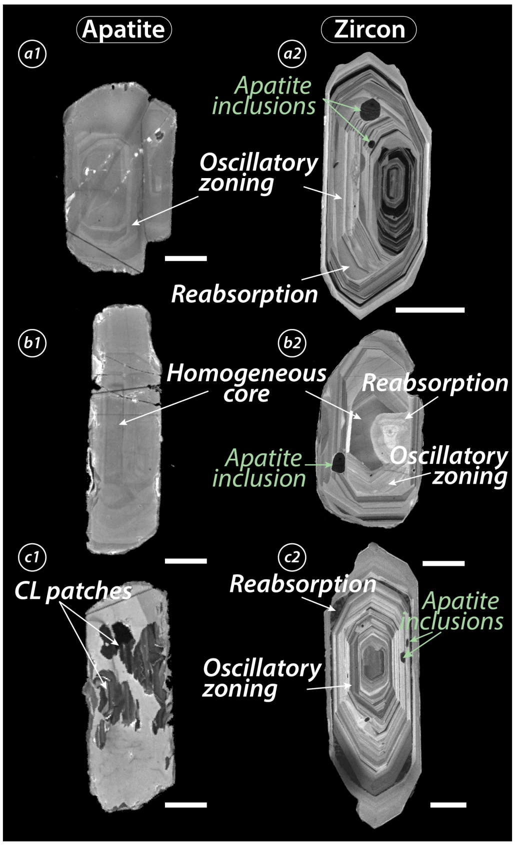

Figure 2. Cathodoluminescence images of apatite (a1, b1, c1) and zircon (a2, b2, c2) grains from mineralised samples showing examples of the most common internal textures and zoning. A 50µm-scale is shown for each grain.

5 Halogens, S content and S isotope of apatite inclusions

The barren samples exhibit variable F-Cl-OH and S compositions. Apatite inclusions from the biotite andesite porphyry show F concentrations of 1.18 to 2.58 wt%, Cl concentrations of 1.85 to 3.92 wt%, and OH concentrations of near zero to 0.83 wt%. Apatite from the quartz monzodiorite exhibits F concentration of 1.67 to 3.20 wt%, Cl concentration of 1.14 to 3.06 wt%, and OH concentrations of 0.19 to 1.16 wt%. The few spots analyses of apatite inclusions from the fine-grained pyroxene-bearing monzodiorite and from the andesitic host rock show F values of 1.03-1.27 wt% and 1.76 wt%, Cl values of 1.88-2.16 and 1.32 wt%, and OH values of 1.25-1.31 and 1.27 wt%, respectively. Apatite inclusions across the regional samples always reveal S concentrations above the detection limit, ranging between 0.13 to 0.75 wt% SO_3. Further future SIMS measurements of apatite inclusions from the unmineralized samples will be carried out for comparison with the barren intrusions.

In the samples hosting the mineralisation, apatite inclusions record variable, but lower Cl concentrations compared to the unmineralized samples (Figure 3), with values spanning from 0.41 to 1.50 wt% Cl and few outliers. On the other hand, in the mineralized porphyries, apatite inclusions record SO_3 concentrations ranging between values below detection limit and 0.73 wt%, thus not showing significant distinctions with the apatite inclusions from the unmineralized samples.

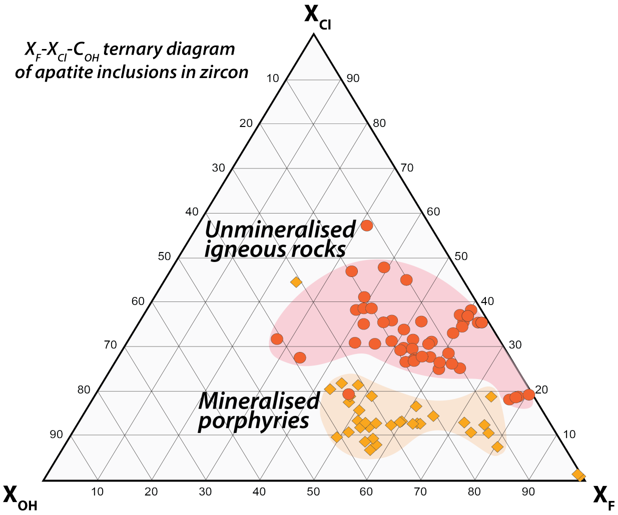

Figure 3. X_F-X_{Cl}-X_{OH} ternary diagram showing the compositional ranges of apatite inclusions in zircon from the studied mineralised and unmineralized samples. Mole fractions of F and Cl in apatite are calculated using the method of Piccoli and Candela (2002).

Apatite inclusions exhibit fairly homogeneous, positive, $\delta^{34}S$ values ($\delta^{34}S > 0‰$), irrespective of the mineralisation stage recorded in the rock sample (i.e., early porphyry, late porphyry). Matrix apatite shows a strong zoning in cathodoluminescence (CL). The dark core under CL of matrix apatite shows positive $\delta^{34}S$ values, similar to those measured in the inclusions. The CL-lighter rims, instead, record $\delta^{34}S$ values trending toward lighter, negative values.

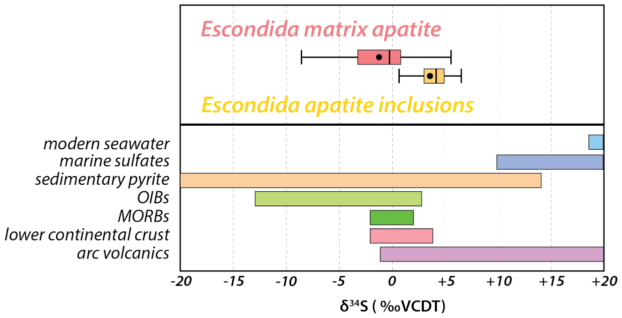

Figure 4. S isotope signature of the investigated apatite inclusions and matrix apatite from the mineralized samples. S isotopic compositions from different reservoirs are reported for comparison. The reader is referred to Hammerli et al. (2021) and reference therein for the full explanation.

6 Discussion and conclusion

The new microanalytical approach for studying the volatile component of apatite inclusions and matrix apatite from the Escondida porphyry Cu district involves a combination of microtextural studies, mineral chemistry and in-situ isotopic investigations. Further analytical measurements and experimental constraints are required to fully understand the physico-chemical conditions that favoured the mineralisation at Escondida. However, our preliminary data identified the potential to discriminate different pathways of halogens and S among different mineralised and barren samples. The grain size of the zircon separates is the first-order observation that differentiates between the mineralised and the barren rocks in Escondida. Specifically, the smaller size of the zircon grains (and associated apatite inclusions) from the mineralised samples compared to those from the barren intrusions could be attributed to a number of factors, including differences in magma ascent rates, depth of crystallization, and water availability. For example, it is possible that the ore-forming magma was emplaced at a shallower depth and cooled rapidly compared to the infertile-magma, resulting in smaller zircon and apatite crystals.

We identified a significant distinction in the Cl concentration of apatite inclusions from the Cl-poor mineralised porphyries and Cl-enriched barren rocks. One possible explanation is that the ore-forming magma lost Cl prior to the crystallization of apatite and its entrapment in the zircon. This loss of Cl may have occurred due to the partitioning of Cl into exsolving aqueous fluids during magma ascent. If this is the case, it would suggest that the Cu-Mo±Au porphyry bearing magma was originally richer in Cl than the apatite inclusions suggest. It is therefore essential to take into consideration the volatile composition of the source component that contributed to the melt as well as the involvement of other processes, such as magma mixing or crustal assimilation. Further constrains on the temperature of zircon crystallisation and apatite entrapment will be applied to fully resolve the original halogens content of the ore-forming magma.

The S concentrations of the apatite inclusions are variably similar between mineralised and unmineralized samples. In the mineralised samples, the S concentrations and isotopic measurements indicate that matrix apatite records a complex magmatic-hydrothermal evolution, which trends toward lighter (and negative) $\delta^{34}S$ values and contrasts with the positive S isotopic signature of the zircon-hosted apatite. This may be attributed to S isotopic fractionation during low-T open-system processes, to the presence of anhydrite in the rock sample, or to the involvement of sulfur from different reservoirs.

Our preliminary data suggest that apatite inclusions in zircon are valuable tools for studying the volatile signature and behaviour of ore-forming and infertile-magmas in the Escondida district. Further research will be needed to fully understand the source of volatiles and their contribution to the Cu-Mo±Au mineralisation in Escondida.

Acknowledgements

BHP is thanked for providing the funds to conduct the field work in Escondida and the analytical work on apatite. Matvei Aleshin is thanked for assisting during the SIMS measurements at CMCA, UWA.

References

Gibbson J (2018) Magmatic-hydrothermal evolution of the pampa Escondida porphyry copper deposit, Northern Chile. Publ. PhD Thesis, The University of Arizona.

Grondahl C, Zajacz Z (2022) Sulfur and chlorine budgets control the ore fertility of arc magmas. Nat Commun 13, 4218. https://doi.org/10.1038/s41467-022-31894-0

Hammerli J, Greber ND, Martin L et al (2021) Tracing sulfur sources in the crust via SIMS measurements of sulfur isotopes in apatite. Chem Geol, 579. https://doi.org/10.1016/j.chemgeo.2021.120242

Hervé M, Sillitoe RH, Wong C, Fernández P, Crignola F, Ipinza M, Urzúa F (2012) Geologic Overview of the Escondida Porphyry Copper District, Northern Chile, in: Geology and Genesis of Major Copper Deposits and Districts of the World. Tribute to Richard H. Sillitoe. Society of Economic Geologists, Special Publication 16, 55-78.

Kendall-Langley LA, Kemp AIS, Hawkesworth CJ, Craven J, Talavera C., Hinton R., Roberts MP, EIMF (2021) Quantifying F and Cl concentrations in granitic melts from apatite inclusions in zircon. Contrib Mineral Petrol 176, 58. https://doi.org/10.1007/s00410-021-01813-5

Piccoli PM, Candela PA (2002) Apatite in Igneous Systems. Reviews in Mineralogy and Geochemistry 4. https://doi.org/10.2138/rmg.2002.48.6

Piquer J, Sanchez-Alfaro P, Pérez-Flores P (2021) A new model for the optimal structural context for giant porphyry copper deposit formation. Geology 49, 597-601. https://doi.org/10.1130/G48287.1

Tattitch B, Chelle-Michou C, Blundy J, Loucks RR (2021) Chemical feedbacks during magma degassing control chlorine partitioning and metal extraction in volcanic arcs. Nat Commun 12, 1774. https://doi.org/10.1038/s41467-021-21887-w

White mica alteration in the Gaby porphyry copper district, Northern Chile

Alexandre Cugerone[1], Kalin Kouzmanov[1], Lluis Fontboté[1], Luis Krampert[1], Carolina Rodríguez[2], Rubén Pardo[2], Sergio Pichott Henríquez[2]
[1]*Department of Earth Sciences, University of Geneva, 1205 Geneva, Switzerland*
[2]*CODELCO, Santiago, Chile*

Abstract. White mica alteration in porphyry systems is often directly associated with economic mineralization. White mica chemistry may record the evolution of the hydrothermal system and could represent an important vectoring tool for Cu-Mo mineralization. However, in such setting, macro to microscale variations in white mica chemistry are still poorly understood. Here, we focus on the white mica alteration in the Gaby porphyry copper district (Northern Chile), using automated mineralogy (QEMSCAN), short-wave infrared (SWIR), and electron microprobe (EMPA) analyses. The Gaby district consists of Late Carboniferous-Early Permian volcano-sedimentary rocks, the Permo-Triassic Pampa Elvira plutonic complex, and Eocene tonalite porphyries. Two main types of white mica alteration are identified: i) Early green Fe-Mg-rich sericite is observed in veins, halos, and as pervasive alteration, frequently intergrown with chalcopyrite-bornite and low amounts of pyrite; ii) Late grey Fe-Mg-poor sericite is found disseminated, locally as secondary alteration on green sericite, and in halos of pyrite-rich veins. In these veins, green sericite is also present as infill, as well as in their outermost zone. Correlation between portable SWIR (TerraSpec) analyses and variations of white mica composition at micrometer scale as determined with QEMSCAN and EMPA demonstrates the strengths and limitations of the SWIR spectroscopy in exploration for porphyry systems.

1 Introduction

White mica alteration zones commonly host high-grade ore in porphyry systems (Reed et al. 2013; Uribe-Mogollon and Maher 2018; Alva-Jimenez et al. 2020). During the evolution of a porphyry system, white mica composition changes due to variations in fluid temperature and composition and is also influenced by the primary composition of the mineral replaced (e.g., plagioclase, biotite). Two general types of white mica/sericite alteration are recognized in porphyry systems (Uribe-Mogollon and Maher 2018; Skarmeta 2021): deep early green sericite alteration is typically associated with chlorite, whereas shallow late grey sericite alteration is not associated with chlorite.

Vectoring using white micas is commonly based on short-wave infrared (SWIR) spectroscopy, which records specific spectral characteristics such as the Al-OH peak position and depth (Chang and Yang 2012; Calder et al. 2022). The spectral signature of white mica is chemically influenced by the Tschermak substitution : $Al^{3+}_{tet} + Al^{3+}_{oct} \leftrightarrow Si^{4+}_{tet} + Mg^{2+}_{oct}$ or Fe^{2+}_{oct} (Guo et al. 2019; Cloutier et al. 2021). A recent study demonstrates the potential of using trace elements in white mica as a vectoring tool in porphyry systems (Uribe-Mogollon and Maher 2020).

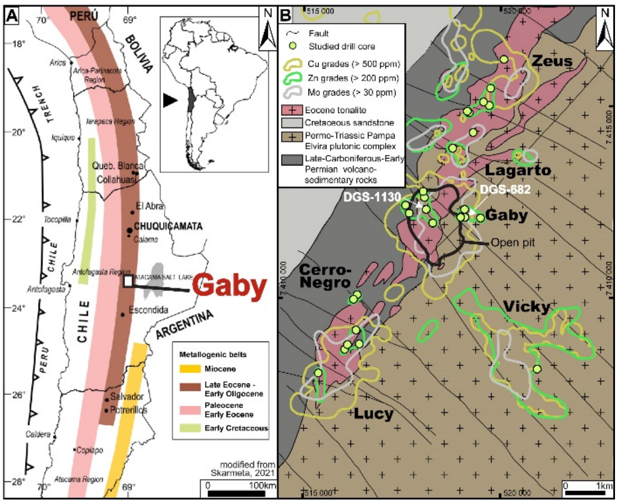

Figure 1. A. Location of the Gaby district within the Upper Eocene-lower Oligocene metallogenic belt in Chile (modified from Skarmeta 2021). B. Schematic geological map of the Gaby district with the reported grades for Cu, Zn and Mo and location of the two drill holes studied (DGS1130 and DGS682).

In porphyry deposits, stockwork veining is commonly a polyphase process, and frequently shows reopening textures with superimposed alteration halos (Rusk et al. 2008; Sillitoe 2010). Consequently, chemistry of white micas can be significantly affected by overprinting of multiple alteration/mineralization events.

In this contribution, we focus on the Gaby porphyry Cu-Mo deposit in Northern Chile. Based on petrographic observations, automated mineralogy (QEMSCAN), short-wave infrared (SWIR), and electron microprobe (EMPA) analyses, we discriminate a large variety of white mica textures and compositions, related to multiple mineralizing events, overprinting each-other in space and time.

2 Geology of the Gaby district

The Gaby district is located in the Late Eocene to Early Oligocene metallogenic belt, in Northern Chile (Figure 1A). The district includes the Gaby deposit, currently in operation, and numerous prospects such as Lucy, Cerro Negro, Vicky, Lagarto, and Zeus (Figure 1B). Mineralization is hosted in Eocene tonalite porphyritic intrusions, emplaced in the large composite Permo-Triassic Pampa Elvira plutonic complex, and locally in Late Carboniferous-Early

Permian volcano-sedimentary rocks of the La Tabla Formation. The Eocene tonalite intrusions follow a general N 040-50E trend, along the contact between the Pampa Elvira plutonic complex and the La Tabla Formation. The Permo-Triassic plutonic complex and most of the Eocene porphyries are similar in terms of texture and geochemistry, whereby the Pampa Elvira plutonic complex shows higher proportion of K-feldspar. Potassic alteration is observed all along strike of the Eocene porphyritic intrusions, as well as in the host Permo-Triassic plutonic complex.

Multiple sets of faults are noticed: NE-SW normal faults, and N-S to NW-SE reverse faults. The NW-SE normal faults show post-mineralization displacement that modifies the architecture of the district. The northern part (Zeus-Lagarto) is structurally deeper than the southern part (Lucy–Cerro Negro prospects; Figure 1B).

Porphyry-style mineralization is mainly disseminated and in veinlets; stockwork mineralization is not common (Figure 2). Chalcopyrite and bornite are the main copper minerals, frequently associated with molybdenite and quartz. Pyrite is typically associated with late D-veins. Supergene chalcocite, atacamite and chrysocolla can be observed at up to ~ 200-250 m below surface.

Late polymetallic veinlets have been noticed so far mainly in the southern part of the district, in the Cerro Negro, Lucy and Vicky prospects (Figure 1B), partly as reopening of pre-existing porphyry-style veinlets (Figure 3A). Sphalerite, galena, tennantite-tetrahedrite, pyrite and chalcopyrite occur together with quartz and/or multiple generations of carbonates including rhodochrosite, siderite, ankerite, siderite, and calcite, in part Fe and/or Mn-bearing.

3 Methods

One hundred thirteen samples were collected approximatively every 5 meters from two drill holes in the Gaby open pit (Figure 1B). The studied interval of hole DGS1130 mostly intersects the Eocene tonalite porphyry (Figure 2) and the one of DGS682, the Pampa Elvira plutonic complex.

SWIR measurements were obtained using an ASD TerraSpec Halo Mineral Identifier. Three analyses were performed on each rock slice from which a thin section was also obtained. Acquisition time was 10s and the standard beam size - 1 cm. Absorption features (Al-OH, Mg-OH, Illite crystallinity) determined by the Terraspec Halo internal software and The Spectral Geologist (TSG) software were compared. The results are generally similar (~ 0.1 nm). Based on the two mineralogical databases (TerraSpec halo and TSG), a last check of each Hull-quotient-transformed spectrum was completed.

Automated mineral analysis and textural imaging were performed using an FEI QEMSCAN Quanta 650F facility at the University of Geneva. The QEMSCAN system is equipped with two Bruker QUANTAX light-element EDS detectors. White mica varieties were discriminated based on their Fe and Mg content and Al/Si ratio, while chlorite varieties - based on their Mg/Fe ratio and Mn content.

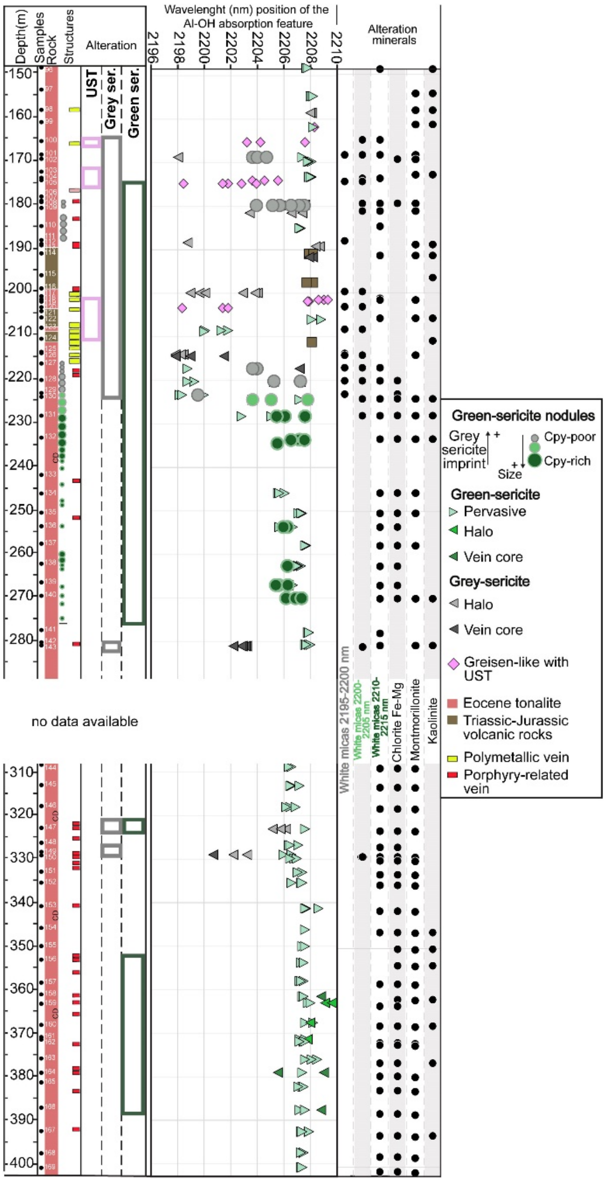

Figure 2. Log of drill hole DGS1130 reporting the type of host rock, the main mineralized structures, the type of alteration, and the Al-OH absorption feature and alteration minerals identified with SWIR.

Major and minor element compositions of white micas were determined by electron microprobe analysis (EMPA) using a JEOL JXA-8200 Superprobe microanalyzer equipped with five wavelength dispersive X-ray spectrometers (WDS) at the University of Geneva. Measured elements include Si, Ti, Al, Cr, Fe, Mn, Mg, Ca, Na, K, Ba and Cl. The acceleration voltage and beam current were 15 kV and 15 nA, and beam diameter used 5 μm.

4 Texture, chemistry, and SWIR signature of green and grey sericite

4.1 Green sericite

Green sericite is mostly observed in the deeper parts of the tonalite porphyries (from ~200 to ~400 m depth; Figure 2) but is also identified at shallow levels in the Pampa Elvira plutonic complex (~50 m in hole DGS682). Green sericite mostly consists of phengite, generally with grain size lower than 1mm. It occurs with chlorite that locally is enriched in Mn (up to 2-3 wt% Mn). Green sericite occurs as: (i) replacing pluri-centimetric magmatic nodules in the tonalite, only located in an interval from 170 to 270 m depth, that show frequently chalcopyrite along their borders; ii) as pervasive alteration; iii) in veinlets; iv) in alteration halos, preferentially in veinlets at around 300-400 m depth (Figures 2 and 3).

Microprobe analyses of green sericite yield relatively high Mg and Fe contents, ranging 0.15-0.35 apfu and 0.10-0.25 apfu, respectively, and low Na and Al contents, 0.01-0.55 and 2.45-2.70 apfu, respectively. Green sericite is frequently intergrown with chalcopyrite and low amounts of bornite (Figure 3).

4.2 Grey sericite

Grey sericite is composed of phengite, generally coarse-grained (up to few millimetres), and postdates the green sericite alteration. Grey sericite is mostly observed in the upper part of the drill hole (around 200 m; Figure 2) and frequently obliterates previous textures, especially green sericite in magmatic nodules. Two types of textures/structures are observed: i) grey sericite in the halos of pyrite-rich D-veins, with local occurrence of K-Fe-Mg-depleted illite close to pyrite (Figure 3 and 4); ii) pervasive alteration overprinting also green sericite alteration in magmatic nodules.

Microprobe data show generally low Fe and Mg contents, ranging 0.02-0.07 and 0.02-0.12 apfu, respectively (Figure 4). Sodium and Al contents in grey sericite reach 0.05-0.06 and 2.73-2.82 apfu, respectively.

Figure 4a illustrates variations of K, Mg and Fe along a transect across grey sericite halo of a pyrite-rich D-vein. Grains replacing former magmatic "book" biotite and occurring close to pyrite grains show the lowest K content. This is attributed to the presence of illite (typically depleted in K; Alva-Jimenez et al. 2020). No change in K content is observed between green and grey sericite. Iron and Mg are depleted in grey sericite compared to green sericite (Figure 4A), Al and Ti have similar content, and Si is higher in grey sericite. Si/(Fe+Mg) ratio (Figure 4B) is above 15 for grey sericite and lower than 15 for green sericite.

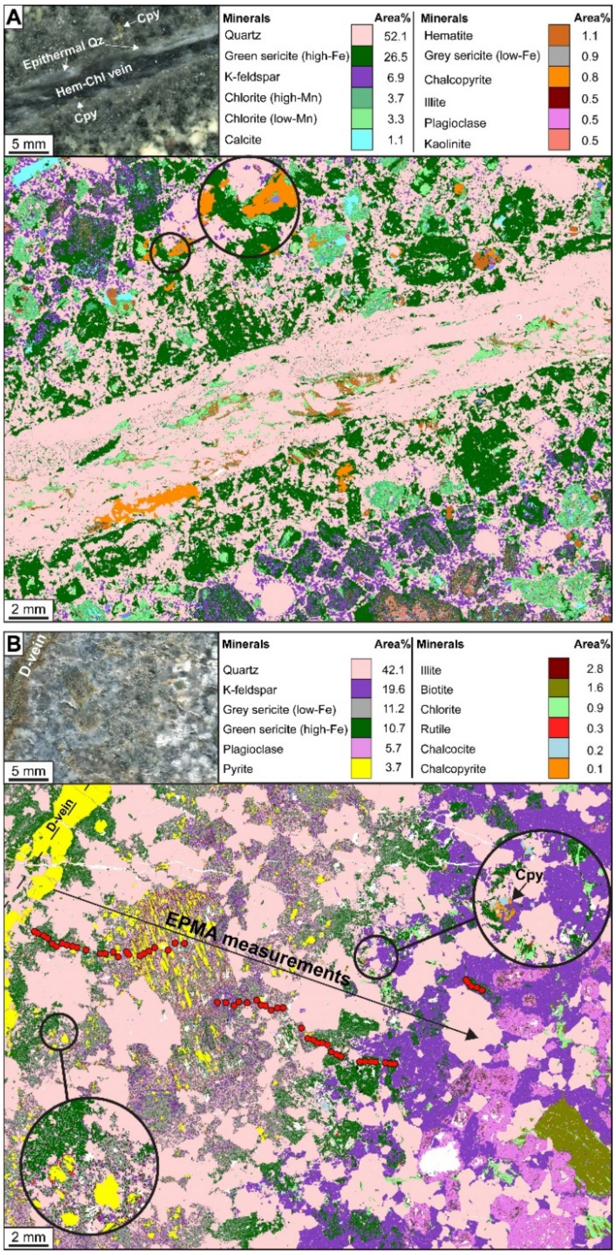

Figure 3. Two QEMSCAN maps of green and grey sericite alteration. A. Quartz-chalcopyrite vein reopened by chlorite-hematite-green sericite vein, subsequently reopened by a quartz-polymetallic vein. The halo of green sericite occurs along the chlorite-hematite vein. B. Pyrite-rich D-vein with halo composed of Fe-rich and Fe-poor sericite. Close to the vein and in the outermost halo, green sericite is observed but most of the halo is composed of grey sericite. K feldspar is intergrown with green sericite in the outer zone. Abbreviations - Chl: chlorite; Cpy: chalcopyrite; Hem: hematite; Qz: quartz)

4.3 Relationship between chemistry of green-grey sericite and SWIR absorption features

Generally, a good discrimination between grey and green sericite is obtained when comparing SWIR analyses (Al-OH absorption feature) and EMPA results (Figure 4C). A threshold around 2203.5 nm could be used to discriminate green sericite (higher Al-OH absorption features of 2203.5-2208 nm) and grey sericite (< 2203.5 nm). However, some analyses corresponding to green sericite inner/outer halo or vein infill fall in the grey sericite field (below 2203.5 nm); they are interpreted as artefacts caused by mixtures of grey and green sericite.

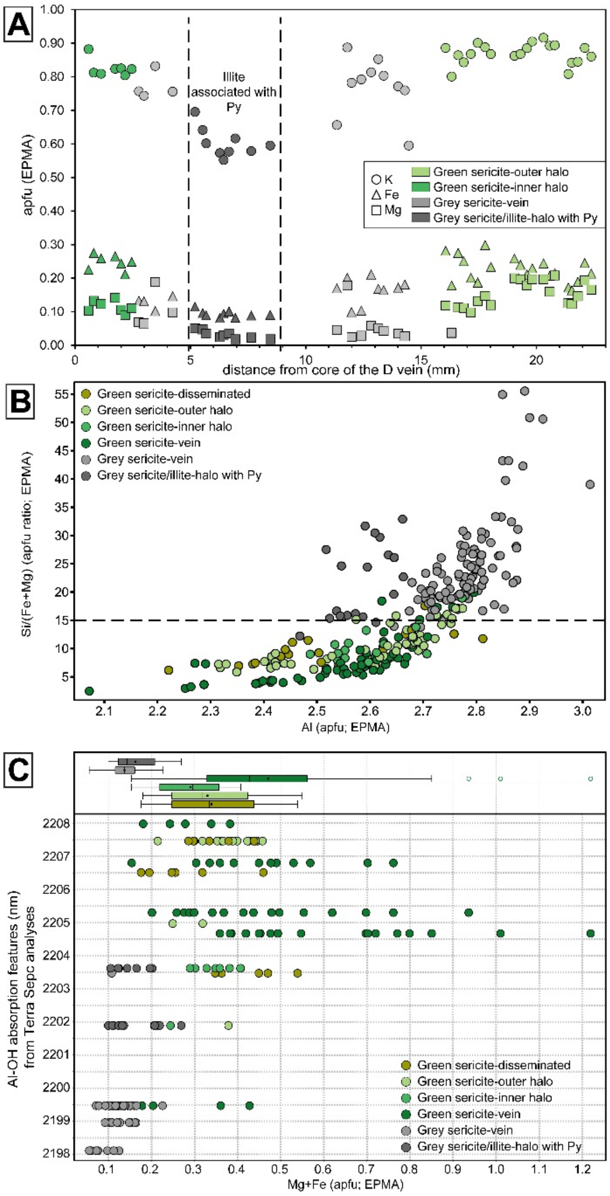

Figure 4. EMPA results on white micas. Green and grey sericite are discriminated. A. Potassium, Fe and Mg content (apfu) in a transect perpendicular to the alteration halo of a D-vein (location shown in Figure 3B). B. Si/(Fe+Mg) ratio vs Al_{tot} plot. C. Comparison between TerraSpec Al-OH absorption features and (Mg+Fe) content (apfu).

5 Conclusion

At Gaby, white mica alteration shows large textural diversity and in general a bimodal chemistry with green (Fe-Mg rich; Na-Al poor) and grey sericite (Fe-Mg poor; Na-Al rich). QEMSCAN mapping can be used to discriminate green and grey sericite alteration successfully. In both, the Eocene tonalite and in the Permo-Triassic Pampa Elvira plutonic complex, a 40 m-thick interval around 200 m below present day surface is enriched in grey sericite alteration that overprints earlier green sericite alteration. This interval can be easily detected with TerraSpec analyses using the Al-OH absorption feature of white micas. Nonetheless, precise detection of the type of sericite is difficult when, at pluri-millimetric scale, a mixture of green and grey sericite exists, especially in D-vein halos.

Acknowledgements

The authors thank Codelco and Exploraciones Mineras S.A (EMSA) for the logistic and financial support, fruitful discussions, and access to the field area.

References

Alva-Jimenez T, Tosdal RM, Dilles JH, Dipple G, Kent AJR, Halley S (2020) Chemical Variations in Hydrothermal White Mica across the Highland Valley Porphyry Cu-Mo District, British Columbia, Canada. Econ Geol 115:903–926.

Calder MF, Chang Z, Arribas A, Gaibor A, Dunkley P, Pastoral J, Kouzmanov K, Spandler C, Hedenquist JW (2022) High-Grade Copper and Gold Deposited During Postpotassic Chlorite-White Mica-Albite Stage in the Far Southeast Porphyry Deposit, Philippines. Econ Geol 117:1573–1596.

Chang Z, Yang Z (2012) Evaluation of inter-instrument variations among short wavelenght infrared (SWIR) devices. Econ Geol 107:1479–1488.

Cloutier J, Piercey SJ, Huntington J (2021) Mineralogy, mineral chemistry and SWIR spectral reflectance of chlorite and white mica. Minerals 11.

Guo N, Thomas C, Tang J, Tong Q (2019) Mapping white mica alteration associated with the Jiama porphyry-skarn Cu deposit, central Tibet using field SWIR spectrometry. Ore Geol Rev 108:147–157.

Reed M, Rusk B, Palandri J (2013) The Butte magmatic-hydrothermal system: One fluid yields all alteration and veins. Econ Geol 108:1379–1396.

Rusk BG, Reed MH, Dilles JH (2008) Fluid inclusion evidente for magmatic-hydrothermal fluid evolution in the porphyry copper-molybdenum deposit at Butte, Montana. Econ Geol 103:307–334.

Sillitoe RH (2010) Porphyry copper systems. Econ Geol 105:3–41.

Skarmeta J (2021) Structural controls on alteration stages at the Chuquicamata Copper-Molybdenum deposit, Northern Chile. Econ Geol 116:1–28.

Uribe-Mogollon C, Maher K (2018) White mica geochemistry of the copper cliff porphyry cu deposit: Insights from a vectoring tool applied to exploration. Econ Geol 113:1269–1295.

Uribe-Mogollon C, Maher K (2020) White mica geochemistry: Discriminating between barren and mineralized porphyry systems. Econ Geol 115:325–354.

Mineralogical and compositional evidence of a district-scale Sn-W skarn system in SW Sardinia: a review

Matteo L. Deidda[1], Alfredo Idini[1], Dario Fancello[1], Lorenzo Tavazzani[2], Florence Bégué[3], Kalin Kouzmanov[3], Giovanni De Giudici[1], Marilena Moroni[4], Stefano Naitza[1]
[1]Department of Chemical and Geological Sciences, University of Cagliari, Italy
[2]Institute of Geochemistry and Petrology, ETH Zürich, Switzerland
[3]Department of Earth Sciences, University of Geneva, Switzerland
[4]Department of Earth Sciences, University of Milan, Italy

Abstract. We studied three representative skarn orebodies of SW Sardinia (Perda Niedda, Monte Tamara and Rosas), related to ilmenite-series ferroan granites to assess their Sn-W and other Critical Raw Materials (CRM) metallogenic potential. The Perda Niedda skarn hosts magnetite, fluorite, cassiterite and minor sulfides in a garnet- (clinopyroxene)-amphibole-chlorite association at contact with granites. At Monte Tamara, scheelite-bearing hydrothermal veins and clinopyroxene-garnet skarns occur with minor cassiterite-stannite-molybdenite and Bi-sulfosalts. Base-metal sulfides with subordinate magnetite-cassiterite-fluorite veinlets prevail at Rosas. Clinopyroxene, garnet and epidote mineral chemistry from the three locations allows a detailed reconstruction of the mineralised systems, in terms of proximity to causative intrusion, compositional variations of ores and Sn-W and CRM enrichment. Overall, the highlighted common features of the three skarns indicate that they may be framed within a single, district-scale Sn-W skarn system. Overall, their different mineralogy and geochemical fingerprint reflect formation mechanisms controlled by their distance from the causative intrusion.

1 Introduction

Skarns are one of the most common classes of deposits for high-grade Sn and W mineralisation. Due to their industrial applications and supply risk, Sn is considered a “medium-scale” critical metal (Lehman 2021), whereas W is included in the Critical Raw Materials (CRM) list for Europe. In fact, Europe accounts only for the 7% of Sn and 4% of W global production, whereas China, Russia, SE Asia and S America, together, produce 78% of Sn and 91% of W. Therefore, re-evaluation of the CRM potential of old mining districts in Europe is now considered necessary by the EU Commission to keep up with these trends.

The Sulcis-Iglesiente (SW Sardinia) is an old mining district hosting numerous skarn orebodies (at least 50 documented occurrences) that were in part exploited for their Zn-Pb sulfide and/or Fe oxide ores. In this study, three representative skarns from the Sulcis-Iglesiente district (Perda Niedda, Monte Tamara and Rosas mines) have been investigated to evaluate the presence of Sn, W and other associated CRM (e.g., Bi, Mo, In) in the ores and, thus, to test the potential of SW Sardinia for Sn-W and CRM mineral exploration.

2 Geological setting

The SW portion of Sardinia (Sulcis-Iglesiente and Arburèse regions) represents the External Zone of the Variscan Chain in the region. The area includes a low-grade and mildly deformed Palaeozoic succession of Lower Cambrian sandstones, massive limestones and dolostones, nodular silty limestones, slates, and Middle-Upper Ordovician conglomerates and sandstones. These rocks were intruded at 289 ± 1 Ma (Boni et al. 2003) by F-bearing, ferroan, reduced (ilmenite-series) and slightly peraluminous monzogranites and leucogranites (GS1 suite: Conte et al. 2017) that were emplaced at less than 2 kbar. Based on these features, common among “tin-granites” (Lehmann 2021), the GS1 suite has been recognized as the metallogenic source for the numerous Sn-Mo-W ores of SW Sardinia (Naitza et al. 2017).

3 Analytical Methods

Field surveys and samplings were performed in the Perda Niedda, Monte Tamara and Rosas old mining areas. Petrographic, SEM-EDS, EPMA and LA-ICP-MS analyses took place at the University of Cagliari, University of Milan and University of Geneva and ETH Zürich.

4 Skarn and ore mineralogy

The Perda Niedda skarn ore consists of large magnetite-fluorite bodies at the exposed contact between Lower Cambrian carbonates and the GS1 Oridda pluton. Sulfides are subordinate, except for sulfide-rich zones containing In-rich sphalerite, arsenopyrite, löllingite, pyrrhotite, native Bi and late-stage pyrite disseminations. The skarn consists of abundant green garnet; clinopyroxene and axinite occur at distal position from the granite contact. Garnet forms large idiomorphic, birefringent and concentrically zoned crystals frequently pervasively altered (chlorite, amphibole, phlogopite, quartz) and associated with fluorite, magnetite and cassiterite. Cassiterite is found (Figure 1a-b): a) as micro-inclusions in the altered garnet rims with magnetite; and b) in magnetite-cassiterite-sphalerite fine layers in a quartz-fluorite-chlorite mass (“wrigglite” textures; Kwak and Askins 1981).

The Monte Tamara skarn occurs at the contact between Lower Cambrian limestones and sandstones at 3 km from the nearest exposure of the GS1 granites. Carbonate-hosted scheelite-

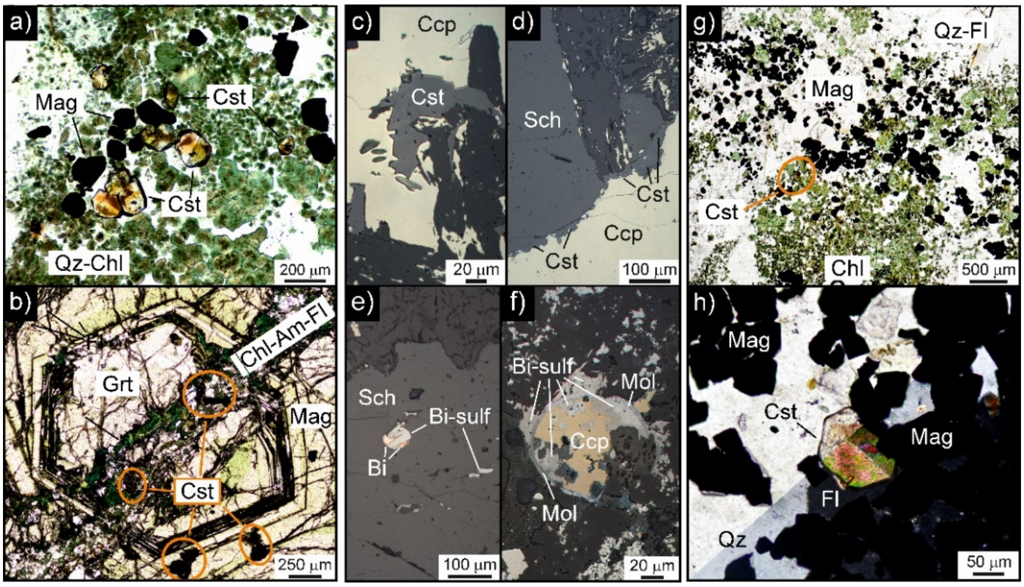

Figure 1. Photomicrographs of the W-Sn and Mo-Bi minerals of the Perda Niedda (a-b), Monte Tamara (c-f) and Rosas (g-h) skarns: a) "wrigglite"-type magnetite-cassiterite in a quartz-chlorite-fluorite gangue (Perda Niedda); b) cassiterite-magnetite enclosed in garnet altered to in chlorite-amphibole-fluorite (Perda Niedda); c) cassiterite associated with chalcopyrite and d) scheelite (Monte Tamara); e-f) Bi-sulfosalts with scheelite, chalcopyrite and molybdenite (Monte Tamara); g-h) "wrigglite"-type magnetite-cassiterite association (Rosas). Am = amphibole; Bi = native Bi; Bi-sulf = Bi-sulfosalts; Ccp = chalcopyrite; Chl = chlorite; Cst = cassiterite; Fl = fluorite; Grt = garnet; Mag = magnetite; Mol = molybdenite; Sch = scheelite.

arsenopyrite-sphalerite hydrothermal veins are found in a distal position (Sinibidraxiu; Deidda et al. 2023). The skarn consists of clinopyroxene and slightly subordinate garnet. Hydrothermal alteration of diopside and garnet produces actinolite, epidote, chlorite, calcite and quartz (Deidda et al. 2023). The ore includes variable proportions of scheelite, cassiterite, stannite, molybdenite, native Bi and Bi-sulfosalts as well as hematite, chalcopyrite, sphalerite, arsenopyrite, galena, pyrrhotite, pyrite and marcasite (Figure 1c-f).

Finally, the Rosas mine area is located on a regional-scale shear zone with numerous skarn orebodies along tectonic slices of Lower Cambrian limestones (Cocco et al. 2022). The nearest GS1 granite exposure is at 5 km distance from the ores, in the SE of the Monte Tamara area. A representative skarn occurrence (Barisonis sector) displays abundant clinopyroxene and minor garnet. Sphalerite, chalcopyrite and galena are the prevailing ore minerals. Cassiterite (Figure 1g-h) occurs with magnetite in "wrigglite"-like quartz-fluorite-chlorite assemblage (Cocco et al. 2022). Secondary phases include Ag-minerals, while some gold grains were observed in quartz.

5 Major and trace elements in silicates

5.1 Clinopyroxene

Clinopyroxene from Perda Niedda mostly belongs to the diopside endmember, with minor hedenbergite and johannsenite components (avg. $Di_{70.9}Hed_{6.5}Jo_{7.5}$; Figure 2). Clinopyroxene from Monte Tamara is diopsidic with moderate hedenbergite and low johannsenite percentages ($Di_{77.8}Hed_{19.6}Jo_{2.6}$). Conversely, clinopyroxene from Rosas is markedly higher in the hedenbergite and johannsenite components (avg. $Di_{17.1}Hed_{64}Jo_{18.9}$). Tin content is usually low at Rosas (< 1 ppm) and Perda Niedda (3-26 ppm); occasionally high values were detected at Monte Tamara (171-4367 ppm). Tungsten does not exceed 1 ppm in all deposits.

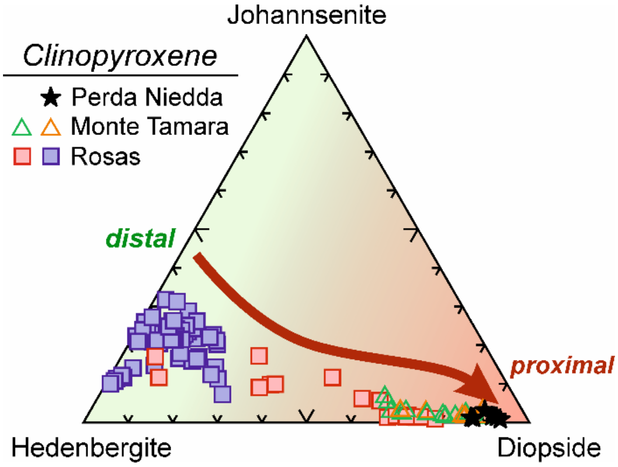

Figure 2. Relative proportions of diopside, hedenbergite and johannsenite endmembers in clinopyroxene from the Perda Niedda, Monte Tamara and Rosas skarn bodies. Higher hedenbergite and johannsenite contents correspond to distal skarns, whereas diopside correlates with proximal skarns (Meinert et al. 2005; Chang and Meinert 2008; Chang et al. 2019)

5.2 Garnet

The composition of garnet from Perda Niedda is andraditic (avg. $\text{Adr}_{96.9}\text{Grs}_{3.1}$), with sporadic grossular enrichments ($\text{Adr}_{100\text{-}40.5}\text{Grs}_{0.00\text{-}59.5}$). Similarly, garnet from Monte Tamara is mostly andradite (avg. $\text{Adr}_{93.1}\text{Grs}_{6.9}$), but grossular may attain 63.2% (Deidda et al. 2023). Garnet from Rosas is variably enriched in grossular ($\text{Adr}_{100\text{-}25.5}\text{Grs}_{25.5\text{-}74.5}$). Tin is remarkably high in green, unaltered garnet from Perda Niedda and Monte Tamara, both with average contents of 1.5 wt% Sn. At Perda Niedda, Sn ranges from 0.2 to around 4 wt%. Tin is lower in garnet cores (avg. 9956 ppm Sn) and becomes moderately higher towards mantle (avg. 2.1 wt% Sn) and rims (avg. of 1.5 wt% Sn; Figure 3a). At Monte Tamara Sn in garnet is in the range 0.02-6 wt%. Similarly, Sn contents increase from cores (avg. 362 ppm Sn) to mantle (1 wt% Sn) and rims (2 wt% Sn; Figure 3b). Garnet from Rosas has markedly lower Sn contents (avg. of 6 ppm and up to 25 ppm).

The average W contents in the three deposits are comparable (113 ppm at Perda Niedda; 491 ppm at Monte Tamara; 82 ppm at Rosas). Garnet from the scheelite-bearing skarn of Monte Tamara attains the highest values of 2800 ppm. Aside from Monte Tamara garnet, tungsten contents tend to be higher in the cores (avg. 132 ppm at Perda Niedda; 9 ppm at Monte Tamara; 161 ppm at Rosas) and to decrease towards mantles (avg. 201 ppm at Perda Niedda; 626 ppm at Monte Tamara; 28 ppm at Rosas) and rims (avg. 71 ppm at Perda Niedda; 515 ppm at Monte Tamara; 37 ppm at Rosas). Indium is within the range 11-126 ppm at Perda Niedda (avg. 57 ppm), 2-110 ppm at Monte Tamara (avg. 31 ppm) and negligible at Rosas (< 1 ppm).

5.3 Epidote

In all studied samples, minerals of the epidote group mainly belong to the epidote ($\text{Ca}_2(\text{Fe}^{3+},\text{Al})_3(\text{SiO}_4)_3(\text{OH})$) endmember, whereas clinozoisite ($\text{Ca}_2\text{Al}_3(\text{SiO}_4)_3(\text{OH})$) and piemontite ($\text{Ca}_2(\text{Al},\text{Mn}^{2+},\text{Fe}^{2+})_3(\text{SiO}_4)_3(\text{OH})$) are subordinate. Average compositions are comparable between Monte Tamara ($\text{Ep}_{77.9}\text{Czo}_{21.6}\text{Pmt}_{0.5}$) and Rosas ($\text{Ep}_{79.1}\text{Czo}_{20.1}\text{Pmt}_{0.9}$). Tin concentrations are remarkably higher at Monte Tamara (339-6688 ppm; avg. 2571 ppm) with respect to the Sn-poor epidote from Rosas (5-552 ppm; avg. 35 ppm). Indium is generally low in both deposits, though more often below the detection limit at Rosas (up to 1 ppm). Moderately higher In values were detected at Monte Tamara (1-42 ppm; avg. 8 ppm). Tungsten occasionally reaches maximum concentrations of 7 ppm at Monte Tamara.

6 Zoning of the Sn-W skarn system

The distance from the causative intrusion is a key-factor in controlling the features of skarn deposits. Typical features of distal skarns include higher proportions of clinopyroxene over garnet, Mn- and Fe-rich clinopyroxene, enrichment in Zn-Pb sulfides (Meinert 1997; Meinert et al. 2005). Conversely, exoskarn formation from F-rich greisen-related hydrothermal fluids (Štemprok 1987; Chang and Meinert 2004), abundance of cassiterite (Lehmann 2021) and molybdenite (Chang et al. 2019), the LREE-rich signature of scheelite (Yuan et al. 2019; Deidda et al. 2023) and the Sn-enrichments in garnet and epidote could be indicators for more proximal skarn mineralisation.

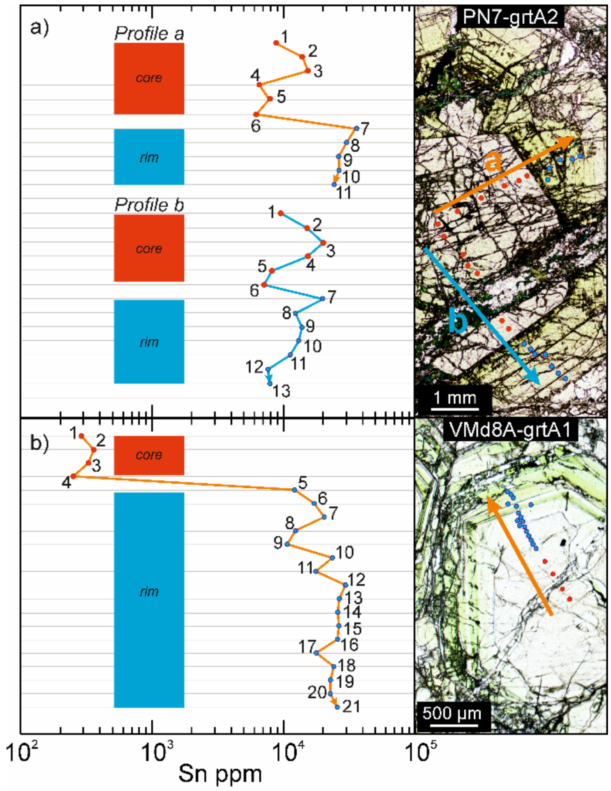

Figure 3. LA-ICP-MS compositional profiles in garnet from Perda Niedda (a) and Monte Tamara (b), showing progressive Sn enrichment from core (red dots) to rim (blue dots).

The Perda Niedda, Monte Tamara and Rosas represent different parts of a district-scale Sn-W skarn system. Each orebody, though, displays some peculiar features reflecting their formation at different relative distances from the intrusive source. In this view:

1. The Perda Niedda skarn represents the most proximal orebody in the system, as demonstrated by: (a) the exposed contact with GS1 granites; (b) greisen-like/endoskarn alteration accompanied by high fluorine activity; (c) the higher proportion of garnet versus clinopyroxene; (d) Sn and In enrichment in garnet; (e) abundant cassiterite associated with magnetite-fluorite, after garnet alteration; (f) diopsidic clinopyroxene.

2. The Monte Tamara skarn features are between proximal and distal, as indicated by: (a) no clear contact with GS1 granites; (b) scheelite prevails over cassiterite and other Sn-Mo-Bi minerals are found (stannite, molybdenite, native Bi and Bi-sulfosalts); (c) abundant Zn-Pb sulfides; (d) clinopyroxene

(diopsidic) more abundant than garnet (f) Sn-rich garnet; (e) high Sn and In epidote.

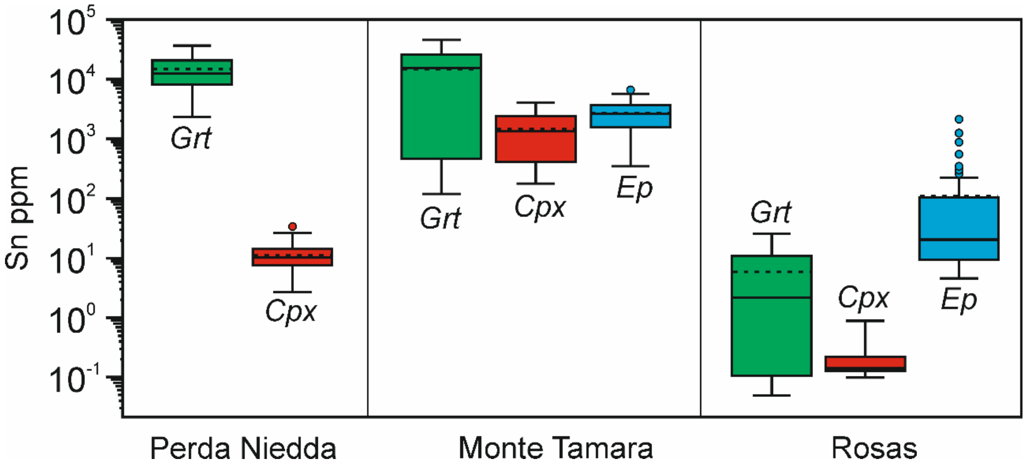

Figure 4. Statistical distribution of Sn in garnet (Grt), clinopyroxene (Cpx) and epidote (Ep) from the Perda Niedda, Monte Tamara and Rosas skarns. Calc-silicates from proximal skarns (Perda Niedda, Monte Tamara) are enriched in Sn if compared to distal skarns (Rosas).

3. Lastly, the Rosas skarn features are indicative of a distal deposit, as suggested by: (a) structural control, favouring extensive infiltration of fluids at larger distance; (b) rare cassiterite, scheelite, Bi-phases and no molybdenite; (c) abundant Zn-Pb sulfides and traces of Ag and Mn sulfides; (d) clinopyroxene more abundant than garnet; (e) hedenbergitic-johannsenitic clinopyroxene; (f) Sn-poor garnet and epidote.

7 Conclusion

All field, mineralogical and compositional evidence highlight the close relationship between the Perda Niedda, Monte Tamara and Rosas skarns and point out the existence of a district-scale Sn-W skarn system in SW Sardinia, strongly related with the GS1 granite intrusive unit. This is supported by the common presence in the orebodies of marker minerals such as cassiterite and, more occasionally, scheelite, Bi-phases, molybdenite and stannite.

Moreover, this work points out that Sn-rich garnet and, to a lesser extent, Sn-rich epidote are important markers for Sn-W mineralisation in skarns of SW Sardinia, similarly to other Sn-W skarn provinces worldwide (e.g., Huangshaping, Erzgebirge, French Massif Central).

In conclusion, our assessment of a zoned, district-scale Sn-W skarn system may have important implications for further and more accurate Sn-W and CRM mineral explorations in the several skarn occurrences in the SW Sardinia district.

Acknowledgements

MLD aknowledges RAS/FdS grant “Sustainable land management: the tools of geology for the environment” (F72F16003080002) and CeSAR (Centro Servizi d’Ateneo per la Ricerca; University of Cagliari).

References

Boni M, Stein HJ, Zimmerman A, Villa IM (2003) Re-Os age for molybdenite from SW Sardinia (Italy): A comparison with 40Ar/39 Ar dating of Variscan granitoids. Miner Explor Sustain Dev 247–250

Chang Z, Meinert LD (2004) The magmatic-hydrothermal transition - Evidence from quartz phenocryst textures and endoskarn abundance in Cu-Zn skarns at the Empire Mine, Idaho, USA. Chem Geol 210:149–171.

Chang Z, Shu Q, Meinert LD (2019) Skarn Deposits of China. SEG Spec Publ 22:189–234.

Cocco F, Attardi A, Deidda ML, et al (2022) Passive Structural Control on Skarn Mineralization Localization: A Case Study from the Variscan Rosas Shear Zone (SW Sardinia, Italy). Minerals 12:.

Conte AM, Cuccuru S, D’Antonio M, et al (2017) The post-collisional late Variscan ferroan granites of southern Sardinia (Italy): Inferences for inhomogeneity of lower crust. Lithos 294–295:263–282.

Deidda ML, Naitza S, Moroni M, et al (2023) Mineralogy of the scheelite-bearing ores of Monte Tamara, SW Sardinia: insights for the evolution of a Late Variscan W–Sn skarn system. Mineral Mag 87: 86-108.

Kwak TAP, Askins PW (1981) The nomenclature of carbonate replacement deposits, with emphasis on Sn-F(-Be-Zn) “wrigglite” skarns. J Geol Soc Aust 28:123–136.

Lehmann B (2021) Formation of tin ore deposits: A reassessment. Lithos 402–403:105756.

Meinert LD (1997) Application of skarn deposit zonation models to mineral exploration. Explor. Min. Geol. 6:185–208

Meinert LD, Dipple GM, Nicolescu S (2005) World Skarn Deposits. Economic Geology One Hundredth Anniv Vol 299–336.

Naitza S, Conte AM, Cuccuru S, et al (2017) A Late Variscan tin province associated to the ilmenite-series granites of the Sardinian Batholith (Italy): The Sn and Mo mineralisation around the Monte Linas ferroan granite. Ore Geol Rev 80:1259–1278.

Paton C, Hellstrom J, Paul B, et al (2011) Iolite: Freeware for the visualisation and processing of mass spectrometric data. J Anal At Spectrom 26:2508–2518.

Štemprok M (1987) Greisenization (a review). Geol Rundschau 76:169–175.

Yuan L, Chi G, Wang M, et al (2019) Characteristics of REEs and trace elements in scheelite from the Zhuxi W deposit, South China: Implications for the ore-forming conditions and processes. Ore Geol Rev 109:585–597.

Trace element and sulphur isotope composition of selected minerals from the W-Mo porphyry deposit Ochtiná-Rochovce

Diego Delgado Yáñez[1], Peter Koděra[1], Manuel Keith[2], Frederik Börner[2], František Bakos[3]
[1] Department of Mineralogy, Petrology and Economic Geology, Comenius University in Bratislava, Ilkovičova 6, 84104 Bratislava, Slovak Republic,
[2] GeoZentrum Nordbayern, Friedrich-Alexander-Universität Erlangen-Nürnberg (FAU), Schlossgarten 5, 91054 Erlangen, Germany
[3] Green View, s.r.o., Rigeleho 1, 811 02 Bratislava, Slovakia

Abstract. Porphyry W-Mo deposits are rare occurrences in the Earth crust and Ochtiná-Rochovce is the only one of its kind in the Western Carpathians. Lithological, mineralogical and veinlet descriptions, complemented by LA-ICP-MS trace element analysis and S isotope measurements of sulphide separates are indicative for a shift from reduced to oxidized conditions during the system evolution. Low Se and Te contents in both molybdenite and pyrite are related to the formation of these minerals at high temperatures, while decreasing Co in pyrite from early to late formed veinlets is related to decreasing temperature. High Nb contents in scheelite, wolframite and rutile reflect more oxidized conditions, while high contents of W, V, Nb and Cr in rutile suggest its hydrothermal origin. The S isotope composition of both molybdenite and pyrite of different generations suggests magmatic-hydrothermal origin of the fluids.

1 Introduction

The W-Mo deposit at Ochtiná-Rochovce (Slovakia) hosts a porphyry-type mineralisation, associated with a Late Cretaceous granite complex emplaced in the Lubeník-Margecany suture line (Bakos *et al.* 2016, Kohút *et al.* 2013)**.** Bakos *et al.* (2016) estimated the resources at 5.0 Mt W ore and 2.4 Mt Mo ore at grades of 0.2% for both metals.

The deposit is hosted in a set of metasedimentary and metabasic rocks such as metasandstones, micaschists, phyllites and metabasalts, belonging to the Ochtiná, Rimava and Slatvina Formations, ranging from Lower Carboniferous to Permian age (Vozárová and Vozár 1988). The mineralisation is divided into a lower molybdenite zone and an upper wolframite-scheelite zone, other ore minerals found in the deposit are pyrite, chalcopyrite, pyrrhotite, among others (Lörincz *et al.* 1993; Bakos *et al.* 2016). The hydrothermal alteration has been described as concentrical, including K-alteration, silicification, sericitisation, chloritisation and late carbonatisation.

Delgado *et al.* (2021) recognize pyrite with inclusions of chalcopyrite, pyrrhotite and galena, hosted in quartz-molybdenite, quartz-wolframite-scheelite and quartz veinlets, as well as veinlets purely formed by pyrite. The related EMPA-WDS results on pyrite from different generations did not show any compositional differences. The same study showed that scheelite commonly replaces wolframite, where the latter contains up to 7 wt. % MgO; similar values were found by Ferenc and Uher (2006). Previous studies (e.g., Bendel, 2017; Ebel, 2021) showed that this mineral contains zones enriched in WO_3 reaching ~17 wt. % with average of 0.5-1 wt. % WO_3.

This work aims to provide an updated lithological, mineralogical, and geochemical characterisation and provides new insights into genetical characterisation of the mineralising fluids by trace element and sulphur isotope data of selected ore minerals.

2 Methodology

Approximately 40 drill core samples were described both macro- and microscopically to classify them by lithology, alteration, and veinlet types. A total of 16 selected samples with variable degrees of alteration, were analysed by whole rock X-ray diffraction (XRD) at the Earth Institute of the Slovak Academy of Sciences in Bratislava. Mineral abundances were quantified by the RockJock 11 software.

The major element composition of selected ore minerals was determined by a JEOL JXA-82000 superprobe at GeoZentrum Nordbayern and followed by in-situ laser ablation inductively coupled plasma mass spectrometry (LA-ICP-MS) for trace elements.

The trace element composition of selected minerals was determined by LA-ICP-MS analyses of minerals by a Teledyne Analyte Excite 193 nm laser attached to an 7500c quadrupole ICP-MS. The measurements were performed in spot mode using 35 microns. Smaller beam diameters were occasional used for smaller minerals. For molybdenite and pyrite the external standards MASS-1 (USGS), Po724 B2 SRM, $(Fe, Ni)_{1-x}S$ and UQAC-FeS-1 were used. The wolframite, scheelite and rutile measurements were standardized by NIST SRM 610 and GSE-1G. Previous EMPA-WDS results on the same spots were used as internal standards: S for sulphides, Ca for scheelite, Fe for wolframite, Ti for rutile. Statistical parameters such as geometrical mean (GM) and its corresponding standard deviation (GSD) were calculated. The ranges shown in these results are based on both parameters and represent where 2/3 of the values fall. Anomalous analyses related to micro-inclusions were discarded.

Sulphur isotope analyses of molybdenite and pyrite separates were performed using a Finnigan MAT 253 IR-MS at the Earth Institute of the Slovak Academy of Sciences in Banks Bystrica, with analytical errors between 0.15-0.20 ‰. This was complemented with data from Lörincz *et al.* (1993) and unpublished results done by the Slovak State Geological Institute Dionýz Štúr. The median (mdn.) was calculated, and the ranges limits shown correspond to the first and third quartile.

3 Lithologies and their alterations

The main lithology in the study area corresponds to a well-foliated micaschist affiliated to the Ochtiná Formation, that includes muscovite intercalated with quartz-plagioclase bands. According to whole rock XRD analyses, the least altered samples contain 35-65 wt. % quartz, 20-50 wt. % muscovite and plagioclase <10 wt. %. The early potassic alteration is manifested by biotite (<30 wt. %) replacing muscovite and K-feldspar (<5 wt. %) altering plagioclase, while silicification lead to high quartz content of up to 70 wt. %. Chloritisation with up to 25 wt. % chlorite accompanied by minor epidote replaces plagioclase and secondary biotite. Argillitisation dominated by illite is found close to major quartz veinlets, rarely reaching clay abundances of up to 15 wt. %.

The previously reported ‘metabasalts’ are indeed amphibolite, locally accompanied by peridotite, intercalated in the micaschist of the Ochtiná Formation. Amphibolite contains 30-40 wt. % actinolite, ~30 wt. % plagioclase, and <10 wt. % pyroxene. It is affected by the same alteration styles, as described above for the micaschist, including K-alteration dominated by biotite (up to 20 wt. %), slight silicification and chloritisation ± epidote (up to 10 wt. %), replacing both earlier-formed amphibole and biotite. Previous alterations are overprinted by argillitisation dominated by smectite with total clays abundances of up to 10 wt. %. Peridotite was not analysed by XRD, but the microscopical description allows to estimate the olivine and pyroxene contents between 20-40 wt. vol % for each mineral, that occur in association with magnetite (< 20 vol. %), possibly derived from olivine decomposition, and undifferentiated serpentines (< 10 vol. %). Pyroxene and olivine are strongly altered to serpentine and chlorite.

The deepest parts of the system consist of an early foliated metasandstone of the Rimava Formation, which is characterised by quartz (60-75 wt. %) that is associated with feldspar and muscovite summing 25-40 wt. %. Low to moderated argillitisation dominated by illite (< 10 wt. %), as well as minor biotite and chlorite (both < 2 wt. %) was determined.

4 Veinlets

The main mineralisation at the deposit is hosted by at least 4 different types of veinlets: quartz-molybdenite±pyrite (1), pyrite±quartz (2), pyrite-scheelite (3) and quartz-wolframite-scheelite-pyrite (4). The early molybdenite-containing veinlets are associated with two quartz generations, namely coarse-grained (0.3-10 mm length) and fine-grained (<0.2 mm length) quartz. Molybdenite is observed as disseminated flakes of 0.3-0.5 mm length in the centre of the veinlets and as finer grained crystals (~0.2 mm length) following cracks in orientation, which is related to the second generation of quartz. This veinlet type locally also contains disseminated pyrite (up to 20 mm) and is accompanied by K-alteration and silicification hosted by micaschist and metasandstone.

Later pyrite-dominated veinlet type is filled by later fine-grained quartz (reaching up to 30 vol. %), are hosted by amphibolite and rarely also micaschist. This veinlet type contains traces of chalcopyrite and pyrrhotite and is accompanied by K-alteration halos, marked by K-feldspar and biotite. No crosscutting relationships were observed between the molybdenite and pyrite veinlets.

The main W-mineralisation is hosted by two types of veinlets. The first one is a pyrite-dominated type hosted by amphibolite, which contains rounded scheelite crystals up to 5 mm in length, rare chalcopyrite and bismuthinite inclusions, and minor quartz. Its alteration halo includes secondary biotite, and late chloritisation and argillitisation. The second group of W-bearing veinlets is characterised by scheelite replacing elongated disseminated wolframite crystals (up to 30 mm long), hosted by micaschist and crosscutting the pyrite±quartz veinlets. Disseminated pyrite inclusions in wolframite are frequent, and this veinlet type also rarely contains molybdenite and muscovite. Bimodal quartz was observed in these veinlets: coarse-grained quartz at the veinlet centres and a finer quartz precipitating at the veinlet margins.

5 Trace elements in selected minerals

Two samples containing molybdenite were analysed by LA-ICPMS: one from a quartz-molybdenite-pyrite veinlet (pyrite in this sample was also analysed) while the other one from the same veinlet type but lacking pyrite and hosted in micaschist.

The LA-ICPMS results indicate that the main trace elements in molybdenite are Fe, Pb, As and Sb. Iron has apparently different contents in the two analysed samples: 84-1043 ppm Fe (GM=297) in the first sample, and 25-82 ppm Fe (GM=45) in the other sample. For all analysed spots, Fe strongly correlates with As (r=0.92) and Sb (r=0.74). Bismuth and nickel are also highly correlated in molybdenite (r=0.84); while if plotted versus Fe+As+Sb to enables to distinguish molybdenite according to its trace element composition (Fig. 1A). Besides Fe, molybdenite in the quartz-molybdenite-pyrite veinlet is also richer in As (2-324 ppm, GM=27) compared to the other sample (2-6 ppm, GM=3) in the quartz-molybdenite veinlet. Complementary, Re, Se and Te do not exceed 40, 87 and 5 ppm in molybdenite, respectively.

Pyrite from the quartz-molybdenite-pyrite (Py1), pyrite (Py2), pyrite-scheelite (Py3) and quartz-wolframite-scheelite (Py4) veinlets were analysed. Manganese, Co and Ni are generally the most abundant trace elements in pyrite (Fig. 1B). Py2 contains 38-1240 ppm Co+As (GM=216), while the other generation ranges 12-202 ppm Co+As (GM=49). Pyrite 2 is also enriched in Ni (45-475 ppm, GM=145) compared to the other pyrite generation (4-164 ppm, GM=27). Additionally, both As and Se are usually below 55 ppm in all pyrite generations.

Scheelite replacing wolframite shows high concentrations of Mn and Fe (up to 2 wt. % Fe+Mn), and it is easily differentiated from scheelite occurring in the pyrite veinlets, where Fe+Mn do not exceed 0.02 wt. %. The two scheelite generations can be distinguished by their LREE, HREE, Nb and Sr contents (Fig. 2). Scheelite in the pyrite veinlets is particularly enriched in both LREE (737-3495 ppm, GM=1605) and HREE (352-1407 ppm, GM=704) compared to scheelite replacing wolframite (LREE: 55-1420 ppm, GM=279; HREE; 2-420 ppm, GM=116).

Wolframite is not particularly enriched in any trace element. Ti and Nb have geometrical means close to 30 ppm, while HREE GM=20 ppm (Fig. 2).

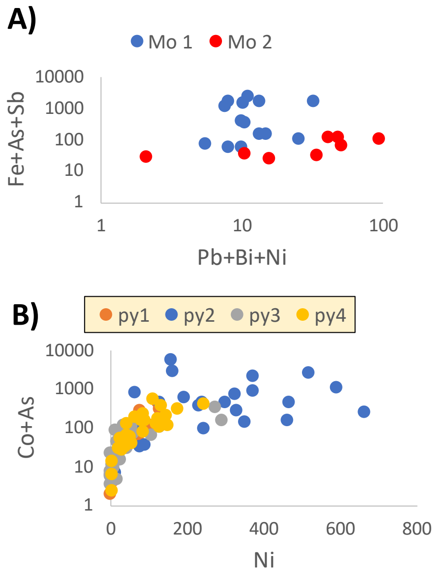

Figure 1. Graphs to discriminate different generations of sulphides by trace elements (in ppm). **A)** Pb+Bi+Ni vs. Fe discriminating Fe-rich molybdenite in quartz-pyrite veins (Mo1) and molybdenite in pyrite-free quartz veins (Mo 2). **B)** Ni vs. Co+As showing the difference among Co-Ni rich pyrite in pyrite veinlets (Py2) and other pyrite generations related to molybdenite (Py1), scheelite (Py3) and wolframite-scheelite (Py4), which are depleted in all those elements.

EMPA-WDS analyses of rutile showed high concentrations of V (0.45-0.9 wt. complement that other important trace elements are Nb, Cr and W. These elements are not correlated and range between 692-2283 ppm Nb, 1789-4600 ppm W, and 142-1460 ppm Cr. Other important trace elements in rutile are Sn (GM=645 ppm), Zr (GM=93 ppm) and Ta (GM=72 ppm). LREE in rutile tend to be higher than HREE, but do not exceed 60 ppm in general. % GM=0.7), while LA-ICPMS results for the same mineral

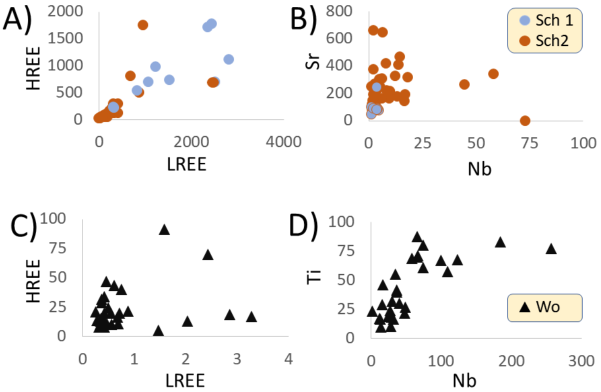

Figure 2. Selected trace elements compositions (all in ppm) of scheelite (Sch) and wolframite (Wo). **A)** LREE vs. HREE for scheelite, showing enrichment in both scheelite replacing wolframite (Sch 2) and scheelite in pyrite veinlets (Sch 1). **B)** Nb vs. Sr differentiates both scheelite generations. **C)** LREE vs. HREE in wolframite, displaying their low contents. **D)** Nb vs. Ti in wolframite, showing a positive correlation.

6 Sulphur isotopic composition

The S isotope values of molybdenite range between -1.0 to -0.4 ‰ (mdn, -0.6 ‰), which distribution is shown in Fig. 3. The $\delta^{34}S$ values in pyrite do not show a significant difference among the veinlet types, as all pyrite generations have most of values in the range 0±0.4 ‰. Exceptions are one outlier with $\delta^{34}S$ 3.2‰ was found in a deep sample representing a quartz-molybdenite-pyrite veinlet hosted by parental granite at ca. 500 m depth and two vales (1.5 and 1.9 ‰) related to quartz-wolframite-scheelite-pyrite veinlets closer to surface.

7 Discussion and conclusions

As pyrite and pyrite-scheelite veinlets mainly occur in amphibolite hosted by muscovite-micaschist it is probable that this rock-type be related to the ore mineralisation. Amphibolite has likely released Ca^{2+} during the potassic alteration to generate scheelite in the pyrite-scheelite veinlets.

Textural evidence of quartz in molybdenite-bearing veinlets and the contrasting Fe concentrations in molybdenite suggest that it was formed in two stages, with the later one affected by enrichment of fluids in Fe, precipitating molybdenite in cracks with up to 1500 ppm of Fe, and fine-grained quartz. The abundance of Pb, As, Sb in molybdenite in contrast to Re, Se, Te could be related to increased fluid temperatures (> 300 °C) as suggested by Pašava *et al.* (2016). The lack of W in molybdenite can be linked to reduced conditions of this mineralisation stage, according to the same authors. Wang *et al.* (2021) relate increasing Co in pyrite with increasing fluid temperatures, thus the pyrite veinlets could have been formed at higher temperatures than pyrite in the molybdenite- and W-bearing veinlets. Studied pyrites from 4 different generations of veinlets show lower Se and Te contents compared to a similar porphyry Mo-Cu-W deposit Myszków in Poland (Naglik *et al.* 2022), which can indicate relatively higher temperatures (> 400 °C) and dominantly reduced fluid (Keith *et al.* 2018). Both scheelite and wolframite are enriched in Nb, which can reflect a shift from reduced conditions related to earlier sulphide-rich veinlets to more oxidised conditions linked to W precipitation (Damian *et al*. 2006). In scheelite, Nb^{5+} and REE^{3+} can be incorporated by coupled substitution replacing Ca^{2+} and W^{6+} (Song *et al.* 2019).

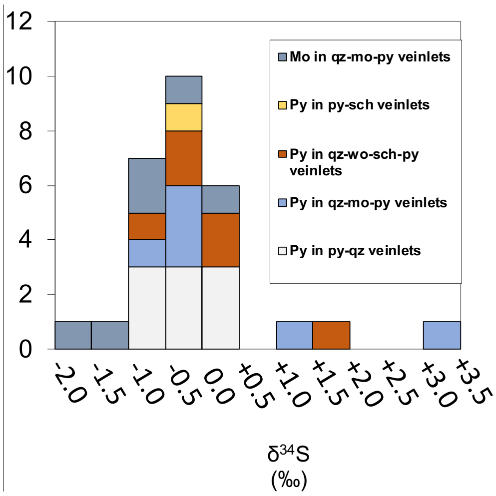

Figure 3. Histogram of sulphur isotopic composition of molybdenite and pyrite. Most of the values do not show significant variation among different veinlet generations.

The presence of high W and Nb contents in rutile, occurring close to W-bearing veinlets, indicate a genetic link to the tungsten mineralisation. The lower LREE content in rutile compared to scheelite can be explained by preferential incorporation of LREE in scheelite by substitution of Ca^{2+}.

The S isotope date are indicative of mostly well-homogenised fluids of magmatic-hydrothermal origin, typical for porphyry type of deposits (Shanks 2014) that enriched in δ^{34}S towards the surface due to increasing water-rock interaction Wilson *et al.* 2006).

Acknowledgements

This work was supported by the Comenius University Grant for Doctoral Students UK/107/2021 and an Erasmus+ short stay scholarship at the GeoZentrum Nordbayern Erlangen in Germany.

Special thanks to Dr. Helene Brätz for guiding the LA ICPMS work and its data reduction.

References

Bakos, F., Jánošík, M. and Sýkora, M. (2016): Final report with reserves calculations - Ochtiná W, Mo, Re mineralisation. GreenView report: 38 p (in Slovak)

Bendel, M. (2017): Mineralogical and technological description of the tungsten ore of Ochtiná, Slovakia (MSc thesis, Friedrich Schiller University Jena, Germany): 88 p.

Damian, G., Damian, F., Konečný, P., and Kollárová, V. (2016). A new occurrence of wolframite-ferberite in Romania; *Romanian Journal of Mineral Deposits*, v. *89*, p.49-54.

Delgado, D., Koděra, P., and Bakos, F. (2021): Advances in lithological, mineralogical, and geochemical characterization of the W-Mo porphyry deposit Ochtiná-Rochovce. In: Proceeding from the conference Geochémia 2021, p. 131-135.

Ebel, H. (2021). Mineralisation of the Kyslá Au-W and Ochtiná W-Mo deposits, Central Western Carpathians, Slovakia (MSc thesis, Eberhard Karls University Tuebingen, Germany), 69 p.

Ferenc, S., and Uher, P. (2006): Magnesian wolframite from hydrothermal quartz veins in the Rochovce granite exocontact, Ochtiná, Western Carpathians, Slovakia. Neues Jahrbuch für Mineralogie-Abhandlungen, v. 183(2), p. 165-172.

Hoefs J. (2009). Stable isotope geochemisty. Springer-Verlag, Berlin Heidelberg, 285 p.

Keith, M., Smith, D. J., Jenkin, G. R., Holwell, D. A., and Dye, M. D. (2018): A review of Te and Se systematics in hydrothermal pyrite from precious metal deposits: Insights into ore-forming processes. *Ore Geology Reviews*, v. *96*, p. 269-282.

Kohút, M., Stein, H., Uher, P., Aimmerman, A., and Hraško, L. U. (2013): Re-Os and U-Th-Pb dating of the Rochovce granite and its mineralisation (Western Carpathians, Slovakia). *Geologica Carpathica*, v. *64*(1), p. 71-79.

Lörincz, L., Švantnerová, E., and Bachňák, M. (1993): Final report: Ochtiná-Rochovce Mo, W, exploration survey, status at 30.9.1993. MS, archive Geofond, Bratislava, 79365, 225 pp (in Slovak).

Naglik, B., Toboła, T., Dumanska-Slowik, M., Dimitrova, D., Derkowski, P., Zielinski, G., Habryn, R. & Nadlonek, W. (2022). Multi-stage ore forming history of the Variscan porphyry Mo-Cu-W Myszków deposit (Poland): evidence from trace elements of pyrite. *Ore Geology Reviews*, 105185.

Pašava, J., Svojtka, M., Veselovský, F., Ďurišová, J., Ackerman, L., Pour, O., Dábek, M., Halodová, P. and Haluzová, E. (2016): Laser ablation ICPMS study of trace element chemistry in molybdenite coupled with scanning electron microscopy (SEM) - an important tool for identification of different types of mineralization. *Ore Geology Reviews*, v. *72*, p. 874-895.

Shanks, W. (2014): Stable Isotope Geochemistry of Mineral Deposits. Treatise on Geochemistry (Second edition), Elsevier Ltd.: Amsterdam, The Netherlands, pp 59-82.

Song, G., Cook, N. J., Li, G., Qin, K., Ciobanu, C. L., Yang, Y., and Xu, Y. (2019): Scheelite geochemistry in porphyry-skarn W-Mo systems: A case study from the Gaojiabang Deposit, East China. *Ore Geology Reviews*, v. *113*, 103084.

Vozárová, A., and Vozár, J. (1988): Late Paleozoic in Western Carpathians. *Slovak Geological Survey, Bratislava:* 314 pp.

Wang, K., Zhai, D., Liu, J., and Wu, H. (2021): LA-ICP-MS trace element analysis of pyrite from the Dafang gold deposit, South China: Implications for ore genesis. *Ore Geology Reviews*, v. *139*, 104507.

Wilson, A. J., Cooke, D. R., Harper, B. J., & Deyell, C. L. (2007). Sulfur isotopic zonation in the Cadia district, southeastern Australia: exploration significance and implications for the genesis of alkalic porphyry gold–copper deposits. *Mineralium Deposita*, *42*, 465-487.

Hydrothermal alteration zonation and Au-Cu footprint of the New York breccia pipe, Ok Tedi, PNG

Jerry Dunga[1], Steffen G. Hagemann[1], Peter J. Pollard[2] and Marco L. Fiorentini[1]
[1]Centre for Exploration Targeting, School of Earth Sciences, University of Western Australia, CRAWLEY, WA, 6009, Australia.
[2]Pollard Geological Services Pty Ltd. Brisbane, Queensland, 4061, Australia.

Abstract. Preliminary findings from field mapping, core logging, assaying, and petrographic analysis of the large (400m by 1500m), deep seated (>1500m) New York breccia pipe adjacent to the Ok Tedi porphyry/skarn deposit indicate that: 1) the breccia itself and gold mineralisation display a significant vertical extension (>1500m); 2) early igneous breccias are overprinted by hydrothermal breccias, which are characterised by abundant hydrothermal infill and late brecciation affecting previously formed breccias (i.e. evidence of multiple brecciation events); 3) there is a strong vertical zonation, which is reflected in the presence of shallow base metal rich sulphides (galena-sphalerite) and gold with crosscutting epithermal-style quartz-rhodochrosite veins, and deep chalcopyrite-magnetite-pyrrhotite mineralisation in veins and breccias with carbonate-adularia alteration; 4) there is a distinct zonation in sulphide and oxide mineral assemblages, which is reflected in the occurrence of shallow pyrite-marcasite-hematite assemblages compared to pyrrhotite-magnetite at depth; and 5) there is evidence for long distance transportation of brecciated clasts, reflected in the presence of fragments of a mapped sandstone formation that underlies a thick (1.5-2.0km) siltstone unit which hosts the breccia. The hydrothermally zoned breccia pipe at New York, Ok Tedi, could represent the continuation of deeper porphyry mineralisation into epithermal environments.

1 Introduction

Breccia-hosted Au±Cu mineralisation in porphyry systems are discovered globally, represent extremely valuable targets, but have so far been poorly documented in terms of their morphologies and internal metallogenic structures. These breccias generally occur as steep, pipe-like bodies that are formed at the top of intrusions; they are often associated with high grade Cu-Au mineralisation (>1.5 %Cu, and > 2g/t Au[1]) and show distinct zonation in ore mineralogy, hydrothermal alteration and brecciation style, displaying different fragment forms, both laterally and vertically.

Porphyry-related breccias are also delineated at Ok Tedi, a world-class porphyry/skarn Cu-Au deposit in Papua New Guinea. Although these breccias constitute a key host rock to mineralisation, they are seldom documented. Arnold and Fitzgerald (1977) first noted that brecciated rocks surrounding the Fubilan Quartz Monzonite Porphyry make up 10 to 20 % of the rocks in the Mt. Fubilan area. Few workers (e.g., Weinberg and van Dongen, unpublished report) briefly described them. Pollard (2014) appreciated the importance of breccias and noted how they control Cu-Au grade distribution at Ok Tedi. In their geochemical and geochronological studies, Large et al. (2018) indicated that brecciation at Ok Tedi is late, and presumably, not ore-bearing, despite Pollard's (2014) observations of the strongly mineralised nature of brecciated rocks within the Fubilan Quartz Monzonite Porphyry.

The New York breccia pipe constitutes a recently discovered (2017) large breccia pipe (400m by >1500m) within 2km of the world-class Ok Tedi porphyry/skarn Cu-Au deposit (Erceg and Pollard 2020). This breccia pipe contains significant gold mineralisation, displays hydrothermal alteration zonation, and indicates evidence of shallow epithermal to deeper porphyry-style mineralisation. The relative and absolute timing, hydrothermal alteration, Cu-Au footprint and the breccia's genetic relationship to the Ok Tedi deposit remain unknown.

In this research, we make a significant contribution to the understanding of mineralised breccia pipes by studying in detail the New York breccia pipe that not only contains significant gold mineralisation, but also shows a close spatial relationship to the world-class porphyry Cu-Au and skarn deposit at Ok Tedi, Papua New Guinea.

2 Geological Setting

The Ok Tedi/Mt. Fubilan porphyry Cu-Au deposit, by comparison to other similar major deposits globally, is an exceptionally young system (1.1-1.3 Ma; Page and McDougal 1975, Large et al. 2018; Pollard et al. 2021). The deposit is located towards the far west of mainland New Guinea (Fig. 1). It lies between the north-west trending Papuan Fold and Thrust Belt (part of the Australian Craton) and the New Guinea Orogenic Belt (part of the oceanic island arc of the Pacific Plate). Regions between the belts are intruded by small but prospective Miocene to Pleistocene intrusions that are responsible for Cu-Au mineralisation in areas including Ok Tedi, Frieda River, Yanderra, Kainantu and the Wafi-Golpu deposits. Magmatism responsible for these intrusions is interpreted to be localised in zones of low stress, as a result of movement of the Pacific and Australian plates (Bamford 1972).

The Mt. Fubilan deposit is located within Tertiary (Oligocene to Mid-Miocene) medium- to fine-grained clastic sedimentary rocks that are up to 1000m in thickness in areas near the Mt. Fubilan deposit (Fig. 1). They have been subdivided into three rock groups based on lithology and regional stratigraphy (Bamford 1972). The first group includes the lower unit of intercalated siltstones and sandstones, a second, middle unit of relatively pure limestone, and a third, upper unit of siltstones and sandstones, corresponding to the Ieru Formation, the Dari Limestone, and the Pnyang Formation, respectively.

The Ieru Formation is part of the Feing Group; it is of Jurassic to Late Cretaceous age (Arnold and Griffin 1978) but may be as young as Paleocene or early Eocene in places (Davies and Norvick 1974). It is composed of gray or gray-green, fine-grained sandstones, siltstones, and mudstones. The Toro Sandstone is also part of the Feing Group. It is the older of the two and consists of clean, partly glauconitic sandstones.

The Darai Limestone consists of massive to thick-bedded carbonates. It is late Eocene to middle Miocene in age. The formation varies from 500 to 1300m in thickness but is significantly thinner (about 240m) in the Mt. Fubilan area (Davies and Norvick 1974).

The Pnyang Formation consists of soft gray calcareous mudstones and siltstones with minor limestone interbeds (Davies and Norvick 1974). It is middle Miocene in age (Hill, 1989). The Pnyang Formation is locally about 1000m in thickness but increases to the west of the Ok Tedi mine area (Fookes et al. 1991).

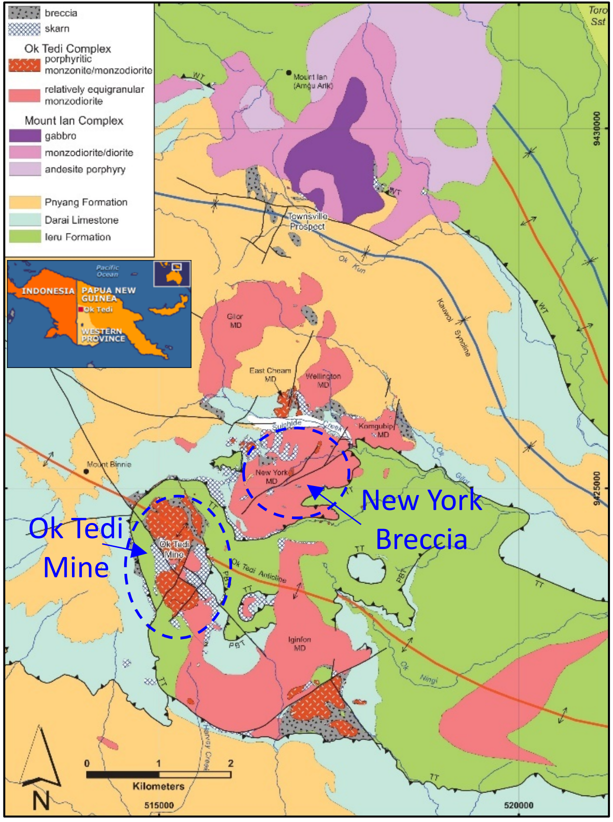

Figure 1. Geological map of the Ok Tedi district with circles indicating the location of the Ok Tedi deposit and the New York breccia pipe. The inset shows the location of the Ok Tedi Mine (Figure adapted and modified from Pollard et al. 2021).

Most of the sedimentary rocks are folded, faulted and intruded by numerous Pliocene to Pleistocene intrusive rocks that are distributed along the flanks of the fold belt. Most of these intrusions are small (several square kilometres outcrop) and are of quartz-dioritic to monzonitic in composition. Two of these intrusions host significant high-grade copper, gold and silver ores that define the Mt. Fubilan deposit. These are the Fubilan Monzonite Porphyry, located in the northern part of the pit, and the Sydney Monzodiorite located to the south. Most of the Cu-Au ore occurs as disseminated mineralisation within the intrusions, adjacent sedimentary rocks, and as massive magnetite-sulphide skarns located at the contacts of the intrusions and limestone units (Fig. 1).

The Ok Tedi deposit is closely associated with two N-dipping thrust faults; the Parrots Beak thrust, and the Taranaki thrust. Both are suggested to have caused a vertical repetition of Darai Limestone and Ieru Siltstone and to have experienced pre- and post-mineralisation movements (Mason 1997; Van Dongen et al. 2013).

3 Breccia characteristics and hydrothermal alteration zonation

3.1 Stages of brecciation at the New York breccia pipe

The New York breccia pipe is a large (400m by >1500m), deep-seated (>1500m) breccia body that contains significant Au-Cu mineralisation. Field mapping, core logging and detailed petrographic analysis reveal two main stages of brecciation at the New York breccia pipe. The earliest (stage 1) is characterised by well-rounded to sub-angular, polymictic monzodioritic and porphyritic dike clasts cemented by igneous quartz and plagioclase matrix. The clast sizes range from mm-scale to 20cm fragments with predominantly matrix support (Fig. 2A, 2B). Rock flour is locally present.

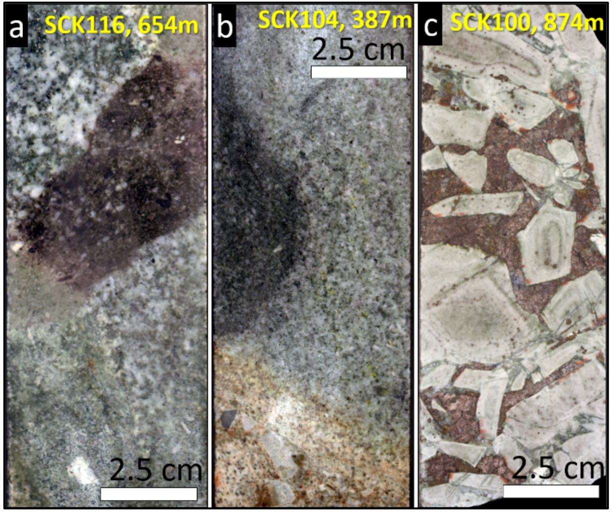

Figure 2. Photographs showing breccia stages within the New York breccia pipe. **a**: Igneous breccia. **b**: Igneous breccia (mafic clast) overprinted by

hydrothermal breccia (brownish discolouration at the bottom). **c**: Hydrothermal breccia dominated by siltstone clasts and cemented by pyrrhotite matrix.

The second breccia stage is characterised by hydrothermal matrix (chlorite, calcite, quartz, adularia, pyrite, pyrrhotite and magnetite) and clasts that are predominantly monomictic. They comprise either siltstone or monzodiorite. Locally, the presence of sandstone clasts, which are stratigraphically 1.5 to 2km beneath the siltstone units, are observed within the breccia. Fragments are angular to sub-rounded, ranging in sizes from mm-scale to 10cm and cemented by rock flour and hydrothermal matrix (Fig. 2B, 2C).

3.2 Vertical zonation of the New York breccia pipe

The New York breccia pipe shows distinct vertical zonation in breccia morphology, ore mineralogy, and hydrothermal alteration mineral assemblages.

Hydrothermal breccia dominates the upper 1000m of the breccia pipe, followed by igneous breccia at depth. At shallow depth (<400m), the hydrothermal breccia is dominated by angular, clast-supported fragments, which gradually become tabular, sub-rounded to well-rounded at depth. Clast composition also changes from monomictic, clast-supported siltstone fragments at shallow regions (<800m) to polymictic (siltstone, felsic dikes, mafic porphyritic dikes and monzodiorite), clast to matrix supported fragments below 800m depth (Fig. 3).

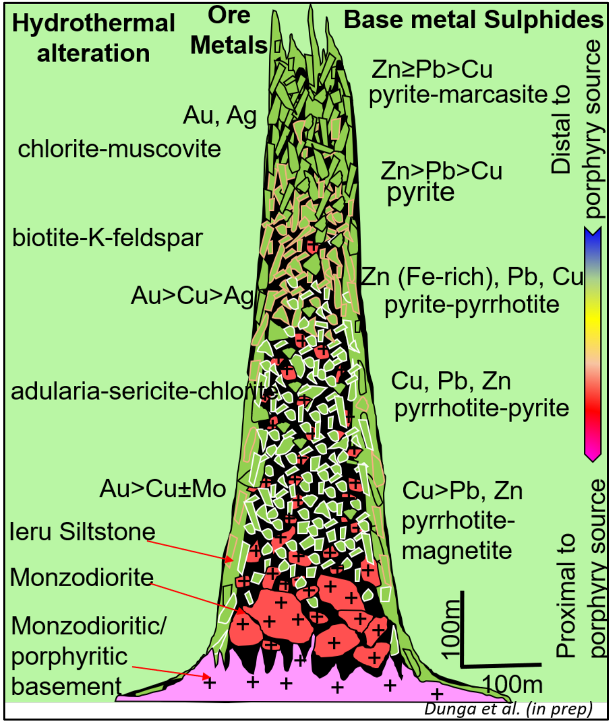

Figure 3. Schematic vertical section through the New York breccia pipe showing vertical hydrothermal alteration zonation, assemblages and metal distribution (drawn using insights from Kirwin 2018).

Clasts of igneous breccias within the hydrothermal breccias are dominant below 800m depth of the breccia pipe. In this zone, sub-rounded to well-rounded fragments of mafic intrusive rocks, felsic dikes and monzodiorite clasts are cemented by quartz and plagioclase matrix. This igneous breccia is then overprinted by hydrothermal breccias (Fig. 2B, 2C). The bottom of the igneous breccia is not intersected by any of the deep (1400m) diamond drill holes yet. However, the extent of the mineralised hydrothermal breccia, even below the 1400m depth, reflects the significant depth of the New York breccia pipe.

The New York breccia pipe also shows strong vertical zonation in ore minerals indicated by shallow, base metal-rich sulphides (galena-sphalerite) and gold-silver with crosscutting epithermal quartz-rhodochrosite veins, and deep magnetite-pyrrhotite-chalcopyrite mineralisation with carbonate-adularia-quartz-chlorite infill (Fig. 2). There is also a distinct zonation in sulphide and oxide mineral assemblages reflected by shallow pyrite-marcasite-hematite compared to pyrrhotite-magnetite assemblages at depth. Hydrothermal alteration zonation ranges from chlorite-muscovite at shallow depth (<300m) to biotite-K-feldspar (between 300 – 400m depth), followed by adularia-chlorite-sericite below 500m depth (Fig. 3).

3.3 Stages of hydrothermal alteration and gold mineralisation

Three main stages of Cu-Au mineralisation are distinguished at the New York breccia pipe. Stages 1 and 2 are related to hydrothermal breccia mineralisation, whereas the final stage is related to thrust-controlled skarn mineralisation.

The first stage is defined by disseminated pyrite-magnetite within wall-rocks to massive and vein-filling pyrrhotite-pyrite-magnetite mineralisation as breccia infills and in thick (5-10cm) veins. Fibrous chlorite, quartz, calcite and ankerite define the gangue minerals (Fig. 4A, 4B). Hydrothermal alteration zonation is defined by chlorite-epidote-calcite, K-feldspar-biotite-sericite-chlorite, and adularia-sericite-chlorite-carbonate assemblages in distal, intermediate and proximal alteration zones, respectively.

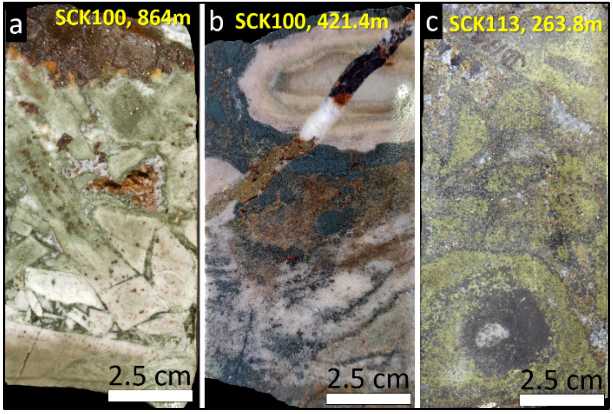

Figure 4. Photographs showing hydrothermal alteration and gold mineralisation stages within the New York breccia pipe. **a**: Stage 1 pyrrhotite-pyrite-galena-sphalerite-gold mineralisation related to the hydrothermal breccia within the Ieru Siltstone unit. **b**. Chlorite-altered Stage 1 breccia mineralisation cut by stage 2 related quartz-carbonate-galena-sphalerite vein. **c**: Skarn-related stage 3 clinopyroxene-actinolite alteration overprinting stage 1 chlorite altered breccia.

The second stage is defined by massive and vein-filling galena-sphalerite-chalcopyrite-pyrite mineralisation, accompanied by chlorite, quartz, calcite and dolomite as gangue minerals. Hydrothermal alteration zonation is similar to stage 1 mineralisation. However, the clear cross-cutting relationships, as displayed in Figure 4B, differentiates both stages.

The third stage is composed of massive magnetite skarn defined by magnetite-pyrite-hematite-galena-sphalerite-pyrrhotite mineralisation, associated with the Taranaki thrust. Quartz, calcite and dolomite constitute the major gangue minerals. Hydrothermal alteration zonation in stage 3 comprises chlorite-epidote-calcite, chlorite-actinolite-clinopyroxene-calcite-dolomite and magnetite-garnet-clinopyroxene-dolomite-phlogopite-actinolite in distal, intermediate and proximal alteration zones, respectively (Fig. 4C).

The different hydrothermal alteration and sulphide-rich mineralisation stages are shown in the paragenetic sequence diagram below (Fig. 5).

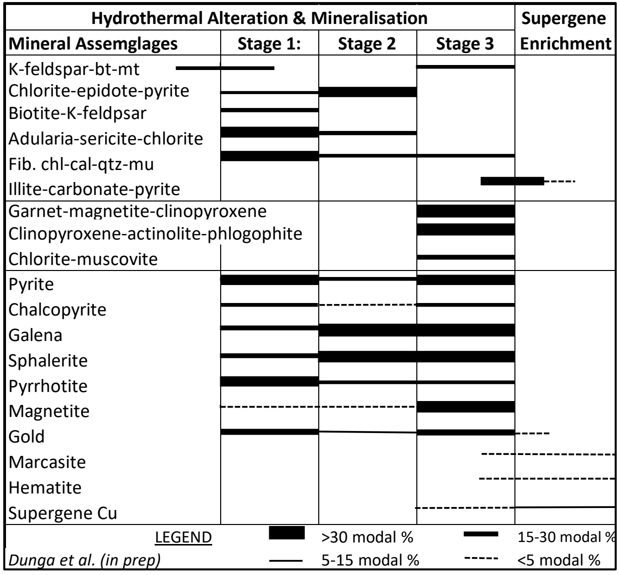

Figure 5. Paragenetic sequence diagram showing the main stages of hydrothermal alteration and gold mineralisation. Abbreviations: cal=calcite, chl=chlorite, Fib.=fibrous, mu=muscovite, qtz=quartz.

5 Conclusion

The New York breccia pipe is strongly mineralogically zoned, is pyrite-rich at the top, and at deeper levels, it displays increasing abundances of pyrrhotite±magnetite. The hydrothermal alteration zonation is characterised by crosscutting epithermal style quartz-rhodochrosite-sphalerite-galena-pyrite-pyrrhotite-chalcopyrite-calcite veins. Note that this hydrothermal alteration assemblage is not observed at Ok Tedi. The breccia fragments include different rock types with variable degrees of hydrothermal alteration and rounding which indicates significant fragment transport. There are abundant hydrothermal infill minerals (matrix), which form several overprinting stages. These observations suggest that there may be more than one magmatic, hydrothermal and brecciation event. Ongoing studies may lead to the identification of new prospective high-grade areas that may be targeted in the future.

Acknowledgements

The Ok Tedi Mining Ltd is thanked for sponsoring this research project through a project grant. The University of Western Australia is also acknowledged for providing a research scholarship for the first author.

References

Arnold, G. and Fitzgerald, F. (1977) Igneous rock types and their alteration, Mt. Fubilan porphyry copper deposit: Geological Survey of Papua New Guinea, Report 77/5, 10 p.

Arnold, G.O. and Griffin, T.J. (1978) Intrusions and porphyry copper prospects of the Star Mountains, Papua New Guinea, Econ. Geol. v. 73, pp. 785-795.

Bamford, R.W. (1972) The Mount Fubilan (Ok Tedi) porphyry copper deposit, territory of Papua and New Guinea, Econ. Geol. Vol. 67, pp..1019-1033.

Davies, H.L. and Norvick, M. (1974) Blucher Range, Papua New Guinea: Australian Bureau of Min. Res., Geology and Geophysics. 1:250 000 Geological Map Series, Explanatory Notes.

Erceg, M and Pollard, J.P. (2020) The discovery and geology of the New York Breccia and associated gold and base-metal mineralisation. Australian Inst. of Geos., Bulletin 70, p. 248-255.

Fookes, P.G., Dale, S.G., Land, J.M. (1991) Some observations on a comparative aerial photography interpretation of a landslipped area: Quarterly Journ. of Engin. Geol. 24, p. 249-265.

Hill, K.C. (1989) The Muller Anticline, Papua New Guinea; basement-cored, inverted extensional fault structures with opposite vergence: Tectonophysics, v. 158, p. 227-245.

Kirwin, D.J. (2018) Characteristics of intrusion-related copper-bearing tourmaline breccia pipes. Metals, Minerals, and Society. Society of Economic Geologists. Keystone, Colorado, USA. September22-25,2018. http://www.segabstracts.org/abstract_summary.php?mode=public&abs_id=1033).

Large, S.J.E., von Quadt, A., Wotzlaw, J-F., Guillong, M., and Heinrich, C.A. (2018) Magma evolution leading to porphyry Au-Cu mineralisation at the Ok Tedi deposit, Papua New Guinea: Trace element geochemistry and high-precision geochronology of igneous zircon: Econ. Geol., v. 113, p. 39–61.

Mason, R. (1997) Structure of the Alice anticline, Papua New Guinea: Serial balanced cross sections and their restoration: Journal of Struct. Geol., v. 19, p. 719–734.

Page, R.W. and McDougal, I. (1972) Ages of mineralisation of gold and porphyry copper deposits in the New Guinea Highlands: Econ Geol., v. 67, p.1034-1048.

Pollard, P.J. (2014) Grade distribution of the giant Ok Tedi Cu-Au deposit, Papua New Guinea – A Discussion, Econ. Geol., v. 109, p 1489-1494.

Pollard, P.J., Jongens, R., Stein, H., Fannings, C.M., Smillie, R (2021) Rapid Formation of Porphyry and Skarn Copper-Gold Mineralisation in a Postsubduction Environment: Re-Os and U-Pb Geochronology of the Ok Tedi Mine, Papua New Guinea: Econ. Geol, v. 116, No. 3. p. 533-558.

van Dongen, M., Weinberg, R.F. and Tomkins, A.G. (2013) Grade distribution of the giant Ok Tedi Cu-Au deposit, Papua New Guinea: Econ. Geol., v. 108, p. 1773-1781.

---

[1] *These average grade values were derived from a literature search of 35 breccia pipe hosting porphyry Cu-Au deposits worldwide.*

Redox state, sulphur and chalcophile element budgets during magma differentiation in thick continental arcs: case study at the Parinacota volcano

Iván Mateo Espinel Pachón[1], Zoltan Zajacz[1], Cristóbal González Rodríguez[2], Michael Schirra[1], Weikai Li[1] and Mara Miranda[1]
[1]*University of Geneva, Switzerland*
[2]*Millenium Institute on Volcanic Risk Research- Ckelar Volcanoes, Chile*

Abstract. Porphyry copper deposits are genetically linked to arc magmatism. Magma fertility for porphyry ore genesis is dependent on volatile element and ore metal budgets and the variation of redox conditions during magma differentiation. In this project, we analysed silicate melt inclusions from several eruptive events of the Parinacota volcano in northern Chile. Major and trace element data reveal the existence of a complex plumbing system with at least three different melts emplaced at different depths within the crust. Furthermore, the most primitive, highest Sr/Y melts show rather high sulphur contents (up to 6000 ppm) and high oxidation state ($\log fO_2$ = FMQ+2.1). This indicates that the initial oxidation of the magma occurs at the source or during the earliest stages of magma differentiation, and that high-Sr/Y, high-S signature can be introduced at the source.

1 Introduction

Arc magmas are most commonly thought to form by partial melting of a mantle source in which accessory sulphides are present, and therefore it is expected that early sulphide saturation takes place during the differentiation of these magmas at greater crustal depths (Matjuschkin et al. 2016; Chiaradia 2022). This may have a negative effect on the ore-forming potential of the magmas because the sulphides may sequester a significant part of the initial chalcophile metal budget of the magma if they are effectively fractionated. The amount of sulphide precipitated during magma differentiation in the crust will be dependent on how the redox state of the magma varies, starting from partial melting in the mantle through crustal magma differentiation, and also on the pressure (P) -temperature (T) - melt composition (X) – dependent shift in the fO_2 range of the sulphide to sulphate transition. Neither of these are fully understood at the moment (Jugo et al. 1999; Jugo 2009; Botcharnikov et al. 2011; Klimm et al. 2012; Matjuschkin et al. 2016; Nash et al. 2019).

Sulphur is also critically important to facilitate the precipitation of porphyry ore. It is most favourable to release S from the magma reservoir in the form of SO_2, which in turn disproportionates to H_2SO_4 and H_2S over a narrow temperature range below 400 °C, leading to spatially focused ore metal sulphide precipitation. Thus, the redox state of the magma at the fluid exsolution state is also critically important. Overall, to understand magma fertility for porphyry ore genesis, it is important to constrain how the redox state of magmas evolve from partial melting in the mantle to the final stages of crystallization at shallow crustal levels, and the interplay between this and S and chalcophile element budgets.

Many previous studies focused on the process of metal sequestration and fluid release from magmas in upper crustal magma reservoirs, whereas the role of deep crustal processes in regulating ore fertility have just started receiving rapidly increasing attention over the past 1-2 decades (Audétat and Pettke 2006; Audétat 2010, 2015; Zajacz et al. 2012; Li et al. 2015; Matjuschkin et al. 2016; Chiaradia and Caricchi 2017, 2022; Grondahl and Zajacz 2017, 2022; Rottier et al. 2020a, b; Chiaradia 2022).

This study aims to investigate volcanic systems on thick continental crust in the fertile Andean arc to study the interplay between magma redox, volatile element and ore metal concentrations during the differentiation of magmas emplaced at different crustal depths and magma fluxes. This presentation focuses on the Parinacota volcano.

The Parinacota volcano is located in northern Chile, near the Bolivian border (Figure 1). It is a stratovolcano that erupted rocks with a broad range of compositions from rhyolites to basaltic-andesites generated by magma differentiation at different levels within one of the thickest continental crust on earth (around 70 km crustal thickness) (Banaszak 2014; Ginibre and Davidson 2014a).The oldest units in the area, the Chungará andesites (CA) (163-116 ka) and the Old cone (oc) (52-20 ka), consist of amphibole-bearing andesites with additional clinopyroxene and plagioclase phenocrysts. Between 20-10 ka, an edifice collapse generated a debris avalanche towards the west. After this event, a new edifice started building up generating the young cone (yc) (8 ka-recent) amphibole-free andesites with clinopyroxene and plagioclase phenocrysts. Simultaneously with the build-up of the main edifice, some flank eruptions produced basaltic andesites that form the Ajatas flows (a1, a2, a3 and a4)

Parinacota represents a dynamic system that, with time, shows increasing magma flux rates (mafic recharge), leading to magma differentiation at shallower depths and less variable, in general more mafic magmas being erupted (Ginibre et al. 2005; Hora et al. 2007; Wörner et al. 2018). All these characteristics make it an excellent study area for our purposes.

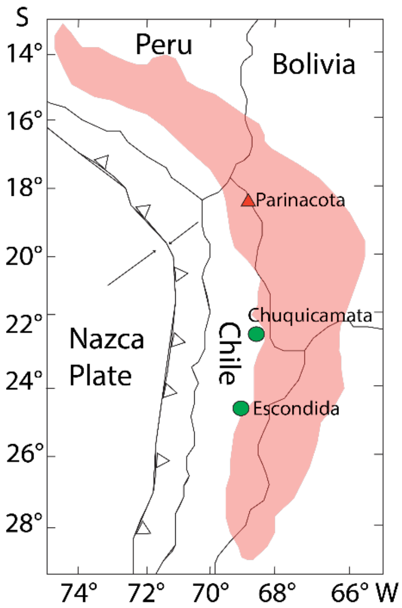

Figure 1. Map of the central volcanic zone of the Andes (red). Green circles are some of the giant porphyry deposits associated with Miocene subduction. Parinacota volcano is represented by the red triangle.

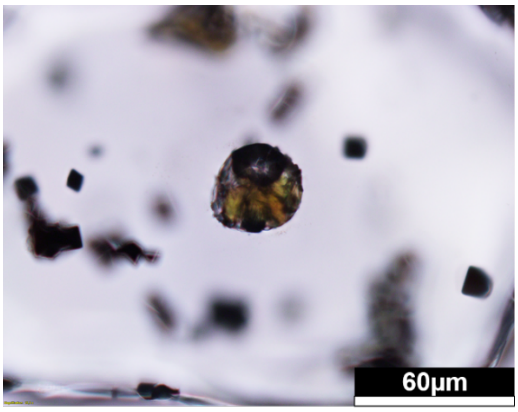

Figure 2. Recrystallized silicate melt inclusion trapped in an olivine phenocryst from Parinacota Volcano (a4 lavas). The olivine also contains Cr-spinel inclusions testifying for the primitive nature of the host magma.

2 Methodology

Volcanic rocks are final products of often complex magma evolution, which may for example involve mixing. Furthermore, their volatile budget is unrepresentative for the original magma due to pre- and syn-eruptive degassing. Therefore, we chose silicate melt inclusions (SMI) in magmatic phenocrysts as our primary source of information, which is complemented by mineral and whole-rock chemistry.

Major and minor element compositions of olivine and pyroxene were determined by using a JEOL 8200 superprobe electron microprobe, equipped with 5 Wavelength Dispersive X-ray Spectroscopy (WDS) detectors at the University of Geneva.

Silicate melt inclusions were analyzed by Laser Ablation Inductively Coupled Plasma Mass Spectrometry (LA-ICPMS) using the methodology of (Halter et al. 2002), which relies on the analysis of the entire inclusion along with its host mineral and subsequent deconvolution of the inclusion and host signals (Figure 2). Important advantages are that the inclusion can be analysed without reheating, and that S and Cl concentrations can be determined simultaneously with major and trace elements without the risk of unrepresentative sampling due missing volatiles that may have partitioned into the vapor bubble (Venugopal et al. 2020; Grondahl and Zajacz 2022). Analyses were done using an NWR 193 HE laser ablation system coupled with an Agilent 8900 triple quadrupole ICP-MS at the University of Geneva. We used a custom-built ablation cell and gas purification system to facilitate accurate determination of S and Cl concentrations along with a broad set of major and trace elements.

3 Petrography

Traditional petrography of the samples selected for melt inclusions studies allowed us to identify the following differences between the pre- (Chungará andesite (ca) and old cone (oc)) and post-collapse (young cone (yc) and Ajatas flows (a1-a2-a3-a4)) units (Fig.2): i) There is a change from amphibole-bearing to amphibole-free eruptive products. ii) Plagioclase phenocrysts in the pre-collapse lavas show more roundish boarders and dissolution textures, which is not observed in post-collapse units. iii) Crystals in the post-collapse lavas are generally smaller iv) In the post-collapse units, except for yc, olivine is present but not as abundant as plagioclase or clinopyroxene.

Magmatic sulphides were not observed, indicating that sulphide saturation might have not taken place. Magnetite is the main oxide present in all the units as small inclusions within phenocrysts (olivine and clinopyroxene) or as an accessory mineral within the matrix, suggesting that it was one of the first phases to crystallize.

Olivine- and clinopyroxene-hosted SMIs are abundant in the yc lavas and the Ajata flows. Their sizes range from 5 to 100 µm. Contrarily, SMIs in the oc and ca are scarce, small (<20 µm) and are typically hosted in clinopyroxene. These latter are yet to be studied.

4 Mineral chemistry and thermobarometry

Diopside is the main clinopyroxene. High chromium oxide concentrations (up to 0.7%) and magnesium numbers (up to 85) in clinopyroxene cores suggest that a2 and a3 were generated from more primitive melts than a2, a4 and yc. Geothermobarometric estimations calculated by using the cpx-only Putirka (2008) thermobarometer yielded temperatures between 1050-1100°C for a2 and a3 and 1000-1050°C for a1, a4, yc and ca. Pressure estimations are less precise and range between 1-7 kbar displaying no systematic variations between the units.

Olivine is a mineral phase present in Ajata flows (a1, a2, a3 and a4). It usually hosts Cr-rich spinel inclusions. In a2 and a3 lava flows, olivine occurs as euhedral phenocrysts in equilibrium with the matrix and have a magnesium number (Mg#) of 79-81 with Ni contents ranging between 400-1100 ppm, whereas olivines in a1 and a4 have Mg# of 74-79 and similar Ni values. Texturally, these more evolved olivines show clear disequilibrium indicated by the presence of orthopyroxene-magnetite symplectite, which have overgrown the olivine.

5 Silicate melt inclusion compositions

Melt inclusion compositions largely overlap with whole rock data but show more variability, in some rocks, suggesting mixing between different magma batches.

N-MORB - normalized trace element plots (Sun et al. 1989) show a depletion in fluid-immobile and an enrichment in fluid-mobile elements, typical of arc magmatism (Figure 3). Trace elements allow to identify two different components within a4: the first component (c1) has high Ba/Th, low Th/Nb and overall lower incompatible trace element concentrations compared to the other units. The second component (c2) has high Th/Nb, low Ba/Th ratios and has higher concentrations of fluid mobile elements. The most primitive melts (a2 and a3) show high Sr values ranging from 1000 up to 2000 ppm while in a1, a4 and yc the maximum value is around 950 ppm.

SMIs display Cl concentrations in the range of 1500-3000 ppm, which is on the high end of the typical range for arc magmas (Wallace 2005). On the other hand, S concentrations vary broadly and reach very high values (up to about 6000 ppm). S concentration positively correlate with the Sr/Y ratio, which can be as high as 100.

Oxygen fugacity was calculated using the partition coefficient of vanadium between olivine and silicate melt (D_V^{Ol-M}) following the method of Shishkina et al. (2018). Analysis of 47 olivine-melt pairs yielded a fO_2 of □QFM + 2.1 ±0.5 for the Ajata flows.

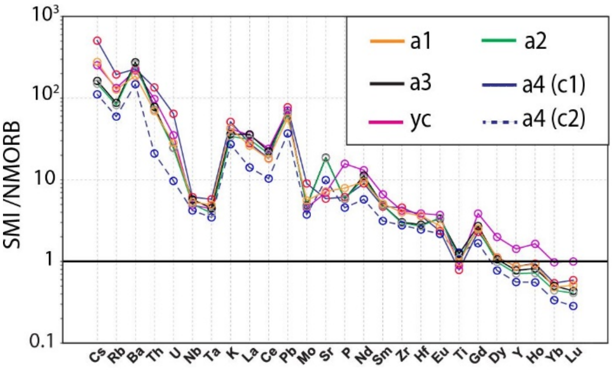

Figure 3. N-MORB normalized trace element variation diagram based on silicate melt inclusion compositions (median values shown for each unit).

6 Magmatic evolution and ore forming potential

We propose that the erupted rocks present in Parinacota are the result of the interaction of at least three different melts: i) A melt that generated a4-c1 with low Ba, Cs, Pb, Th/Nb, La/Yb, Th/U and high Ba/Th. These characteristics may be attributed to the input of slab-derived aqueous fluids to the mantle source of the magma combined with higher degree of melting ii) A high Sr/Y, Ba, Pb, Th/U and La/Yb, medium Th/Nb melt that yielded units a2 and a3, suggesting the additional influence of a subducted sediment component. iii) A low Sr/Y, Ba/Th, Nb/Ta, Sr and high Cs, Pb and Th/Nb melt that generate a4c2 and yc, suggesting a different mantle source with both sediment and aqueous fluid input. Overall, the high Th/U indicate that the metasomatic fluids derived from the slab or associated sediments were rich in silicate components. The high Ba/Th observed in some melts indicates a cooler slab fluid component, while high Th/Nb points towards a deep sediment melt component.

The high Sr/Y (80-100) component also correspond to high S values (3000-6000 ppm) well above the typical range of arc magmas. As this is a fairly primitive mantle melt, the enrichment cannot be a result of AFC processes at deep crustal level as originally proposed for other systems by Loucks (2014). Therefore, it appears the incorporation of high-Sr, high-S components in the mantle source may be an alternative way to generate positive correlation between Sr/Y ratio and S concentration, and at the same time, also to increase ore fertility. Based on the relatively high Th/Nb ratio and previously published isotope data (Ginibre and Davidson 2014b), we hypothesize that this component is subducted sediment, but further investigation is warranted.

Most Cu and Mo concentrations fall between 25-100 ppm and 1-3 ppm, respectively, which represent typical concentrations of the Andean Southern Volcanic Zone (33–40 °S) (Grondahl and Zajacz 2022) and arc magmas in general. They are consistent with minor to moderate sulphide fractionation at deeper crustal levels.

The nearly identical fO_2 estimates for all studied units at Parinacota, including the near-primitive mantle melts from a2, suggest that oxidation does not occur during early magma differentiation and that the oxidized nature of the Parinacota magmas is rather produced at the source. However, we do not discard the possibility that further changes in magma redox state can occur during differentiation, which will be revealed by the investigation of the more differentiated units (yc, oc and ca), which is currently in progress. Concentrations of Au and Pt will be also determined in large SMI, and will be used along with the concentrations of Cu and S to assess the amount and type of magmatic sulphides involved in the genesis of the various Parinacota magmas at greater crustal and mantle depths.

Acknowledgements

The European Research Council is thanked for the ERC Consolidator Grant funding to project OXYGEN.

References

Audétat A (2010) Source and evolution of molybdenum in the porphyry Mo(-Nb) deposit at Cave Peak, Texas. Journal of Petrology 51:1739–1760. https://doi.org/10.1093/petrology/egq037

Audétat A (2015) Compositional evolution and formation conditions of magmas and fluids related to porphyry mo mineralization at Climax, Colorado. Journal of Petrology 56:1519–1546. https://doi.org/10.1093/petrology/egv044

Audétat A, Pettke T (2006) Evolution of a porphyry-Cu mineralized magma system at Santa Rita, New Mexico (USA). Journal of Petrology 47:2021–2046. https://doi.org/10.1093/petrology/egl035

Banaszak M (2014) Differentiation regimes in the Central Andean magma systems: case studies of Taapaca and Parinacota volcanoes, Northern Chile. Universität Göttingen

Botcharnikov RE, Linnen RL, Wilke M, et al (2011) High gold concentrations in sulphide-bearing magma under oxidizing conditions. Nat Geosci 4:112–115. https://doi.org/10.1038/ngeo1042

Chiaradia M (2022) Distinct magma evolution processes control the formation of porphyry Cu–Au deposits in thin and thick arcs. Earth Planet Sci Lett 599:. https://doi.org/10.1016/j.epsl.2022.117864

Chiaradia M, Caricchi L (2017) Stochastic modelling of deep magmatic controls on porphyry copper deposit endowment. Sci Rep 7:1–11. https://doi.org/10.1038/srep44523

Chiaradia M, Caricchi L (2022) Supergiant porphyry copper deposits are failed large eruptions. Commun Earth Environ 3:. https://doi.org/10.1038/s43247-022-00440-7

Ginibre C, Davidson JP (2014a) Sr isotope zoning in plagioclase from parinacota volcano (Northern Chile): Quantifying magma mixing and crustal contamination. Journal of Petrology 55:1203–1238. https://doi.org/10.1093/petrology/egu023

Ginibre C, Davidson JP (2014b) Sr Isotope Zoning in Plagioclase from Parinacota Volcano (Northern Chile): Quantifying Magma Mixing and Crustal Contamination. 55:1203–1238. https://doi.org/10.1093/petrology/egu023

Ginibre C, Davidson JP, Wörner G (2005) Lower crustal influence on CVZ magmas: Insights from chemical and isotopic zoning in plagioclase at Parinacota volcano, North Chile. In: 6th International Symposium on Andean Geodynamics. pp 323–326

Grondahl C, Zajacz Z (2022) Sulfur and chlorine budgets control the ore fertility of arc magmas. Nat Commun 13:. https://doi.org/10.1038/s41467-022-31894-0

Grondahl C, Zajacz Z (2017) Magmatic controls on the genesis of porphyry Cu–Mo–Au deposits: The Bingham Canyon example. Earth Planet Sci Lett 480:53–65. https://doi.org/10.1016/j.epsl.2017.09.036

Halter WE, Pettke T, Heinrich CA, Rothen-rutishauser B (2002) Major to trace element analysis of melt inclusions by laser-ablation ICP-MS : methods of quantification. 183:63–86

Hora JM, Singer BS, Wörner G (2007) Volcano evolution and eruptive flux on the thick crust of the Andean Central Volcanic Zone: 40Ar/39Ar constraints from Volcán Parinacota, Chile. Bulletin of the Geological Society of America 119:343–362. https://doi.org/10.1130/B25954.1

Jugo PJ (2009) Sulfur content at sulfide saturation in oxidized magmas. Geology 37:415–418. https://doi.org/10.1130/G25527A.1

Jugo PJ, Candela PA, Piccoli PM (1999) Magmatic sulfides and Au:Cu ratios in porphyry deposits: an experimental study of copper and gold partitioning at 8508C, 100 MPa in a haplogranitic melt-pyrrhotite-intermediate solid solution-gold metal assemblage, at gas saturation

Klimm K, Kohn SC, Botcharnikov RE (2012) The dissolution mechanism of sulphur in hydrous silicate melts. II: Solubility and speciation of sulphur in hydrous silicate melts as a function of fO 2. Chem Geol 322–323:250–267. https://doi.org/10.1016/j.chemgeo.2012.04.028

Li W, Audétat A, Zhang J (2015) The role of evaporites in the formation of magnetite-apatite deposits along the Middle and Lower Yangtze River, China: Evidence from LA-ICP-MS analysis of fluid inclusions. Ore Geol Rev 67:264–278. https://doi.org/10.1016/j.oregeorev.2014.12.003

Loucks RR (2014) Distinctive composition of copper-ore-forming arcmagmas. Australian Journal of Earth Sciences 61:5–16. https://doi.org/10.1080/08120099.2013.865676

Matjuschkin V, Blundy JD, Brooker RA (2016) The effect of pressure on sulphur speciation in mid- to deep-crustal arc magmas and implications for the formation of porphyry copper deposits. Contributions to Mineralogy and Petrology 171:. https://doi.org/10.1007/s00410-016-1274-4

Nash WM, Smythe DJ, Wood BJ (2019) Compositional and temperature effects on sulfur speciation and solubility in silicate melts. Earth Planet Sci Lett 507:187–198. https://doi.org/10.1016/j.epsl.2018.12.006

Rottier B, Audétat A, Koděra P, Lexa J (2020a) Magmatic evolution of the mineralized Štiavnica volcano (Central Slovakia): Evidence from thermobarometry, melt inclusions, and sulfide inclusions. Journal of Volcanology and Geothermal Research 401:. https://doi.org/10.1016/j.jvolgeores.2020.106967

Rottier B, Audétat A, Koděra P, Lexa J (2020b) Magmatic evolution of the mineralized Štiavnica volcano (Central Slovakia): Evidence from thermobarometry, melt inclusions, and sulfide inclusions. Journal of Volcanology and Geothermal Research 401:. https://doi.org/10.1016/j.jvolgeores.2020.106967

Shishkina TA, Portnyagin M V., Botcharnikov RE, et al (2018) Experimental calibration and implications of olivine-melt vanadium oxybarometry for hydrous basaltic arc magmas. American Mineralogist 103:369–383. https://doi.org/10.2138/am-2018-6210

Sun S, Mcdonough WF, Sun S, Mcdonough WF (1989) Chemical and isotopic systematics of oceanic basalts: implications for mantle composition and processes. Geological Society, London, Special Publications 1989, 42:313–345. https://doi.org/10.1144/GSL.SP.1989.042.01.19

Venugopal S, Schiavi F, Moune S, et al (2020) Melt inclusion vapour bubbles: the hidden reservoir for major and volatile elements. Sci Rep 10:. https://doi.org/10.1038/s41598-020-65226-3

Wallace PJ (2005) Volatiles in subduction zone magmas: Concentrations and fluxes based on melt inclusion and volcanic gas data. Journal of Volcanology and Geothermal Research 140:217–240. https://doi.org/10.1016/j.jvolgeores.2004.07.023

Wörner G, Mamani M, Blum-Oeste M (2018) Magmatism in the central andes. Elements 14:237–244. https://doi.org/10.2138/gselements.14.4.237

Zajacz Z, Candela PA, Piccoli PM, et al (2012) Gold and copper in volatile saturated mafic to intermediate magmas: Solubilities, partitioning, and implications for ore deposit formation. Geochim Cosmochim Acta 91:140–159. https://doi.org/10.1016/j.gca.2012.05.033

Fluid evolution and Re enrichment in the Maronia Cu-Mo±Au porphyry, NE Greece. Insights from mineral microanalysis and fluid inclusions constraints

Jan J. Falkenberg[1], Manuel Keith[1], Vasilios Melfos[2], Max Hohl[3], Karsten M. Haase[1], Panagiotis Voudouris[4], Alica Höss[1], Julia Wenske[1], Reiner Klemd[1], Christoph Beier[5], Martin Kutzschbach[6], Harald Strauss[7]

[1] *Friedrich-Alexander-Universität (FAU) Erlangen-Nürnberg, GeoZentrum Nordbayern, Germany*

[2] *Aristotle University Thessaloniki, Faculty of Geology, Thessaloniki, Greece*

[3] *University of Tasmania, CODES, Australia*

[4] *National and Kapodistrian University of Athens, Faculty of Geology & Geoenvironment, Athens, Greece*

[5] *Department of Geosciences and Geography, University of Helsinki, Helsinki, Finland*

[6] *Technische Universität Berlin, Chair of Applied Geochemistry, Berlin, Germany*

[7] *Westfälische-Wilhelms-Universität Münster, Institut für Geologie und Paläontologie, Münster, Germany*

Abstract. Maronia is an exceptional Re-rich Cu-Mo ± Au porphyry systems in Thrace, NE Greece. Here, we present a micro-analytical, S isotope, and fluid inclusion approach in order to reveal the hydrothermal prerequisites required for the extreme Re enrichment which are poorly constrained up to date. Based on petrography, trace element chemistry of hydrothermal quartz (e.g., Al/Ti, Ge/Ti), and fluid inclusion microthermometry of consecutive vein generations, we establish the spatial and temporal fluid evolution. The fluid inclusions give evidence for systematic fluid cooling and continuous phase separation which is the main ore-forming process during the porphyry stages. The later epithermal stage formed by vapor condensation into meteoric water. This is consistent with salinity-sensitive (Co/As, As/Sb), temperature-sensitive (Se/Tl) and fluid source-sensitive (Se/Ge) pyrite trace element ratios. δ^{34}S values in pyrite vary in response to SO_2 disproportionation, phase separation, host rock buffering and fluid fO_2. Early extremely Re-rich molybdenite (6631 ± 4308 ppm) is related to higher temperatures and fO_2 compared to later molybdenite generations with lower Re (1746 ± 1184 ppm) contents. We conclude, that fluid cooling below 400 – 350°C and decreasing fO_2 are the main control on the Re precipitation efficiency in the potassic alteration on the deposit-scale.

1 Introduction

Porphyry Cu-Mo ± Au ± Re deposits are one of the most important global sources for base (Cu, Mo), precious, critical and rare (Se, Ag, Te, Re, Au, PGE) metals (Tabelin et al. 2021), which are essential for various high-tech applications, such as semiconductors, catalysts for petroleum refining, high temperature superalloys and photovoltaic production. However, their scarcity and poorly constrained enrichment processes, will likely lead to a supply risk in the near future (Grandell et al. 2016).

The Maronia Cu-Mo ± Au porphyry system is host to rare rheniite (ReS_2) and exceptional Re-rich molybdenite (up to 13800 ppm). It is associated to a high-K calc-alkaline to shoshonitic monzonite-monzogabbro intrusion into the metamorphic basement at 29.6 to 29.8 Ma in NE Greece (Fig.1A, B) (Schaarschmidt et al. 2021). The pluton was subsequently intruded by a microgranite porphyry. It is associated with concentric zones of pervasive potassic, sodic-calcic, propylitic, sericitic, and argillic alteration that host the Re-rich quartz-sulfide vein networks (Fig.1C) (Melfos et al. 2020). The mineralized vein samples represent a lateral profile along the coastline of the Maronia porphyry (Fig. 1) and the hydrothermal stockworks are associated with qz-py-cpy-po A- and qz-py-mbl-rhn B-type veins in the potassic alteration, with qz-py-mbl D-type veins in the sericitic alteration and with qz-cc-py-ss E1, and qz-py-mcr-asp-ss E2-type veins in the argillic alteration.

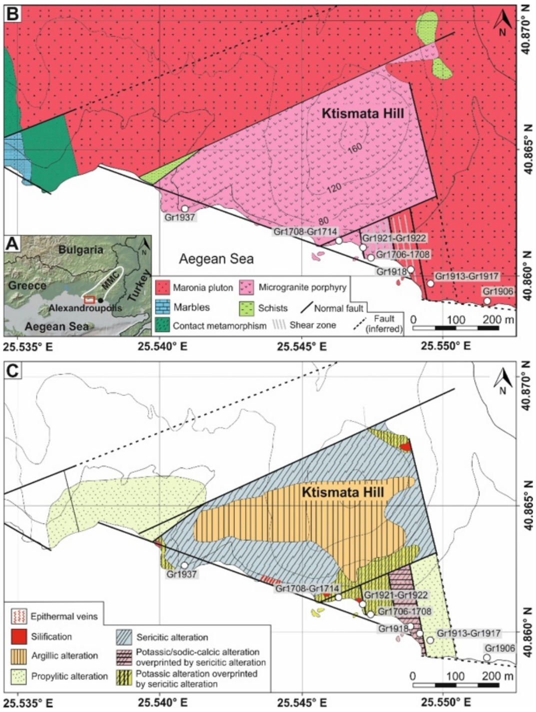

Figure 1. (A) Regional overview, (B) geological and (C) alteration map of the Maronia porphyry-epithermal system. Modified after Melfos et al. 2020

The trace element and S isotope composition of hydrothermal sulfides (e.g., pyrite, molybdenite) and hydrothermal quartz from consecutive porphyry-epithermal vein generations can provide valuable spatial and temporal information about the evolution of the ore-forming fluids (Hutchison et al. 2020; Rottier and Casanova 2021; Keith et al. 2022). Quartz-hosted fluid inclusions give information on the temperature, salinity, and entrapment pressure of hydrothermal fluids and can record processes related to fluid phase separation (Bodnar et al. 2014).

Molybdenite commonly hosts most of the Re in porphyry deposits and its trace element composition can provide insights into the ore-forming processes. However, based on experimental studies (Xiong et al. 2006) and natural observation (Barton et al. 2020) Re shows a complex behaviour with respect to varying physicochemical fluid parameters (e.g., temperature, fO_2) and thus the major control on Re enrichment is enigmatic.

Here, we combine a multi-method trace element, S isotope and fluid inclusion approach in spatial and temporal consecutive vein generations allowing us to fingerprint the fluid evolution and establish the hydrothermal prerequisites favourable for extreme Re enrichment in distinct paragenetic stages.

2 Methodology

2.1 Microanalytical techniques

BSE and CL imaging by SEM was used to identify different mineral phases and to avoid microinclusions during subsequent LA-ICP-MS analysis. The trace element composition of pyrite, molybdenite, and arsenopyrite were measured by LA-ICP-MS at the GeoZentrum Nordbayern using a Teledyne Analyte Excite 193nm laser coupled with an Agilent 7500c ICP–MS. MASS-1 and FeNiS1 were used as primary and UQAC-FeS1 as secondary standards.

In-situ LA-ICP-MS trace element measurements of hydrothermal quartz were carried out at HelLabs, Department of Geosciences and Geography, University Helsinki using a coherent GeoLas MV 193 nm laser coupled with an Agilent 7900s ICP–MS. NIST SRM 612 was used as primary and NIST 610, BHVO-2G, and BCR-2G were used as secondary standards.

2.2 Fluid inclusion microthermometry

Following the CL imaging to distinguish different quartz generations, fluid inclusion microthermometry was carried out with a LINKAM THM-600/MS 90 heating-freezing stage, at the Department of Mineralogy, Petrology and Economic Geology at the Aristotle University of Thessaloniki, Greece.

2.3 δ^{34}S of pyrite, molybdenite and arsenopyrite

Sulfide powders (pyrite, molybdenite, arsenopyrite) were extracted and homogenized by a diamond microdrill from the vein matrix and analysed for their S isotopic composition by a Flash EA IsoLink elemental analyser interfaced to a ThermoScientific Delta V Advantage isotope ratio mass spectrometer (EA-IRMS) at the Westfälische Wilhelms-Universität, Münster.

The in-situ S isotope values of pyrite have been determined at the MAGMA Lab TU Berlin using an Agilent8900 ICP-MS/MS (oxygen reaction gas) coupled to a Teledyne Analyte Excite 193 nm excimer laser. Mass fractionation was corrected using PPP-1 pyrite (Gilbert et al. 2014) as primary standard. Accuracy was verified on Balmat pyrite (Crowe and Vaughan 1996).

3 Results

3.1 Trace element composition of hydrothermal quartz, pyrite, molybdenite and arsenopyrite

Titanium contents in hydrothermal quartz systematically decrease during the porphyry-epithermal evolution and correlate with the CL intensity. Quartz trace element ratios of Al/Ti and Ge/Ti from the different vein types are consistent with quartz from other porphyry-style deposits (Fig. 2) and confirm the vein classification (Rottier and Casanova 2021). Based on an unpaired two-tailed t-test the mean Re content in molybdenite in earlier B-type (6631 ± 4308 ppm) and in later D-type (1746 ± 1184 ppm) is considered significantly ($p = <0.01$) different (Fig. 3). Pyrite compositions show a systematic increase of trace elements such as Au, Te, Ag, Pb, Tl, and As from the porphyry to the epithermal stages and porphyry pyrite is related to high Se/Tl, Co/As and Se/Ge but low As/Sb ratios where epithermal pyrite shows the opposite (Fig. 4).

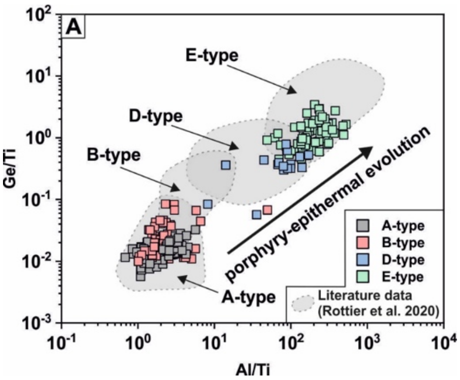

Figure 2. Quartz trace element ratios (Ge/Ti, Al/Ti) classify different vein types (Rottier and Casanova 2021).

3.3 δ^{34}S of pyrite, molybdenite and arsenopyrite

δ^{34}S values of sulfide separates (pyrite, molybdenite and arsenopyrite) range from 2.6 to 4.6 ‰, with the epithermal veins showing the highest and the porphyry veins yielding lower values. The δ^{34}S of molybdenite from B- (~3.2 ‰) and D-type (~3.3 ‰) veins are comparable (Fig. 5).

The in-situ δ^{34}S values of pyrite show a larger variation than pyrite separates and vary between -4.1 and 14.8 ‰ with multiple negative values in A-and B-type veins as well as large intra-grain variations (up to $\Delta\delta^{34}S$ = 9.5‰). Based on an unpaired two-tailed t-test the lower average $\delta^{34}S$ observed in the B-type veins (~2.9 ‰) is significantly (p = <0.01) different than the similar $\delta^{34}S$ of A-, D- and E1- veins (~5.0 ‰) (Fig. 5).

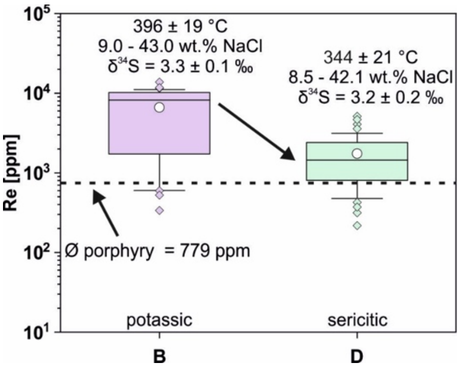

Figure 3. Rhenium content in molybdenite from B- and D-type veins at Maronia. The average Re content from porphyry molybdenite is adapted from Barton et al. 2020.

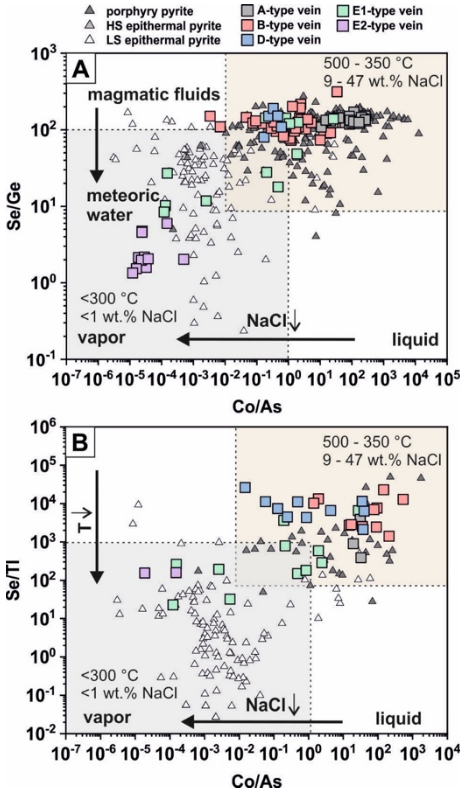

Figure 4. Fluid mixing-sensitive (Se/Ge), temperature-sensitive (Se/Tl) and salinity-sensitive (Co/As) pyrite trace element ratios.

3.4 Fluid microthermometry

Homogenization temperatures of quartz-hosted fluid inclusion decrease from early porphyry (~500°C) to later epithermal (~280°C) veins. Porphyry veins are associated with coexisting hypersaline (47.2 – 34.5 wt. % NaCl equiv.) and intermediate saline (20.4 – 8.5 wt. % NaCl equiv.) vapor-rich fluids. By contrast, epithermal veins are characterized by low saline (<0.7 wt. % NaCl) liquid-rich fluids (Fig. 6).

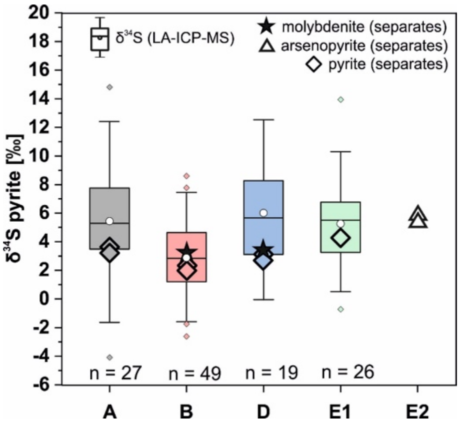

Figure 5. $\delta^{34}S$ of sulfide separates (pyrite, arsenopyrite, molybdenite) and in-situ $\delta^{34}S$ LA-ICP-MS of pyrite.

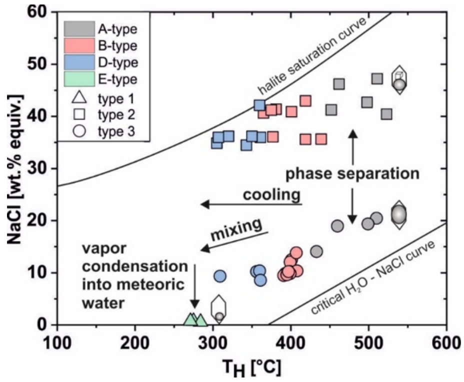

Figure 6. Homogenization temperature vs. salinity diagram of the different hydrothermal veins.

4 Discussion

4.1 Spatial and temporal fluid evolution

The combined use of quartz trace elements, alteration assemblages and fluid inclusion constraints reveal a systematic fluid evolution from neutral high temperature (~500°C) to moderate acidic low temperature (~280°C) conditions during the porphyry-epithermal transition (Fig. 2 – 6). During the formation of A-, B-, and D-type veins, phase separation was the main ore-forming process, whereas the E-type veins formed from the condensation and mixing of a vapor-rich fluid into meteoric waters (Fig. 6).

4.2 Effect of phase separation and fluid evolution on pyrite chemistry

Enrichment of trace elements like Au, Te, Ag, Pb, Tl, and As in epithermal stages is consistent with the formation at lower temperatures as revealed by fluid inclusion microthermometry and Ti-in-quartz thermometry. Similarly, temperature-sensitive trace element ratios of e.g., Se/Tl record the systematic cooling history of the fluid at Maronia. Co/As <1 in epithermal pyrite from Maronia is consistent with the formation from low salinity vapors whereas

Co/As >1 (Fig. 4) is rather indicative for precipitation from hypersaline liquids due to the different vapor-liquid partitioning of Co and As (Pokrovski et al. 2013). High Se/Ge of ~100 in porphyry pyrite is consistent with the pyrite precipitation from magmatic fluids, whereas Se/Ge <100 (Fig. 4A) observed in the epithermal pyrite suggests a contribution of meteoric waters (Keith et al. 2022) as also revealed by fluid inclusion constraints at Maronia (Fig. 6). High intra-grain $\delta^{34}S$ variation of pyrite can be related to S isotope fractionation during phase separation due to preferential partitioning of ^{34}S into SO_4^{2-} during the oxidation of H_2S to SO_4^{2-} (Börner et al. 2022).

4.3 Magmatic-hydrothermal controls on Re enrichment

The extremely high Re content (Fig. 3) and the occurrence of distinct ReS_2 phases suggest an anomalous high Re budget for the magmatic-hydrothermal fluids at Maronia. This may be linked to the subduction of Re-rich sediments, such as phosphorites or shales, in the Oligocene in NE Greece. As Re is essentially insoluble in reduced fluids (Xiong et al. 2006) systematic decrease of fO_2 is a strong process inducing Re precipitation and saturation from the ore-forming fluids. The decrease in fO_2 at Maronia is visible by the change from magnetite-bearing to magnetite-free mineral assemblages from the potassic to the sericitic alteration zone, decreasing of W contents in molybdenite, and lower $\delta^{34}S$ in B-type veins induced by high SO_4/H_2S ratios of the fluids (Hutchison et al. 2020). The observed fluid temperatures suggest a possible Re solubility threshold between 350 to 400°C favouring formation of Re-rich molybdenite at temperature of ~400°C in B-type veins of the potassic alteration.

5 Conclusion

Vein and alteration mineralogy, trace element chemistry of hydrothermal quartz and pyrite as well as fluid inclusion microthermometry define the systematic fluid evolution and porphyry-epithermal transition at the exceptional Re-rich Maronia Cu-Mo ± Au porphyry-epithermal system. The Re enrichment in molybdenite in different paragenetic stages is favoured by high temperature (~400°C), oxidized fluids of the potassic alteration, whereas cooler (~350°C) fluids of the sericitic alteration result in lower Re contents. The rare occurrence of rheniite and the high Re content at Maronia compared to molybdenite from other porphyry systems globally suggest an exceptional high Re budget, which might be related to an enriched magmatic source induced by extensive sediment subduction in the Aegean region during the Oligocene.

Acknowledgements

This study was funded by project KE2395/21 (Priority Program DOME SPP 2238) of the Deutsche Forschungsgemeinschaft (DFG).

References

Barton, I.F.; Rathkopf, C.A.; Barton, M.D. (2020): Rhenium in molybdenite: a database approach to identifying geochemical controls on the distribution of a critical element. Mining, Metallurgy & Exploration 37, 21–37.

Bodnar, R.J.; Lecumberri-Sanchez, P.; Moncada, D.; Steele-MacInnis, M. (2014): 13.5–Fluid inclusions in hydrothermal ore deposits. Treatise on geochemistry. 2nd edn. Elsevier, Oxford 119, p. 142.

Börner, F.; Keith, M.; Buecker, J.L.; Voudouris, P.; Klemd, R.; Haase, K.M. et al. (2022): In-situ trace element and S isotope systematics in pyrite from three porphyry-epithermal prospects, Limnos Island, Greece. Frontiers in Earth Science, p. 1637.

Crowe, D.E.; Vaughan, R.G. (1996): Characterization and use of isotopically homogeneous standards for in situ laser microprobe analysis of 34 S/ 32 S ratios. American Mineralogist 81, 187–193.

Gilbert, S.E.; Danyushevsky, L.V.; Rodemann, T.; Shimizu, N.; Gurenko, A.; Meffre, S. et al. (2014): Optimisation of laser parameters for the analysis of sulphur isotopes in sulphide minerals by laser ablation ICP-MS. Journal of Analytical Atomic Spectrometry 29, 1042–1051.

Grandell, L.; Lehtilä, A.; Kivinen, M.; Koljonen, T.; Kihlman, S.; Lauri, L.S. (2016): Role of critical metals in the future markets of clean energy technologies. Renewable Energy 95, 53–62.

Hutchison, W.; Finch, A.A.; Boyce, A.J. (2020): The sulfur isotope evolution of magmatic-hydrothermal fluids: insights into ore-forming processes. Geochimica et Cosmochimica Acta 288, 176–198.

Keith, M.; Haase, K.M.; Chivas, A.R.; Klemd, R. (2022): Phase separation and fluid mixing revealed by trace element signatures in pyrite from porphyry systems. Geochimica et Cosmochimica Acta.

Melfos, V.; Voudouris, P.; Melfou, M.; Sánchez, M.G.; Papadopoulou, L.; Filippidis, A. et al. (2020): Mineralogical Constraints on the Potassic and Sodic-Calcic Hydrothermal Alteration and Vein-Type Mineralization of the Maronia Porphyry Cu-Mo±Re±Au Deposit in NE Greece. Minerals 10, p. 182.

Pokrovski, G.S.; Borisova, A.Y.; Bychkov, A.Y. (2013): Speciation and transport of metals and metalloids in geological vapors. Reviews in mineralogy and geochemistry 76, 165–218.

Rottier, B.; Casanova, V. (2021): Trace element composition of quartz from porphyry systems: a tracer of the mineralizing fluid evolution. Mineralium Deposita 56, 843–862.

Schaarschmidt, A.; Klemd, R.; Regelous, M.; Voudouris, P.C.; Melfos, V.; Haase, K.M. (2021): The formation of shoshonitic magma and its relationship to porphyry-type mineralisation: the Maronia pluton in NE Greece. Lithos 380, p. 105911.

Tabelin, C.B.; Park, I.; Phengsaart, T.; Jeon, S.; Villacorte-Tabelin, M.; Alonzo, D. et al. (2021): Copper and critical metals production from porphyry ores and E-wastes: A review of resource availability, processing/recycling challenges, socio-environmental aspects, and sustainability issues. Resources, Conservation and Recycling 170, p. 105610.

Xiong, Y.; Wood, S.; Kruszewski, J. (2006): Hydrothermal transport and deposition of rhenium under subcritical conditions revisited. Economic Geology 101, 471–478.

Evidence for a High-Level Porphyritic Intrusion Below the Sunnyside Epithermal Vein Deposit, Colorado

Mario Guzman [1,2], Thomas Monecke [2], T. James Reynolds [2,3], Thomas Casadevall [1]
[1]U.S. Geological Survey, Denver Federal Center, Denver, Colorado, USA
[2]Department of Geology and Geological Engineering, Colorado School of Mines, Golden, Colorado, USA
[3]FLUID INC., 1401 Wewatta Street #PH3, Denver, Colorado, USA

Abstract. High-temperature quartz veins were identified in drill core at ~600 m below the Sunnyside epithermal base and precious metal deposit in southwestern Colorado. The veins consist of early anhedral quartz that shows a bluish cathodoluminescence emission and hosts heterogenous silicate melt inclusions. The early quartz is overgrown by a later generation of quartz that exhibits euhedral terminations with oscillatory growth zones showing a bright pink to purple cathodoluminescence emission. Both types of quartz are crosscut by ubiquitous planes of vapor-rich inclusions and some hypersaline liquid inclusions. In addition, secondary planes of intermediate-density inclusions occur. The petrographic characteristics of the two quartz types are similar to those in ‘A’ and ‘B’ veins encountered in shallow- and intermediate-depth porphyry deposits. The relationships at Sunnyside imply that these high-temperature veins formed from magmatic-hydrothermal fluids derived from an intrusion located not far below the lowest level of drilling. Sunnyside appears to be a rare example of an epithermal deposit that is directly connected to a high-level porphyritic intrusion.

1 Introduction

The Miocene Sunnyside intermediate-sulfidation epithermal deposit in the Eureka mining district in southwest Colorado comprises a set of near-vertical precious and base metal veins. Between 1902 and 1987, underground mining at Sunnyside yielded 800,000 ounces of gold and 14 million ounces of silver, making it one of the most prolific precious metal producers in Colorado (Bartos 1993).

Previous studies of the Sunnyside deposit largely focused on the epithermal mineralization occurring at 3,250-3,840 m above sea-level (Casadevall and Ohmoto 1977). However, exploration drill hole B-1 collared from the American Tunnel to a depth of 2,670 m above sea-level provides a unique opportunity to study the nature of veining up to ~600 m below the base of known epithermal mineralization.

This study is based on a petrographic and fluid inclusion study of the earliest quartz veins occurring at depth in the B-1 drill hole. The results demonstrate that early quartz veins formed from high-temperature magmatic-hydrothermal fluids, which suggests that the formation of the epithermal veins at Sunnyside deposit can be linked to a high-level porphyritic intrusion. This revises the earlier model by Casadevall and Ohmoto (1977), which inferred that the deposit formed from a hydrothermal system dominated by meteoric waters.

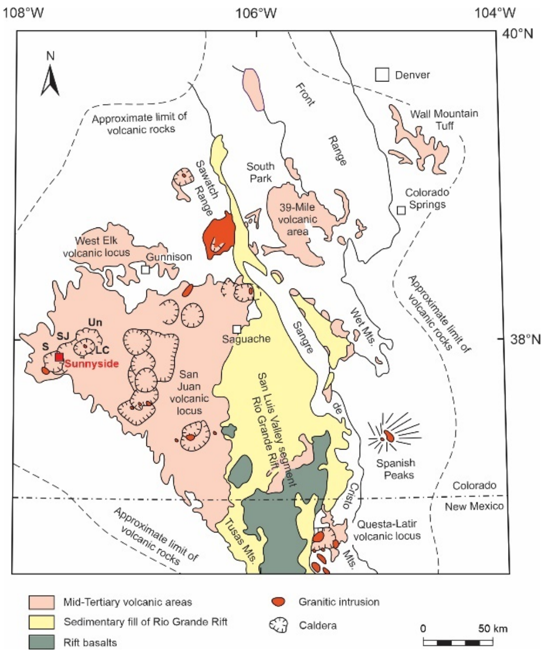

Figure 1. Geologic map of the Eocene to Oligocene Southern Rocky Mountain volcanic field in southwestern Colorado. The map also shows the locations of the Sunnyside deposit and major ignimbrite calderas. Un = Uncompahgre, LC = Lake City, SJ = San Juan, S = Silverton (modified from Lipman 2007).

2 Regional geology

The Sunnyside deposit is located within the San Juan Mountains of southwestern Colorado, an erosional remnant of the late Eocene to Oligocene Southern Rocky Mountain volcanic field that originally covered an area exceeding 100,000 km^2 stretching from southern Colorado to northern New Mexico (Fig. 1). Ignimbrite flareup-style continental arc volcanism developed on thick continental crust as the subducting Farallon oceanic plate rolled back from a flat configuration to a steeper dip (Lipman 2007).

The Sunnyside intermediate-sulfidation deposit is part of the Eureka mining district. The epithermal vein deposits in the district formed during and after the formation of the 28.35 Ma San Juan-Uncompahgre calderas and the younger, nested 27.6 Ma Silverton caldera (Lipman 2007). Mineralization at Sunnyside occurs within a dilatant zone between the Ross Basin and Sunnyside faults that crosscut the ring fractures produced during the collapse of the Silverton caldera.

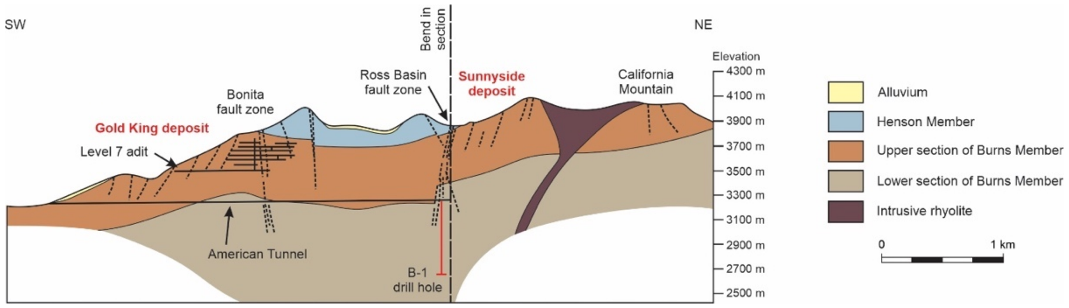

Figure 2. Cross section through the volcanic succession hosting the Sunnyside deposit (modified from Burbank and Luedke 1969).

At Sunnyside, porphyritic dark-grey or dark-green andesite or rhyodacite from the lower section of the Burns Member is recognized in deep drilling and exposures in the American Tunnel (Fig. 2). They are overlain by quartz latite lavas with minor intercalated tuffaceous deposits and flow breccias that comprise the upper section of the Burns Member, which is the main host of epithermal veins at Sunnyside (Casadevall and Ohmoto 1977). The volcanic rocks of the Burns Member are overlain by pyroxene-phyric andesite lavas of the ~28.3 Ma Henson Member (Fig. 2). These lavas outcrop extensively on the surface (Casadevall and Ohmoto 1977).

The lower part of the volcanic succession hosting the Sunnyside deposit has been affected by pervasive quartz-sericite alteration. The quartz-sericite alteration gradually changes into a propylitic alteration assemblage upwards (Casadevall and Ohmoto 1977).

3 Materials and methods

Representative vein samples were collected from drill core B-1 (Fig. 2), which is now located at the Core Research Center of the U.S. Geological Survey. Doubly polished 80-µm-thick sections were prepared. These were studied in transmitted and reflected light to document vein textures and paragenetic relationships. Optical cathodoluminescence (CL) microscopy was performed on the thick sections using an HC5-LM hot-cathode CL microscope by Lumic Special Microscopes, Germany. The instrument was operated at 14 kV with a current density of ~10 µA mm^{-2}. Colour images were acquired using a high-sensitivity, Teledyne Lumenera Infinity 5-5 digital camera.

As fluid inclusions in quartz formed in the porphyry environment can be subjected to post-entrapment modification (Sun et al. 2021; Audétat 2022), microthermometry was conducted only on secondary assemblages of intermediate-density fluid inclusions that showed consistent liquid to vapor ratios. A procedure outlined in Goldstein and Reynolds (1994) was employed to identify the inclusion assemblage with the highest homogenization temperature (bracketed to a 5°C interval) in a given sample, which involved making a measurement and then scanning the sample identifying other assemblages where bubbles had not yet homogenized until finally no other higher homogenization temperatures were measured. The microthermometric investigations were performed using a FLUID INC.-adapted U.S. Geological Survey gas-flow heating and freezing stage.

4 Petrography of deep veins

Drill core B-1 contains abundant narrow veinlets composed of vitreous, white or light grey quartz at depths of 510-585 m below the Sunnyside deposit (Fig. 3a). Microscopically, most of the quartz in these veins is anhedral, with individual grains ranging up to 200 µm in size (Fig. 3b). The quartz exhibits a dark blue CL emission (Fig. 3c). Locally, the anhedral quartz grains are overgrown by quartz forming euhedral crystal terminations. These later quartz overgrowths exhibit oscillatory growth zoning and are characterized by a bright pink or purple CL emission (Fig. 3c). Chalcopyrite and pyrite are paragenetically late forming ribbons or coatings along late fractures that that crosscut the quartz. Contacts between the sulphides and both types of quartz are irregular or scalloped at the microscale (Fig. 3b, c).

The early anhedral quartz in the deep veins has unique fluid inclusion characteristics. The quartz contains abundant secondary fluid inclusions forming trails having a wispy appearance but lacks primary fluid inclusions defining growth zones (Fig. 3d). The fluid inclusion assemblages are dominated by vapor-rich fluid inclusions although hypersaline liquid inclusions also occur. Many fluid inclusions in the quartz have been affected by post-entrapment modification. These fluid inclusions have irregular shapes and exhibit variations in the vapor to liquid volumetric proportions within individual assemblages. In many cases, microcracks or planar arrays of neonate inclusions radiate outward from the inclusions (Fig. 3e). The early anhedral quartz also contains heterogeneous silicate melt inclusions. These typically consist of vapor bubbles deformed by unknown minerals filling the inclusions (Fig. 3f).

The euhedral quartz overgrowths on the earlier anhedral quartz grains are largely devoid of fluid inclusions (Fig. 4a). Secondary assemblages of inter mediate-density fluid inclusions (Fig. 4b), hypersaline liquid inclusions (Fig, 4c), and vapor-rich

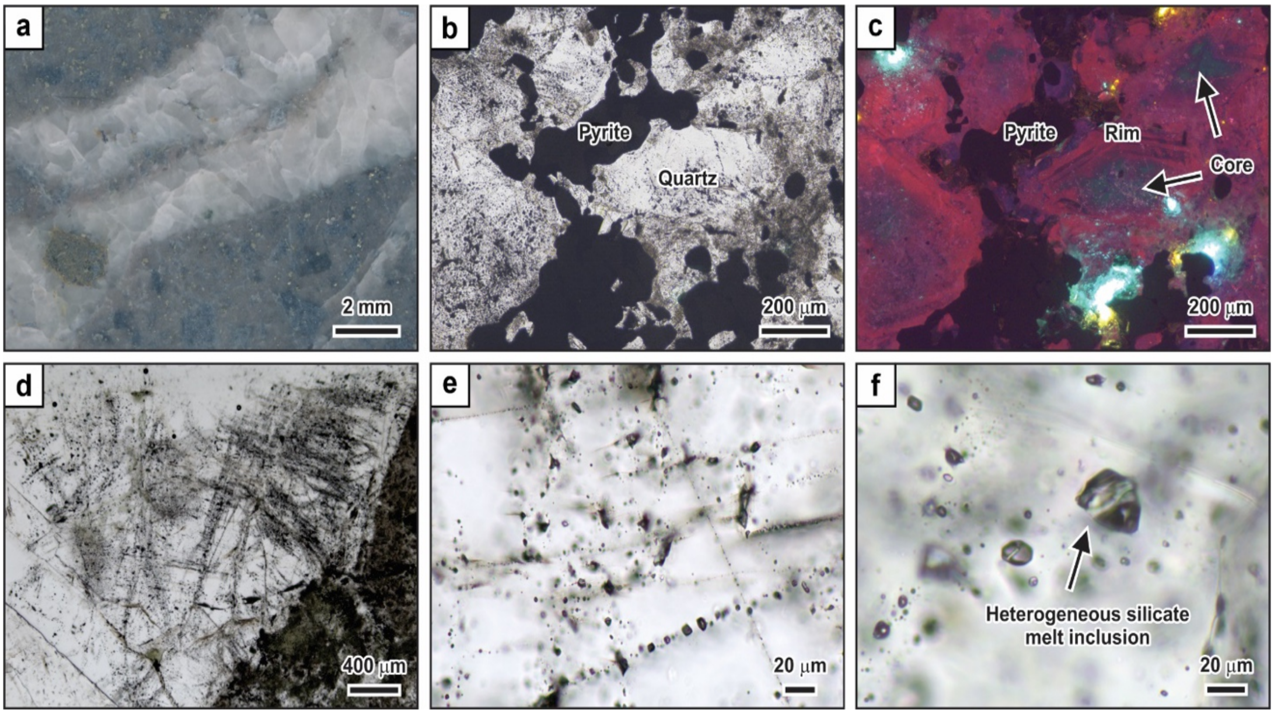

Figure 3. Microtextures and fluid inclusion inventory of high-temperature quartz from a deep drill hole at the Sunnyside deposit, Colorado. **a** Light grey quartz vein hosted by quartz latite. Sample V244-1674 (drill hole depth of 510 m). **b** Anhedral and granular quartz in a light grey quartz vein. Sample V244-1919 (drill hole depth of 585 m) **c** Corresponding optical cathodoluminescence image. The cores of the grains show a dark blue cathodoluminescence colour whereas the outer growth zones are banded and dark pink and purple. **d** Anhedral quartz grain containing ubiquitous healed microfractures defined by secondary inclusions. Sample V244-1674 (drill hole depth of 510 m). **e** Arrays of fluid inclusions that have been affected by post-entrapment modification. The fluid inclusions are highly irregular in shape, commonly with microcracks extending outward from the dark inclusions. Sample V244-1674 (drill hole depth of 510 m). **f** Heterogenous silicate melt inclusion in an anhedral quartz grain. Sample V244-1674 (drill hole depth of 510 m).

inclusions (Fig. 4a-c) that show no visual evidence of post-entrapment modification locally crosscut both quartz types. Heterogeneous silicate melt inclusions are not present in the clear quartz overgrowths. The highest homogenization temperature (380–385°C) for an intermediate-density, secondary fluid inclusion assemblage was measured in sample V244-1674 at a drill hole depth of 513 m. The assemblage has a salinity of 2.4 wt% NaCl equiv.

5 Discussion and conclusions

The petrographic evidence suggests that the quartz veins deep in the B-1 exploration drill hole below the Sunnyside deposit are similar to high-temperature ‘A’ veins in shallow- to intermediate-depth porphyry Cu deposits (Monecke et al. 2018). Quartz precipitation occurred in the two-phase field of the H_2O-NaCl system as the early quartz contains abundant vapor-rich fluid inclusions in addition to some hypersaline liquid inclusions, as originally noted by Casadevall and Ohmoto (1977). The presence of heterogeneous silicate melt inclusions suggests that that the quartz could have formed at temperatures as high as $\gtrsim$600°C (cf. Rottier et al. 2016). Formation of the deep veins from such high-temperature magmatic-hydrothermal fluids implies the presence of a high-level porphyritic intrusion below Sunnyside.

Quartz formation at high temperatures in the deep veins at Sunnyside took place at lithostatic conditions as the volcanic wall rocks were likely heated within the contact metamorphic aureole of the inferred high-level porphyritic intrusion. The ductile nature of the host rocks at these temperatures would have prevented the formation of a fracture network connected to the surface and the establishment of hydrostatic pressure conditions. However, after the formation of the anhedral quartz containing the heterogeneous silicate melt inclusions, the isotherms surrounding the high-level porphyritic intrusion must have retracted to depth. The fluid inclusion inventory of the anhedral quartz in the high-temperature veins was affected by post-entrapment modification due to the significant pressure differential (cf. Sterner and Bodnar 1989) caused by the change from lithostatic to hydrostatic conditions. Secondary fluid inclusion assemblages crosscutting the euhedral quartz overgrowths, which is equivalent to quartz in ‘B’ veins in porphyry deposits (cf. Monecke et al. 2018), have not been affected by post-entrapment modification. These inclusion assemblages containing vapor-rich and hypersaline liquid inclusions must, therefore, have been entrapped at hydrostatic conditions and likely never experienced significant pressure fluctuations after their formation. Quartz in ‘B’ veins in porphyry deposits forms close to the ductile-brittle transition at temperatures as low as ~400°C, which allows establishment of through-going fracture networks to surface (Monecke et al. 2018). Intermediate-density fluid inclusions hosted by the ‘B’ vein quartz were entrapped at a minimum temperature of 380–385°C and a minimum pressure of ~240 bar, which corresponds to a minimum depth of ~2400 m below the paleosurface at hydrostatic conditions.

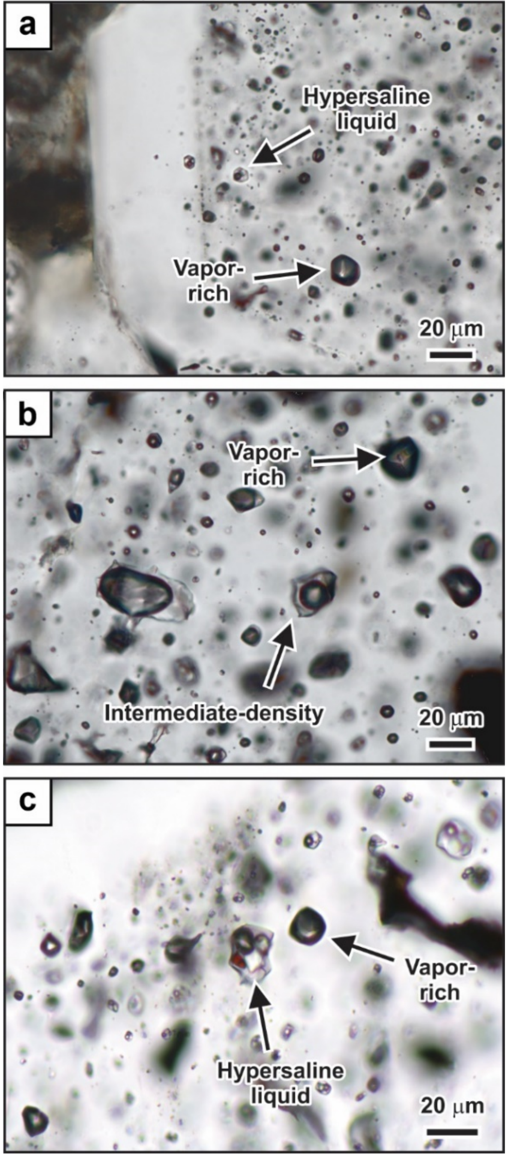

Figure 4. Fluid inclusion inventory of high-temperature quartz from a deep drill hole at the Sunnyside deposit, Colorado. **a** Euhedral quartz crystal with a clearer outer growth zone. The core contains abundant unmodified fluid inclusions, including hypersaline liquid and vapor-rich inclusions. **b** Intermediate-density and vapor-rich inclusions. **c** Hypersaline liquid and vapor-rich inclusions in the core of a euhedral quartz crystal. All images from sample V244-1684 (drill hole depth of 513 m).

It is envisaged here that the epithermal veins at Sunnyside are an integral part of the evolution of a magmatic-hydrothermal system driven by a high-level porphyritic intrusion. Intermediate-density fluids released from the intrusion ascended along major faults forming the epithermal veins at Sunnyside. As the magmatic-hydrothermal system waned, minor base metal veins similar to those found at the Sunnyside deposit telescoped onto the earlier high-temperature veins in the deep part of the B-1 drill core.

The deep drilling at Sunnyside provides important constraints on the depth of the porphyritic intrusion. The exploration drill hole B-1 extends to a depth of ~600 m below the Sunnyside deposit. The presence of the high-temperature veins suggests that a high-level intrusion is in close proximity. The situation at Sunnyside contrasts with other epithermal deposits in the San Juan Mountains. For instance, Creede is located above, and laterally offset from, a deeply seated intrusion that is located several kilometres below the base of the epithermal mineralization (Barton et al. 2000).

Acknowledgements

This research was supported by the U.S. Geological Survey Mineral Resources Program and the Society of Economic Geologist Hugh McKinstry Student Research Grant. E. Anderson and D. Yager of the USGS assisted with sampling and provided helpful insights on the mine geology. Any use of trade, firm, or product names is for descriptive purposes only and does not imply endorsement by the U.S. Government.

References

Audétat A (2022) A plea for more skepticism toward fluid inclusions: Part II. Homogenization via halite dissolution in brine inclusions from magmatic-hydrothermal systems is commonly the result of postentrapment modifications. Econ Geol, doi: 10.5382/econgeo.4974

Barton PB, Rye RO, Bethke PM (2000) Evolution of the Creede caldera and its relation to mineralization in the Creede mining district, Colorado. Geol Soc Amer Spec Pap 346:301–326

Bartos PJ (1993) Comparison of gold-rich and gold-poor quartz-base metal veins – Western San Juan Mountains, Colorado: The Mineral Point area as an example. SEG Newsl 15:1,6–11

Burbank WS, Luedke RG (1969) Geology and ore deposits of the Eureka and adjoining districts, San Juan Mountains, Colorado. US Geol Surv Prof Pap 535, 73 p.

Casadevall T, Ohmoto H (1977) Sunnyside mine, Eureka mining district, San Juan County, Colorado: Geochemistry of gold and base metal ore deposition in a volcanic environment. Econ Geol 72:1285–1320

Lipman PW (2007) Incremental assembly and prolonged consolidation of Cordilleran magma chambers: Evidence from the Southern Rocky Mountain volcanic field. Geosphere 3:42–70

Monecke T, Monecke J, Reynolds TJ, Tsuruoka S, Bennett MM, Skewes WB, Palin RM (2018) Quartz solubility in the H_2O-NaCl system: A framework for understanding vein formation in porphyry copper deposits. Econ Geol 113:1007–1046

Rottier B, Kouzmanov K, Bouvier AS, Baumgartner LP, Wälle M, Rezeau H, Bendezú R, Fontboté L (2016) Heterogeneous melt and hypersaline liquid inclusions in shallow porphyry type mineralization as markers of the magmatic-hydrothermal transition (Cerró de Pasco district, Peru). Chem Geol 447:93–116

Sterner SM, Bodnar RJ (1989) Synthetic fluid inclusions—VII. Re-equilibration of fluid inclusions in quartz during laboratory simulated metamorphic burial and uplift. J metamorph Geol 7:243–260

Sun M, Monecke T, Reynolds TJ, Yang Z (2021) Understanding the evolution of magmatic-hydrothermal systems based on microtextural relationships, fluid inclusion petrography, and quartz solubility constraints: Insights into the formation of the Yulong Cu-Mo porphyry deposit, eastern Tibetan Plateau, China. Mineral Deposita 56:823–842

Switch in magma source linked to an evolving geodynamic environment in the Farallon Negro Volcanic Complex, NW Argentina

Madeleine Ince[1], Steffen Hagemann[1], Marco Fiorentini[1], Tony Kemp[1], Nora Rubinstein[2]
[1]Centre for Exploration Targeting, School of Earth Sciences, University of Western Australia, Perth, Australia
[2]IGEBa, Departamento de Ciencias Geologicas, Facultad de Ciencias Exactas y Naturales, Buenos Aires, Argentina

Abstract. Constraining the source and processes contributing to porphyry Cu-Au formation on a district scale is fundamental for understanding the formation of Cu-Au mineralisation. The Farallon Negro Volcanic Complex contains the world-class Bajo de la Alumbrera porphyry Cu-Au deposit with weakly mineralised and barren porphyry intrusions, including El Durazno, San Lucas and Las Pampitas. Zircon trace element and isotope systematics are used to track the magmatic evolution of the Farallon Negro Volcanic Complex. The intrusions can be grouped into several stages. Stage 1 includes the El Durazno Au-Cu deposit (8.0 ± 0.3 Ma). El Durazno, whose emplacement was facilitated by localised extension, is from an enriched mantle-derived source (zircon $\delta^{18}O = 5.7 \pm 0.3‰$; zircon $\varepsilon Hf = -0.3 \pm 1.8$) with minor crustal assimilation. Stage 2 encompasses San Lucas (7.4 ± 0.1 to 7.3 ± 0.1 Ma), Las Pampitas (7.2 ± 0.2 to 7.0 ± 0.1 Ma) and Bajo de la Alumbrera (6.9 ± 0.1 to 6.8 ± 0.2 Ma). These display a mixed mantle-derived and supracrustal source (zircon $\delta^{18}O > 6.7‰$, zircon $\varepsilon Hf = < -2.2 \pm 1.0$) that homogenised in a lower-crustal MASH zone facilitated by regional compression. The combination of an enriched mantle source and accumulation in a lower-crustal MASH zone was favourable for Cu-Au mineralisation.

1 Introduction

Constraining the magma source is fundamental for understanding the petrogenetic processes leading to the genesis of giant porphyry Cu-Au deposits, especially in a gold-rich system (Park et al. 2021). The natural laboratory investigated here is the Farallon Negro Volcanic Complex (FNVC), which is a pre-eminent Cu-Au district in the Sierras Pampeanas of northwest Argentina (Fig. 1). It is a back-arc volcanic complex that hosts Cu-Au porphyry (Bajo de la Alumbrera, El Durazno, Agua Rica) and epithermal (Farallon Negro) deposits within an andesitic to dacitic volcanic complex (Proffett 2003). The FNVC contains other porphyritic intrusions that are of similar age and composition, but are significantly less mineralised, such as the San Lucas and Las Pampitas intrusions (Halter et al. 2004). Through comparison of zircon trace element and isotopic data from the Bajo de la Alumbrera porphyry intrusions to the San Lucas, Las Pampitas and El Durazno deposits, we assess the relationship between magma source and/or magma evolution and Cu-Au mineralisation.

2 Geological background

2.1 Geodynamic environment

The FNVC is located in the Sierras Pampeanas, which is in the northern part of the Pampean flat-slab segment (~27 to 33°S; Fig. 1), a section where the Nazca plate has been subducting under the South American plate at a dip of ~5-10° since 9 Ma (Kay and Mpodozis 2002). The shallow subduction angle can be attributed to the combination of coeval trench-ward motion of thick cratonic lithosphere and trench retreat during subduction of the Juan Fernandez Ridge (JFR; Fig. 1), as discussed in Manea et al (2012) and Yáñez et al (2001). This process caused thinning of the continental lithospheric mantle and reduction of the asthenospheric wedge, causing cessation of volcanism and hydration of the lithosphere (Kay et al. 1999).

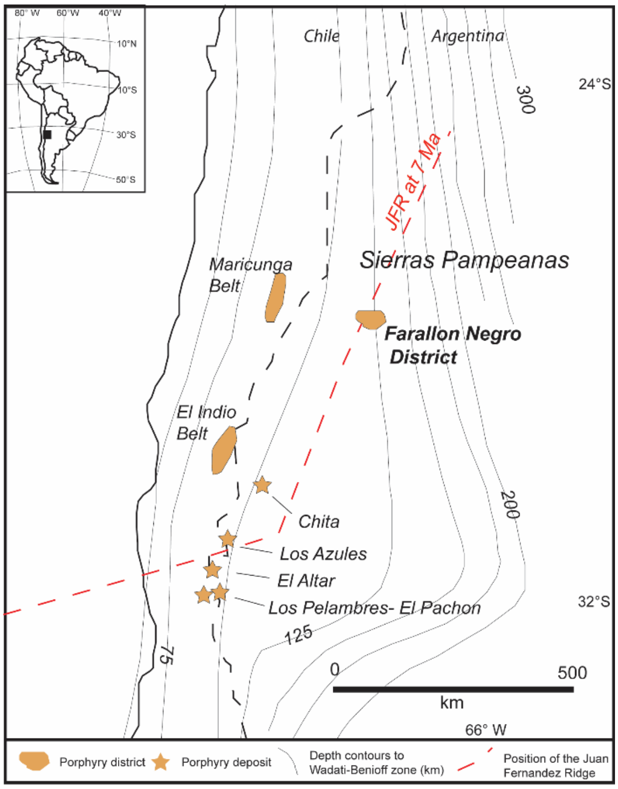

Figure 1. Location of the Farallon Negro Volcanic Complex and Miocene porphyry deposits. Light grey lines indicate depth to the Wadati-Benioff zone (Ramos et al. 2002) and the red dashed line indicates the position of the Juan Fernandez Ridge at 7 Ma (Yáñez et al. 2001).

2.2 Local geology and sample selection

Magmatism in the FNVC occurred from ~9.7 to 6 Ma (Ar-Ar hornblende and U-Pb zircon dating), broadly shifting from andesitic to dacitic in nature (Halter et al. 2004; Buret et al. 2016). The El Durazno porphyry intrusion was emplaced during the early stage of magmatism, and the Bajo de la Alumbrera, Las Pampitas and San Lucas systems later, from 7.3 to 6.0 Ma (Buret et al. 2016). The Bajo de la Alumbrera system comprises a stock of dacitic porphyries (intrusions P2, EP3, LP3, P4) intruding the surrounding basaltic andesite and andesite units (Fig. 3A). The main mineralizing event associated with dacitic porphyries P2 and EP3 has been previously dated between 7.22 ± 0.02 and 7.13 ± 0.02 Ma (zircon U-Pb CA-ID-TIMS; Buret et al. 2016). The grade of this deposit is 767 Mt @ 0.51% Cu and 0.64 g/t Au (Rubinstein et al. 2021).

The San Lucas porphyry is located ~6 km to the southeast of the Bajo de la Alumbrera deposit and largely comprises a rhyodacitic porphyry stock intruding a diorite (Fig. 3b) (Alderete 1999). The highest grade is 0.26% Cu, 0.35 g/t Au and 1.9 g/t Ag in the potassic alteration zone; however, mineralisation is considered uneconomic (Alderete 1999). Two samples were selected from San Lucas: a quartz andesite porphyry and a rhyodacite porphyry.

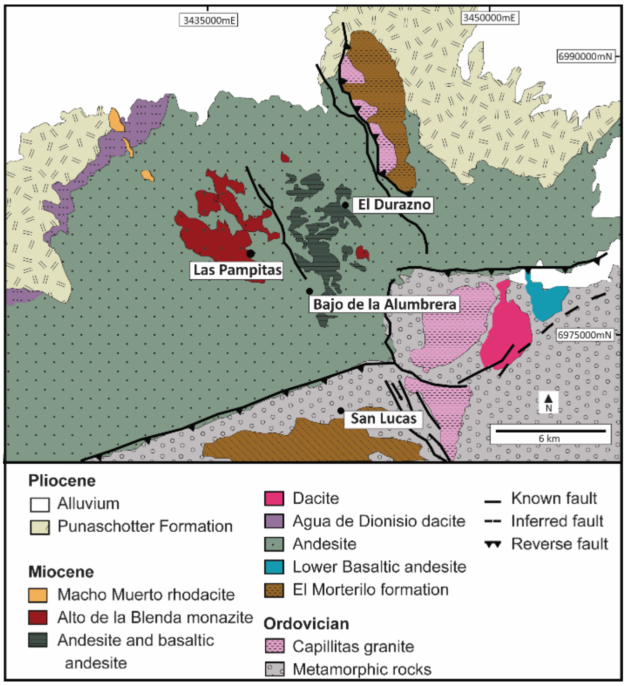

Figure 2. Geological map of the Farallon Negro Volcanic Complex showing those intrusions that were investigated in detail in this study. After Proffett (2003).

The Las Pampitas prospect is located ~4 km to the northwest of Bajo de la Alumbrera (Fig. 2) and has grades up to 0.13% Cu, 0.006% Mo and up to 1.06 g/t Au (average 0.07 g/t Au), and is considered uneconomic (Gutiérrez et al. 2006; Rubinstein et al. 2021). Three samples were analysed from Las Pampitas: a finer grained dacite porphyry, a coarser grained dacitic porphyry and a quartz andesite porphyry.

The El Durazno deposit is considered economically viable and contains 93 Mt at 0.15% Cu, 0.41 g/t Au (Glencore 2017). It was emplaced during the earlier stages of volcanism (Halter et al. 2004), with mineralisation hosted in a basaltic andesite porphyry (Fig. 2), which was analysed in this study.

3 Zircon U-Pb geochronology

The SHRIMP U-Pb ages generated in this study cannot resolve the within-deposit intrusive ages but can resolve the difference in ages between deposits. The El Durazno andesite porphyry is markedly older than the other intrusions, with an age of 8.0 ± 0.3 Ma (n=10, MSWD=1.3, 95% confidence). The San Lucas andesite porphyry and rhyodacite porphyries are ~0.4 my younger with ages of 7.4 ± 0.1 Ma (n=10, MSWD=1.0, 95% confidence) and 7.3 ± 0.1 Ma (n=10, MSWD=1.0, 95% confidence), respectively. The Las Pampitas dacitic porphyry intrusions have zircon U-Pb ages of 7.3 ± 0. 1 Ma (n=10; MSWD=1.5, 95% confidence) and 7.0 ± 0.1 Ma (n=10, MSWD=2.1, 95% confidence), respectively. The quartz andesite porphyry has a zircon U-Pb age of 7.2 ± 0.2 Ma (n=9, MSWD=2.6, 95% confidence). The Bajo de la Alumbrera P2 and EP3 intrusions have the same zircon U-Pb age of 6.9 ± 0.2 Ma (P2: n=13, MSWD=1.8; EP3: n=11, MSWD=1.8, 95% confidence). LP3 also has the same age with a smaller uncertainty of 6.9 ± 0.1 Ma (n=13, MSWD=0.6, 95% confidence). P4 is the youngest intrusion, with a zircon U-Pb age of 6.8 ± 0.2 Ma (n=10, MSWD=0.6, 95% confidence).

These data can be combined with U-Pb ages of Halter et al. (2004), Borba et al. (2016) and Buret et al. (2016) to define three key stages of magmatism in the FNVC: (1) 9.5 to 8.0 Ma, (2) 7.5 to 6.5 Ma, and (3) 6.5 to 5 Ma (Fig. 3).

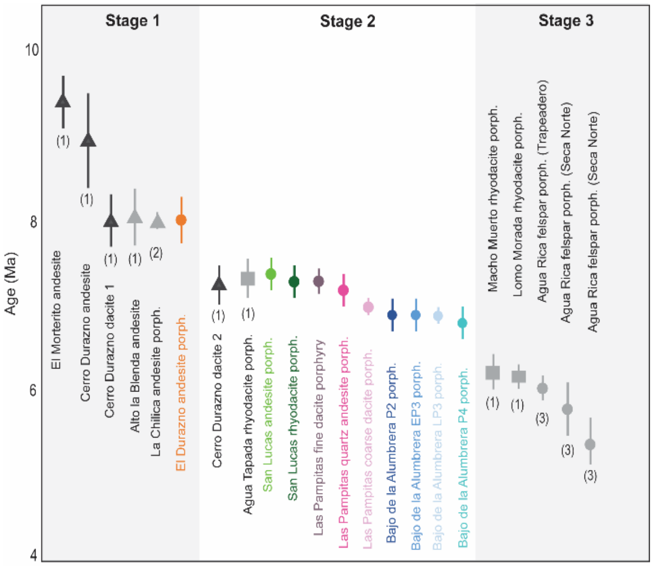

Figure 3. Summary of geochronological data from this study and the literature. Error bars are plotted at 95% confidence. Circles indicate ^{238}U-^{206}Pb ages, triangles ^{40}Ar-^{39}Ar biotite ages and squares $^{40}Ar/^{39}Ar$ hornblende

ages. Sources: (1) Halter et al. (2004), (2) Sasso (1997), and(3) Borba et al. (2020). Coloured points are from this study.

4 Magma source linked to geodynamic environment

4.1 Stage 1 magmatism (9.5 – 8.0 Ma)

The first stage of magmatism was primarily extrusive, basaltic to andesitic, and occurred during a period of localised extension (Halter et al. 2004).

The El Durazno intrusion formed at the end of stage 1 magmatism and was preceded by andesitic and basaltic lava flows and intrusions (Fig. 2). These units are hydrous (Halter et al. 2004). There is no trend towards a silicic composition over time as would be expected during fractional crystallisation, so therefore it is interpreted that a long-lived magma chamber was not established during this stage (Halter et al. 2005). Emplacement of El Durazno was facilitated by localised extension (Halter et al. 2004). The El Durazno porphyry has a zircon $\delta^{18}O$ signature of 5.7 ± 0.1‰ and εHf value of -0.3 ± 0.6 (2 SD, Fig. 4). The $\delta^{18}O$ value is consistent with a mantle-derived source (Valley et al. 2005). The εHf value is lower than those of ocean island basalt and mid ocean ridge basalts, which are generally above εHf = +5 (Janney et al. 2005), indicating the presence of a crustal component in the El Durazno magma. Contamination of magma source in the mantle can decrease the $^{176}Hf/^{177}Hf$ ratio, but may not shift the O isotope signature (Roberts et al. 2013). Based on the subduction-zone tectonic setting, the source was likely to be mantle wedge that was recently contaminated by subducted crust and sediments (Chauvel et al. 2009). This may also include a contribution from sub-continental lithospheric mantle and/or minor assimilation of continental crust during the ascent of the magma.

4.2 Stages 2 and 3 magmatism (7.5 to 5 Ma)

The second stage of magmatism was mostly intrusive and is defined by intermediate to felsic magmatism. This period encompasses the San Lucas, Las Pampitas and Bajo de la Alumbrera intrusions (Fig. 3). Zircon crystals from all intrusions have an initial εHf of < - 2.2 and $\delta^{18}O$ of > 6.7 ‰ (Fig. 4), indicative of an older supracrustal component in the source melt (Hawkesworth and Kemp 2006). Because of the distinctly elevated $\delta^{18}O$ values, it is likely that this supracrustal component was introduced in the crust rather than in the metasomatized mantle (Hawkesworth and Kemp 2006), perhaps in a lower crustal MASH zone (Hildreth and Moorbath 1988). The Agua Rica porphyry intrusions (stage 3 magmatism), to the south-east of Bajo de la Alumbrera, are interpreted as having the same source as Bajo de la Alumbrera, with a greater degree of crustal contamination (Borba et al. 2016).

Stages 2 and 3 of magmatism are likely a mix of stage 1 magmatism (mantle-derived) and a supracrustal component incorporated due to stalling of the magmas in the lower crust. The onset of regional transpression, linked to the peak of flat slab subduction at ~ 8 Ma (Kay and Mpodozis 2002), likely stalled the ascent of the mantle-derived magma, resulting in pooling in a lower crustal MASH zone, and mixing with felsic crust. It is suggested that this process in the lower-crustal MASH zone facilitated the build-up of volatiles and metals (Cu).

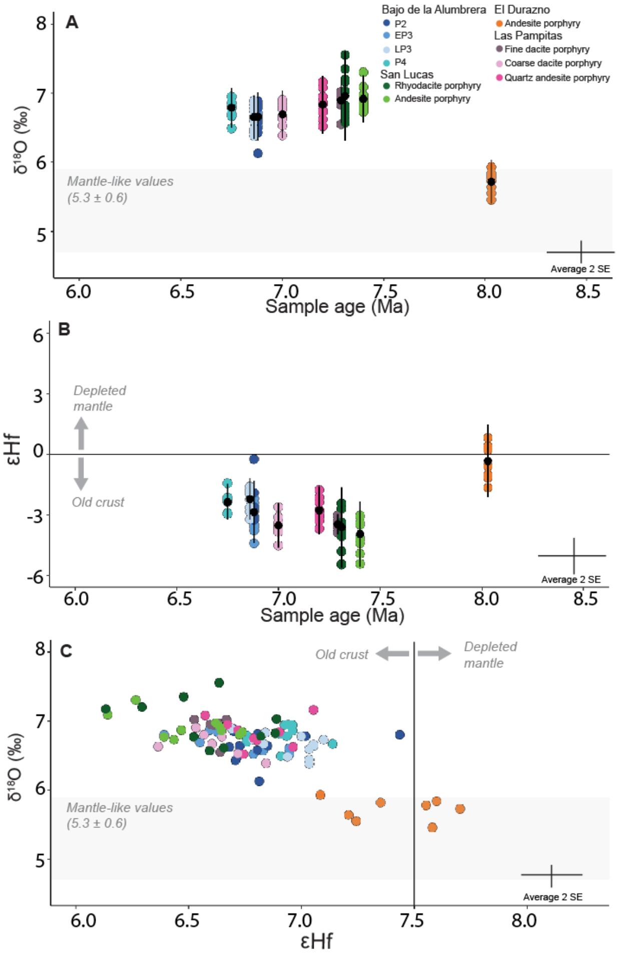

Figure 4. A: Zircon εHf vs sample age. Black bars indicate mean and 2 standard deviations. **B:** Zircon $\delta^{18}O$ vs εHf. Mantle-like oxygen value is after Valley et al. (2005). Average error bars are 2 standard errors (2 SE) of each spot.

5 Conclusion

Zircon Lu-Hf and O isotopic data record a switch in magma source between stage 1 and stage 2. The earlier magmatism of the FNVC, represented by the El Durazno porphyry, has a mantle source with minor crustal input, with magma ascent facilitated by localised extension (Halter et al. 2004). The early Cu-Au mineralisation of El Durazno indicates a mantle component with enrichment in Cu and Au. After ~8 Ma, the stalling of this magma in a lower crustal MASH zone and mixing with supracrustal material led to the accumulation of S, Cu and volatiles in the magma, with eventual sulfur saturation and exsolution of volatiles leading to porphyry Cu-Au mineralisation at higher crustal levels. The combination of an enriched magma and favourable tectonic environment likely led to Cu-Au mineralisation at Bajo de la Alumbrera.

Acknowledgements

The authors would like to acknowledge the Centre for Microscopy, Characterisation and Analysis (CMCA) at UWA, where O isotope analysis and SEM CL imaging were undertaken and the John de Laeter Centre, Curtin University, where U-Pb zircon analyses were undertaken. We would like to acknowledge staff at Minera Alumbrera and YMAD for field support and technical support in collecting samples.

References

Alderete MC (1999) Bajo de San Lucas, Catamarca In: Zappettini EO (ed) Recursos Minerales de la Republica Argentina. Instituto de Geologia y Recursos Minerales SEGEMAR, Buenos Aires, pp 1471-1473.

Borba ML, Chemale F, Kawashita K, Takehara L, Babinski M, Bruckman M (2016) The Bajo de la Alumbrera and Agua Rica Cu–Au (Mo) porphyry deposits of Argentina: Genetic constraints on ore formation and sources based on isotope signatures. Ore Geology Reviews 75:116-124. doi: https://doi.org/10.1016/j.oregeorev.2015.12.010.

Borba ML, Tassinari CCG, Kirk J, Ruiz J (2020) Ages and isotope evolution of the Agua Rica Cu-Au porphyry-epithermal deposit, NW Argentina. Ore Geology Reviews 119:103395. doi: https://doi.org/10.1016/j.oregeorev.2020.103395.

Buret Y, von Quadt A, Heinrich C, Selby D, Wälle M, Peytcheva I (2016) From a long-lived upper-crustal magma chamber to rapid porphyry copper emplacement: Reading the geochemistry of zircon crystals at Bajo de la Alumbrera (NW Argentina). Earth and Planetary Science Letters 450:120-131. doi: https://doi.org/10.1016/j.epsl.2016.06.017.

Glencore (2017) Resources and reserves as at 31 December 2017.

Gutiérrez AA, Chong GD, Espinoza SR (2006) Exposures levels of the deposits of the Agua de Dionisio (YMAD) mining district, Catamarca. Revista de la Asociacion Geologica Argentina 61:269-278.

Halter W, Bain N, Becker K, Heinrich C, Landtwing M, VonQuadt A, Clark A, Sasso A, Bissig T, Tosdal R (2004) From andesitic volcanism to the formation of a porphyry Cu-Au mineralizing magma chamber: The Farallón Negro Volcanic Complex, northwestern Argentina. Journal of Volcanology and Geothermal Research 136:1-30. doi: 10.1016/j.jvolgeores.2004.03.007.

Halter WE, Heinrich CA, Pettke T (2005) Magma evolution and the formation of porphyry Cu–Au ore fluids: evidence from silicate and sulfide melt inclusions. Mineralium Deposita 39:845-863. doi: 10.1007/s00126-004-0457-5.

Hawkesworth CJ, Kemp AIS (2006) Using hafnium and oxygen isotopes in zircons to unravel the record of crustal evolution. Chemical Geology 226:144-162.

Hildreth W, Moorbath S (1988) Crustal contributions to arc magmatism in the Andes of Central Chile. Contributions to Mineralogy and Petrology 98:455-489. doi: 10.1007/BF00372365.

Janney PE, Le Roex AP, Carlson RW (2005) Hafnium Isotope and Trace Element Constraints on the Nature of Mantle Heterogeneity beneath the Central Southwest Indian Ridge (13°E to 47°E). Journal of Petrology 46:2427-2464. doi: 10.1093/petrology/egi060.

Kay S, Mpodozis C (2002) Magmatism as a probe of Neogene shallowing of the Nazca Plate beneath the modern Chilean flat-slab. Journal of South American Earth Sciences 15:39-57. doi: 10.1016/S0895-9811(02)00005-6.

Kay SM, Mpodozis C, Coira B (1999) Neogene Magmatism, Tectonism, and Mineral Deposits of the Central Ande (22° to 33° S Latitude) In: Skinner BJ (ed) Geology and Ore Deposits of the Central Andes. Society of Economic Geologists, pp 0.

Manea vc, Perez-Gussinye M, Manea M (2012) Chilean flat slab subduction controlled by overriding plate thickness and trench rollback. Geology 40:35-38. doi: 10.1130/G32543.1.

Park J-W, Campbell IH, Chiaradia M, Hao H, Lee C-T (2021) Crustal magmatic controls on the formation of porphyry copper deposits. Nature Reviews Earth & Environment 2:542-557. doi: 10.1038/s43017-021-00182-8.

Proffett J (2003) Geology of the Bajo de la Alumbrera Porphyry Copper-Gold Deposit, Argentina. Economic Geology 98:1535-1574. doi: 10.2113/98.8.1535.

Ramos V, Cristallini E, Perez D (2002) The Pampean flat-slab of the Central Andes. Journal of South American Earth Sciences 15:59-78. doi: 10.1016/S0895-9811(02)00006-8.

Rubinstein NA, Zappettini EO, Gómez ALR (2021) Porphyry CU deposits in the Central Andes of Argentina: An overview. Journal of South American Earth Sciences 112:103543. doi: https://doi.org/10.1016/j.jsames.2021.103543.

Sasso A (1997) Geological evolution and metallogenetic relationships of the Farallon Negro Volcanic Complex, NW Argentina. . Queen's University, Kingston
pp 842.

Valley JW, Lackey JS, Cavosie AJ, Clechenko CC, Spicuzza MJ, Basei MAS, Bindeman IN, Ferreira VP, Sial AN, King EM, Peck WH, Sinha AK, Wei CS (2005) 4.4 billion years of crustal maturation: oxygen isotope ratios of magmatic zircon
Contributions to Mineralogy and Petrology. doi: 10.1007/s00410-005-0025-8.

Yáñez GA, Ranero CR, von Huene R, Díaz J (2001) Magnetic anomaly interpretation across the southern central Andes (32°–34°S): The role of the Juan Fernández Ridge in the late Tertiary evolution of the margin. Journal of Geophysical Research: Solid Earth 106:6325-6345. doi: https://doi.org/10.1029/2000JB900337.

Unravelling Hypogene to Supergene Processes in a Concealed Porphyry: Insights from the Santa Cruz Copper Deposit, Arizona, USA

Simon Kocher[1], Ben M. Frieman[1], Thomas Monecke[1], Holly J. Stein[2,3], Christopher J. Seligman[4], Harry Hanneman[4], Shawn Vandekerkhove[4]
[1]Center to Advance the Science of Exploration to Reclamation in Mining, Department of Geology and Geological Engineering, Colorado School of Mines, Golden, CO, USA
[2]AIRIE, Applied Isotope Research for Industry and the Environment, Fort Collins, CO, USA
[3]Department of Geosciences, University of Oslo, Oslo, Norway
[4]Ivanhoe Electric, Casa Grande, AZ, USA

Abstract. An increasing demand for copper and lack of deposits exposed at surface force exploration to focus on targets at increasing depth or under deep cover. Recent exploration drilling at the Santa Cruz deposit in the southern Basin and Range Province has provided an opportunity to study a well-preserved example of a Laramide-aged hypogene deposit with a supergene enriched domain under up to 1000 m of post-mineral sedimentary cover. Paragenetic investigations are combined with Re-Os dating of molybdenite samples that establish new perspectives on emplacement and enrichment processes of the deposit. These results are compared to regional Re-Os data to establish a distinct Laramide-aged spatial trend in the distribution of deposits in the southern Arizona copper porphyry district. This comparison defines favourable temporal windows for deposit formation at ~75–70 Ma, ~65 Ma, and 60–55 Ma that likely relate to overriding tectonic controls.

1 Introduction

Porphyry deposits are the primary source of copper for the global economy. The discovery and development of deeper and/or concealed porphyry deposits will be critical to support green energy infrastructure in the 21st century and beyond. These deposits are typically associated with intermediate to felsic subvolcanic intrusions located in magmatic arc settings (Sillitoe 2010). Hypogene mineralisation in porphyry deposits comprises stockwork-hosted and disseminated sulphides that form large volumes of low-grade ore. However, supergene enrichment processes can lead to a significant increase in relative ore grade (Sillitoe 2005).

The Santa Cruz deposit is located 11 km west of Casa Grande, and approximately 9 km southwest of the previously mined Sacaton deposit in southern Arizona (Fig. 1). It was discovered in 1974 but not put into production due to low copper prices at the time.

The Santa Cruz deposit is primarily hosted by the ~1450–1350 Ma Oracle Granite (Tosdal and Wooden 2015) and minor diabase sills and dykes that are ~1100 Ma (Banks et al. 1972). Hypogene mineralisation is associated with Laramide aged quartz monzonite porphyry intrusions (Schmidt 1971; Vikre et al. 2014). Subsequently, the deposit underwent an extended period of erosion and oxidation, leading to the formation of a supergene enrichment blanket (Cook 1994; Kreis 1995). Basin and Range extension is marked by basaltic magmatism forming diatreme-like structures and volcanic deposits (Vikre et al. 2014). Further extension and normal faulting dismembered the deposit into a series of fault blocks and led to the deposition of up to 1000 m of post-mineral sedimentary cover (Fig. 1). Based on recent estimates, the Santa Cruz deposit and related satellite zones contain 2.8 and 1.8 Mt total contained copper in indicated and inferred mineral resources, respectively (Nordmin Engineering 2023). Despite hosting significant resources, the age, structural framework, and a detailed understanding of the hypogene and supergene mineralisation are poorly constrained. This study includes paragenetic and geochronological results that further understanding of the emplacement and supergene enrichment processes recorded in the Santa Cruz deposit and establish when the deposit formed within the broader Arizona copper porphyry province.

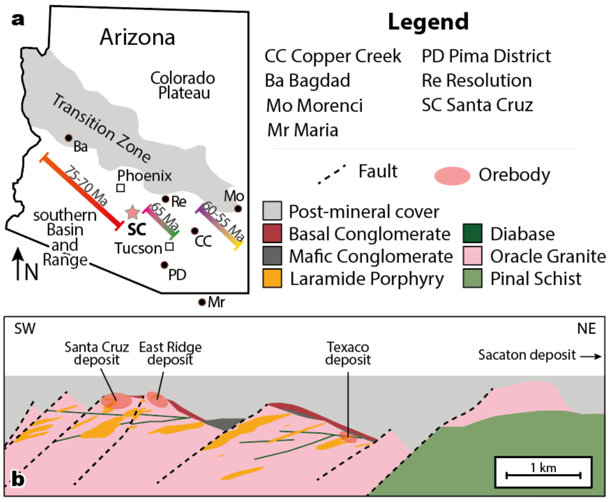

Figure 1. (a) Simplified regional map of Arizona showing the location of Santa Cruz and other major porphyry deposits discussed in the text. Age trends are derived from Re-Os dating (modified after Enders et al. 2006). (b) Schematic cross section through the Santa Cruz deposit (modified from Nordmin Engineering 2023).

2 Methodology

2.1 Optical petrography

Representative samples were collected of variably mineralised hypogene and supergene samples. From these, ~50 thin sections and polished resin blocks were prepared and examined in transmitted and reflected light, prior to scanning electron microscopy.

2.2 Geochronology

Four vein samples containing visible molybdenite were selected from the Santa Cruz and Texaco deposits for Re-Os geochronology at the newly re-established Applied Isotope Research for Industry and the Environment (AIRIE) laboratory following the procedures of Stein et al. (2001). Molybdenite was carefully separated, and the separates were equilibrated with a mixed Re-double Os spike using inverse *aqua regia* for sample digestion in a Carius tube. Isotopic ratios were measured by NTIMS (negative thermal ionisation mass spectrometry) on a Triton instrument.

3 Results

3.1 Hypogene and supergene mineralogy

Petrographic observations suggest the presence of at least three individual porphyry phases, based on mineralogical and textural characteristics. These are referred to as granodiorite porphyry, quartz latite porphyry, and latite porphyry.

Typical porphyry-style veins in the form of A, B, C, and D veins (Gustafson and Hunt 1975) are present in the porphyry dykes and to a much lesser extent in the Oracle Granite. Veins frequently show signs of reopening. Potassic alteration is observed in association with A and B veins, resulting in secondary, shreddy biotite, often replacing other mafic minerals, and minor K-feldspar. C veins are accompanied by chlorite alteration, primarily affecting earlier biotite. Sericite alteration is most strongly developed in halos surrounding D veins.

The hypogene assemblage consists of chalcopyrite and minor bornite hosted in C and reopened B veins as well as in disseminations associated with vein halos. The occurrence of molybdenite is limited to the margins of B veins where it forms coarser aggregates intergrown with quartz and/or fine-grained smears. Pyrite is primarily associated with D veins, forming discrete sulphide-filled fractures and disseminations.

Supergene mineralisation at Santa Cruz forms three distinct zones. The deepest zone is characterised by the replacement of hypogene chalcopyrite by covellite, bornite, and multiple other copper sulphide phases. At shallower depths the supergene assemblage comprises chalcocite and minor hematite partially or completely replacing pyrite. In the upper parts of the supergene enrichment blanket, the mineralogy is dominated by oxidised copper species, including abundant atacamite and chrysocolla.

3.2 Re-Os dating of molybdenite

The four molybdenite samples analysed yield highly precise dates that indicate molybdenite deposition at ~72–71 Ma. These analyses define a model age of 71.3 ± 1.4 Ma with an initial Os ratio of 0.2 (Fig. 2a). A weighted average for these four analyses yields a similar date of 71.6 ± 0.8 Ma (Fig. 2b).

In order to compare, the Santa Cruz Re-Os results are plotted with published molybdenite results for Arizona and northern Mexico, including the Bagdad, Resolution, Copper Creek, Pima District, Morenci, and Maria deposits (Figs. 1 and 2). Together these results define three temporally distinct episodes of hypogene porphyry copper mineralisation in the region. The Santa Cruz results are comparable to the Bagdad porphyry, which gives Re-Os dates of ~76 Ma and ~72 Ma (Barra et al. 2003). To the east, Re-Os dates for molybdenite from the Resolution porphyry deposit yield younger ages that cluster around ~65 Ma (Hehnke et al. 2012). Deposits in southeastern Arizona and along the US-Mexico border have relatively young Re-Os ages of ~60–55 Ma (McCandless and Ruiz 1993).

4 Discussion and preliminary synthesis

Paragenetic studies conducted on the hypogene mineralisation preserved within deeper portions of the Santa Cruz deposit indicate the presence of A, B, C, and D veins. Molybdenite is associated with early B veins formed at high temperatures whereas chalcopyrite and bornite are present in C veins and reopened earlier veins. The pyrite-rich D veins are consistently late and associated with pervasive sericite alteration. Supergene processes have resulted in significant enhancement of copper grades.

Re-Os dating indicates that the hypogene mineralisation at Santa Cruz was emplaced at ~71.5 Ma (Fig. 2). This date is similar to molybdenite deposition ages in the Bagdad deposit (Barra et al. 2003; Figs. 1 and 2), suggesting broadly contemporaneous formation of these deposits. However, these Re-Os dates are relatively old when compared to porphyry deposits to the east and southeast of Santa Cruz. For example, Re-Os dates for the Resolution deposit are ~65 Ma (Hehnke et al. 2012), while all other deposits to the southeast (Copper Creek, Morenci, Pima District, and Maria) yield younger dates of ~60–55 Ma (Figs. 1 and 2). This west-northwest to east-southeast trend was recognised by McCandless and Ruiz (1993), who suggested that differences in the age and thickness of Precambrian crust of Arizona may have controlled the timing of mineralisation, wherein older (>1700 Ma) crust was spatially associated with the 75–70 Ma deposits while younger (<1700 Ma) Precambrian

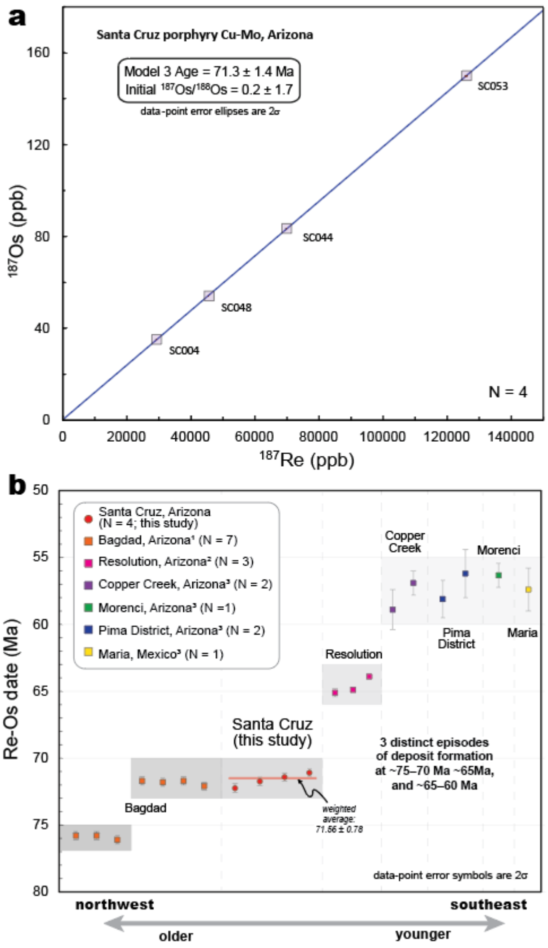

Figure 2. (a) Re-Os results for the Santa Cruz molybdenite samples shown as an isochron age for the four samples analysed. (b) Re-Os dates for molybdenite samples from Santa Cruz compared to Re-Os dates from other copper deposits in Arizona (1 = Barra et al. 2003; 2 = Hehnke et al. 2012; 3 = McCandless and Ruiz 1993).

basement is host to the younger deposits. However, the Santa Cruz deposit is hosted by the 1450–1350 Ma Oracle Granite, indicating that <1700 Ma Precambrian basement can also host ~75–70 Ma porphyry deposits. This observation, when combined with an intermediate age for the Resolution deposit of ~65 Ma (Hehnke et al. 2012), may indicate that subduction-related porphyry copper deposits migrated progressively to the southeast (present-day distribution) and the major episodes of mineralisation occurred at distinct temporal intervals of ~75–70 Ma, ~65 Ma, and 60–55 Ma (Fig. 2) that may broadly coincide with changes in the overriding plate kinematics such as a transition to flat-slab subduction, ridge-subduction and/or oceanic plateau subduction (Cooke et al. 2005).

Constraining Laramide-aged spatial and temporal trends in the formation of porphyry copper deposits is hampered by extensive, Tertiary-aged structural dismemberment within the Basin and Range Province. While this history complicates the interpretation of primary tectonic trends it also served to exhume and enrich many Arizona deposits through supergene processes. Understanding Tertiary modification of Laramide hypogene mineralisation is critical to assess the economic potential of these deposits, particularly in concealed deposits like Santa Cruz where the supergene enriched zone is well-preserved and is host to a large proportion of known resources.

Acknowledgements

This work was supported by the National Science Foundation and conducted within CASERM, a joint industry-university collaborative research centre between the Colorado School of Mines and Virginia Tech under award numbers 1822146 and 1822108.

References

Banks NG, Cornwall HR, Silberman ML, Creasey SC, Marvin RF (1972) Chronology of intrusion and ore deposition at Ray, Arizona: Part I, K-Ar ages. Econ Geol 67:864–878

Barra F, Ruiz J, Mathur R, Titley S (2003) A Re-Os study of sulfide minerals from the Bagdad porphyry Cu-Mo deposit, northern Arizona, USA. Mineral Deposita 38:585–596

Cook SS III (1994) The geologic history of supergene enrichment in the porphyry copper deposits of southwestern North America. PhD thesis, University of Arizona

Cooke DR, Hollings P, Walshe JL (2005) Giant porphyry deposits: Characteristics, distribution, and tectonic controls. Econ Geol 100:801–818

Enders MS, Knickerbocker C, Titley SR, Southam G (2006) The role of bacteria in the supergene environment of the Morenci porphyry copper deposit, Greenlee County, Arizona. Econ Geol 101:59-70

Gustafson LB, Hunt JP (1975) The porphyry copper deposit at El Salvador, Chile. Econ Geol 70:857–912

Hehnke C, Ballantyne G, Martin H, Hart W, Schwarz A, Stein H (2012) Geology and exploration progress at the Resolution porphyry Cu-Mo deposits, Arizona. SEG Spec Publ 16:147–166

Kreis HG (1995) Geology of the Santa Cruz porphyry copper deposit. Ariz Geol Soc Dig 20:364–365

McCandless TE, Ruiz J (1993) Rhenium-osmium evidence for regional mineralization in southwestern North America. Science 261:1282–1286

Nordmin Engineering (2023) Mineral resource estimate update and S-K 1300 technical report summary for the Santa Cruz, Texaco and East Ridge deposits, Arizona, USA. Internal report to Ivanhoe Electric Inc., 230 p. https://rb.gy/uzbjtg

Schmidt EH (1971) Belts of Laramide-age intrusive rocks and fissure veins in south central Arizona. Ariz Geol Soc Dig 9:61–69

Sillitoe RH (2005) Supergene oxidized and enriched porphyry copper and related deposits. In: Hedenquist JW, Thompson JFH, Goldfarb RJ, Richards.JP (eds) Economic Geology 100th Anniversary Volume. Society of Economic Geologists, Littleton, pp 723–768

Sillitoe RH (2010) Porphyry copper systems. Econ Geol 105:3–41

Stein HJ, Markey RJ, Morgan JW, Hannah JL, Scherstén A (2001) The remarkable Re-Os chronometer in molybdenite: How and why it works. Terra Nova 13:479−486

Tosdal RM, Wooden JL (2015) Construction of the Jurassic magmatic arc, southeast California and southwest Arizona. Geol Soc Amer Spec Pap 513:189–221

Vikre PG, Graybeal FT, Koutz FR (2014) Concealed basalt-matrix diatremes with Cu-Au-Ag-(Mo)-mineralized xenoliths, Santa Cruz porphyry Cu-(Mo) system, Pinal County, Arizona. Econ Geol 109:1271–1289

Texture, composition, alteration styles in the Permo-Triassic Pampa Elvira plutonic complex and the Eocene tonalite porphyry at the Gaby porphyry copper deposit, Chile

Luis Krampert[1], Kalin Kouzmanov[1], Alexandre Cugerone[1], Lluís Fontboté[1], Carolina Rodríguez[2], Rubén Pardo[2], Sergio Pichott Henríquez[2]
[1]Department of Earth Sciences, University of Geneva, 1205 Geneva, Switzerland
[2]CODELCO, Santiago, Chile

Abstract. In some porphyry copper deposits, the similarity between pre-, syn- and post-mineral intrusions in terms of texture and geochemistry is a known issue. This is also the case at the Gaby porphyry Cu deposit in Northern Chile. This study aims to find features to discriminate between the Permo-Triassic Pampa Elvira plutonic complex (PEPC) which is volumetrically the main host rock of the deposit, and the ore-related Eocene tonalite porphyry (TP). Various field and analytical methods have been applied to a drill hole in the district's center to properly characterize the two lithologies. Fieldwork (core logging, magnetic susceptibility), automated mineralogy (QEMSCAN), whole rock geochemistry, and electron microprobe are techniques used so far. They reveal important variations in texture, grain size distribution, mineralogy, and chemistry. Relative proportions between the major rock-forming minerals plagioclase, alkali feldspar, quartz, and biotite are contrasting between the magmatic units. The Eu anomaly and element ratios (especially Sr/Y and Zr/Hf) strongly differ between the two magmatic suites and in combination, these features allow discrimination. Chemical features of alteration minerals such as white mica, chlorite, and biotite (Fe enrichment in chlorite) do show significant variations between the units but need complementation with trace element data by LA-ICP-MS.

1 Introduction

Northern Chile is recognized for hosting numerous small to very large porphyry copper deposits (Zappettini et al. 2001). One of the giant deposits is Chuquicamata. Zentilli et al. (2018) reported that one fundamental challenge during the exploration of the deposit was the discrimination between "ore-carrying Eocene porphyries" and a Triassic granodiorite with similar textural and geochemical characteristics.

Despite the extended research that was carried out on the Chuquicamata cluster, only recently Zentilli et al. (2018) attempted to solve this issue with whole-rock analyses and presented geochemical tools to distinguish the Triassic granodiorite from the Eocene porphyry stocks in the area. Standard geochemical characterization methods for trace elements (e.g., Winchester and Floyd 1977) did not yield a clear separation. The only consistent geochemical difference found by Zentilli et al. (2018) was that the main Eocene–Oligocene porphyries carry relatively less Fe and Ni than the Triassic granodiorite.

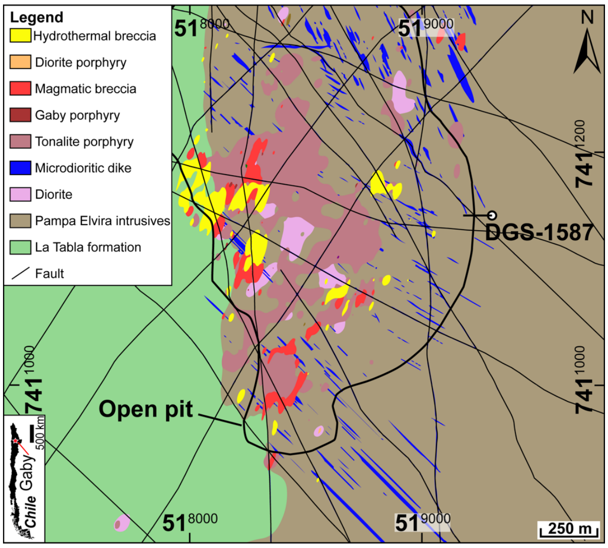

Figure 1. Simplified geological map of the Gaby district atan elevation of 2540 m.a.s.l. with an outline of the open pit. The location and trace of the drill hole DGS-1587 are marked (modified after Reygadas et al. 2023).

This study addresses a similar problem at the Gaby porphyry deposit, located around 120 km south of the Chuquicamata district. Here, the Permo-Triassic Pampa Elvira plutonic complex (PEPC) is one of the hosts for copper mineralization generated by Eocene porphyry intrusions (Dilles et al. 2000). The dominant composition found in the PEPC is granodiorite. Both lithologies are similar in texture and chemistry and have not yet been exhaustively investigated. This study uses magnetic susceptibility, bulk and mineral chemistry, and alteration styles to define criteria for differentiation and describe similarities between the PEPC and the tonalite porphyry (TP). The research focuses on part of a drill hole located in the center of the district (Figure 1), intercepting the contact between the two lithologies.

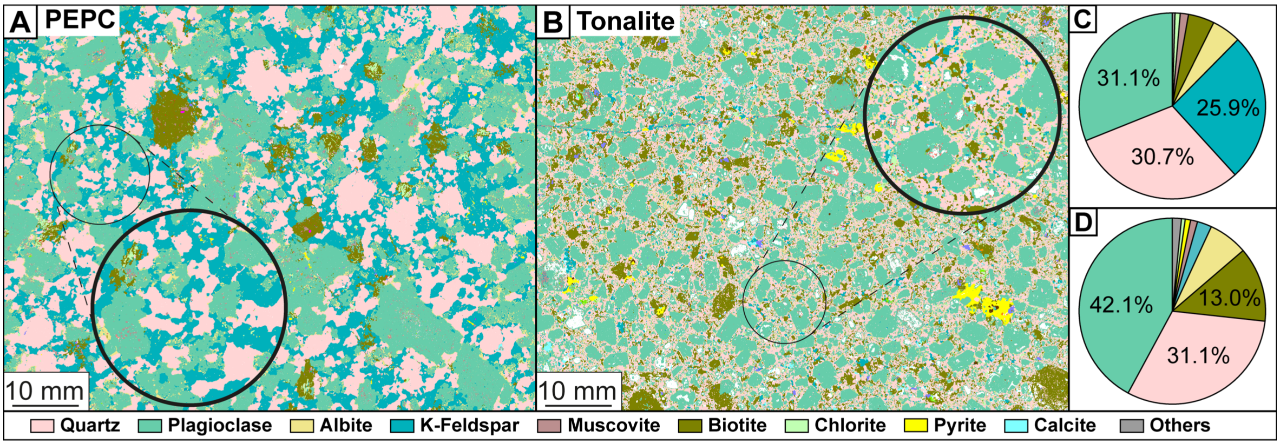

Figure 2. QEMSCAN maps of the two lithologies. **A** Non-mineralized sample of the PEPC. **B** Non-mineralized sample of the TP. **C** and **D** Pie charts of the area % of the selected samples in the PEPC (**A**) and in the TP (**B**). The low amount of alkali feldspar is demonstrated.

2 Methods

The analyzed samples (n=44) are mainly from a single drill hole (DGS-1587) in the center of the district intersecting the two main host lithologies, the PEPC and the TP. Geochemical and electron microprobe (EPMA) data are complemented with measurements from other drill holes in the vicinity of the Gaby open pit (Figure 1; Cugerone et al., this volume).

The magnetic susceptibility (MS) was recorded over the length of the drill core with a handheld magnetic susceptibility meter (KT-10). Measurements were taken in 50 cm intervals to increase the accuracy of the dataset.

Scanning electron microscopy–based automated mineralogy analysis (QEMSCAN) followed petrographic observations on thin sections. This method was used to generate mineral and elemental maps and define the relative mineral proportions on a thin-section scale.

Whole rock analyses of major and trace elements were performed by inductively coupled plasma atomic emission spectroscopy (ICP-AES) and by inductively coupled plasma mass spectroscopy (ICP-MS), respectively. As, Bi, Hg, In, Re, Sb, Se, Te, and Tl were measured with ICP-MS on an aqua regia solution and base metals by four acid digestion followed by ICP-AES. The results were filtered before using them in discrimination diagrams and strongly altered and mineralized samples were left out for these tasks.

White mica, chlorite, and biotite chemistry were studied with a JEOL JXA8200 SuperProbe EPMA at the University of Geneva. The following elements were measured: Si, Al, Ti, Fe, Ca, Mg, Na, K, Mn, Cr, Ba, and Cl. The results were normalized to 11 oxygen atoms per formula unit (apfu) for white mica and 28 apfu for chlorite.

Besides, X-ray diffraction analysis combined with short-wave infrared light spectroscopy was be applied to target alteration minerals. LA-ICP-MS will be used to supplement the EPMA data.

3 Geology of the deposit

Porphyry copper deposits in northern Chile including the Gaby deposit formed during the Andean cycle of magmatism in the area. The largest deposits were developed in a relatively short period of around 10 m.y. during the Eocene-Oligocene (Maksaev and Zentilli 1988), forming the Paleogene metallogenic belt (e.g., Piquer et al. 2021). An essential factor for the formation of large deposits is the Domeyko fault zone. Structures belonging to the latter are also present at Gaby, where they preferentially align the intrusive bodies NE-SW (Piquer et al. 2021).

The major host rocks at Gaby are the Permo-Triassic Pampa Elvira plutonic complex consisting mainly of the granodiorite (GD), intruded by the Eocene TP, and the Late Carboniferous–Early Permian (Gardeweg et al. 1994 in Niemeyer et al. 2008) volcano-sedimentary La Tabla formation to the west (Camus 2003). There are multiple Eocene porphyry intrusions recognized in the area, but the TP is volumetrically the most abundant (Dilles et al. 2000). All units show internal heterogeneity in texture and degree of alteration.

The focus herein lies on a comparison of the distinctive texture, alteration, and mineralization styles of the PEPC and the TP near the Gaby open pit.

4 Texture, mineralogy, and geochemistry of the PEPC and the TP

The Pampa Elvira intrusive body can be described as a light grey phaneritic and moderately porphyritic rock consisting of quartz, alkali feldspar, altered plagioclase, and biotite. The magnetic susceptibility (MS) is relatively low and strongly dependent on vein distribution and alteration styles. At the district and drill hole scale, the PEPC can be relatively heterogeneous. Plagioclase and alkali feldspar commonly present sodic alteration (albite). QEMSCAN analyses suggest that roughly twice as much albite is present in the PEPC than in the TP (Figure 2). Albite is present as a product of pervasive alteration and as vein alteration halos.

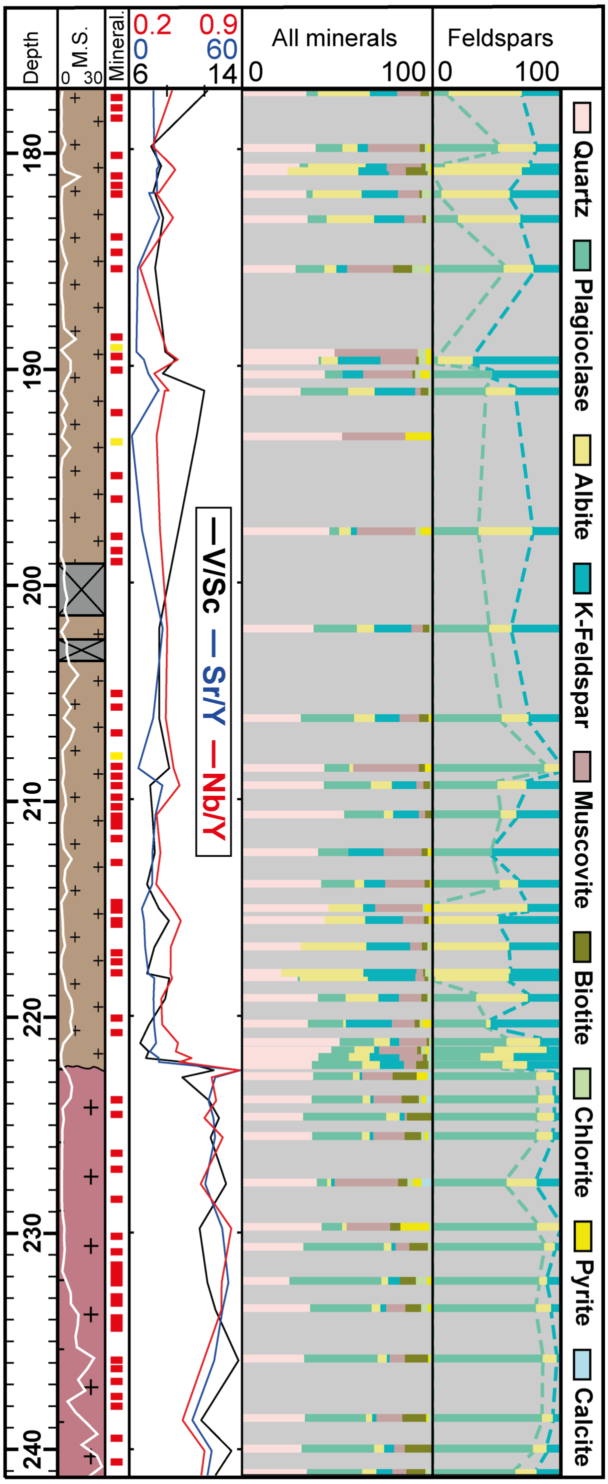

Figure 3. Drill log of DGS-1587 combining core logging with magnetic susceptibility data (MS in 10^{-3} SI) over depth, elemental ratios, and QEMSCAN mineral fractions(area %). The second column of QEMSCAN results presents the variation in feldspar content. Mineralization (Mineral.) type is presented as porphyry-style (red) and polymetallic (yellow) veins. Lithology color codes as in Figure 1.

Potassic alteration is observed overprinting the sodic alteration. Like albitization, it exists both along veins and as a background alteration in the host rock. The mineralization style does not vary between the PEPC and the TP and cannot be used to differentiate these lithologies. However, several geochemical parameters can be used to separate the two igneous lithologies. The Eu anomaly is the tool with the best potential to easily discriminate the two units. The PEPC has an average negative Eu anomaly of 0.69. Variations of element ratios such as V/Sc, Sr/Y, Zr/Hf, and Nb/Y are strongly dependent on major magmatic processes and can also be used to differentiate the igneous units (Winchester and Floyd 1977; Halley 2020). Figure 3 shows their good correlation over depth and sharp increase at the igneous contact with the TP. The most consistent here appear to be Sr/Y (depending on plagioclase fractionation and the water content of the magma; Richards et al. 2012) and Zr/Hf (related to the fractional crystallization of zircons; Lowery Claiborne et al. 2006). The PEPC has an average Zr/Hf ratio of 34.6.

The TP is a dark grey porphyritic rock with an aphanitic groundmass. Its MS signal is higher in the deeper part of the core which is related to stronger potassic alteration. The rock consists mainly of large plagioclase phenocrysts in a fine-grained groundmass of quartz, alkali feldspar, and biotite. The amount of biotite is higher than in the PEPC (Figure 2). As aforementioned, the alteration is fundamentally different in the TP. Like in the PEPC, albitization is also present, but here it occurs as a weak background sodic alteration. Potassic alteration is characterized by an increase in hydrothermal biotite associated with minor alkali feldspar and magnetite. The TP has an average Eu anomaly of 0.95. This means that the anomaly is close to neutrality and therefore could be successfully used to discriminate the porphyritic intrusion from the host PEPC. Additionally, the Zr/Hf ratio is around 39.9 (compared to 34.6 in the PEPC). QEMSCAN was used to quantify the mineral proportions for each sample according to their depth in Figure 3. The increase in plagioclase and drop in alkali feldspar and albite contentsare demonstrated.

5 Alteration mineral chemistry

White mica alteration does not vary significantly between the two lithologies. The white mica composition corresponds to muscovite–phengitic muscovite (Tischendorf et al. 2004). The compositional trends in white mica chemistry are presented in Figure 4A, showing higher variability in white mica chemistry in the PEPC.

Changes in chlorite chemistry between the PEPC and TP are also noticeable. All the chlorite grains analyzed can be described as trioctahedral Mg- and Fe-chlorites (Figure 4B). In the PEPC, the Fe and partly Al contents are higher than in the TP.

The magmatic and hydrothermal biotite chemistry reveals variation between the targeted grains but is inconclusive at this stage.

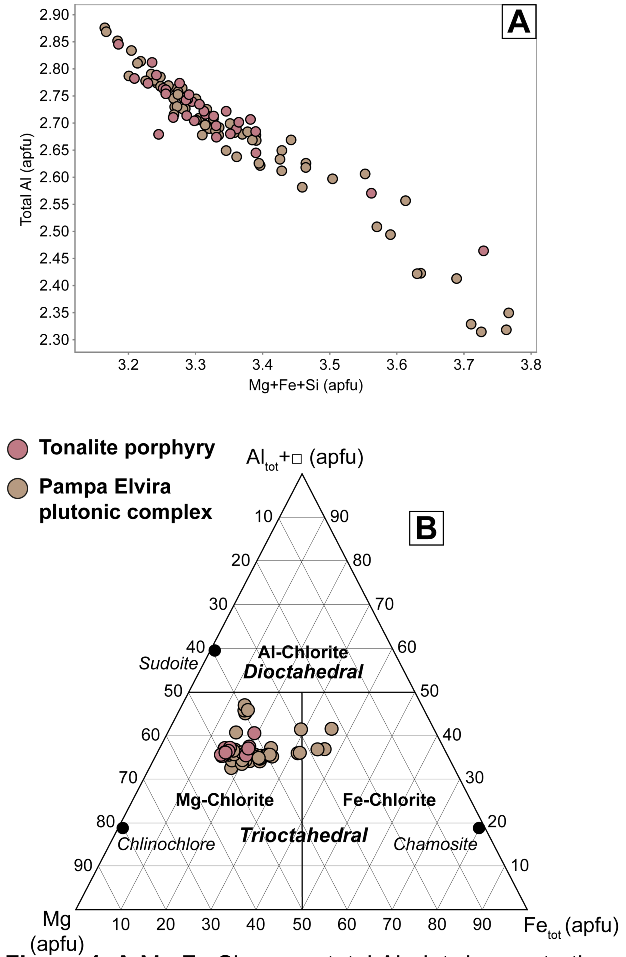

Figure 4. A Mg-Fe-Si versus total Al plot demonstrating the similarity in white mica chemistry. **B** Chlorite Total Al + octahedral vacancy-Mg-Fe compositional diagram, showing a range of Mg- to Fe-rich chlorite in the GD (after Zane and Weiss 1998).

6 Discussion and conclusions

While the PEPC and TP at the Gaby porphyry copper deposit cannot always be differentiated macroscopically, dominant alteration styles and some geochemical characteristics prove to be good vectors to discriminate them. The proportions of feldspars are largely controlled by lithology. The Eu anomaly, as well as Sr/Y and Zr/Hf ratios also yield good results. It is demonstrated that these methods can be applied on a single drill core or district scale and present a powerful tool for correct discrimination between macroscopically similar-looking lithologies.

White mica, chlorite, and biotite compositions revealed by EPMA indicate distinct trends in chemistry (e.g., chlorite depleted in Fe in TP), but require additional verification with trace element analysis by LA-ICP-MS technique.

Acknowledgements

The authors thank Codelco and Exploraciones Mineras S.A. (EMSA) for funding this project, granting access to their facilities, and for continued support.

References

Camus F (2003) Geología de los sistemas porfíricos en losAndes de Chile. Servicio Nacional de Geología y Minería. Cugerone A, Kouzmanov K, Fontboté L, Krampert L,Rodríguez C, Pardo R, Pichott Henríquez S (this volume) White mica alteration in the Gaby porphyry copper district,

Northern Chile.

Dilles JH, Winkler M, Essman J, Duncan R (2000) Petrologicand Geochemical Studies of the Gaby Sur Porphyry Copper Deposit, Northern Chile. Internal Report.

Gardeweg M, Pino H, Ramirez CF, Davidson J (1994) Mapa geológico del área de Imilac y Sierra de Almeida, Regiónde Antofagasta. Servicio Nacional de Geología y Minería, Documentos de Trabajo No. 7, Escala 1:100.000. Santiago, Chile.

Halley S (2020) Mapping magmatic and hydrothermal processes from routine exploration geochemical analyses. Econ Geol 115: 489–503.

Lowery Claiborne L, Miller CF, Walker BA, et al (2006) Tracking magmatic processes through Zr/Hf ratios in rocks and Hf and Ti zoning in zircons: An example from the Spirit Mountain batholith, Nevada. Mineral Mag 70: 517–543.

Maksaev V, Zentilli M (1988) Marco metalogenico regional de los megadepósitos de tipo porfido cuprifero del norte grande de Chile. Congreso Geologico Chileno 1: 181–212.

Niemeyer H, Zavattieri AM, Ballent S, Zamuner A, Gallego O (2008) Triassic age of the continental Pular Formation, Sierra de Almeida, Antofagasta, northern Chile. Revista Geológica de Chile, 35(1), 147–161.

Piquer J, Sanchez-Alfaro P, Pérez-Flores P (2021) A new model for the optimal structural context for giant porphyry copper deposit formation. Geology 49:597–601.

Reygadas W, Chepillo J, Pardo R (2023) Programa Exploración. Mapa Litología-Estructuras, 1:20,000. Distrito Garbiela Mistral. Internal Report.

Richards JP, Spell T, Rameh E, et al (2012) High Sr/Y magmas reflect arc maturity, high magmatic water content, and porphyry Cu ± Mo ± Au potential: Examples from the Tethyan arcs of central and eastern Iran and western Pakistan. Econ Geol 107: 295–332.

Tischendorf G, Rieder M, Förster H-J, et al (2004) A new graphical presentation and subdivision of potassium micas. Mineral Mag 68: 649–667.

Winchester JA, Floyd PA (1977) Geochemical discrimination of different magma series and their differentiation products using immobile elements. Chem Geol 20: 325– 343.

Zane A, Weiss Z (1998) A procedure for classifying rock-forming chlorites based on microprobe data. Rend LinceiSci Fis Nat 9: 51–55.

Zappettini E, Miranda-Angles V, Rodríguez C, et al (2001) Mapa metalógenico de la región fronteriza entre Argentina, Bolivia, Chile y Perú (14oS-28oS). PublicaciónGeológica Multinacional 2

Zentilli M, Maksaev V, Boric R, Wilson J (2018) Spatial coincidence and similar geochemistry of late Triassic and Eocene–Oligocene magmatism in the Andes of northern Chile: evidence from the MMH porphyry type Cu–Mo deposit, Chuquicamata district. International Journal of Earth Sciences 107: 1097–1126.

Genesis of Mineralized Skarns: reanalysis of decarbonation reactions, decarbonatization, and carbonate melting during infiltrative contact metasomatism

David R Lentz[1]
[1]Dept. of Earth Sciences, University of New Brunswick, Fredericton, NB Canada

Abstract. The integration of silica activities (solubilities) in analysis of infiltrative metasomatic calc-silicate formation in limestones-marbles helps to reconcile available mineral-fluid phase modelling, fluid inclusion, and stable isotopic evidence. Very low X(CO_2) (<0.01) is consistent with these volatiles, very high F/R, and the general absence of residual carbonates in prograde skarns. H_2CO_3 in this reaction, with low pH volatiles enhance carbonate solubilities, but also enhance carbonate melting, and mobilization. Mass-balance calculations consistently reveal substantial Ca-Mg carbonate loss from the system, beyond decarbonation. Carbonate-rich "veins" within and around contact metasomatic skarn systems, are generally devoid of silica, and variably mineralized in sulphides and sulfates, so maybe carbonate dykes consistent with their textures and mineral-chemical equilibria. Carbonate, salt, sulfate, and phosphatic melts are ionic liquids of very low viscosity and have different solution properties for many components, including mineralizing components introduced in the fluid infiltration process.

1 Introduction

Skarn deposits are some of the richest deposit systems in terms of grade, but also overall metal endowment. The prograde development of skarns has long been at issue as the traditional interpretation of calc-silicate forming reactions lead to erroneous interpretation of the X(CO_2) of these fluids. Virtually all fluid inclusion studies of mineralized skarns do not exhibit CO_2 even with Raman or evidence of boiling, which had been advocated for these systems. Lentz and Suzuki (2000) showed that using silica activities (not 1 for quartz) applied to the T-P-X(CO_2) result in calc-silicate assemblages and zonation consistent with observations, i.e. X(CO_2) < 0.01. Lentz (2005a) described extensive loss of carbonate (~ 50%) from selected skarn systems using mass-balance techniques consistent with these those findings. In addition, silica mass balancing supports extremely high fluid-rock ratio (F/R) associated with all infiltrative skarns. Lentz (2005b) further elaborated on this to demonstrate that this was not simple dissolution of carbonates that were stripped from skarns, but in fact carbonate melts were formed; these ideas were built off of Lentz (1999) were evidence was presented showing that this equilibria was consistent with the eutectic in the carbonate melt system (> 600°C) with a maximum of carbonic acid formed, so I postulated that some carbonatitic systems might be from either volatile fluxing and (or) syntectic reactions (Lentz 1998; Lentz 2005a). Many of these complex reactions between limestones-marbles and a wide range of silicate melts were described by the infamous Reginald Daly over a century ago (see Lentz 2017).

2 Infiltrative metasomatism and decarbonation

Lentz and Suzuki (2000) used existing interpolations of silica solubility and their activities to show how the interpreted calc-silicate assemblages form at very low X(CO_2) showing the consistency of silica solubility induced metasomatism with interpreted low CO_2 (< 1 %) in the H_2O infiltrating the skarn system (Fig. 1).

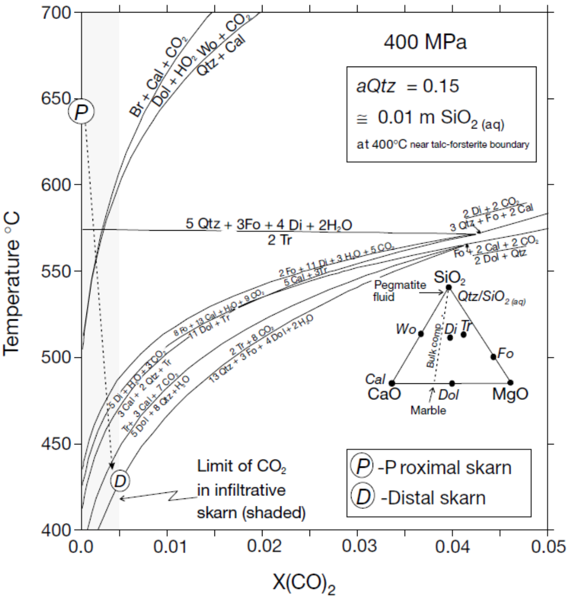

Figure 1. Temperature vs. X(CO_2) in the Ca-Mg-Si-C-O-H system (400 MPa), illustrating the estimated stability of calc-silicate assemblages ($CaCO_3$, $MgCO_3$, SiO_2 projection) (modified after Lentz and Suzuki 2000).

Key is these mixed volatile equilibria and zoning relationships are valid over a huge range of P-T conditions to very low temperatures (T), consistent with critically low CO_2 contents of fluid inclusions, as well in all skarn-related magmatic hydrothermal systems. All prograde decarbonation is driven by infiltrating silica forming calc-silicates, so is limited by its solubility in water, so the system naturally stays very low in CO_2; therefore there is no need to invoke

CO_2–H_2O immiscibility and no reason to expect high CO_2 (>1 %) in fluid inclusions.

3 Decarbonatization

Most skarns have minimal evidence for residual carbonates in the system, especially in prograde skarns. Lentz (2005a) noted that greater than 50% mass decrease occurred with skarnification, i.e. the carbonates were mobilized from the system. Although exsolving magmatic fluids are commonly invoked as the culprits in contact metasomatic skarns and they are known to be acidic, the amount of acidic fluids is considerable and beyond the capability of the infiltrative fluid. Carbonates have a retrograde solubility so at prograde infiltrative temperatures carbonates are typically negligibly soluble. Lentz (1998, 1999) reproposed from the much earlier literature that carbonates could easily be melted at the P-T conditions of typical prograde skarn formation (see Fig. 2); there was never an intention to infer all carbonate melts were derived by these volatile fluxing or syntectic reactions with limestones, but rather help develop a realization that magmas could react in complex ways with limestones and marbles that helped explain some phenomena in and around skarn systems.

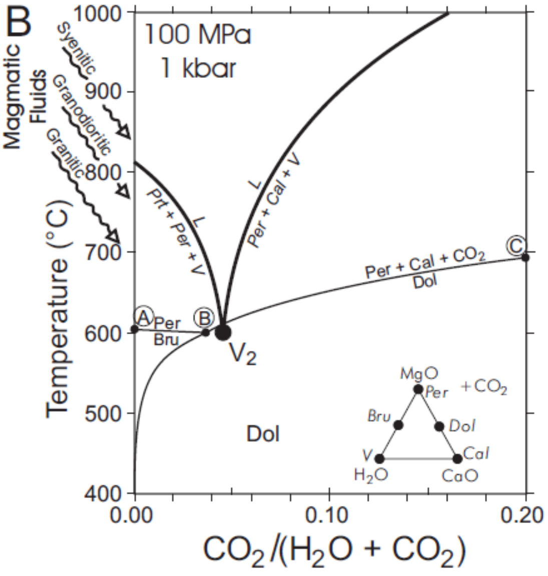

Figure 2. Temperature vs. X(CO_2) diagram illustrating decarbonation reaction dolomite ↔ periclase (or brucite) + calcite + CO_2 [at a X(CO_2) = 0.05 relative to portlandite-calcite-periclase-vapor-liquid (melt) eutectic (MgO-CaO-CO_2-H_2O system) (modified after Lentz 1999).

The substantial loss of carbonate during calc-silicate generation is probably a combination of dissolution by acidic volatiles and at advanced prograde stages by volatile-induced melting of carbonates during infiltration as described by Lentz (2005b).

3.1 Carbonate melt inclusions

Crystallized carbonate melt inclusions (cMIs) have been recognized in many magmatic systems including some related to skarns including vesuvianite skarn clasts erupted from Vesuvius (see Veksler and Lentz 2006). Trapping of melt inclusions is a natural consequence of calc-silicate formation, although the highly reactive and ephemeral nature of carbonates in continually reacted skarns makes them elusive in many systems. Saline brines to salt melts have a continuum with sparingly soluble carbonates or high T molten carbonate. Carbonates readily crystallize, and melt inclusions formed would immediately crystallize as well in the presence of the water-rich fluid; carbonate melts have as much dissolved volatiles as a silicate melt, so volatile fluxed carbonates easily have up to 10% H_2O in any pressurized system. Water and salts and sulfates, sulfides, and oxides associated with the original infiltrating volatiles are known to coexist with varieties of cMIs in skarns systems (Xu et al. 2023), as well as iron oxide (apatite) systems (cf. Lentz 2018, Bain et al. 2020).

4 Carbonate dykes with skarn association

Although rarely described, there are numerous carbonate vein and (or) dike-like features around contact metasomatic skarns. These features have commonly been considered veins, but many have dike like features. Chemically and isotopically they are consistent with a skarn derivation. Numerous researchers have referred to crustal carbonatites, some with and others without an obvious relation to skarns, although they are quite distinctive to any mantle carbonatitic system. Around large porphyry-related skarns, including iron skarns, they have been considered as veins, and even have magnetite-sulfides, as well as apatite, but rarely quartz. Carbonatitic to salt melts are ionic melts, so have extremely low viscosity, and depressurization during buoyant ascent-emplacement readily yields (exsolves) volatiles that enhances ascent beyond the distal skarn environment. Textures are wide ranging, but pseudo-aplitic to pegmatitic textures are evident reflecting the role of water-rich volatiles differentially exsolving and reacting with these ionic melts as quenching-crystallization occurs; it is easy to see how these could be interpreted as veins, and in the past many have referred to similar things descriptively as vein-dykes (see Lentz 1998).

5 Conclusions

This brief review highlights the intimate role silica-bearing magmatic volatiles have with formation of infiltrative (contact metasomatic) skarns that are mineralized. The silica solubilities are a controlling factor in decarbonation equilibria, which are consistent with observed X(CO_2) and fluid inclusions. These very low X(CO_2) are coincident with carbonate melting at Ts > 600°C and the maximum in the formation of carbonic acid that acts as a flux with H_2O. The extremely high F/R inferred from silica mass balance constraints and the considerable loss of carbonates (decarbonatization) from the system suggest that carbonate melting in addition to carbonate dissolution by acidic magmatic volatiles are responsible. Crystallized carbonate melt inclusions are not uncommon, and have generally been overlooked for the most part in skarns and complex carbonate dykes that originated from skarns; these typically have evidence of association with saline brines or salt melts, as well as sulfates, sulphides, oxides, and magnetite with some calc-silicates to name a few as they are highly fluid ionic melts. Geochemically and isotopically these have been described as crustal carbonatites as they crystallize distal to most contact metasomatic skarn systems. Further work is needed to examine these carbonate-rich systems to ascertain if they are indeed veins or dykes, using cMIs to aid in that analysis.

Acknowledgements

I was financially supported as IAGOD Distinguished Lecturer (2020-2023).

References

Bain, W.M., Steele-MacInnis, M., Li, K., Li, L., Mazdab, F.K. and Marsh, E. (2020): A fundamental role of carbonate-sulfate melts in formation of iron oxide–apatite deposits; Nature Geoscience, v. 13, p. 751–757, https://doi.org/10.1038/ s41561-020-0635-9.

Lentz, D.R. (1998): Late-tectonic U-Th-Mo-REE skarn and carbonatitic vein-dike systems in the southwestern Grenville Province: a Pegmatite-Related Pneumatolytic Model linked to Marble Melting (limestone syntexis); *In* Mineralized Intrusion-Related Skarn Systems (D.R. Lentz ed.). Mineralogical Association of Canada Short Course Volume 26, p. 519-657.

Lentz, D.R. (1999): Carbonatite Genesis: a reexamination of the role of intrusion-related pneumatolytic skarn processes in limestone melting; Geology, v. 27, p. 335-338.

Lentz, D.R. (2005a): Mass-balance Analysis of Mineralized Skarn Systems: Implications for Replacement Processes, Carbonate Mobility, and Permeability Evolution; SGA 2005, Mineral Deposit Research, Meeting the Global Challenge, Beijing, v. 1, p. 421-424.

Lentz, D.R. (2005b): Reinterpretation of infiltrative skarn phase equilibria: implications for fluid phase composition and behaviour; ECROFI VIII Conference, Abstract volume.

Lentz, D.R. (2017): Syntectic Reactions involving Limestones and Limestone-Derived Carbonatitic Melts in the Generation of some Peralkalic Magmas: Reflections on Reginald Daly's Insights 100 Years Later; American Geophysical Union.

Lentz, D.R. (2018): Iron Oxide Copper-Gold (IOCG) Systems: examination of end-member models, physiochemical processes, and possible modern analogies. IAGOD Salta, Argentina.

Lentz, D.R. and Suzuki, K. (2000): A low-F, pegmatitic granite-related Mo skarn from the southwestern Grenville Province, Ontario, Canada: petrology to phase equilibria implications; Economic Geology, v. 95, p. 1319-1337.

Veksler, I.V. and Lentz, D.R. (2006): Parental magmas of plutonic carbonatites, carbonate-silicate immiscibility and decarbonation reactions: evidence from melt and fluid inclusions; In Melt inclusions in Plutonic Rocks, Edited by J. Webster. Mineralogical Association of Canada, Short Course volume 36, p. 123-150.

Xu, X., Szmihelsky, M., Yan, J., Xie, Q. and Steele-MacInnis, M. (2023): Melt inclusion evidence for limestone assimilation, calc-silicate melts, and "magmatic skarn". Geology https://doi.org/10.1130/G50893.1

Oxidation and hydration states of porphyry-copper ore-forming magmas recorded by trace elements in zircon

Robert R. Loucks [1,2], **Marco L. Fiorentini** [1,2]
[1]*Centre for Exploration Targeting, School of Earth Sciences, University of Western Australia, 35 Stirling Highway, Crawley WA 6009, Australia*
[2]*ARC Centre of Excellence for Core to Crust Fluid Systems, University of Western Australia, 35 Stirling Highway, Crawley WA 6009, Australia*

Abstract. Trace elements in magmatic zircon preserve a record of the hydration state as well as oxidation state of the ore-forming silicate melts. The zircon trace-element ratio $(Eu/Eu^*)/Yb_N$ is formulated as an indicator of silicate melt hydration state and is empirically validated by comparison with hygrometry and geobarometry on coexisting hornblende phenocrysts. Zircon records tandem rise of oxidation state and hydration state of arc magmas during fluid-undersaturated magmatic differentiation at lower-crustal depths. Zircon records dehydration and further oxidation of ascending silicate melts as exsolving hydrothermal fluid segregates at lower- to upper-crustal depths. Porphyry-copper ore-forming melts have distinctive values and trends on zircon oxybarometer vs hygrometer plots. Our zircon oxybarometer and hygrometer are applicable to detrital zircons, permitting identification of watersheds that contain a copper-fertile igneous complex (exploration target) upstream from the sediment sampling site.

1 Zircon $(Eu/Eu^*)/Yb_N$ indicator of silicate melt hydration state

Arc magmas parental to porphyry copper deposits (PCDs) typically have high whole-rock Sr/Y and Eu/Yb ratios and $Ho_N/Yb_N < 1$ that indicate suppressed plagioclase and enhanced hornblende production over most of the course of mafic-to-felsic magmatic differentiation. Al-in-hornblende geobarometry and hygrometry on phenocrysts and experimental petrology indicate that those features are attributable to unusually high hydration state of the magmas over most of the course of mafic-to-felsic differentiation at Moho-vicinity pressures. Zircon inherits the $(Eu/Eu^*)/Yb_N$ feature of its parent melt, warped by zircon/melt partition coefficients. We formulate and empirically validate the trace-element ratio $(Eu/Eu^*)/Yb_N$ in zircon as an indicator of relative hydration states of silicate melts, including ones parental to PCDs.

2 Zircon $Ce/\sqrt{(U \times Ti)}$ oxybarometer

Magmas parental to porphyry copper deposits commonly have igneous anhydrite and/or sulphate-rich apatite phenocrysts that indicate higher oxidation state than ordinary granitoid arc magmas (Hutchinson and Dilles, 2019). The ratio $Ce/\sqrt{(U_i \times Ti)}$ in zircon has been formulated and calibrated by Loucks et al. (2020) as a quantitative measure of the parent melt's oxidation state, $\Delta FMQ = \log fO_2^{sample} - \log fO_2^{FMQ}$ wherein FMQ represents the reference buffer fayalite + magnetite + quartz, and U_i represents radioactive-decay-corrected initial U content at the time that dated zircons crystallised. Empirical calibration using 1042 analysed zircons in 85 natural populations having independently constrained $\log fO_2$ in the range FMQ–4.9 to FMQ+2.9 retrieves the calibration data with a standard error of ±0.6 log unit fO_2. We deploy it here to monitor the evolving oxidation state of melts during trans-crustal ascent and decompression-induced fluid exsolution at many igneous complexes.

3 Observed co-variation trends of magmatic hydration and oxidation states

Geobarometry, hygrometry, and oxybarometry on cores and rims of hornblende phenocrysts yield trends that corroborate our zircon-based indicators of silicate melt hydration state and oxidation state in the same igneous units, providing "proof of concept", as shown in Figure 1. The hornblende data indicate continuous exsolution of H_2O-rich C-O-H-S-Cl fluid from ~700-800 MPa (~26-30 km depth) to subvolcanic, ore-forming depths, with concomitant oxidation of residual melt. Zircon records the same trends of melt oxidation during melt dehydration.

Figure 2 shows zircon hygrometry and oxybarometry trends in a succession of epizonal intrusions in the 35-21 Ma Meghri-Ordubad igneous complex in Armenia and in the 67-55 Ma Yarabamba-Quellaveco complex in southern Peru. Zircons in early intrusions form arrays of positive slope, with rising oxidation state as hydration state rises. Zircons in later intrusions, including ore-forming ones, define arrays having negative slopes, with further rise in oxidation state accompanying melt dehydration.

4 How PCD magmas become oxidised

4.1 Oxidation as dissolved H_2O increases in melts

Magmas stored in hot country rock near the Moho tend to last long enough to experience intermittent replenishments by hydrous basaltic melt from the mantle. Over successive cycles of replenishment and fractional crystallization, hybrid melts can accumulate high concentrations of inherited chemical components that are largely excluded from ultramafic cumulates—H_2O, CO_2, Cl, Eu^{2+}, Fe^{3+}, etc.

In Figure 2, segments having steep positive slope are at least partially attributable to selective sequestering of Fe^{2+} relative to Fe^{3+} by cumulus olivine, clinopyroxene and hornblende in ultramafic cumulates all of which have lower Fe^{3+}/Fe^{2+} ratios than equilibrated silicate melt. However, the principal mechanism of melt oxidation is likely to be a rising ratio of molecular H_2O to hydroxyl as total dissolved H_2O accumulates in the melt during crystallisation:

$$\tfrac{1}{2}\,H_2O_m + Fe^{2+} + \tfrac{1}{4}\,O_2 = OH^- + Fe^{3+} \qquad (1a)$$

wherein H_2O_m represents molecular water dissolved in the melt, and OH^- replaces a bridging oxygen linking Al and Si in the tetrahedral framework. Activities of these species in the melt are related to the equilibrium constant K_1 by

$$\log\,[Fe^{3+}/Fe^{2+}] = \log K_1 + \log\,[H_2O_m^{1/2}/OH^-] + \tfrac{1}{4}\log fO_2 \qquad (1b)$$

wherein brackets denote activities. Equation 1b shows that at a specified T and P (constant K_1) and specified fO_2, a rising ratio of H_2O_m/OH^- in the melt requires a tandem rise of its Fe^{3+}/Fe^{2+} activity ratio, as theoretically predicted by Moretti (2005) and experimentally demonstrated by Gaillard et al (2003) and by Schuessler et al (2008).

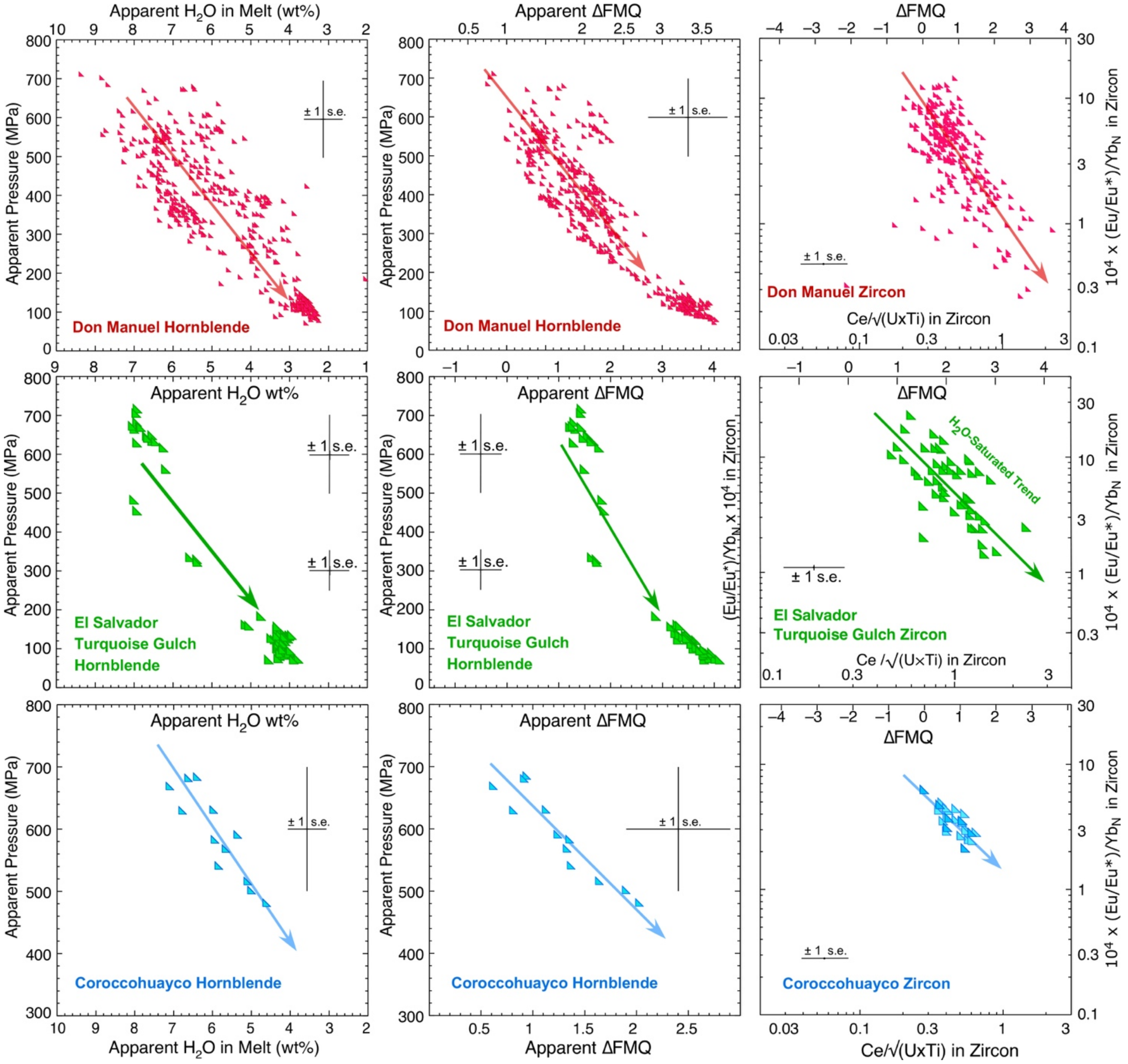

Figure 1. Proof of concept. Hornblende geobarometry-hygrometry-oxybarometry corroborates trends in zircon indicators of parent melt hydration state and oxidation state during trans-crustal ascent. Al-in-hornblende barometry on phenocryst cores and rims by the calibration of Mutch et al (2016) are plotted against apparent ΔFMQ and wt % H_2O dissolved in the melt according to the calibrations by Ridolfi et al (2010). Arrows show trends during decompression of ascending magmas and concomitant exsolution of hydrothermal fluid and oxidation of dehydrating melt. Panels on the right illustrate applications of our zircon composition parameters in the same igneous units. Hornblende and zircon analyses in the Don Manuel PCD and related intrusions, central Chile, are from Gilmer et al (2018); All analyses from host intrusions except xenoliths and mafic enclaves are plotted. Hornblende phenocryst compositions in the Cu(-Mo)-ore-forming L Porphyry stock in the Turquoise Gulch intrusive complex, El Salvador, Chile, were reported by Lee (2008). Zircon compositions in the L Porphyry were reported by Lee et al (2017). Amphibole compositions in Coroccohuayco Hornblende Porphyry intrusion, central Peru, were reported by Chelle-Michou et al (2015). Zircon compositions in Hornblende Porphyry and Hornblende-Biotite Porphyry dacitic intrusions were reported by Chelle-Michou and Chiaradia (2014).

4.2 Melt oxidation as hydrothermal fluid segregates

H_2O solubility in granitic melts decreases ~4-fold during magma ascent from 800 MPa to 100 MPa (Holtz et al 1995). Al-in-hornblende barometry and hornblende hygrometry in Figure 1 indicate onset of fluid segregation at 700-800 MPa in response to decompression of ascending magma. A transition from fluid movement by intergranular filtration to channelling via propagating conduits tends to occur at greater depth and lower vesicularity in moving magma than in stagnant magma, which facilitates gravitational segregation of exsolving volatiles to the top of the ascending magma column. To the degree that channelling and collection of segregated fluid remove it from effective diffusive communication with its parent melt, the residual melt's chemical evolution may be regarded as fractional distillation in a chemically open system.

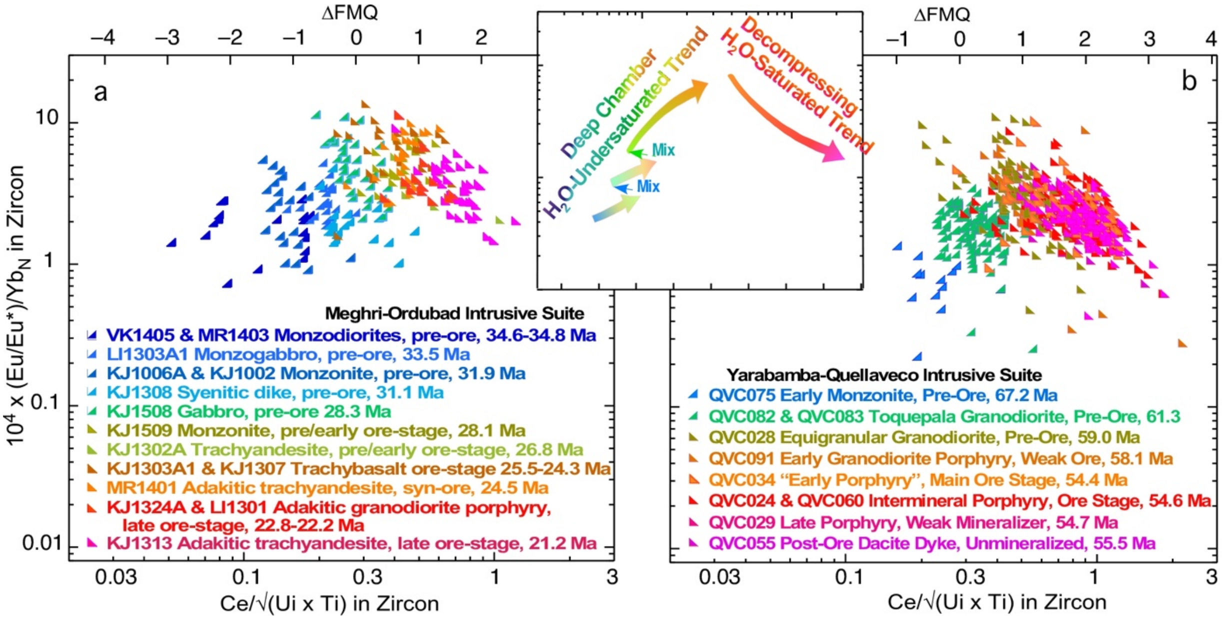

Figure 2. Co-evolution of melt oxidation and hydration states according to our indicators during magmatic differentiation. **(a)** LA-ICPMS analyses of zircons in successive pre-mineralisation and copper-mineralising intrusions in the Meghri-Ordubad intrusive complex, Armenia, showing sample number, lithologic unit and U-Pb age as reported by Rezeau et al (2019); **(b)** zircon analyses in successive pre-mineralisation and copper-mineralising intrusions and a post-ore intrusion in the Yarabamba-Quellaveco intrusive complex, southern Peru as reported by Nathwani et al (2021). Arrows in the inset panel schematically represent rising hydration state and oxidation state of melts through successive cycles of fluid-undersaturated magmatic differentiation and chamber replenishment (positive slope), followed by melt dehydration and further oxidation during fluid-saturated magma ascent (negative slope).

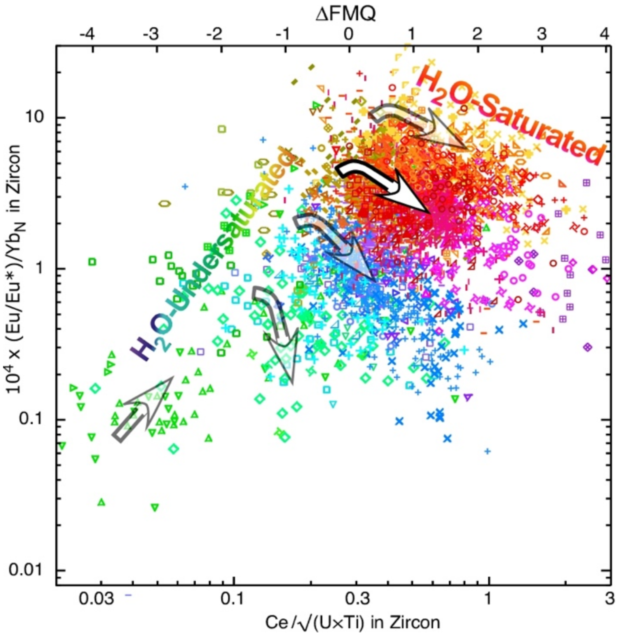

Figure 3. Zircons from PCD-forming intrusions in 37 districts are shows as red and orange symbols. Brown symbols represent zircons in pre-ore and post-ore intrusions in ore-hosting igneous complexes. Green, turquoise, blue, and purple symbols represent barren arc igneous suites. Arrows schematically represent the turn in trajectory at the transition from fluid-undersaturated melt (positive slope) to fluid-saturated evolution (negative slope) in granitoid melts of varied volatile content at the onset of fluid saturation.

Reduced members of the principal redox couples in the granitoid melts—H_2-H_2O, S^{4+}-S^{6+}, and Fe^{2+}-Fe^{3+}—partition into exsolving hydrothermal fluid more strongly than oxidised members, so segregation of exsolving fluid leaves a more oxidised residual melt (Humphreys et al, 2015; Scaillet et al, 1998; Bell and Simon, 2011). The 1982 eruption of El Chichón volcano (Mexico) and the 1991 eruption of Mt. Pinatubo (Philippines) released vastly more SO_2 than could have been dissolved in the erupted mass of melt, which implies that most of the erupted sulphur was in hydrothermal fluid that had accumulated at the top of the pre-eruption magma column (Luhr et al., 1984; Gerlach et al., 1994). The El Chichón eruption included lithic fragments of porphyry-copper-style mineralisation (Luhr, 1983). The Pinatubo stratocone hosts the Dizon porphyry Cu-Au ore deposit and several Cu-Au prospects (Hattori and Keith, 2001).

Figure 3 is a plot of 5777 zircon compositions compiled from our own and other publications. The dataset includes 2220 zircons from intrusions inferred by the respective authors to have exsolved ore-forming magmatic-hydrothermal fluids in 37 major magmatic-hydrothermal Cu-rich ore deposits of Phanerozoic age worldwide. Those are compared to 3557 zircons from non-ore-forming magmas at Phanerozoic convergent plate margins. It is evident that these composition parameters in zircon effectively discriminate metallogenically fertile arc magmas from infertile ones.

5 CONCLUSION

Trace-element features of zircons that are diagnostic of unusually high hydration and oxidation states of their parent magma effectively discriminate Cu-ore-forming igneous complexes from ordinary, unmineralised arc igneous suites. Our discriminants of porphyry copper fertility are applicable to detrital zircons. The watershed-scale "footprint" of this diagnostic tool is much larger than the detection range of conventional geochemical sampling techniques and is applicable to paleo-watersheds. In application to paleo-drainages, it may identify fertile igneous complexes that formerly were exposed to erosion but are now buried under younger volcanic or sedimentary cover.

Acknowledgements

We thank Paul Agnew of Rio Tinto Exploration and Cam McCuaig and Natalie Caciagli of BHP Exploration for encouragement and helpful discussions. This study was supported in part by Rio Tinto Exploration. Additional financial support was provided by the Australian Research Council Centre of Excellence for Core to Crust Fluid Systems grant CE110001017.

References

Bell AS, Simon A. (2011) Experimental evidence for the alteration of the $Fe^{3+}/\Sigma Fe$ of silicate melt caused by the degassing of chlorine-bearing aqueous volatiles. Geology 39:499–502.

Chelle-Michou C, Chiaradia M, Béguelin P, Ulianov R (2015) Petrological evolution of the magmatic suite associated with the Coroccohuayco Cu(-Au-Fe) porphyry–skarn deposit, Peru. J Petrol 56:1829-1862

Chelle-Michou C, Chiaradia M, Ovtcharova M, Ulianov A, Wotzlaw J-F (2014) Zircon petrochronology reveals the temporal link between porphyry systems and the magmatic evolution of their hidden plutonic roots (the Eocene Coroccohuayco deposit, Peru). Lithos 198-199:129-140.

Gaillard, F, Pichavant, M, Scaillet, B (2003) Experimental determination of activities of FeO and Fe_2O_3 components in hydrous silicic melts under oxidising conditions. Geochim Cosmochim Acta 67:4389-4409.

Gerlach TM, Westrich HR, Symonds RB. (1996) Pre-eruption vapor in magma of the climactic Mount Pinatubo eruption: source of the giant stratospheric sulfur dioxide cloud. In: Newhall CG, Punongbayan RS (Eds.), Fire and Mud: Eruptions and Lahars of Mount Pinatubo. University of Washington Press, Seattle, WA; Quezon City: Philippine Institute of Volcanology and Seismology, pp. 415-434.

Gilmer AK, Sparks RSJ, Blundy JD, Rust AC, Hauff F, Hoernle K, Spencer CJ, Tapster S (2018) Petrogenesis and assembly of the Don Manuel igneous complex, Miocene-Pliocene porphyry copper belt, central Chile. J Petrol 59: 1067-1108.

Hattori K., Keith JD (2001) Contribution of mafic melt to porphyry copper mineralization: evidence from Mount Pintaubo, Philippines, and Bingham Canyon, Utah, USA. Mineral Deposita 36:799–806.

Holtz F, Behrens H, Dingwell DB, Johannes W (1995) H_2O solubility in haplogranitic melts: Compositional, pressure, and temperature dependence. Am Mineral 80:94-108.

Humphreys MCS, Brooker RA, Fraser DG, Burgisser A, Mangan MT, McCammon C (2015) Coupled interactions between volatile activity and Fe oxidation state during arc crustal processes. J Petrol 56:795-814.

Hutchinson MC, Dilles JH (2019) Evidence for magmatic anhydrite in porphyry copper intrusions. Econ Geol 114:143–152.

Lee RG (2008) Genesis of the El Salvador porphyry copper deposit, Chile and distribution of epithermal alteration at Lassen Peak, California. PhD thesis, Corvallis, OR, Oregon State University, 344 p.

Lee RG, Dilles JH, Tosdal RM, Wooden JL, Mazdab FK (2017) Magmatic evolution of granodiorite intrusions at the El Salvador porphyry copper deposit, Chile, based on trace element composition and U/Pb age of zircons. Econ Geol 112:245-273.

Loucks RR, Fiorentini ML, Henriquez G, (2020) New magmatic oxybarometer using trace elements in zircon. J Petrol 61: egaa034.

Luhr JF (1983) The 1982 eruptions of El Chichón and the relationship to mineralized magmatic-hydrothermal systems [abs.]: Geol. Soc. Am., Abs. w Prog. 15:632.

Moretti R (2005) Polymerisation, basicity, oxidation state and their role in ionic modelling of silicate melts. Annals Geophys. 48:583–608.

Mutch, EJF, Blundy JD, Tattitch, BC, Cooper FJ, Brooker RA (2016) An experimental study of amphibole stability in low-pressure granitic magmas and a revised Al-in-hornblende geobarometer. Contrib Mineral Petrol 171: 85.

Nathwani CL, Simmons AT, Large SJE, Wilkinson JJ, Buret Y, Ihlenfeld C (2021) From long-lived batholith construction to giant porphyry copper deposit formation: petrological and zircon chemical evolution of the Quellaveco District, Southern Peru. Contrib Mineral Petrol 176:12.

Rezeau H, Moritz R, Wotzlaw J-F, Hovakimyan S, Tayan R (2019) Zircon petrochronology of the Meghri-Ordubad pluton, Lesser Caucasus: fingerprinting igneous processes and implications for the exploration of porphyry Cu-Mo deposits. Econ. Geol. 114:1365-1388.

Ridolfi F, Renzulli A, Puerini M (2010) Stability and chemical equilibrium of amphibole in calc-alkaline magmas: an overview, new thermobarometric formulations and application to subduction-related volcanoes. Contrib Mineral Petrol 160:45-66.

Scaillet B, Clemente B, Evans B, Pichavant M (1998) Redox control of sulfur degassing in silicic magmas. J Geophys Res 103:23937–23949.

Schuessler JA, Botcharnikov RE, Behrens H, Misiti V, Freda C (2008) Oxidation state of iron in hydrous phono-tephritic melts. Am Mineral 93:1493–1504.

Early zircon saturation and low Zr content of PCD-forming magmatic differentiation series: a guide for exploration targeting

Robert R. Loucks [1,2], **Marco L. Fiorentini** [1,2]
[1]*Centre for Exploration Targeting, School of Earth Sciences, University of Western Australia, 35 Stirling Highway, Crawley WA 6009, Australia*
[2]*ARC Centre of Excellence for Core to Crust Fluid Systems, University of Western Australia, 35 Stirling Highway, Crawley WA 6009, Australia*

Abstract. In orogenically deforming segments of convergent plate margins, horizontal compressive stress provides resistance to opening of tensile dike fractures and promotes entrapment of mantle-derived basaltic melts in magma chambers embedded in hot country rock at Moho-vicinity depths, where magmas cool slowly, and residual melts tend to last long enough to experience intermittent chamber replenishment by basaltic melts from the deeper mantle. Over several cycles of replenishment and fractional crystallisation, residual melts acquire high concentrations of inherited chemical components that were largely excluded from cumulus minerals—H_2O, Cl, CO_2, SO_3, etc. Accumulating H_2O re-orders the high-pressure crystallisation sequence of igneous minerals in successive cycles and leads to zircon saturation in mafic melts (basaltic andesite to mafic andesite compositions) of later cycles. Porphyry copper deposit (PCD) ore-forming magmas are chemically distinguished from ordinary arc granitoids by low Zr at zircon saturation, as well as by “adakitic” high Sr/Y and Eu/Yb that indicate unusually high dissolved H_2O in residual melts over most of the course of magmatic differentiation. Whole-rock Sr/Zr in rock samples retaining igneous plagioclase is a useful discriminant of Cu-fertile intrusive complexes.

1 Introduction

Lateral variations of tectonic stress along convergent plate margins have profound effects on the chemical course of magmatic differentiation of mantle-derived basaltic magmas. In non-compressive to weakly compressive stress settings, arc magmas follow a tholeiitic trend; in moderately compressive settings, a calc-alkalic trend is typical; in highly compressive, orogenically deforming arc segments, an adakitic differentiation trend is typical (Loucks, 2021).

2 Early to late zircon saturation in compressive to non-compressive arc segments

We illustrate the contrasting behaviour of Zr during magmatic differentiation in four magmatic arcs featuring adjacent compressive and non-compressive stress settings above the same subduction zone, and in which compression is induced by different tectonic mechanisms. Three of these case studies have major magmatic-hydrothermal Cu(-Au) ore deposits in the compressive segments.

2.1 Behaviour of Zr in adakites at the type locality on Adak Island

Figure 1 shows alternating compressive and non-compressive intervals due to rotation of block segments in response to tangential shear by oblique subduction. There is a correlative alternation of volcanic edifices that are large shields of mainly basaltic composition at the eastern ends of the rotating blocks, but small stratocones of mainly andesitic and dacitic composition in the compressional western ends of the rotating blocks (Kay et al., 1982). Figure 1b shows trends of whole-rock ppm Zr versus wt% SiO_2. Semisopochnoi is the next major magmatic centre west of Adak that is erupting primitive basalts. In the Semisopochnoi suite (and other centres in non-compressive settings in the Aleutians), the ppm Zr trend rises steeply until zircon saturates at around 70% SiO_2. In the Adak suite (and other compressive segments), the Zr v SiO_2 trend is flatter. In Figure 1c, the Sr/Zr ratio shows divergent differentiation trends from initially similar mafic parent magmas. Evidence that andesitic lavas on Adak and nearby Kanaga evolved at high pressure is in their abundant xenoliths of tectonised spinel peridotite and cognate xenoliths of ultramafic cumulates and hornblende gabbro for which mineral barometry gives pressures in the 28-22 km depth range, where basaltic magmas pond just beneath the base of the crust and fractionally crystallise to residual melts of adakitic andesitic-dacitic compositions (DeBari et al., 1987; Conrad and Kay, 1984).

2.2 Early and late zircon saturation in other compressive and non-compressive pairs

Trends of whole-rock ppm Zr versus wt% SiO_2 in differentiation series parental to major porphyry-type Cu(±Mo±Au) deposits (El Teniente and Batu Hijau) and a high-sulphidation-epithermal-type Au-Cu deposit (Chinkuashih) are compared in Figure 2 with contemporaneous suites lacking significant Cu mineralisation in adjacent arc segments overlying the same subduction zone. In all three cases, the compressive intervals are over-riding buoyant features in the subducting plate. In all three panels, the data trends represent rising accumulation of Zr in residual melt as SiO_2 increases until the melt attains zircon saturation, followed by declining Zr content of residual melt as zircon segregates with other cumulus minerals. The Cu(-Au-Mo)-ore-forming magmatic differentiation trends (red) reach zircon saturation at an earlier stage of magmatic differentiation than do Cu-infertile suites (green).

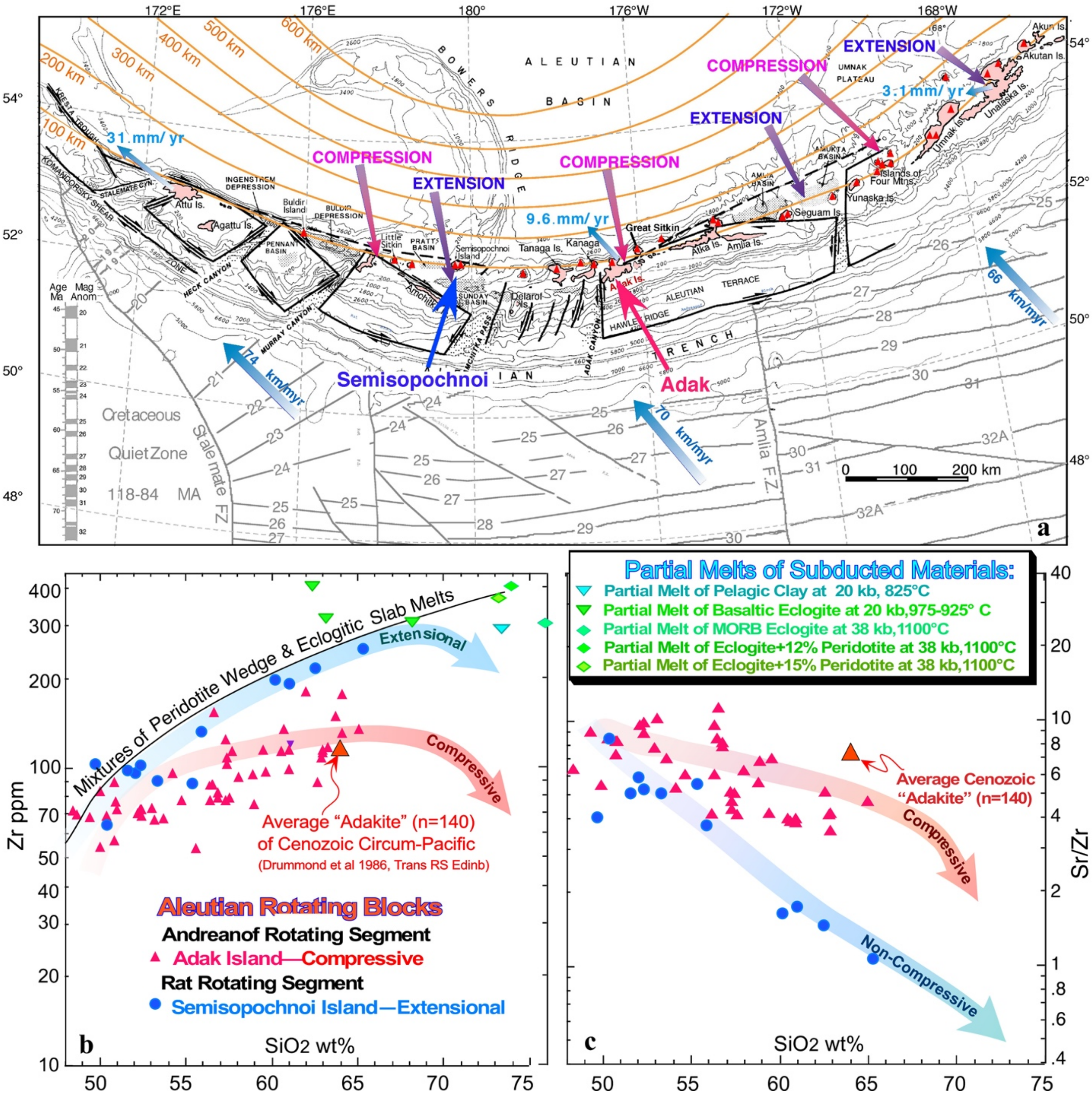

Figure 1. (a). In the eastern Aleutians, the plate convergence is nearly orthogonal to the trench, but westward along the Aleutians the convergence becomes increasingly oblique. Increasing tangential shear in the central and western Aleutians has caused the arc to break up into a lateral succession of block segments rotating clockwise (Geist et al., 1988). Seismically active transverse faults and coincident submarine canyons define the ends of the rotating blocks. Clockwise rotation of the eastern ends of the blocks away from the North American plate has produced extensional "summit basins" along the crest of the arc. Orange contours labelled "100 km" to "600 km" are depths to the top of the subducting slab, determined by local seismicity on the Wadati-Benioff zone at shallow depths ≤ 270 km, and determined by teleseismic tomographic imaging in aseismic portions of the slab at greater depths (Boyd and Creager, 1991). Locations of the calc-alkalic-adakitic Adak magmatic centre at the western end of the rotating Andreanof Block and of the tholeiitic Semisopochnoi magmatic centre at the eastern end of the rotating Rat Block are identified. **(b)** All available published whole-rock analyses of Quaternary samples are shown on this plot of ppm Zr in compiled analyses of samples from the Adak and Semisopochnoi magmatic centres. In Aleutian extensional settings, the trend of Zr vs SiO_2 rises steeply until zircon saturates at around 70% SiO_2. In the Adak suite and volcanoes in other compressive segments, the Zr v SiO_2 trend is flatter. Adak magmas apparently attain zircon saturation at a mafic stage of magmatic differentiation. These trends are compared with Zr contents of compiled experimental partial melts of subducted materials (green symbols; data from Johnson and Plank, 1999; Rapp et al, 1999; Xiong, 2006). Plainly, the Adak series does not lie along a mixing line between slab melts and melts of asthenospheric mantle wedge, which invalidates the hypothesis by Defant and Drummond (1990) that adakites at Adak and other circum-Pacific localities were produced by partial melting of subducted materials. The composition of "average Cenozoic circum-Pacific adakite" is taken from the compilation by Drummond et al (1996). *The Zr-SiO_2 plot effectively discriminates actual melts of subducted materials from "adakites", which are widely misinterpreted*

to be partial melts of subducted materials. **(c)** Contrasting trends of whole-rock Sr/Zr ratio in the compiled volcanic samples from Adak and Semisopochnoi. The Sr/Zr ratio shows divergent differentiation trends from initially similar mafic parent magmas, with a sub-horizontal trend in the compressive segments, and a steep, steady decline in the extensional settings.

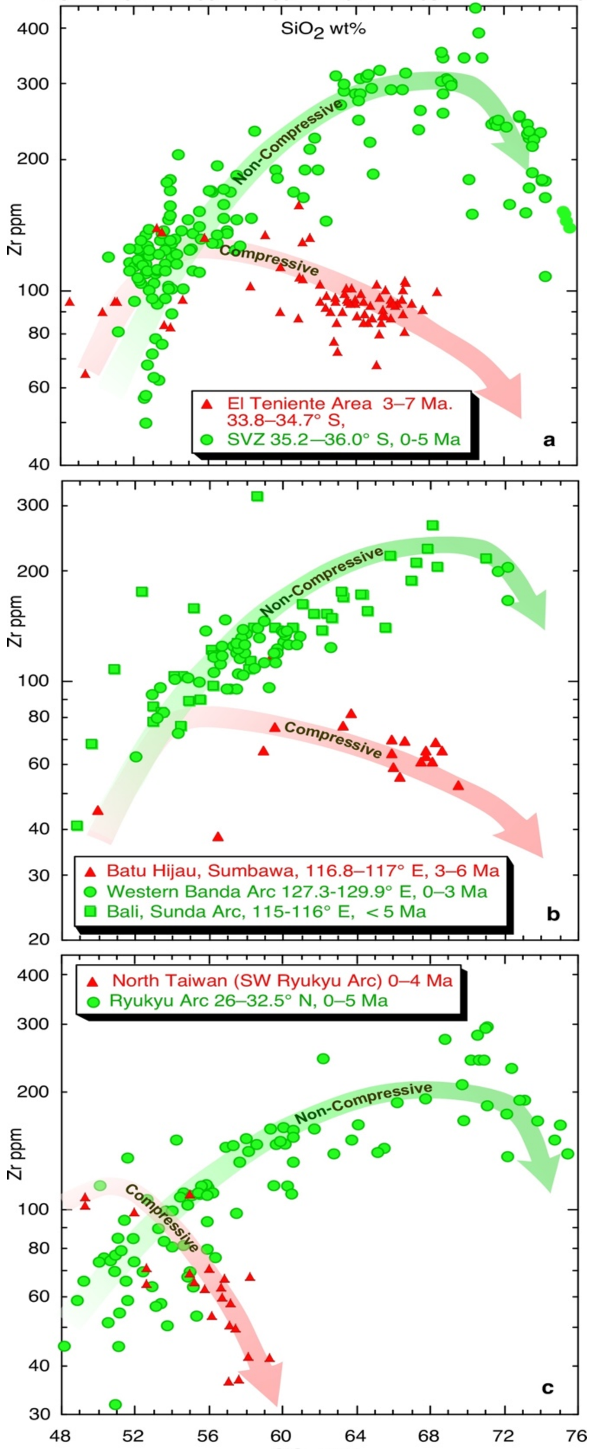

Figure 2(a,b,c). Compilation all available whole rock analyses (http://www.earthchem.org/portal) representing mafic-to-felsic differentiation series parental to major porphyry-type (El Teniente, Chile, and Batu Hijau, Indonesia) and high-sulfidation-epithermal-type (Chinkuashih, Taiwan) Cu(± Au ± Mo) deposits, compared with contemporaneous suites in adjacent, unmineralized arc segments overlying the same subduction zone. In all three panels, the data trends represent rising accumulation of Zr in residual melt as SiO_2 increases until the melt attains zircon saturation, followed by declining Zr content of the residual melt as zircon segregates along with other cumulus minerals. The Cu(-Au-Mo)-ore-forming magmatic differentiation trends (red) reach zircon saturation at an earlier stage of magmatic differentiation than do Cu-infertile suites (green).

In Figure 2a, red symbols represent all available analyses of fresh or little-altered samples in the orogenically deforming region above the subducting Juan Fernandez aseismic ridge and encompassing the early Pliocene El Teniente porphyry Cu(-Mo) deposit. Green dots represent samples from the Southern Volcanic Zone (SVZ) compiled from many sources. The ore-related suite at Batu Hijau is from Fiorentini and Garwin (2009). Other Sunda and Banda arc samples are compiled from many sources. Ryukyu arc data in Figure 2c are compiled from many sources.

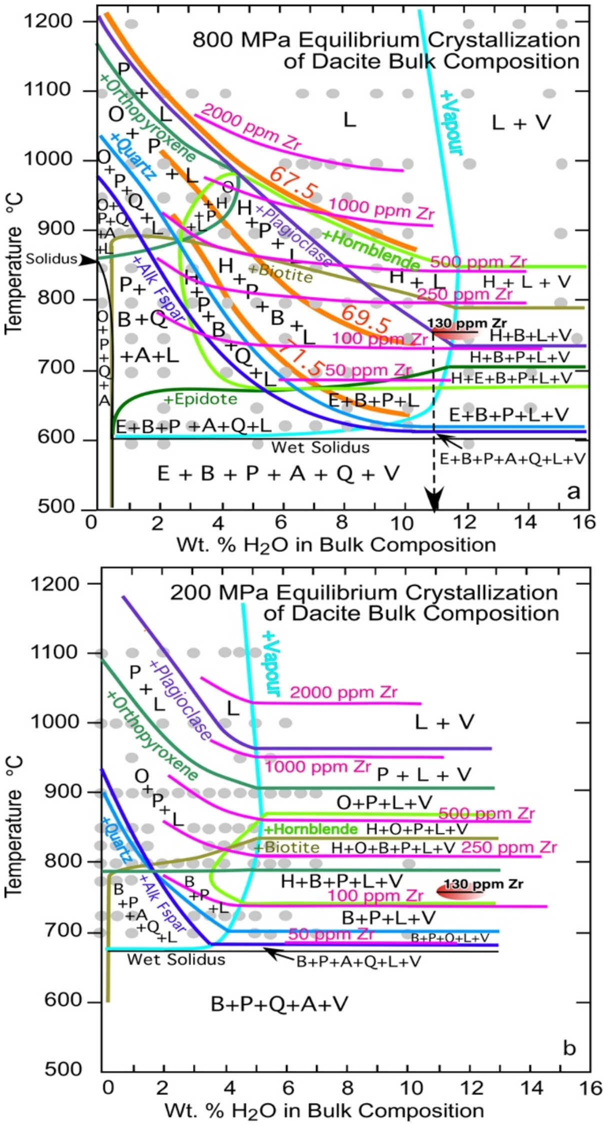

Figure 3(a,b). Stable phase assemblages at 800 MPa **(a)** and 200 MPa **(b)** in a dacitic bulk composition of varied H_2O content and temperature (grey dots; Naney, 1983). Orange contours show wt% SiO_2 in the melt (anhydrous basis). Pink contours show zircon solubility (ppm Zr) as calibrated by Crisp and Berry (2022). Phase labels: L = liquid (hydrous silicate melt), V = hydrothermal fluid, P = plagioclase, Q = quartz, A = alkali feldspar, B = biotite, H = hornblende, O=orthopyroxene, E = epidote. Crystallisation paths are vertical lines of constant bulk composition. At 800 MPa, hornblende saturates before plagioclase in bulk compositions having $\gtrsim$4.5 wt% H_2O, yielding adakitic high Sr/Y and Eu/Yb in residual melts. The average 130 ppm Zr in PCD-forming melts plots at the edge of the 800 MPa plag-undersaturated, hbld-saturated adakitic field.

3 Cause of low Zr in PCD-forming magmas

Al-in-hornblende evidence compiled by Loucks (2021, his Fig. 7) shows that PCD-forming magmas undergo magmatic differentiation mainly at Moho-vicinity pressures near 700-1100 MPa. Figure 3 shows experimentally determined phase relations in a granodiorite bulk composition at 800 and 200 MPa. At 800 MPa, as H_2O dissolved in the melt increases, saturation temperatures of anhydrous minerals are depressed more than the saturation temperature of zircon (subhorizontal contours), so in more hydrous melts, zircon advances in the saturation sequence of igneous minerals to precede plagioclase.

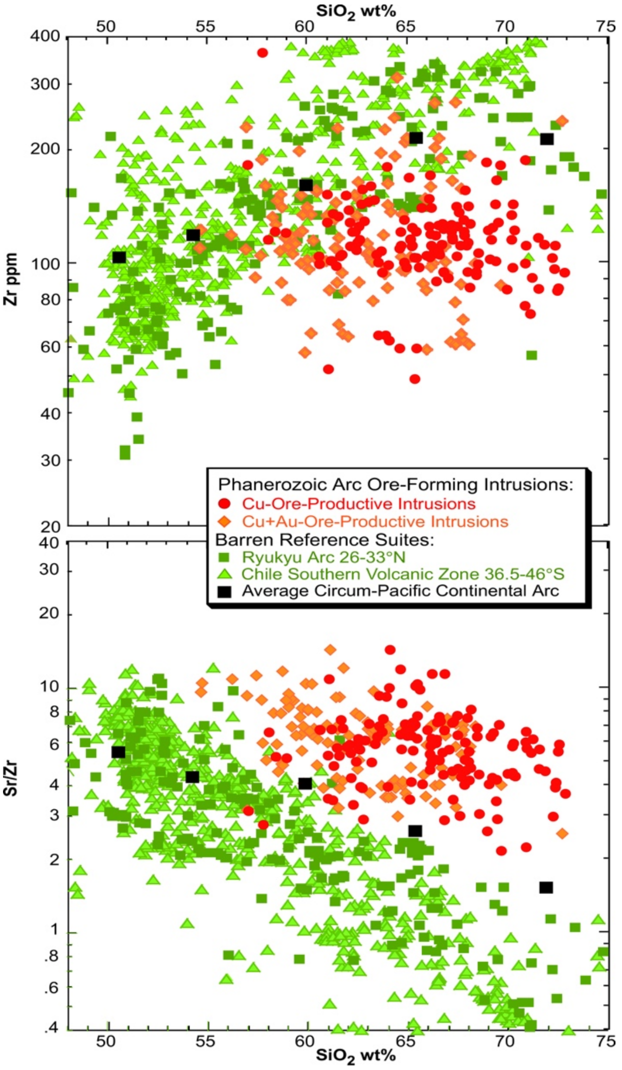

Figure 4(***a***). Zr contents of least-altered samples of intrusions directly parental to 120 major porphyry Cu(-Au-Mo) and high-sulphidation epithermal Cu-Au deposits of Phanerozoic age worldwide (compilation by Loucks, unpub) are represented by red and orange symbols . The Zr contents of these ore-stage magmas are compared to the Cu-infertile mafic-to-felsic differentiation series along the volcanic front of the continent-margin Ryukyu arc in the latitude interval 26–33°N. Black squares represent the Zr contents of average circum-Pacific continental-arc basalt, basaltic andesite, andesite, dacite, and rhyolite (from global compilations by R. Loucks, unpub).

(***b***) Cu-ore-forming calc-alkalic arc magmas have high Sr and low Zr contents, so the whole-rock Sr/Zr ratio is an effective discriminant of Cu-fertile intrusions having >57wt% SiO_2.

Very hydrous differentiation series reach plagioclase saturation and dacitic residual melt compositions at low temperatures, often <750°C. At such low temperatures, the Zr content of zircon-saturated melt is low. At 200 MPa, no crystallisation path (vertical) produces hornblende before plagioclase, so high-Sr/Y adakitic melts cannot develop at low pressures.

4 Application to mineral exploration

Figure 4 illustrates the effectiveness of whole-rock Zr and Sr/Zr ratios as discriminants of Cu-fertile magmas at convergent plate margins. The Sr/Zr ratio is applicable to samples retaining fresh or nearly fresh plagioclase.

Acknowledgements

This study was supported in part by the Australian Research Council Centre of Excellence for Core to Crust Fluid Systems grant CE110001017

References

Boyd TM, Creager KC (1991) The geometry of Aleutian subduction: three-dimensional seismic imaging. J Geophys Res 96: 2267-2291.

Conrad WK, Kay RW (1984) Ultramafic and mafic inclusions from Adak Island: crystallization history, and implications for the nature of primary magmas and crustal evolution in the Aleutian arc. J Petrol 25: 88-125.

Crisp LJ, Berry AJ (2022) A new model for zircon saturation in silicate melts. Contrib. Mineral. Petrol. 177, 71.

DeBari S, Kay SM, Kay RW (1987) Ultramafic xenoliths from Adagdak volcano, Adak, Aleutian Islands, Alaska: deformed igneous cumulates from the Moho of an Island arc. Jour Geol 9: 329-341.

Defant MJ, Drummond, MS (1990) Derivation of some modern arc magmas by melting of young subducted lithosphere. Nature 347: 662-665.

Drummond MS, Defant MJ, Kepezhinskas PK (1996) Petrogenesis of slab-derived trondhjemite–tonalite–dacite/adakite magmas. Trans Roy Soc Edinburgh, Earth Sci 87: 205-215.

Fiorentini, ML and Garwin, SL (2010) Evidence of a mantle contribution in the genesis of magmatic rocks from the Neogene Batu Hijau district in the Sunda Arc, southwestern Sumbawa, Indonesia: Contrib Mineral and Petrol 159: 819-837

Geist EL, Childs JR, Scholl DW (1988) The origin of summit basins of the Aleutian Ridge: implications for block rotation of an arc massif. Tectonics 7:327-341.

Johnson, MC., Plank, T (1999) Dehydration and melting experiments constrain the fate of subducted sediments. Geochem Geophys Geosyst 1: 1999GC000014

Kay SM, Kay RW, Citron GP. (1982) Tectonic controls on tholeiitic and calc-alkalic magmatism in the Aleutian arc. J Geophys Res 87: 4051-4072.

Loucks, RR (2021) Deep entrapment of buoyant magmas by orogenic tectonic stress: its role in producing continental crust, adakites, and porphyry copper deposits. Earth Sci. Rev. 220: 103744.

Naney MT (1983) Phase equilibria of rock-forming ferromagnesian silicates in granitic systems. Am. J. Sci. 283: 993-1033.

Rapp, RP, Shimizu N, Norman MD, Applegate GS (1999) Reaction between slab-derived melts and peridotite in the mantle wedge: experimental constraints at 3.8 GPa. Chem Geol 160:335-356.

Xiong X-L (2006) Trace element evidence for growth of early continental crust by melting of rutile-bearing hydrous eclogite. Geology 34: 945-948.

Pyrite as a porphyry Cu indicator mineral: new insights from the Myszków Mo-Cu-W deposit (Poland) and future perspectives

Beata Naglik[1], **Magdalena Dumańska-Słowik**[2], **Ryszard Habryn**[1], **Tomasz Toboła**[2], **Artur Sosnal**[1]
[1]*Polish Geological Institute-National Research Institute, Upper Silesian Branch, Sosnowiec, Poland*
[2]*AGH University of Science and Technology, Krakow, Poland*

Abstract. Due to rapid technological progress and copper's growing importance as a green metal for renewable energy solutions, the demand for this metal increases annually. Hence, there is a strong need to develop new exploration tools, which will be helpful to discover new, deep-seated, and possibly smaller deposits with high-grade ore mineralization. Nowadays, geochemical prospecting seems to show a big potential to vector concealed ore bodies as a good alternative to deep drilling, and what is more important it might be implemented ahead of time at relatively lower costs. Several geochemical proxies for tracking pathways of metal precipitation have been established (e.g. chlorite, epidote, alunite proximators). While the potential of pyrite appears not to have been fully exploited yet to predict the likely direction of mineralized ore centers. In this work, we conclude on the typomorphic characteristics, microtexture, solid inclusions, and major and trace composition of various generations of pyrite from the Myszków Mo-Cu-W deposit (Poland) to confirm its ability to preserve petrogenetic information on different ore-grade mineralized events. A pilot study of sulphur isotope composition in pyrite from this deposit seems to be a promising tool for detecting proximity to mineralized centres.

1 Introduction

The low-carbon future of our societies relies on access to numerous mineral raw materials, the majority of which are closely linked to renewable energy sources (e.g. the production of solar panels, wind turbines, and energy-efficient lighting) and sustainable mobility (e.g. electric vehicles), in which the strategic metals are currently irreplaceable. Increasing demand for strategic elements cannot be met solely by recycling; so primary resources mining will be still crucial in the near future. The most important world's primary source of mineral raw materials for modern industry such as Cu and Mo as well as important contents of critical and precious metals such as Au, Ag, W, and Re are porphyry Cu deposits (PCDs) and related epithermal Au deposits. They are intrusion-centered ore bodies, in which metal-bearing minerals precipitated from hydrothermal fluids within an intrusive host and surrounding country rocks. Porphyry ore deposits typically occur within an alteration halo with characteristic mineralogical and chemical zoning patterns (e.g. Sillitoe 2010).

If one takes into account the exploration degree of the geological structure of the European Union countries, the discovery of new deposits with outcrops on the surface seems unlikely. To meet future demand for the strategic metals (e.g. copper, tungsten), deep drilling and costly geophysical surveys are needed to discover deeper and possibly smaller deposits, including porphyry-Cu deposits, which are usually emplaced several kilometers below the Earth's surface. To assist porphyry exploration, the development of new pathfinders to target high-grade mineralization at reduced environmental and economic risk is therefore of significant interest.

Geochemical exploration seems to provide the response to these ongoing challenges. To date, significant research efforts have been made to develop effective geochemical vectoring tools, mostly based on whole rock geochemistry, e.g. Hf concentration, the Sr/Y, V/Sc, and Th/U ratios (Richards 2011; Loucks 2014). However, these proxies have limited applicability, since the hydrothermal fluids associated with ore deposits commonly obliterate the primary minerals and alter the whole-rock geochemical composition (e.g. Seedorff et al. 2005).

Quite recently, an alternative approach has been proposed that uses the compositions of individual magmatic and hydrothermal minerals to predict the likely direction and distance to mineralized centers, and the potential metal endowment of a research area, i.e. Ti-in chlorite proximitor. (Wilkinson et al. 2015). However; the utility of mineral indices depends on the question of whether they are reproducible enough to be applicable in any porphyry-style system worldwide or maybe they are useful only in some specific terranes. The development of appropriate geochemical tools for exploration under cover is therefore a very challenging task and requires many validation studies in different geological settings to make them mature tools for tracing fluid flow pathways.

Pyrite is one of the indicator mineral that shows chemical and structural variations in response to a changeable ore-forming environment. In addition to being an important carrier of metalloids (As), precious (Au), and base (Cu) metals, pyrite also could be considered as a proxy indicator of physico-chemical conditions of its crystals growth (pH, temperature, redox, fluid-wall interactions, the composition of host rocks, phase separation and/or boiling). However; it is still a matter of debate if this robust mineral could be also used as an exploratory guide. Up to date, most studies have been focused on pyrite geochemistry as a tool for distinguishing different deposit types, mostly based on the Co/Ni ratio. The recent advances in LA-ICP-MS have stimulated debates regarding the possibility to use pyrite geochemistry as a proxy for the mineralization centre in some hydrothermal ore deposits (e.g. Genna and Gaboury, 2015).

Hence, different generations of pyrite from the Myszków Mo-Cu-W deposit (the Kraków-Lubliniec Fault Zone - KLFZ, Central Poland) were comprehensively studied by mineralogical and geochemical techniques (Naglik et al. 2021; Naglik et al. 2022) and this paper concludes with an outlook to the future of the pyrite potential for further mineral prospecting in the porphyry Cu environment. The special interest given to the Myszków Mo-Cu-W deposit comes from the fact, that it has been recognized in detail through several dozen deep boreholes, and thus gives a unique opportunity to study systematic variations of pyrite characteristics with high resolution. It also remains the only European porphyry-style deposit of the Variscan age, and undergoing active exploration (Sutphin et al. 2013).

2 Geological settings

Porphyry copper mineralization of the Myszków Mo-Cu-W deposit is located at the contact zone between two distinctive tectonic units: (1) the Upper Silesian Block (USB) and (2) the Małopolska Block (MB), which have been considered as terranes of Gondwana and Baltica affinity, respectively. The most recent zircon U–Pb dating by SHRIMP (Jarmołowicz-Szulc 2020; Mikulski et al. 2019) together with Re-Os data of molybdenites (Stein et al. 2005) indicate Late Carboniferous to Early Permian age of magma generation and related mineralization events. Since most Variscan igneous rocks are either deeply eroded or petrochemically unsuitable for porphyry copper association, the Myszków Mo-Cu-W deposit provides an unusual example of porphyry copper mineralization with no analogue in Europe.

Despite the different age of the Myszków Mo-Cu-W deposit, the overall geochemical characteristics, mineralogy, and vein morphology are typical of calc-alkaline porphyry copper deposits elsewhere. The ore mineralization resulted here from both contact metamorphism (early, skarn type mineralization) and post-magmatic hydrothermal activity (main hydrothermal mineralization). Generally, three periods of mineralization have been defined at the Myszków deposit: (1) early, skarn-forming (period I), (2) main, hydrothermal (period II), and (3) late, post-ore (period III) (Ślósarz 2001, 1985). Period I is represented by magnetite-sulfide mineralization found in hornfelses, skarns, and metasomatites. Within period II, different stages of ore deposition have been distinguished: (1) feldspar-molybdenite veins with biotite, (2) quartz-feldspathic, pegmatitic veins, (3) quartz veins with molybdenite and scheelite (stockwork system), (4) black quartz veins with molybdenite, and (5) quartz-polymetallic veins (without molybdenite). Finally, period III produced mainly ankerite and barite-fluorite mineralization.

3 Typomorphic of porphyry-style pyrite in different mineralization stages

Four various generations of pyrite from the Myszków Mo-Cu-W deposit were analyzed by Naglik et al. (2021; 2022): (1) the I-type pyrite from the early, skarn-forming stage of mineralization; (2) the II-type pyrite coming from quartz-feldspathic pegmatitic veins; (3) the III-type pyrite from quartz veins with coexisting molybdenite and scheelite; and (4) the IV-type pyrite representing quartz-polymetallic assemblage.

The I-type pyrite, representing the early, skarn-forming stage of mineralization forms anhedral, fractured grains, often intergrown with biotite and magnetite. Generally, the I-type pyrite is characterized by a porous texture with clustered pores and abundant mineral inclusions, interpreted as a result of vigorous boiling (Naglik et al. 2021). Py-I shows relatively high average amount of Ni (~740 ppm) and Co (~640 ppm); however concentration of those elements exhibits a heterogenous, non-concentric mode. Such non-uniform trace elements distribution in pyrite was interpreted as another evidence of boiling. Elevated concentrations of Ni and Co in Py-I may point to the origin of mineralizing fluids with some mafic affinity (Naglik et al. 2022). The I-type pyrite probably crystallized over a wide range of temperatures. Some pyrite grains occur in close spatial association with biotite and magnetite and also host inclusions of these minerals. Hydrothermal biotite and magnetite are stable at a temperature higher than 450°C and such conditions probably also reflect the crystallization environment of I-type pyrite. However, the crystallization of pyrite continued until the fluids became much cooler, as evidenced by the presence of grains containing inclusions of Bi-minerals (e.g. bismuthinite).

The II-type pyrite comes from quartz-feldspathic pegmatitic veins. It contains numerous voids that can be relics of fluid inclusions. This generation of pyrite was probably formed under boiling conditions as evidenced by e.g. its co-existence with bladed-like calcite (Naglik et al. 2021). The most distinctive geochemical feature of Py-II is the relatively high Se/Te ratio, calculated at 28.30. It goes beyond the overall trend for the Myszków deposit according to which the Se/Te ratio decreases with a temperature of vein formation. Subtle differences between Py-II from central and more distal parts of the deposit were captured, including an increase of Co and Ni content toward the mineralization centre.

The III-type pyrite occurs in stockwork veins filled with quartz, molybdenite and scheelite. It formed under gentle to non-boiling conditions, and is characterized by a relatively diversified set of inclusions but their number within the single grain is relatively low. The III-type pyrite was probably precipitated from fluids of low oxygen fugacity (fO2) which is suggested by the Te enrichment and the occurrence of cassiterite inclusions (Naglik et. al. 2022). It was formed from fluids of moderate temperature, locally exceeding 400°C (primary inclusions of rutile). In contrast, associated quartz crystallized from oxidized fluids with tracers of boiling, at a temperature ranging from 360-240°C (Ślósarz 2001). Interestingly, the solid inclusions assemblages hosted in stockwork pyrite vary laterally and thus reflect the decreasing temperature outward from a central heat source.

The IV-type pyrite represents the final stage of main hydrothermal activity in the system. Pyrite forms euhedral to subhedral grains with cataclastic texture and numerous microfractures filled with galena and sphalerite. It shows scarcity of solid inclusions as being deposited under stable physicochemical conditions. Py-IV is rather depleted in trace elements; however, it contains the significant traces of As that correspond to the detectable content of structurally-bonded Au and Sb (Naglik et al. 2022). It bears, therefore, a quasi-epithermal signature. In addition, the association of As and Sb in Py-IV could be considered as a characteristic feature of fluids that underwent boiling at depth. The IV-type pyrite probably crystallized at a lower temperature range, as manifested by the presence of pyrite-hosted inclusions of aikinite-group minerals, which form at about 300°C. In this case, pyrite-hosted solid inclusions provided quite a good approximation to microthermometric results from co-existing gangue phases, according to which ores were formed from fluids at a temperature ranging from 298°C to 275°C (Ślósarz 2001).

4 The outlook

The critical economic value of PCDs caused the long-lasting research interest given to their origin and zonality patterns. However, still more research data is needed to be provided to broaden our knowledge about the metallogeny of this type of deposit. Some of the most challenging issues in that field include: (1) the tectonic regime of mineralization (i.e. a relation of porphyry deposits to large-scale tectonic events); (2) the physicochemical properties of mineralizing fluids (i.e. mechanisms of sulfides transport and their deposition, the origin of fluids salinity essential for mobilizing large quantities of the base metals, direct temperature-pressure conditions); (3) life span of magmatic/post magmatic activity; (4) the variation of fluids composition along with time and their impact on the ore minerals distribution; and (5) the influence of mafic magmas inputs on the deposit formation.

Another aspect is related to mineral prospecting. New mineral deposits are becoming more and more difficult to find and hence, further new proxies toward mineralization centre are very welcome to aid exploration wherever bulk or mineral indices are ineffective.

A new way of detecting proximity to the mineralized porphyry systems could be obtained with isotope geochemistry, including sulphur isotope composition of pyrite. To provide significant added value and novelty for prospecting, further new geochemical indices should provide more precise information than can be obtained from bulk or mineral proxies, which hopefully will be more reproducible, i.e. enable to successfully localize centre of high-grade mineralization irrespective of the deposit geotectonic settings, the composition of the host intrusive, nature of the wall rocks, age of mineralization, erosion level, and size of the ore body. It is believed that the isotopic-based approach meets these criteria as probably being sensitive to the widespread boiling phenomena. Commonly, extensive boiling of hydrothermal fluids accompanies deposition of ore and gangue minerals, and thus, boiling horizons are considered a key-guides for exploration (e.g. Ham 1978). Hence, isotopic proxies provide vectors directly to the zones of the economic-grade mineralization, not to the source of heat, as do the mineral indices, i.e. Ti-in chlorite proximitor (Cook et al. 2020). Sulphides precipitate in response to the temperature decrease and therefore, the center of thermal anomaly is not the center of high-grade mineralization (Cook et al. 2020).

A pilot study related to the isotopic signature of pyrite from the Myszków Mo-Cu-W deposit has already started at PGI-NRI. A small systematic variation of the S isotopic composition of pyrite is being recognized *via* SHRIMP. If some lateral zoning in the S composition of pyrite does exist in the porphyry Cu system, this new mineral indice might be utilized in the other perspectives areas at the Kraków-Lubliniec Fault Zone – one of the most promising tectonic unit for discovering new concealed Cu deposits of porphyry-type in Central Europe. It must be stated that systematic variations in sulphur isotope composition of pyrite were previously recognized in alkalic porphyry deposits of British Columbia (Pass 2010) and in the Cadia district, Australia (Wilson et al. 2007).

Moreover, as being formed under vigorous *via* gentle to non-boiling conditions (Naglik et al. 2021), pyrite and associated quartz from the KLFZ make this system a natural laboratory to investigate the geochemical behaviour of trace elements during boiling phenomena. The combination of microthermometry and geochemistry of pyrite- and quartz-hosted fluid inclusions (FIs) offers a unique opportunity to explore the vapour-liquid partitioning of metals over the wide range of temperature, pressure, and salinity of fluids. The boiling-induced effects on the distribution of elements in the studied area is not well-understood. This question becomes more intriguing when one takes into account the different geochemical behaviour of ore-forming components in various hydrothermal systems. For example, Au could be either preferentially partitioned into the brine (e.g. Keith et al. 2020) or the vapour (e.g. Heinrich et al. 1999) during boiling, and thus, redeposited at different distances from causative porphyry (or dispersed in country rocks).

5 Summary

Pyrite from the Myszków porphyry Mo-Cu-W deposit (the Kraków-Lubliniec Fault Zonce, Poland) possesses several distinctive features with respect to spatial and temporal system evolution. It shows a diversified set of solid inclusions that reflect geobarometric and geothermometric information as well as represent the fluid conditions reached before their entrapment by the host mineral. Variations in compositional features of pyrite from different mineralization stages point to the changes in ore-forming processes along with time. Some geochemical differences between pyrites formed under boiling to non-boiling events were also found (e.g. Co, As, Sb and Au distribution). Our results confirm therefore that pyrite retains typomorphic characteristics of its ore and bears key-petrogenetic information, i.e. fingerprints of boiling.

Further studies of pyrite are therefore required and should include near-infrared microthermometric measurements and geochemical analysis *via* LA-ICP-MS of pyrite-hosted fluid inclusions.

However, when considering geochemical and morphological features of pyrite as a function of the proximity to high-grade mineralization the differences between specimens of main-stage pyrite are rather subtle and include changes in solid inclusions assemblages and small variations in geochemical composition, e.g. Co and Ni content. However, the isotopic characterization of pyrite might bring new solutions in this regard.

Acknowledgements

The final editorial work was financially supported by the Polish Geological Institute-National Research Institute statutory funds (Project No. 62.9012.2317.00.0 for B.N.) and the AGH University of Science and Technology (Project No. 16.16.140.315).

References

Cooke D. R., Wilkinson J.J., Baker M., Agnew P., Phillips J., Chang Z., Chen H., Wilkinson C.C., Inglis S., Hollings P., Zhang L., Gemmell J.B., White N.C., Danyushevsky L., Martin H. (2020) Using mineral chemistry to aid exploration: A case study from the Resolution porphyry Cu-Mo deposit, Arizona. Econ. Geol. 115(4): 813-840.

Genna D., Gaboury, D. (2015) Deciphering the hydrothermal evolution of a VMS system by LA-ICP-MS using trace elements in pyrite: an example from the Bracemac-McLeod deposits, Abitibi, Canada, and implications for exploration. Econ. Geol. 110(8): 2087-2108.

Ham C.G.C. (1978) Pressure gradients and boiling as mechanisms for localizing ore in porphyry systems. US Department of the Interior, 6(6): 745-754.

Heinrich C.A., Gunther D., Audétat A., Ulrich T., Frischknecht R. (1999) Metal fractionation between magmatic brine and vapor, determined by microanalysis of fluid inclusions. Geology, 27(8): 755-758.

Jarmołowicz-Szulc K. (2020) A reappraisal of K-ar and new U-pb age data for felsic rocks in the vicinity of the kraków-lubliniec fault zone (Southern Poland). Geol. Q. 64: 754–765. https://doi.org/10.7306/gq.1549.

Keith M., Smith D.J., Doyle K., Holwell D.A., Jenkin G.R., Barry T.L., Becker J., Rampe J. (2020) Pyrite chemistry: A new window into Au-Te ore-forming processes in alkaline epithermal districts, Cripple Creek, Colorado. Geochim. Cosmochim. Acta, 274: 172-191.

Loucks R.R. (2014) Distinctive composition of copper-ore-forming arcmagmas. Austral. J. Earth Sci. 61(1): 5-16.

Mikulski S.Z., Williams I.S., Markowiak M. (2019) Carboniferous-Permian magmatism and Mo-Cu (W) mineralization in the contact zone between the Małopolska and Upper Silesia Blocks (south Poland): An echo of the Baltica-Gondwana collision. Int. J. Earth Sci. 108(5): 1467-1492.

Naglik B., Dumańska-Słowik M., Toboła T., Derkowski P., Habryn R., Markowiak M. (2021) Diversity of Pyrite-Hosted Solid Inclusions and Their Metallogenic Implications — A Case Study from the Myszków Mo-Cu-W porphyry deposit (the Kraków-Lubliniec Fault Zone, Poland). Minerals 11: 1426.

Naglik B., Toboła T., Dumanska-Slowik M., Dimitrova D., Derkowski P., Zielinski G., Habryn R., Nadlonek, W. (2022) Multi-stage ore forming history of the Variscan porphyry Mo-Cu-W Myszków deposit (Poland): evidence from trace elements of pyrite. Ore Geol. Rev. 105185.

Pass H.E. (2010) Breccia-hosted chemical and mineralogical zonation patterns of the Northeast Zone, Mt. Polley Cu-Ag-Au alkalic porphyry deposit, British Columbia, Canada. Dissertation, University of Tasmania.

Richards J.P. (2011) High Sr/Y arc magmas and porphyry Cu±Mo±Au deposits: just add water. Econ. Geol. 106(7): 1075-1081.

Seedorff E., Dilles J.H., Proffett J.M., Einaudi M.T., Zurcher L., Stavast W.J., Johnson D.A., Barton M.D. (2005) Porphyry deposits: Characteristics and origin of hypogene features. Society of Economic Geologists.

Sillitoe R.H. (2010) Porphyry Copper Systems. Econ. Geol. 105: 3-41. https://doi.org/10.2113/gsecongeo.105.1.3.

Stein H., Markowiak M., Mikulski S.Z. (2005) Metamorphic to magmatic transition captured at the Myszków Mo-W deposit, southern Poland. In: Mao J., Bierlein F.P. (eds) Mineral Deposit Research: Meeting the Global Challenge. Springer Berlin Heidelberg, Berlin, pp. 833-836.

Sutphin D.M., Hammarstrom J.M., Drew L.J., Large D.E., Berger B.R., Dicken C., DeMarr M.W. (2013) Porphyry Copper Assessment of Europe, Exclusive of the Fennoscandian Shield, In: Global Mineral Resource Assessment (No. 2010-5090-K), US Geological Survey.

Ślósarz J. (2001) Mineralogical characteristics of the mineralization. In: Podemski M. (ed) Palaeozoic Porphyry Molybdenum-Ungsten Deposit in the Myszków Area, Southern Poland. Polish Geological Institute, Special papers, Warsaw, pp. 43-53.

Wilkinson J.J., Chang Z., Cooke D.R., Baker M.J., Wilkinson C.C., Inglis S., Chen H., Gemmell, J.B. (2015) The chlorite proximitor: A new tool for detecting porphyry ore deposits. J. Geochem. Explor. 152: 10-26.

Wilson A.J., Cooke D.R., Harper B.J., Deyell C.L. (2007) Sulfur isotopic zonation in the Cadia district, southeastern Australia: exploration significance and implications for the genesis of alkalic porphyry gold–copper deposits. Miner. Depos. 42: 465-487.

Cold arc magma differentiation linked to porphyry copper deposit formation?

Chetan Nathwani[1,2,3], Simon Large[1], Jon Blundy[4], Matthew Loader[1], Yannick Buret[1], Jamie J. Wilkinson[1,2], Katie McCann[1,2], Cyril Chelle-Michou[3]
[1]*London Centre for Ore Deposits and Exploration (LODE), Natural History Museum, London, United Kingdom*
[2]*Department of Earth Science and Engineering, Imperial College London,* United Kingdom
[3]*Institute of Geochemistry and Petrology, Department of Earth Sciences, ETH Zürich, Switzerland*
[4]*Department of Earth Sciences, University of Oxford, United Kingdom*

Abstract. The key processes responsible for the genesis of world-class porphyry copper deposits remain ambiguous. A high water content of parental magmas evolved in the deep crust is posited to be one key control on their formation, yet remains controversial. Here, we report trace element compositions of whole-rocks and zircons that pre-, syn- and post-date mineralisation from several major porphyry copper districts. We find clear temporal trends of decreasing zircon Ti and whole-rock Zr. Across all studied deposits and literature data, we find low zircon Ti and whole-rock Zr concentrations are inherent to intrusive rocks associated with porphyry Cu deposits. According to the Ti-in-zircon thermometer and zircon solubility models, these concentrations are consistent with porphyry Cu-related magmas being cold relative to other intermediate-felsic magmas (<800°C). We perform thermodynamic modelling to demonstrate that such low temperature magma differentiation can be readily explained by elevated water concentrations (>6 wt.%) of porphyry Cu magmas at depth which displaces the liquidus to lower temperatures. By integrating this with the latest zircon solubility models, we show that wet magma differentiation leads to zircon appearing as a relatively early crystallising phase at low temperature. Our study therefore provides new evidence that magmas related to porphyry Cu deposits contain characteristically high water contents (>6 wt.%).

1 Introduction

Porphyry copper deposits account for the majority of global copper and molybdenum production. Many of these systems are associated with syn-subduction magmatism and form during periods of strong compression and crustal thickening (Sillitoe 2010). The key magmatic processes responsible for the formation of an economic porphyry copper deposit, as opposed to a barren or subeconomic intrusion remain debated. Some have suggested that high magmatic water contents may be important, where differentiation of magmas at high pressure allows significant water to accumulate in derivative melts. This can subsequently enhance the ability of a magma to generate large volumes of copper-charged fluid (Richards 2011, Chiaradia and Caricchi 2017). However, it has been argued that particularly wet arc magmas will rarely reach upper crustal levels, because they water saturate at depth leading to crystallisation and stalling (Chiaradia 2020). Other authors have argued that alternative processes may be more important including: high magmatic oxidation state, chalcophile fertility, large volumes of magma accumulation and rates of magma flux (Wilkinson 2013, Chelle-Michou and Rottier 2021).

Here we report whole-rock and zircon trace element compositions for rocks which overlap with batholith assembly and porphyry copper mineralisation in several porphyry copper districts. We focus in particular on the Los Bronces district, Central Chile, which is hosted by the San Francisco Batholith that records up to ~10 Myr of barren pluton assembly. We focus on temporal changes in whole-rock Zr and zircon Ti concentrations, and their ability to track changes in melt temperature and water content which reach minima and maxima, respectively, during porphyry Cu mineralisation.

2 Methodology

2.1 Sampling

Samples were collected from the Los Bronces porphyry Cu-Mo district (Fig. 1). Rocks were sampled from several discrete phases of the San Francisco Batholith and pre-mineralisation, sub-economic porphyry intrusions from across the district, in order to span the period leading up to porphyry Cu mineralisation. Samples of intrusions at Los Bronces interpreted to be coeval with porphyry mineralisation were collected from drillcore.

Samples were also collected from a range of other porphyry systems including Los Pelambres (Central Chile), Corcapunta (Peru), Chipispaya (Southern Peru) and Cerro Colorado (Northern Chile). Data were also compiled from a range of literature sources which report zircon trace element compositions in porphyry copper districts.

2.2 Whole-rock geochemistry

Rocks were crushed and pulverised to pulps and were analysed by inductively-coupled plasma atomic emission spectrometry for major elements and inductively-coupled plasma mass spectrometry for trace elements.

2.3 Zircon trace element geochemistry

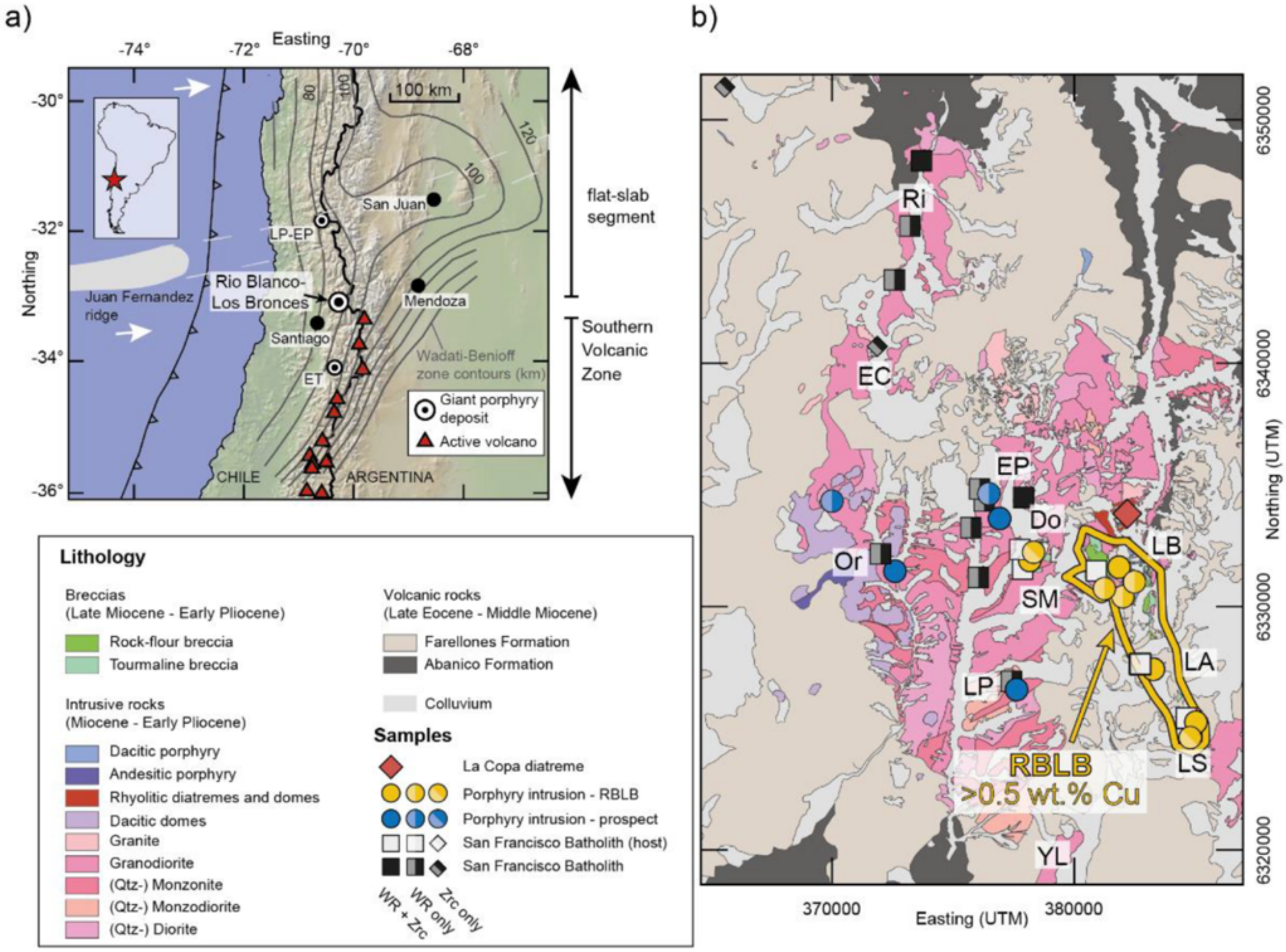

Figure 1. Geological map and setting of the San Francisco Batholith (SFB) and Rio Blanco-Los Bronces (RBLB) porphyry deposit cluster. A) Regional topographic map of Central Chile highlighting location of RBLB and neighbouring giant porphyry Cu clusters (Los Pelambres-El Pachon – LP-EP and El Teniente – ET). B) District-scale geological map of RBLB deposit cluster (modified after Piquer 2015). Sample localities are shown together with the surface expression of the domain containing >0.5 wt.% Cu (yellow line). District deposits/prospects are also shown: Do: Quebrada Dolores, EC: El Cruce, LA: La Agustina, LB: Los Bronces, LP: Los Piches, LS: Los *Sulfatos, Or: Ortiga, Ri: Riecillos, SM: San Manuel, YL: Yerba Loca.*

Zircons were separated from a subset of sampled rocks using conventional mineral separation techniques. They were first imaged using scanning electron microscope cathodoluminescence, and then analysed for trace element compositions using laser ablation inductively-coupled plasma mass spectrometry (LA-ICP-MS) synchronously with the isotopes required for U-Pb geochronology. All analyses were performed in the Imaging and Analysis Centre at the Natural History Museum, London.

2.3 Modelling of zircon saturation

The effect of melt water content on melt temperatures was modelled using rhyolite-MELTS (Ghiorso and Gualda 2015). Equilibration of a starting andesite-dacite was carried out over a range of temperatures, water contents and pressures. Zircon solubility was also integrated into this model using the latest empirical models (Crisp and Berry 2022).

3 Zr systematics and zircon Ti concentrations

Whole-rock Zr concentrations decrease over time in the Los Bronces district, from 200-300 ppm to ca. 100 ppm Zr. Zircon Ti decreases over the same time period, with the pre-mineralisation zircons predominantly having concentrations between 20 and 5 ppm, whereas zircons from the porphyry intrusions associated with peak Cu mineralisation have < 5 ppm Ti.

In other porphyry systems studied here and reported from literature data, whole-rock Zr and zircon Ti generally decrease over time. Low whole-rock Zr (<150 ppm) and low zircon Ti (<7 ppm) are observed in all rocks associated with porphyry Cu mineralisation.

4 Do low temperatures and high water contents characterise porphyry magmas?

Crystallisation temperatures were calculated for zircon based on Ti concentrations using the experimental calibration of Ferry and Watson (2007) and implementing a pressure correction (Loucks et al. 2020). Assuming an activity of titania ($aTiO_2$) of 0.6, an activity of silica of 1.0 ($aSiO_2$) and a pressure of 400 MPa, porphyry zircons yield temperatures of 850-750ºC. Based on an evaluation of the influence of variable $aTiO_2$ and pressure on zircon Ti concentrations we suggest that these parameters cannot fully account for the inherently low Ti in porphyry-related zircons.

We also attempted to calculate temperatures from whole-rock Zr in porphyry rocks, assuming porphyry rocks represent crystallised liquids and implementing Zr saturation thermometry. This approach yielded crystallisation temperatures of 700-740 ºC.

The low temperatures inferred for porphyry magmas from the zircon record may be related to the timing of zircon saturation in such magmas and/or intrinsically lower magma temperatures. One key control on this may be melt water content, since previous work has suggested that magmas forming porphyry Cu deposits may have elevated water contents relative to typical arc magmas. In wet magmas, the liquidus is displaced to lower temperatures. Such low temperatures would thus be recorded upon zircon saturation.

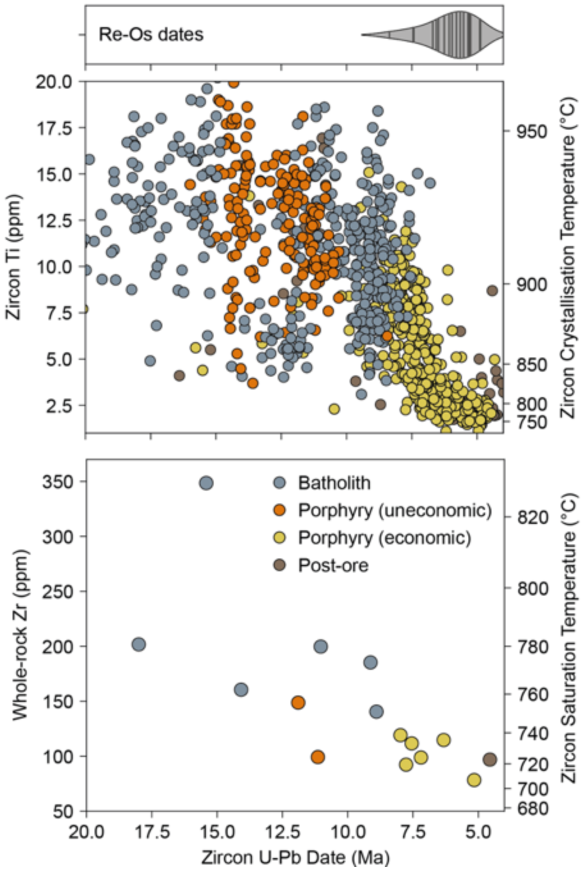

Figure 2. Zircon Ti and whole-rock Zr concentrations in the Los Bronces district over time. For zircon Ti concentrations, the U-Pb dates are single grain LA-ICP-MS analyses, whereas for whole-rock Zr these are weighted mean U-Pb dates. Temperature axes are given to show approximate temperature ranges according to Ti-in-zircon thermometry (Ferry and Watson 2007) and zircon saturation thermometry (Crisp and Berry 2022). Density distribution of molybdenite Re-Os mineralization dates is derived from data in Toro et al. (2012).

In order to test this, we used rhyolite-MELTS to model the influence of increasing water contents on the liquidus temperature and thermal trajectory of magmas during their storage and crystallisation. We also monitored the timing of zircon saturation in these models. We find that increasing initial melt H_2O from 2 to 6 wt.% can decrease the temperature of zircon saturation by ~100ºC and that the initial Zr concentration of the magma strongly influences the temperature of zircon saturation. Decreasing initial Zr from 200 to 100 ppm leads to a ~70ºC decrease in the temperature of zircon saturation.

Our results suggest that porphyry-related magmas contain elevated concentrations of water (>6 wt.%) and that zircons in these magmas crystallised at low temperatures at mid-crustal depths (>400 MPa), where, in intermediate to felsic melts, such water solubility is possible. This finding is in accordance with studies linking porphyry copper deposit formation to wet, high-pressure arc magma differentiation.

5 Conclusions

Low whole-rock Zr and low zircon Ti are characteristic signatures of intrusive rocks associated with porphyry copper mineralisation. Distinct trends of decreasing whole-rock Zr and decreasing zircon Ti over multi-Myr durations in porphyry Cu districts track decreasing temperatures of magmas over time. We interpret these lower temperatures to reflect increasing melt water contents, which displaces the liquidus to lower temperatures. High water contents lead to zircon appearing as a relatively early crystallising phase at low temperatures. We suggest that zircons in porphyry Cu deposits record a history of deep, hydrous arc magma differentiation. Our study highlights that elevated melt water contents (>6 wt.%) are a key feature of magmas associated with porphyry Cu deposit formation.

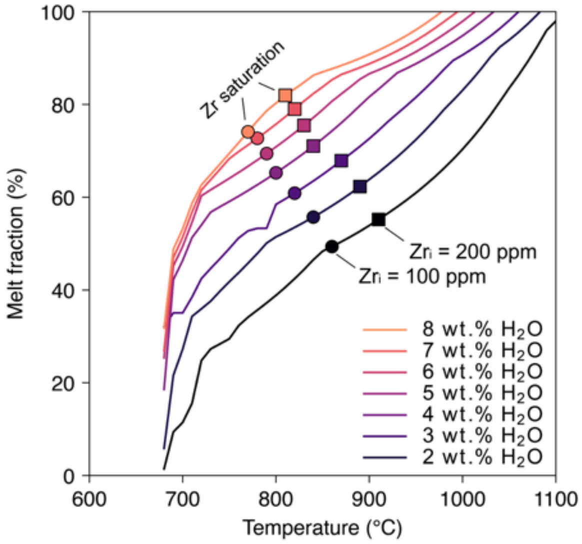

Figure 3. Results of rhyolite-MELTS modelling showing the temperature versus melt fraction of a cooling magma for different water contents between 2 and 8 wt.% H_2O. Symbols indicate the point of zircon saturation in each model given an initial Zr concentration (Zr_i) of 100 ppm (circles) and 200 ppm (squares).

Acknowledgements

This study was funded by NERC grant NE/P017452/1 “From Arc Magmas to Ore Systems” (FAMOS). CN also acknowledges funding from an ETH Zürich postdoctoral research fellowship. We are grateful to Anglo American, BHP and Antofagasta Minerals for providing access to samples and sampling localities for this project, and on-site geologists and staff for their support.

References

Chelle-Michou C, Rottier B (2021) Transcrustal magmatic controls on the size of porphyry Cu systems–State of knowledge and open questions. Society of Economic Geologists Special Publication 1:. https://doi.org/doi: 10.5382/SP.24.06

Chiaradia M (2020) How Much Water in Basaltic Melts Parental to Porphyry Copper Deposits? Frontiers in Earth Science 0: https://doi.org/10.3389/feart.2020.00138

Chiaradia M, Caricchi L (2017) Stochastic modelling of deep magmatic controls on porphyry copper deposit endowment. Scientific Reports 7:44523. https://doi.org/10.1038/srep44523

Crisp LJ, Berry AJ (2022) A new model for zircon saturation in silicate melts. Contrib Mineral Petrol 177:71. https://doi.org/10.1007/s00410-022-01925-6

Ferry JM, Watson EB (2007) New thermodynamic models and revised calibrations for the Ti-in-zircon and Zr-in-rutile thermometers. Contributions to Mineralogy and Petrology 154:429–437. https://doi.org/10.1007/s00410-007-0201-0

Ghiorso MS, Gualda GAR (2015) An H2O–CO2 mixed fluid saturation model compatible with rhyolite-MELTS. Contributions to Mineralogy and Petrology 169:53. https://doi.org/10.1007/s00410-015-1141-8

Loucks RR, Fiorentini ML, Henríquez GJ (2020) New Magmatic Oxybarometer Using Trace Elements in Zircon. Journal of Petrology 61:. https://doi.org/10.1093/petrology/egaa034

Richards JP (2011) High Sr/Y arc magmas and porphyry Cu ± Mo ± Au deposits: just add water. Economic Geology 106:1075–1081. https://doi.org/10.2113/econgeo.106.7.1075

Sillitoe RH (2010) Porphyry Copper Systems. Economic Geology 105:3–41. https://doi.org/10.2113/gsecongeo.105.1.3

Toro JC, Ortúzar J, Zamorano J, et al (2012) Protracted magmatic-hydrothermal history of the Río Blanco-Los Bronces district, Central Chile: Development of world’s greatest known concentration of copper. Society of Economic Geologists Special Publication 16:105–126

Wilkinson JJ (2013) Triggers for the formation of porphyry ore deposits in magmatic arcs. Nature Geoscience 6:917–925. https://doi.org/10.1038/ngeo1940

LA-ICP-MS trace element analysis of pyrite from the Bakoudou gold deposit, South Gabon: Implications for ore genesis

Nazaire Nzaou Mabika[1] **, Amina Wafik** [1] **, Abdellah Boushaba** [2] **, Damien Gaboury**[3]**, Lhou Maacha** [4]**, Gharrabi Mohamed** [4]**, Benyounes Maamar** [4]
[1] *Cadi Ayyad University, Marrakech, Morocco*
[2] *Sidi Mohamed Ben Abdellah University, Fes, Morocco*
[3] *Université du Québec à Chicoutimi, Chicoutimi, Canada*
[4] *Managem Mining Company (SA), Casablanca, Morocco*

Abstract. The Bakoudou gold deposit, southern Gabon, is hosted in the Archean basement granitoids of the Chaillu Massif. The orebody of the Bakoudou gold deposit occurs as quartz veins hosted in shear zones crosscutting TTG intrusive rocks. Quartz is the main gangue mineral, with minor sulfides such as pyrite and chalcopyrite. Gold is present in solid solution (Au^{+1}) and as nanoparticles of native gold (Au^0) in pyrite and mostly as free gold. Pyrite samples analysed by laser ablation inductively coupled plasma mass spectrometry (LA-ICP-MS) show high Ni (3.24–3600 ppm) and Co (4.68–4140 ppm) and low As (<34.50 ppm) and Au concentrations (<2.90 ppm) compared to Cu, which has rather high concentration of <3570 ppm. Moreover, the Au–As relationships of pyrites show a porphyry–epithermal transitional signature. Therefore, the Bakoudou gold deposit can be considered an example of Archean porphyry–epithermal transitional gold system, formed from magmatic fluids originating from a hidden porphyry system at depth. The disseminated free gold grains in the quartz veins may have originated from boiling of the mineralizing fluid (phase separation) and/or from remobilization of invisible gold in pyrite by later tectonic events and surficial weathering.

1 Introduction

The Precambrian basement of western Central Africa is represented by the Congo Craton, which covers the Gabon-Democratic Republic of Congo border and extends to the Cameroon-Gabon border (Nédélec et al. 1990). This basement is composed of Archean cratons welded together by Meso- and Paleoproterozoic belts (De Wit and Linol 2015) and is mainly represented on the Gabonese territory by the Chaillu Massif and the North Gabon Massif (Thieblemont et al. 2009) (Figure 1). Gold mineralizations are common in the Archean basement of Gabon, and many placers have been exploited by artisans (Thiéblemont et al. 2009). However, primary gold mineralizations are rare, and the main representative example is the Bakoudou gold deposit (Thiéblemont et al. 2009). It is located in southeastern Gabon, in Haut-Ogooué Province, more precisely on the edge of the Chaillu Massif, approximately 100 km southwest of the Franceville basin (Thiéblemont et al. 2009, Figure 1). The gold mineralization occurs as quartz veins hosted in the gray granitoids of the Chaillu Massif (Thiéblemont et al. 2009). In this abstract, we provide and interpret trace element data from pyrite to constrain the origin and typology of the Bakoudou gold mineralization.

2 Methodology

Trace element concentrations from 23 pyrite grains were acquired by laser ablation inductively coupled plasma mass spectrometry (LA-ICP-MS) on polished thin sections of quartz vein samples. The analyses were performed at LabMaTer at the University of Quebec at Chicoutimi (UQAC), Canada, using an Excimer 193 nm Resonetics Resolution M-50 laser ablation system coupled with an Agilent 7700x mass spectrometer. The following isotopes were measured: 28Si, 33S, 34S, 51V, 52Cr, 55Mn, 57Fe, 59Co, 60Ni, 65Cu, 66Zn, 71Ga, 72Ge, 75As, 82Se, 107Ag, 111Cd, 115In, 118Sn, 121Sb, 126Te, 197Au, 205Tl, 208Pb and 209Bi. Analyses were performed using lines and rare spots, depending on the pyrite size, with laser beam diameters from 25 to 43 μm, a range of stage movement speeds from 2.5 to 5 μm/s, laser frequencies from 10 to 15 Hz and power from 4 to 5 mJ/pulse.

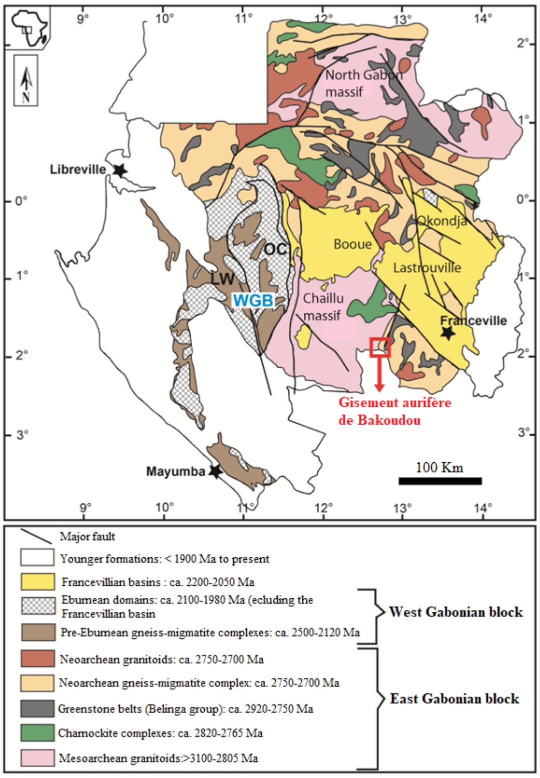

Figure 2. Geological map of the Gabonese Republic, modified from Thiéblemont et al. (2009)

3 Trace element geochemistry of pyrite

Pyrite is the predominant sulfide mineral in the orebody. It occurs as medium to coarse idiomorphic crystals, fractured and disseminated in the quartz veins (Figure 2). Some pyrites have chalcopyrite inclusions (Figure 2). Pyrites have high Co (4.68–4140 ppm) and Ni (3.24–3600 ppm) contents, with Co/Ni ratios between 0.02 and 15.54 (average = 3.33 for 23 analyses). The concentrations of invisible gold and silver vary up to 2.90 ppm and 58 ppm, respectively. These pyrites are As-poor (≤34.50) but show high Cu (≤3570 ppm) contents. Antimony contents are very low (average = 0.03 ppm) and generally below the limit of detection in the majority of samples. However, Te values are above the detection limit and up to 136 ppm.

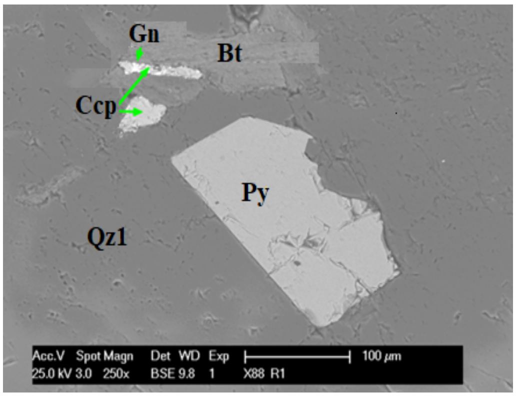

Figure 3. SEM images showing pyrite and chalcopyrite enclosed in quartz, with galena inclusions in chalcopyrite

4 Typology of the deposit

It has been shown that pyrite can record valuable information about the chemical evolution of the fluids from which it precipitated (e.g. Augustin and Gaboury 2019; Gaboury and Ore Sanchez 2020). In the Bakoudou gold deposit, pyrite represents the dominant sulfide mineral that formed during the main stage of mineralization. Therefore, trace element data for these pyrites can provide valuable information regarding the typology of this deposit (e.g. Deditius et al. 2014 and Le Mignot et al. 2017), as well as the origin of the potential mineralizing fluids (e.g. Large et al. 2013; Hu et al. 2016; Augustin and Gaboury 2019).

The pyrite trace element budget in this study shows that concentrations of invisible Au are low and vary from <0.01 to 2.90 ppm. Pyrite crystals are enriched in Cu (up to 3570 ppm) and poor in As (<34.50 ppm). In the Cu–Ni + Co–As ternary diagram of Deditius et al. (2014) (Figure 3), all pyrite samples plot within the field of porphyryrelated pyrites. On the As (mol%) vs. Au (mol%) diagram of Deditius et al. (2014) (Figure 4), the pyrite samples plot within the porphyry and transitional porphyry-epithermal fields. Furthermore, the presence of high Co (up to 4140 ppm) and Ni (up to 3600 ppm) concentrations in the pyrites of quartz veins, yielding Co/Ni ratios between 0.02 and 15.54 (average = 3.33), is consistent with a magmatic-hydrothermal origin (e.g. Zhang et al. 2014; Yu et al. 2018). This is supported by the As/Ag vs. Sb/Bi discriminant diagram of Augustin and Gaboury (2019), where our pyrite samples plot within the magmatic field for the mineralizing fluid source (Figure 5). Therefore, the Bakoudou gold deposit is considered to represent a porphyry– epithermal transitional gold system that shows a magmatic-hydrothermal signature.

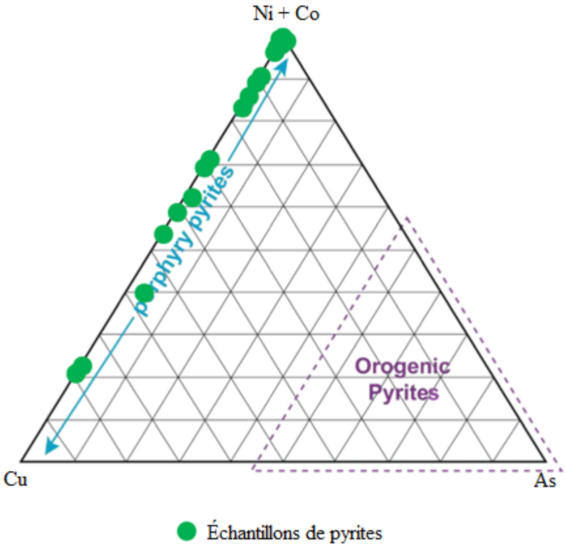

Figure 4. Cu–As-(Ni+Co) ternary diagram of Deditius et al. (2014) showing the porphyry character of the pyrites from the Bakoudou gold deposit.

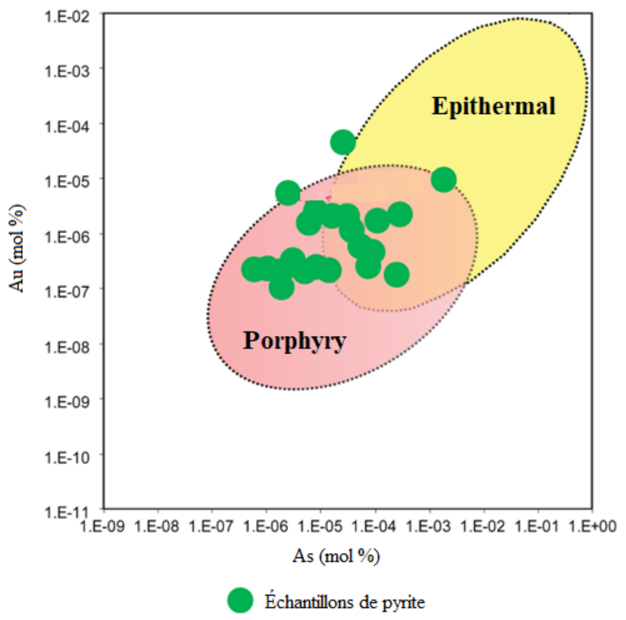

Figure 6. Au vs. As diagram (in mol%) of Deditius et al. (2014) showing the epithermal-porphyry character of the pyrites from the Bakoudou gold deposit.

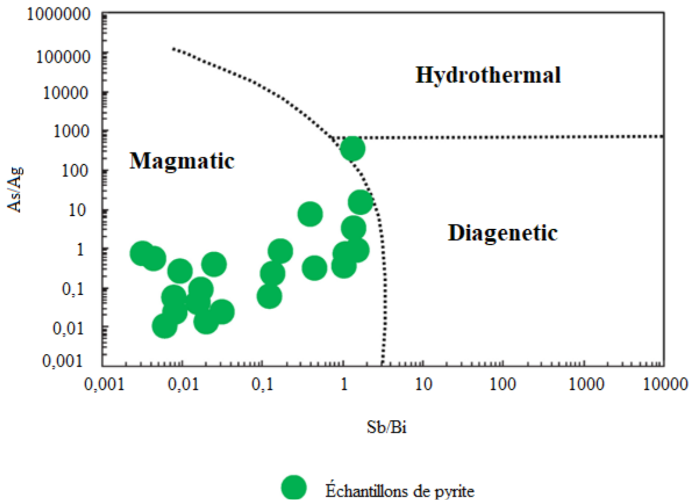

Figure 5. As/Ag vs. Sb/Bi diagram of Augustin and Gaboury (2019) indicating a magmatic fluid source for the pyrites from the Bakoudou gold deposit.

The Bakoudou gold deposit is hosted in shear zones. The orebody occurs as quartz veins, where quartz is the main gangue mineral. Minor sulfides, such as pyrite and chalcopyrite, occur within the deposit. Trace element data for pyrites from the quartz veins indicate that the Bakoudou gold deposit is a porphyry–epithermal transitional gold system that formed from magmatic fluids. Gold mineralization in quartz vein occurs as invisible gold in pyrite, but mostly as free gold. Free gold is interpreted to be a second event, resulting from of phase separation of the mineralizing fluids or remobilization of invisible gold from pyrite grains by later tectonic events and/or pyrite oxidation in the upper part of the deposit.

Acknowledgements

This work was supported by the Managem Mining Company and the DLGR Laboratory (Department of Geology, Faculty of Sciences Semlalia, Cadi Ayyad University, Marrakech, Morocco). LAMEQ of Université du Québec à Chicoutimi (UQAC) are thanked for the use of their LA-ICP-MS which enabled to measure trace element concentrations some pyrite grains.

References

Augustin, J. and Gaboury, D. (2019): Multi-stage and multi-sourced fluid and gold in the formation of orogenic gold deposits in the world-class Mana district of Burkina Faso Revealed by LA-ICP-MS analysis of pyrites and arsenopyrites. Ore Geology Reviews 104, 495–521.

De Wit, M.J. and Linol, B. (2015): Precambrian Basement of the Congo Basin and its Flanking Terrains. Geology and Resource Potential of the Congo Basin. pp. 19–37.

Deditius, A., Reich, M., Kesler, S.E., Utsunomiya, S., Chryssoulis, S., Walshe, J.L., Hough, R., Ewing, R.C. (2014): The coupled geochemistry of Au and as in pyrite from hydrothermal ore deposits. Geochem. Cosmochim. Acta 140, 644–670.

Gaboury, D. and Ore Sanchez, C. (2020): Electrochemical gold precipitation to explain extensive vertical and lateral mineralization in the world-class Poderosa-Pataz district, Peru. Terra Nova 32, 97–107.

Hu, S.Y., Evans, K., Fisher, L., Rempel, K., Craw, D., Evans, N.J., Cumberland, S., Robert, A., Grice, K. (2016): Associations between sulfides, carbonaceous material, gold and other trace elements in polyframboids: implications for the source of orogenic gold deposits, Otago Schist, New Zealand. Geochem. Cosmochim. Acta 180, 197–213.

Large, R.R., Meffre, S., Burnett, R., Guy, B., Bull, S.,Gilbert,S., Goemann, K.,Danyushevsky, L. (2013): Evidence for an intrabasinal source and multiple concentration processes in the formation of the carbon leader reef, Witwatersrand supergroup, South Africa. Economic Geology 108, 1215–1241.

Le Mignot, E., Siebenaller, I., Beziat, D., Andre-Mayer, A.S., Reisberg, L., Salvi, S.,Velasquez, G., Zimmermann, C., Nare, A. (2017): The Paleoproterozoic copper-gold deposits of the Gaoua district, Burkina Faso: superposition of orogenic gold on a porphyry copper occurrence? Economic Geology 112, 99–122.

Nedelec, A., Nsifa, E.N., Martin, H. (1990): Major and trace element geochemistry of the Archaean Ntem plutonic complex (South Cameroon): petrogenesis and crustal evolution. Precambrian Research 47, 35–50.

Thieblemont, D., Castaing, C., Billa, M., Bouton, P., Preat, A. (2009): Notice explicative de la Carte geologique et des Ressources minerales de la Republique Gabonaise a 1/1000000: Editions DGMG - Ministere des Mines, du Petrole, des Hydrocarbures. pp. 384p Libreville.

Yu, B., Zeng, Q., Frimmel, H.E., Wang, Y., Guo, W., Sun, G., Zhou, T., Li, J. (2018): Genesis of the Wulong gold deposit, northeastern North China Craton: constraints from fluid inclusions, H-O-S-Pb isotopes, and pyrite trace element concentrations. Ore Geology Reviews 102, 313–337.

Zhang, J., Deng, J., Chen, H.Y., Yang, L.Q., Cooke, D., Danyushevsky, L., Gong, Q.J., 2014. LA-ICP-MS trace element analysis of pyrite from the Chang'an gold deposit, Sanjiang region, China: implication for ore-forming process. Gondwana Research 26, 557–575

Sulfur and chalcophile metal transfer via sulfide-volatile compound drops during magma mixing: evidence from the Christiana-Santorini-Kolumbo volcanic field

C.G.C. Patten[1], S. Hector[1], S. P. Kilias[2], M. Ulrich[3], A. Peillod[1], A. Beranoaguirre[1], P. Nomikou[2], E. Eiche[1], J. Kolb[1]
[1] *Chair of Geochemistry and Economic Geology, Institute of Applied Geosciences, Karlsruhe Institute of Technology, Germany*
[2] *Department of Geology and Geoenvironment, National and Kapodistrian University of Athens, Greece*
[3] *Institut Terre et Environnement de Strasbourg, Université de Strasbourg, CNRS, Strasbourg, France*

Abstract. Efficient transfer of S and chalcophile metals through the Earth's crust in arc magmatic-hydrothermal systems is paramount for the formation of large magmatic-hydrothermal ore deposits. Formation of sulfide-volatile compound drops in magmatic systems has been recognized as a potential key mechanism for such transfer but their behavior and evolution during dynamic arc magmatism remain cryptic. In this study, we report evidence of compound drops preserved in the active Christiana-Santorini-Kolumbo volcanic field. Two sulfide populations are defined: 1) micrometric sulfide blebs associated with vesicles and trapped within mafic enclave phenocrysts and 2) larger millimetric sulfide ovoids present at the margins between mafic enclaves and felsic host rocks. The sulfide ovoids form by accumulation and coalescence of compound drops and are eventually oxidized to magnetite during sulfide-volatile interaction. In-situ mineral analysis allows for the evaluation of metal mobility during oxidation with Bi, Cd, Cu, Ag, Tl, Te and Au showing high mobility into the volatile phase. Formation, coalescence, accumulation and oxidation of compound drops during magma mixing is a particularly efficient mechanism for transferring S and chalcophile metals in magmatic-hydrothermal arc systems.

1 Introduction

Effective fluxes of S and chalcophile metals (e.g. Cu, Au, Ag, Tl, Te, Bi) in the Earth's crust at arc settings are key for the formation of large hydrothermal ore deposits (porphyry, epithermal, volcanogenic massive sulfide, skarns; Richards 2011). The processes controlling such fluxes, however, are complex, with competitive effects during arc magmatic-hydrothermal evolution. Sulfur and chalcophile metals can be trapped in the lower crust via sulfide segregation or can be released in the upper crust via magmatic volatile degassing. The relative timing between such processes is critical in determining the fate of S and chalcophile metals. The formation of sulfide-volatile compound drops (i.e., droplets of sulfide melt attached to magmatic volatile phases) during magmatic evolution appears as an alternative and efficient mechanism for the transport of both S and chalcophile metals to the shallow crust (Mungall et al. 2015). Although such compound drops have been shown experimentally (Mungall et al. 2015) and identified in magmatic ultramafic systems (Le Vaillant et al. 2017), their preservation in complex magmatic-hydrothermal arc environments is scarce (Nadeau et al. 2010). Magmatism in arc environments is dynamic, involving mixing and/or mingling of variably evolved melts. Injection of mafic melt into differentiated magmatic chambers appears as a key process for transferring S and chalcophile metals to shallower magmatic-hydrothermal systems (Wallace and Edmonds 2011). The fate of the compound drops in such dynamic environments is, however, poorly known and their role in the formation of arc-related hydrothermal ore deposits, although stipulated, remains cryptic.

In this study, we document the presence of compound drop remnants in the active magmatic-hydrothermal system of the Christiana-Santorini-Kolumbo (CSK) volcanic field, Greece. Based on detailed petrography, high-resolution X-ray fluorescence mapping and in-situ mineral chemistry analysis we highlight the complex mineral reactions and elemental transfers which occur in compound drops during complex magmatic evolution. The findings have important implications for S and chalcophile metals fluxes in arc-related shallow magmatic-hydrothermal systems.

2 Methods

Micro-XRF measurements were done using a Micro X-Ray Fluorescence (μ-XRF) Brucker M4 Tornado at the Institut Terre et Environnement de Strasbourg. μ-XRF chemical mappings were acquired with a 30 μm step interval and a dwell time of 700 ms/pixel. Phase maps were calculated using the calculation procedure developed in house.

In-situ analyses of sulfide and oxide phases were carried out by Electron Micro Probe Analysis (EMPA) and by Laser Ablation-Inductively Coupled Plasma-Mass Spectrometry (LA-ICP-MS). EMPA analyses were carried out at the Institute of Geological Sciences from the University of Bern using a JEOL JXA-8200 Superprobe. LA-ICP-MS analysis were carried out at the Laboratory of Environment and Raw materials Analysis (LERA), Karlsruhe Institute of Technology, using a Teledyne 193 nm Excimer Laser coupled to an ICP-MS (Element XR ThermoFisher). Calibration and data quality checking was done using the sulfide pressed pellets Fe-S1, Fe-S4 and PTC1b from UQAC University for sulfide analyses and basaltic glasses BHVO-2, BCR-2 and BIR-1 from the USGS for oxide analysis

3 Evidence for sulfide-volatile compound drop remnants in the CSK volcanic field

The CSK volcanic field is an active and complex magmatic-hydrothermal system (Nomikou et al. 2019) showing evidence of magma mixing and mingling at the Nea Kameni and Kolumbo volcanoes.

Two sulfide populations related to volatile phases have been observed Nea Kameni and Kolumbo volcanoes (Fig. 1). The first population is defined by micrometric sulfide blebs related to micrometric vesicles hosted by pyroxene phenocrysts from andesitic enclaves in porous dacite from Nea Kameni (Fig. 1c). The sulfide blebs are mainly spherical and contain pyrrhotite and chalcopyrite with minor magnetite (Fig. 1c), characteristic of magmatic sulfide blebs. The vesicle associated with the sulfides varies from few microns up to tens of microns (Fig. 1c). They are either directly in contact with or closely related to the sulfides. The sulfide-vesicle pairs have similar shapes, sizes and mineralogy as those observed at the Merapi volcano (Nadeau et al. 2010), analogous to compound drops (Mungall et al. 2015) and, hence, are interpreted as well as compound drop remnants.

The second sulfide population observed is characterized by variably oxidized sulfide ovoids up to a few millimeters in diameter. They have a spherical to elongated ellipsoidal shape, are associated with large millimetric vesicles (Fig. 1a,b,d), and occur mainly at the interface between andesitic enclaves and dacitic host rocks The sulfide ovoids are either embayed in, in contact with or disconnected from the vesicles; the latter ranging in size range from several hundreds of microns to few millimeters (Fig. 1a). The sulfide ovoids are constituted mainly of pyrrhotite and pyrite with minor pentlandite, chalcopyrite and covellite. Pyrrhotite appears as large grains (up to few mm) with discrete exsolution of pentlandite. Pyrite occurs as a replacement of pyrrhotite generally along fractures filled with magnetite; additionally, pyrite proportion increases towards magnetite-rich zones (Fig. 1d). Chalcopyrite is scarce and has been observed in partly oxidized areas (Fig. 1d). It is often replaced by covellite associated with pyrite. Sulfides are replaced by fine-grained micrometric subhedral magnetite with discrete sulfide grains preserved in between (Fig. 1a,d). Sulfide replacement by magnetite ranges from limited, with discrete magnetite along fractures and at vesicle margins, to extensive, with almost magnetite-pure aggregates with discrete sulfides and porosity between the grains (Fig. 1 d).

4 Sulfide and oxide mineral compositions

In-situ analysis of sulfide and oxide phases from the sulfide blebs and ovoids allows the characterization of their origin and a better understanding of metal behavior during compound drop evolution.

Unaltered sulfide blebs of compound drops in silicate phenocrysts show a distinctive magmatic signature characterized by relatively high chalcophile element concentrations (Ni, Co, Cu, Ag

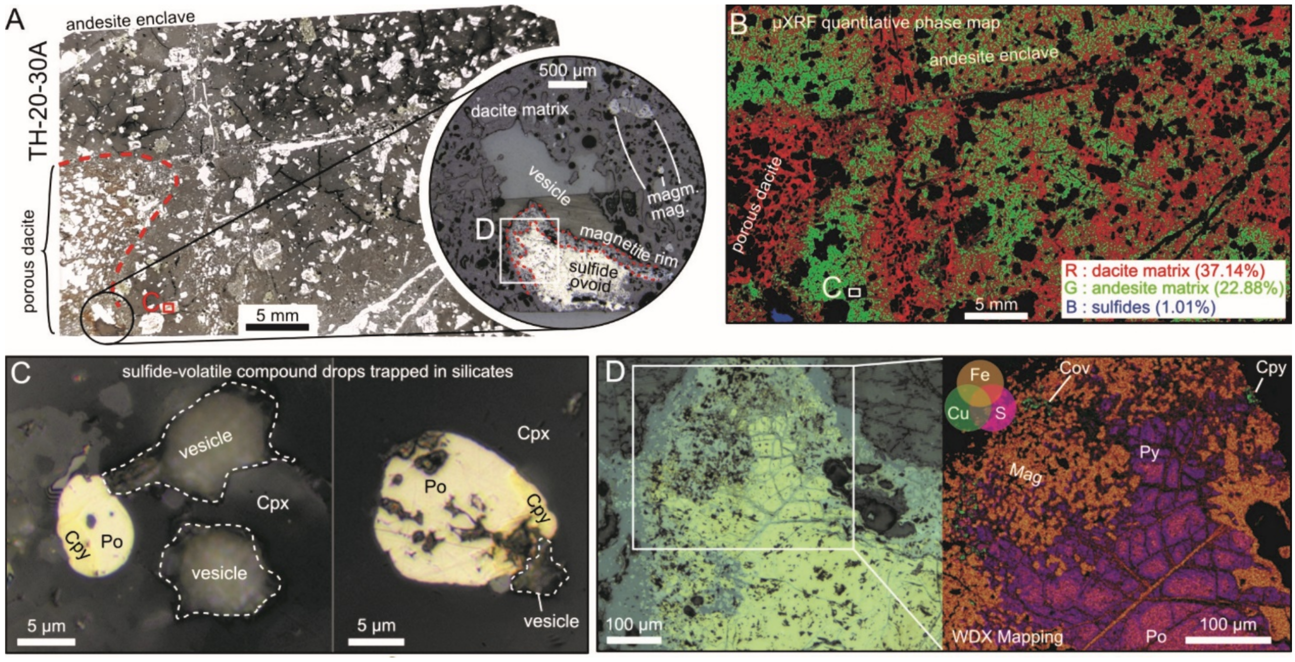

Figure 1. Petrology of sulfide and oxide phases related to sulfide-volatile compound drops at Nea Kameni volcano. A) Thin section of an andesite enclave in contact with porous dacite host rock. Sulfide ovoid associated with large vesicle at andesite/dacite margin (insert). B) micro-XRF quantitative phase map of A) showing the proportion of dacite matrix, andesitic matrix and sulfide phases (pyrrhotite and chalcopyrite). Mineral proportions are calculated from elemental micro-XRF mapping. Black zones represent porosity and silicate phenocrysts. C) Sulfide blebs and associated vesicles in pyroxene phenocryst. Sulfide blebs contain pyrrhotite (Po) and chalcopyrite (Cpy). D) Ovoid-shaped, partly oxidized sulfide melt occurring at the dacite/andesite interface in A). The sulfide ovoid is characterized by pyrrhotite (Po) in the core, pyrite (Py), chalcopyrite (Cpy), covellite (Cov) and magnetite (mag) in the rim. A' shows WDX scanning electron microscopy elemental mapping of S, Fe and Cu.

and Au; Fig. 2a) and an overall similar metal enrichment to compound drops from the Merapi volcano (Nadeau et al. 2010), and to mid-ocean ridge basalt (MORB) sulfide droplets (Patten et al. 2013). These similarities imply that the sulfide blebs formed from a sulfide-saturated melt. The sulfide blebs from the CSK volcanic field are more enriched in weakly chalcophile elements (Pb, Zn, As, Sn, Sb, Fig. 2a) compared to MORB sulfide droplets, which are enriched in strongly chalcophile elements (Au, Te, Ni), supporting that sulfide saturation occurred in an andesitic melt, slightly more evolved than a MORB.

Pyrrhotite, pyrite and partly oxidized chalcopyrite from the sulfide ovoids show comparable metal enrichment to the sulfide blebs (Fig. 2b). The partly oxidized chalcopyrite phases show marked enrichment in Tl, Au, Ag, Bi, Pb and As relative to pyrrhotite and pyrite, while the latter are enriched in Ni, Co and Mo (Fig. 2b). Such metal fractionation is akin to metal distribution during magmatic sulfide crystallization into monosulfide solid solution (MSS) and intermediate solid solution (ISS; Patten et al. 2013) supporting that the sulfide ovoids are well-differentiated magmatic sulfides overprinted by oxidation reactions.

The magnetite present within the sulfide ovoids has low concentrations in Ti, V, Mn, Zn, Co and Ni, which are usually enriched in magmatic magnetite crystallizing from a silicate melt (Dare et al. 2014). Hence, the analyzed magnetite did not form through magmatic process but rather by oxidation and replacement of the magmatic sulfides, as supported by petrographic observations

4 Sulfide and magmatic volatile fates during magmatic evolution at the Nea Kameni and Kolumbo volcanoes

Despite their spatial proximity, the Nea Kameni and Kolumbo volcanoes share distinct and complex magmatic plumbing systems. However, they are both characterized by shallow magmatic chambers (~4 and ~5 km deep, respectively) fed by mafic melts from deeper sources. The presence of magmatic sulfide blebs within the andesitic enclaves as well as the high S concentrations in andesite-hosted melt inclusions from Nea Kameni (~900-1000 ppm; Michaud et al. 2000) imply that the andesitic melt was sulfide-saturated upon injection into the shallow magmatic chamber. Additionally, the presence of trapped fluid inclusions in olivine and pyroxene in andesitic enclaves at Nea Kameni (Rizzo et al. 2015) suggests that magmatic volatile exsolution occurred within a similar timeframe to sulfide saturation; allowing bubble nucleation on magmatic sulfide droplets and formation of sulfide-volatile compound drops.

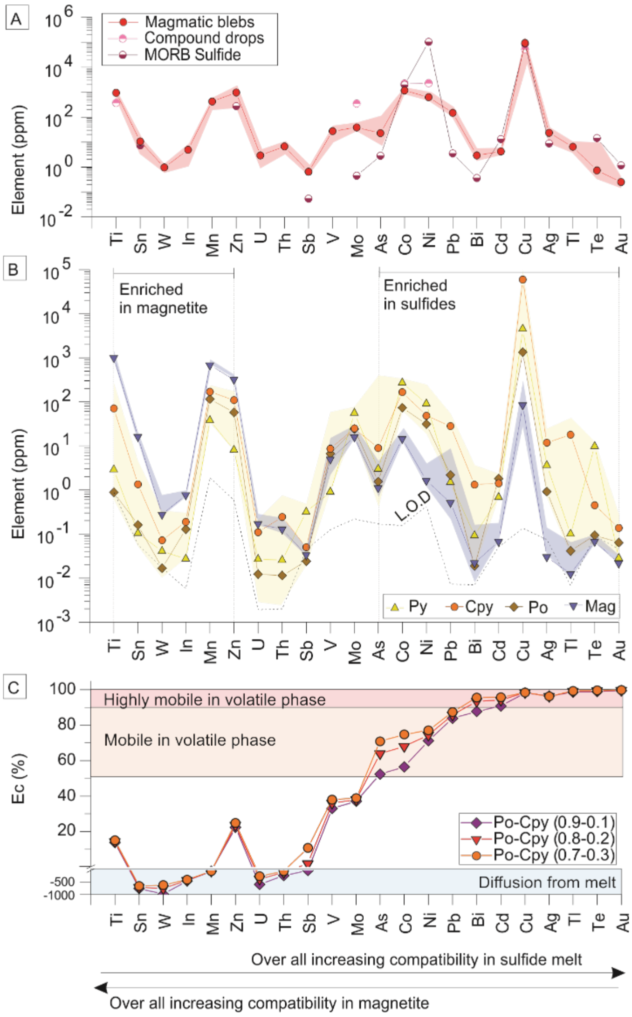

Figure 2. Trace metal content in sulfides and magnetite related to compound drops and magmatic volatile-sulfide emission coefficients. A) Median metal concentrations in magmatic sulfide bleb. Shaded area corresponds to the upper and lower quartiles. B) Median metal concentrations in pyrrhotite (Po), pyrite (Py), partly replaced chalcopyrite (Cpy) and magnetite (Mag) of ovoids. The yellow and blues shaded areas correspond to the upper and lower quartiles of all sulfides and magnetite, respectively. L.O.D = limit of detection. C) Calculated magmatic volatile-sulfide emission coefficients with various fractions pyrrhotite and chalcopyrite. Negative values are due to element diffusion from the melt to the magnetite during oxidation as the compound drops are not closed systems.

The similar mineralogy and composition, the spatial proximity as well as the close association with vesicles imply a genetic link between the magmatic sulfide blebs and the larger sulfide ovoids. The formation of the sulfide ovoids is likely to have occurred during magma mixing. Repeated injections of volatile-rich mafic (andesitic/basaltic) melts at Nea Kameni and Kolumbo result in their accumulation at the bottom of the magmatic chambers without extensive mixing with the felsic/intermediate melts. Continuous volatile exsolution from the mafic melts can lead to the formation of an intermediate hybrid layer between the mafic and felsic melts (Plail et al. 2018) as revealed by µXRF mineral mapping (Fig. 1b) where the interface between the enclave and host rock is not sharp but rather diffuse. The interface between an underplating mafic melt and an overlying felsic melt is often a place where volatile bubbles, which have exsolved from the mafic melt, accumulate (Plail et al. 2018). Hence, it is inferred that compound drops formed within the mafic melt rise toward the interface with the felsic melt where they stagnate and accumulate due to differences in physico-chemical conditions. During migration, stagnation and accumulation, the compound drops then coalescence (Iacono-Marziano et al. 2022) resulting in the formation of the larger sulfide ovoids.

During compound drops coalescence into sulfide ovoids, the temperature difference between the basaltic/andesitic and dacitic/rhyolitic melts (~1000-1200 °C and 750-900 °C, respectively) allows the sulfide liquid to crystallize as monosulfide solution (MSS, ~1050-1100 °C) and intermediate solid solution (ISS, ~850 °C) accounting for the differentiated pyrrhotite and chalcopyrite texture preserved in partly oxidized sulfide ovoids (Fig. 1). Sulfide differentiation is shortly followed by oxidation of the sulfides by the magmatic volatiles leading to progressive replacement of the MSS and ISS into pyrite and covellite and ultimately into magnetite.

The variably oxidized ovoids are either embayed into, partially associated with vesicles, or disconnected from vesicles (Fig. 1). This diversity of sulfide/oxide ovoid-vesicle textures suggests that the coalesced compound drop might eventually become unstable. The magmatic volatile phase, once disconnected with the oxide/sulfide phase will rise within the magmatic chambers as plume, through volatile pathways or from cracks in the magma crystal framework directly feeding shallower hydrothermal systems which can be involved ore deposit formation.

5 Element mobility during compound drop oxidation

Sulfide oxidation by magmatic fluids has been recognized as a key process for mobilizing S and metals to the shallow parts of arc magmatic-hydrothermal systems (Edmonds et al. 2018). The efficiency, however, for metal transfer from the sulfide to the magmatic volatiles remains unknown. Metal concentrations of the sulfide ovoids and associated magnetite are used as proxies for calculating emanation coefficients (Edmonds et al. 2018) defined as:

$$Ec_i = \left(\frac{C_{i\,sulf}}{d_{i\,sulf}} - \frac{C_{i\,mag}}{d_{i\,mag}}\right) \Big/ \left(\frac{C_{i\,sulf}}{d_{i\,sulf}}\right) * 100$$

with $C_{i\ \mathrm{sulf}}$ and $C_{i\ \mathrm{mag}}$ the concentration of a given element in the sulfide phases and in the magnetite, respectively and $d_{i\ \mathrm{sulf}}$ and $d_{i\ \mathrm{mag}}$ the density of the sulfide phases and magnetite respectively. During oxidation Ti, Sn, W, In, Mn, Zn, U and Th are incompatible and remain in the magnetite while Te, As, Au, Co, Ni, Pb, Bi, Cd, Ag, Cu and Tl are efficiently transferred into the magmatic volatiles (Fig. 2).

6 Conclusion

Study of the sulfide population at the Kameni and Kolumbo volcanoes reveal that sulfide-volatile compound drops can form and evolve during the complex magmatic evolution of arc systems. Magma mingling between a mafic sulfide and volatile saturated melt with a felsic melt can lead to compound drops accumulation and coalescence at the melts' interface. The sulfide melt is eventually differentiated and then oxidize to magnetite due to the interaction with the volatile phase. During oxidation, trace elements present within the sulfide phases are variably released into the volatile phase with Bi, Cd, Cu, Ag, Tl, Te and Au being highly mobile. The volatile phase is eventually separated from the sulfide/oxide phases and is transported to the shallower part of the magmatic-hydrothermal system, possibly feeding magmatic-hydrothermal ore deposits.

References

Edmonds M, Mather TA, Liu EJ (2018) A distinct metal fingerprint in arc volcanic emissions. Nat Geosci 11:790–794 . doi: https://doi.org/10.1038/s41561-018-0214-5

Iacono-Marziano G, Le Vaillant M, Godel BM, et al (2022) The critical role of magma degassing in sulphide melt mobility and metal enrichment. Nat Commun 13:1–10 . doi: https://doi.org/10.1038/s41467-022-30107-y

Le Vaillant M, Barnes SJ, Mungall JE, Mungall EL (2017) Role of degassing of the Noril'sk nickel deposits in the Permian–Triassic mass extinction event. Proc Natl Acad Sci 114:2485–2490 . doi: https://doi.org/10.1073/pnas.1611086114

Michaud V, Clocchiatti R, Sbrana S (2000) The Minoan and post-Minoan eruptions, Santorini (Greece), in the light of melt inclusions: chlorine and sulphur behaviour. J Volcanol Geotherm Res 99:195–214

Mungall JE, Brenan JM, Godel B, et al (2015) Transport of metals and sulphur in magmas by flotation of sulphide melt on vapour bubbles. Nat Geosci 8:216–219 . doi: 10.1038/ngeo2373

Nadeau O, Williams-Jones AE, Stix J (2010) Sulphide magma as a source of metals in arc-related magmatic hydrothermal ore fluids. Nat Geosci 3:501–505 . doi: https://doi.org/10.1038/ngeo899

Nomikou P, Hübscher C, Carey S (2019) The Christiana–Santorini–Kolumbo Volcanic Field. Elem An Int Mag Mineral Geochemistry, Petrol 15:171–176 . doi: https://doi.org/10.2138/gselements.15.3.171

Patten CGC, Barnes S-J, Mathez EA, Jenner FE (2013) Partition coefficients of chalcophile elements between sulfide and silicate melts and the early crystallization history of sulfide liquid: LA-ICP-MS analysis of MORB sulfide droplets. Chem Geol 358: . doi: 10.1016/j.chemgeo.2013.08.040

Plail M, Edmonds M, Woods AW, et al (2018) Mafic enclaves record syn-eruptive basalt intrusion and mixing. Earth Planet Sci Lett 484:30–40 . doi: https://doi.org/10.1016/j.epsl.2017.11.033

Richards JP (2011) Magmatic to hydrothermal metal fluxes in convergent and collided margins. Ore Geol Rev 40:1–26 . doi: https://doi.org/10.1016/j.oregeorev.2011.05.006

Rizzo AL, Barberi F, Carapezza ML, et al (2015) New mafic magma refilling a quiescent volcano: Evidence from He-Ne-Ar isotopes during the 2011–2012 unrest at Santorini, Greece. Geochemistry, Geophys Geosystems 16:798–814

Wallace PJ, Edmonds M (2011) The Sulfur Budget in Magmas: Evidence from Melt Inclusions, Submarine Glasses, and Volcanic Gas Emissions. Rev Mineral Geochemistry 73:215–246 . doi: 10.2138/rmg.2011.73.8

Meinert LD, Dipple GM, Nicolescu S (2005) World skarn deposits. Econ Geol 100th Anni:299–336.

Fluid inclusion study in quartz of the Rudnik Pb-Zn-Cu-Ag skarn deposit, Serbia

Stefan Petrović[1], Ronald J. Bakker[2], Vladica Cvetković[1], Rade Jelenković[1]
[1]University of Belgrade, Faculty of Mining and Geology, Serbia
[2]Montanuniversität Leoben, Department of Applied Geosciences and Geophysics, Austria

Abstract. Six types of fluid inclusions were identified in three growth zones of hydrothermal quartz from the Rudnik skarn deposit. In the core zone, primary two-phase fluid inclusions of high (type 1) and moderate salinity (type 2) homogenized to liquid between 350-430 °C and 340-420 °C, respectively. Raman analysis revealed that the vapour phases are a CO_2-CH_4 gas mixture, with a predominance of CO_2. The core contains and dispersed vapour-rich fluid inclusions of low salinity (type 3) composed of CO_2-CH_4-H_2S gas mixture with significant amounts of H_2S, as well as liquid-rich fluid inclusions (type 4) predominantly composed of pure water and small vapour phase with lower homogenization temperatures between 174-284 °C. In the transition zone, primary fluid inclusions arranged perpendicular to the growth zone (type 5) homogenize over a wide range of temperatures between 235-401 °C. The vapour phase is a CO_2-CH_4 gas mixture additionally enriched in CH_4 compared to the other types. Fluid inclusions in paths of the rim zone of the quartz (type 6) have a homogenization temperature between 259-385 °C. The vapour phase is a CO_2-CH_4 mixture with reduced CH_4 content, while the liquid phase has a low salinity.

1 Introduction

The Rudnik deposit is located in central Serbia and present one of the most significant polymetallic skarn deposits in the Serbo-Macedonian metallogenic province (Figure 1). Over 13 Mt of polymetallic ore (Pb-Zn-Cu-Ag) was found in the Rudnik deposit so far. Ore bodies are hosted in the complex of contact-metasomatically altered areas of the Upper Cretaceous flysch units (Djoković 2013) (Figure 2). Genesis of the ore deposit is temporally associated with the formation of the Oligocene-Miocene volcanic-intrusive complex and results of subsequent hydrothermal activities (Cvetković et al. 2016).

Quartz is commonly associated with the ore mineralization in the deposit. According to field and petrographic observations, we can distinguish two generations of quartz. The first, syn-ore generation of quartz is characterised by well-developed prismatic crystals intergrowth with ore minerals. This generation of quartz commonly has well-developed oscillatory growth zoning. The second generation is primarily represented by anhedral or, less extent, small idiomorphic quartz crystals which are coevally with calcite filling the voids between ore mineralization.

Until now, there are only preliminary studies on the presence of fluid inclusions (Blečić 1974). The primary task of the study is to determine the characteristics of fluid inclusions hosted in syn-ore quartz and to provide a contribution to define the multiple events in the magmatic-hydrothermal system that led to the formation of the deposit.

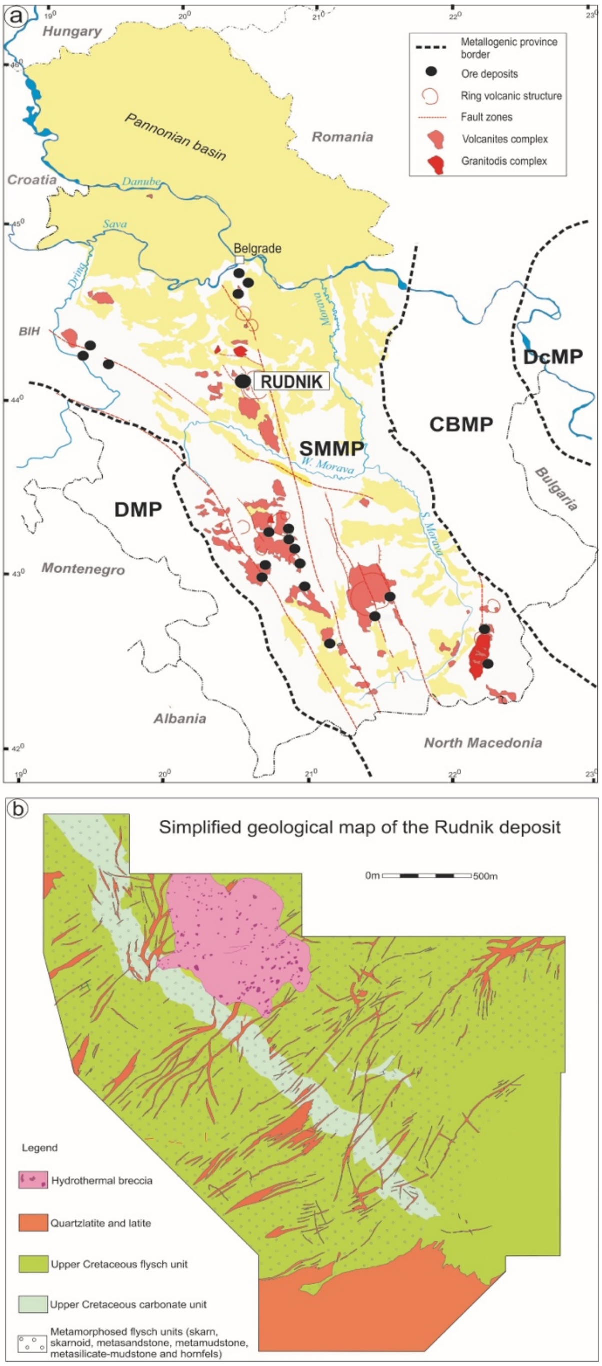

Figure 1. a Location of the Rudnik ore deposit in Serbo-Macedonian metallogenic province (adapted from Jelenkovic et al. 2008). **b** Simplified geological map of the Rudnik deposit (adapted from Djoković 2013)).

2 Methodology

Preparation of thick section was performed at the University of Belgrade, Faculty of Mining and Geology at the Department of Mineralogy, Crystallography, Petrology and Geochemistry and at the Department of Economic Geology. Fluid inclusions were studied from doubly polished thick sections of thickness ~150 µm.

Microthermometry of fluid inclusions was conducted at the Department of Applied Geosciences and Geophysics, chair of Resource Mineralogy at the University of Leoben in Austria and Fluid inclusion Laboratory at the Faculty of Mining and Geology at the University of Belgrade.

Microthermometry was carried out using a Linkam MDS 600 stage mounted on an Olympus BX 60 optical microscope in Leoben. Calibration of the Linkam stage was performed using synthetic fluid inclusion standards (pure H_2O, CO_2–H_2O mixtures) for the melting temperatures of CO_2 at -56.6 °C, of H_2O at 0.0 °C and the critical homogenisation temperature of H_2O at 374.0 °C. Microthermometry measurements at the Faculty of Mining and Geology in Belgrade were carried out on a THMSG600 heating stage connected to an Olympus BX51 microscope. The primary CO_2 standard WRECT-006160 was used for calibration. The reproducibility is ±0.1 °C between -60 °C and +100 °C and ±0.3 °C at higher temperatures.

Calculations of microthermometric parameters were performed using AqSo_NaCl software (Bakker 2018).

Raman spectroscopy was performed with a LabRAM (Department of Applied Geosciences and Geophysics, chair of Resource Mineralogy, Leoben) instrument, from the company Horiba Scientific, Jobin Yvon Technology. The LabRAM is operated with an Olympus microscope, and an LMPlanFI 100x/0.80 numerical aperture objective lens. A frequency-doubled 100 mW Nd-YAG laser with an excitation wavelength of 532.068 nm is used, with a laser power of about 1 to 2 mW at the sample surface. The scattered light is dispersed by 1800 grooves/mm gratings. The detector is an air-cooled (Peltier) CCD-3000 (1024 x 256 pixels) operating at -60 °C. Spectra are collected using multiple spectral windows between 100 to 3000 cm^{-1}, corresponding to a pixel resolution of about 1.64 cm^{-1} at relative low wave numbers, and 1.35 cm^{-1} at relative high wave numbers. A 100 µm slit combined with a 1000 µm confocal hole aperture is used to obtain the best resolved spectra.

3 Petrography

Colourless and transparent syn-ore quartz, in the form of idiomorphic crystals, has three visible crystal growth zones with fluid inclusions (Figure 2).

The core zone contains four types of fluid inclusions: 1) semi-irregular shaped fluid inclusions, up to 25 µm that occur in small groups. The volume fraction of the vapour phase varies between 20-30 vol. %. 2) fluid inclusions in trails that reflected partly healed cracks and internal growth zones. They have a regular locally negative-crystal shape, usually sizes up to 20 µm, and the volume fraction of the vapour phase varies between 50-60 vol. %. 3) regular, locally negative crystal shaped fluid inclusions, length up to 10 µm and extremely rich in vapour phase 90 vol. %. 4) elongated irregular shaped fluid inclusions liquid-rich to all-liquid, up to 40 µm in length, in trails (healed cracks) in the core.

The transition zone contains abundant fluid inclusions of irregular shape that are mainly elongated in an orientation perpendicular to growth-zone traces. These fluid inclusions have a length of 50-300 µm and the volume fraction of the vapour phase varies between 10-20 vol. %.

The rim contains traces of growth zones with fluid inclusions of regular shape, with an average length of 30 µm, and volume of the vapour phase varies between 20-30 vol. %.

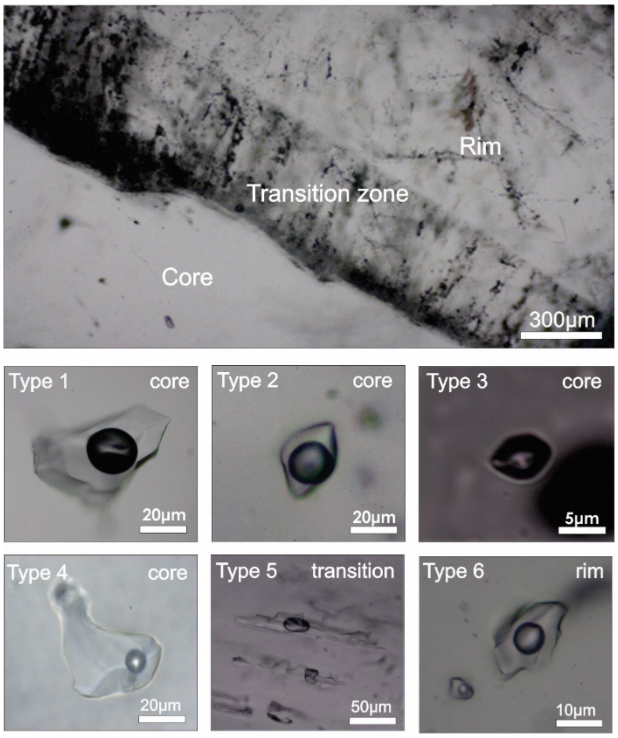

Figure 2. Photomicrograph of a piece of a quartz crystal with three visible growth zones and fluid inclusions. Below are the photomicrographs of single fluid inclusion types.

4 Raman spectroscopy

In the core, type 1 inclusions are characterised by a relatively high salinity of the liquid phase. The vapour phase is a gas mixture of CO_2-CH_4, with a predominance of CO_2. The relative low intensity of the CO_2 and CH_4 Raman spectra implies a low density of the vapour phase and high salinity.

Type 2 inclusions have an H_2O spectrum which corresponds to a moderate salinity, and the vapour phase is slightly enriched in CH_4 compared to type 1, but remains a CO_2-rich gas mixture. Some inclusions reveal minor amounts of additional H_2S.

Type 1 and 2 contain occasionally solid phases, i.e., accidentally trapped small crystals of calcite and mica.

Type 3 inclusions have a vapour phase consisting of a CO_2-CH_4-H_2S gas mixture that is enriched in CH_4 and with significant amounts of H_2S. The H_2O spectrum of the liquid phase reveals a relatively high shoulder at about 3200 cm^{-1}, which corresponds to low salinity.

Raman spectra of Type 4, liquid-rich to all-liquid fluid inclusions, reveal nearly pure CO_2 vapour and a H_2O liquid phase.

In the transitional zone, type 5 inclusions have a vapour phase that is relatively enriched in CH_4 in a mixture with CO_2. The Raman band of the liquid phase corresponds to a low salinity aqueous solution, similar to type 3.

Fluid inclusions in the rim zone, type 6, have a CO_2-enriched vapour phase with minor CH_4. The Raman spectrum of the liquid phase resembles a low salinity aqueous solution.

5 Microthermometry

Type 1 inclusions have a temperature of homogenization in the range of 350-430 °C with a mode at 380-390 °C. Ice melting temperatures are from -6 to -23 °C, corresponding to a calculated salinity between 9 and 24 wt.% NaCl eq., with a mode in the 12 to 16 wt.% NaCl eq..

Type 2 inclusions have relatively similar homogenization temperatures that range between 340 and 420 °C as type 1 inclusions and a slightly lower mode at 370-380 °C. Ice melting temperatures are in the range of -2 to -9 °C while salinity is from 4 to 12 wt.% NaCl eq. with a mode at 6-7 wt.% NaCl eq..

The low density of the vapour phase in type 3 does not allow any microthermometric analyses, i.e. homogenization or melting of CO_2 is not observed. Locally, the final ice melting temperature of the frozen aqueous phase occurs at temperatures of -1.0 to -4.0 °C, corresponding to a salinity of 1 to 6 wt.% NaCl eq..

Homogenization temperatures of type 4 inclusions are significantly lower than the previous types and are in the range of 148 to 245 °C. Ice melting temperatures occur from -0.7 to -4.9 °C while the salinity of this type varies between 1 and 8 wt.% NaCl eq..

Inclusion in the transition zone homogenize at a mode of 360 to 380 °C similar to type 2, but a wider range of 235-401 °C has been measured. Dissolution of ice occurs between -1 and -6 °C corresponding to a salinity of 2 to 8 wt.% NaCl eq..

Inclusions in the rim of quartz have homogenization temperatures between 259 and 385 °C with a mode at 340-360 °C. These temperatures are significantly lower than type 5 and higher than type 4. The melting temperature of ice ranges from -2 to -3 °C, which corresponds to a low salinity of 2 to 5 wt.% NaCl eq..

6 Conclusion

The different fluid inclusions from the quartz growth zones reveal that deposition of the ore mineralization was the result of a multiphase evolution of the hydrothermal ore-forming fluid, similar to skarn deposits worldwide (Kwak, 1986; Meinert et al., 2003).

These events are preserved in distinguished types of fluid inclusions and reflected through their varying temperature of homogenization, salinity, and fluid composition.

The study shows that the examination of fluid inclusions from quartz can considerably contribute to tracing the evolution of hydrothermal ore-bearing fluid, which is associated with the genesis of the Rudnik skarn deposit.

Acknowledgements

Gratitude to Company Rudnik and flotation Rudnik for the sampling permit and helpful internal documentation material for the study.

The study was carried out within the Central European Exchange Program for University Studies-CEEPUS (Network: RS-0038-17-2122).

References

Bakker RJ (2018) AqSo_NaCl: Computer program to calculate pTVx properties in the H2O-NaCl fluid system applied to fluid inclusion research and pore fluid calculation. Computers & geosciences, 115, 122-133. https://doi.org/10.1016/j.cageo.2018.03.003

Blečić N (1974) Tečno-gasne inkluzije i njihova primena pri istraživanju pojedinih jugoslovenskih ležišta mineralnih sirovina [Fluid inclusions and their application in the exploration of certain Yugoslav deposits of mineral raw materials. Master's thesis-*in Serbian*] Faculty of Mining and Geology, Belgrade.

Cvetković V, Šarić K, Pécskay Z, & Gerdes A (2016) The Rudnik Mts. volcano-intrusive complex (central Serbia): An example of how magmatism controls metallogeny. Geologia Croatica, v. 69 (1), p. 89-99. https://doi.org/10.4154/GC.2016.08

Djoković I (2013) Izveštaj o strukturno-geološkim karakteristikama ležišta Rudnik. [Report of structural and geological features of the Rudnik deposit-*in Serbian*]. Fund of internal documents of the Rudnik mine company, Rudnik.

Jelenković R, Kostić A, Životić D, & Ercegovac M (2008) Mineral resources of Serbia. Geologica carpathica, 59(4), 345-361.

Kwak TAP (1986) Fluid inclusions in skarns (carbonate replacement deposits). Journal of Metamorphic Geology, 4(4), 363-384.

Meinert LD, Dipple GM, Nicolescu S (2005) World skarn deposits. Econ Geol 100th Anni:299–336.

El Chichón volcano, Mexico: A window into an active Porphyry-Cu-Mo-Au system.

María F. Reyes Gonzalez[1], Julie Roberge[1], Celestine N. Mercer[2], Angelica Adriana Camacho Pérez[1], Gerardo Arrieta Garcia[3], Sujitha Suresh Babu[1], Pablo E. Carbajal Martínez[1]
[1]Posgrado ESIA Ticomán, Instituto Politécnico Nacional, CDMX, Mexico
[2]U.S. Geological Survey, Geology, Geophysics and Geochemistry Science Center, Denver, CO.
[3]Laboratorio Universitario de Geoquímica Isotópica (LUGIS), Instituto de Geofísica, Universidad Nacional Autónoma de México (UNAM), CDMX, Mexico

Abstract. The 1982 eruption of El Chichón volcano, Mexico, left an acid crater lake with energetic fumaroles and thermal spring activity. El Chichón displays mineralogical and geochemical characteristics that are unique with respect to typical arc volcanoes and other volcanic centers within the Chiapas belt, including mineralized lithic fragments. Several decade-old published research studies have alluded to the possible connection between El Chichón magmatism and porphyry Cu mineralization. We aim to summarize these observations, and along with new hornblende mineral thermobarometry demonstrate that they complement current models for the genesis of fertile parental magmas and the development of Porphyry Cu-Mo-Au Systems. We suggest that while the 1982 plinian eruption revealed the epithermal portion of the magmatic-hydrothermal system, the altered lithic fragments found in pyroclastic deposits likely represent a mineralized zone from an actively developing porphyry deposit at depth.

1 Introduction

The powerful 1982 eruption of El Chichón volcano in Mexico is recognized as the largest disaster in modern Mexican history, destroying villages and killing over 2,000 people analogous to Pompeii. The El Chichón plinian eruption of high-sulfur, anhydrite-bearing magma destroyed the summit lava dome exposing the shallow epithermal portion of an actively mineralizing magmatic-hydrothermal system. Although deposits in the Chiapas region may never see development due to its status as a Natural Reserve, El Chichón offers a spectacular natural laboratory to investigate active geologic processes important to the development of mineralization in Porphyry-Cu-Mo-Cu Systems.

2 Complex tectonic setting

El Chichón is an active stratovolcano located in the state of Chiapas, southeast of Mexico City. It is the only active volcano in the Chiapanecan Volcanic Arc (CVC), which is a short arc segment that extends along the state of Chiapas in a NW-SE direction (Damon and Montesinos 1978).

The tectonic setting at El Chichón is complex. It is located near the intersection of three plates: the Cocos, American, and Caribbean plates. To the SW, the Cocos plate subducts beneath the North American plate, while to the SE the North American plate borders the Caribbean plate by the Motagua-Polochic fault (Fig. 1). Seismicity is intense along the offshore trench and is deep-seated beneath Chiapas inland (Damon and Montesinos 1978). The Chiapanecan Volcanic Arc aligned with the NE trending Tehuantepec fracture zone (Fig. 1), which has been interpreted as a torn segment of the Cocos plate that facilitates the ascent of hot asthenospheric mantle in the region (de Ignacio et al. 2003). The Tehuantepec fracture zone is associated with a drastic change in subduction angle of the Cocos plate, transitioning from 10° west of the ridge to 30° east of the ridge. This complex geometry may prime the Chiapas region for high heat flow, high influx of S-rich magma, and high permeability to magmas and hydrothermal fluids.

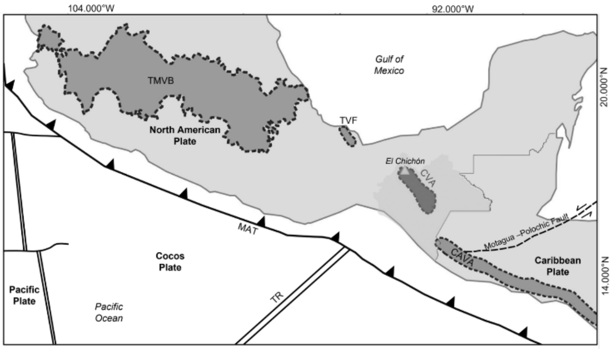

Figure 1. Location of the El Chichón volcano within the tectonic framework of Mexico (CVA=Chiapanecan Volcanic Arc; MAT= Middle America Trench; TR=Tehuantepec Ridge; TMVB=Trans-Mexican Volcanic Belt; TVF=Tuxtlas Volcanic Field; CAVA=Central America Volcanic Arc.

3 El Chichón eruptive and petrogenetic history

The El Chichón volcanic complex has had eleven eruptive events in the last 8,000 years (Espíndola et al. 2000), but the construction of the actual edifice probably started during the Middle Pleistocene (Layer et al. 2009). Cathedral volcano, 4 km NW of the present edifice (Fig. 2), is the remnant of the oldest volcanic activity in the area (~1.64 Ma; Macias et al. 2010). The most recent eruptive event occurred between March 28 and April 4, 1982. The eruption began with the destruction of the previous dome, built after the 550 B.P. eruption, and gave rise to a crater lake that currently has numerous active fumaroles and thermal springs (Fig. 3).

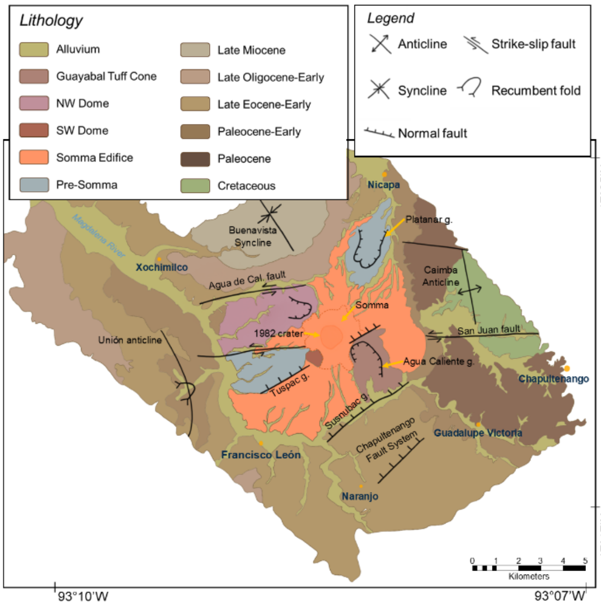

Figure 2. Geological map of El Chichón volcanic complex from Layer et al. (2009).

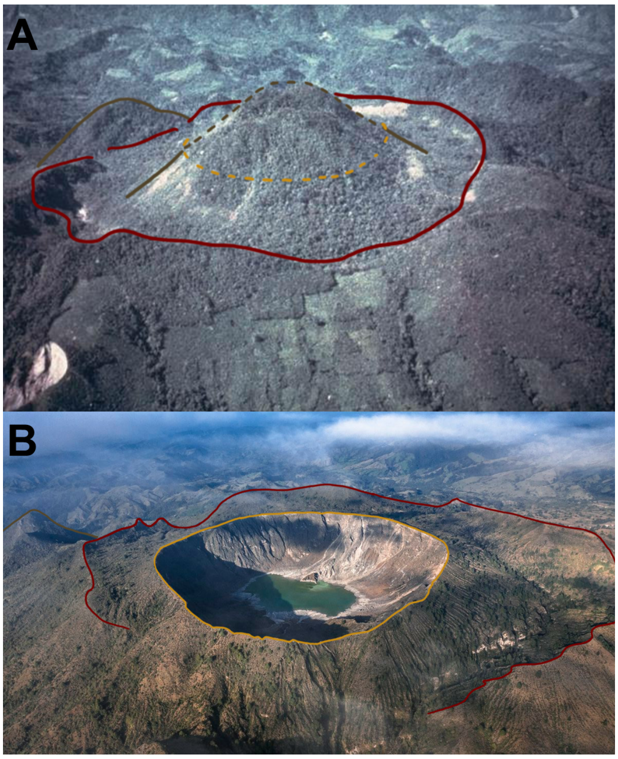

Figure 3. Photograph of El Chichón volcano before (A) and after (B) the 1982 eruption. The red outline represent the Somma Crater produced 279-209 ka while the yellow outline is the crater formed by the 1982 eruption.

More than 7 million tons of SO_2 was released into the atmosphere during the eruption and 9 surrounding towns were devastated, punctuated by the death of nearly 2,000 people (Sigurdsson et al. 1984).

Whole rock geochemical analysis of El Chichón eruptive products show a transitional calc-alkaline to adakite composition. Trachybasalt enclaves have been identified and there is a clear cogenetic relationship between all of the El Chichón eruptive products (Fig. 4).

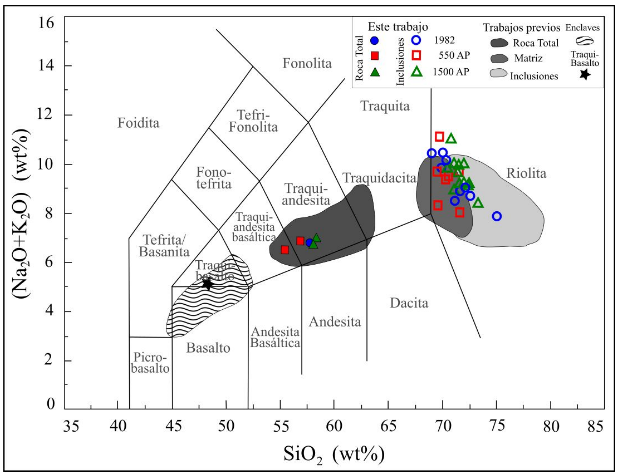

Figure 4. Total alkali versus silica diagram (LeBas et al. 1986) for El Chichón product. Colored symbols are from this work and shaded areas are from Luhr et al. (1984), Rose et al. (1984), Varekamp et al. (1984), Espíndola et al. (2000) and García-Palomo et al. (2004).

4 Late Neogene and Quaternary metallogenesis in the Chiapanecan Volcanic Arc

Mineralization identified in the Chiapas region is part of a larger Au-Ag belt (Fig. 5). It includes several Miocene deposits that have been proposed as IOCG-clan deposits (Cerro Colorado, 18 Ma; El Carmen, 13-12 Ma; Cerro Colorado - Cerro Bustillo, <12.7 Ma) and the Toliman porphyry Cu deposit (5.75Ma; Camprubi 2009, and references therein). The most recent mineral deposits in the region include the porphyry Au-Ag, Cu-Au-Mo, and low sulfidation Au epithermal deposits of Ixhuatan (2.8 Ma) and the “Santa Fe” Cu-Au skarn deposit (2.29-2.24 Ma).

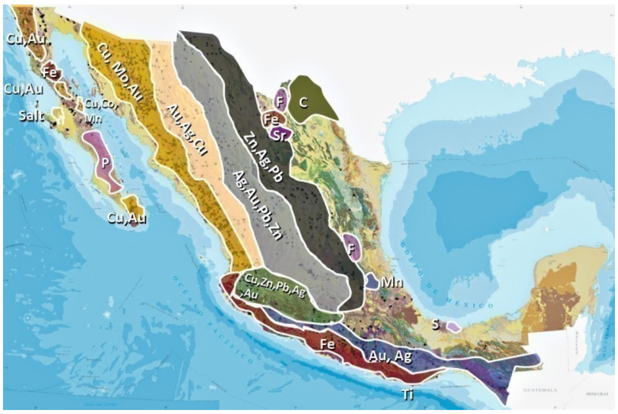

Figure 5. Distribution of mineral deposit belts throughout Mexico (map credit: Mexican Geological Survey).

Several observations indicate that active porphyry deposit mineralization is likely occurring within El Chichón. El Chichón eruptive products display mineralogical and geochemical characteristics that are unique with respect to typical arc volcanoes and other volcanic centers within the Chiapas belt. Pervasive magmatic anhydrite and titanite indicate a noteably oxidized (>NNO+0.5) and sulfur-rich system. Our recent hornblende analyses demonstrate magmas to be water rich (4-7 wt% H_2O) and evolving at great depths (200-700 MPa; 8-20 km depth) and at high temperatures (900-1000°C; Fig. 6). These data are in agreement with the CO_2 and He^3/He^4 data from El Chichón fumaroles that also suggest a greater depth of magma generation than is typical for arc volcanoes (Mazot et al. 2011).

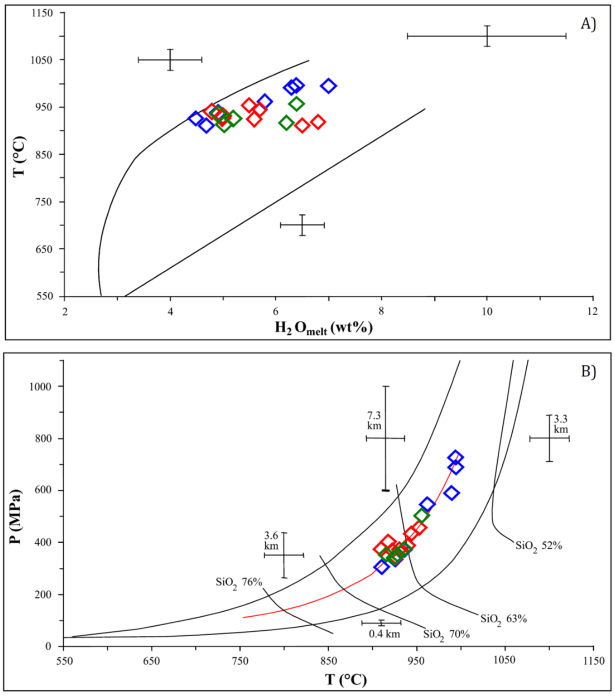

Figure 6. Application of the Ridolfi et al. (2010) geo-baro-hydrometer with newly acquired hornblende compositions.

Additionally, magmas are characterized by high Sr/Y values (~45; de Ignacio et al. 2003) coupled with moderate to low Y (<25 ppm). While this has been interpreted as adakite generation by direct melting of the subducting oceanic plate (Yogodzinsku et al. 2001), an alternative or additional interpretation is that these “adakite-like” magmas have undergone deep-crustal evolution conducive to high magma fertility with respect to porphyry Cu-Mo-Au systems (e.g., Richards 2011). Given the unique tectonic setting and evidence for high water and sulfur contents, both of these processes could be at play. Modeling by Chiaradia and Carrichi (2017) also suggest that deep crustal magma processing >500 MPa may be key in generating fertile magmas with potential to produce economic ore deposits.

Magmatism at El Chichón has been relatively long-lived (1.6 Ma), which has also been shown to promote the development of large mineralized porphyry Cu-Mo-Au systems (Chiaradia et al. 2022). Analysis of $^{87}Sr/^{86}Sr$ isotopic zoning profiles in plagioclase by Tepley et al. (2000) demonstrated that the El Chichón system was repeatedly recharged by high temperature mafic magma, consistent with observations of mafic enclaves. This process is also conducive to keeping the magmatic system mobile and long-lived.

Finally, Luhr (2009) and Damon and Montesinos (1978) noted mineralized lithic fragments collected from pyroclastic deposits that appear to contain alteration indicative of deeper porphyry-style mineralization. These fragments contain host rock similar to the 1982 dome rock, but overprinted with mineralization including potassic alteration with abundant Mg-rich biotite with veinlets of anhydrite, reminiscent of early potassic, high temperature porphyry-style alteration (Reed 2013).

We suggest that while the 1982 plinian eruption revealed the epithermal portion of the magmatic-hydrothermal system, the altered lithic fragments likely represent a mineralized zone from an actively developing porphyry deposit at depth (Fig. 7; Sillitoe 2010; John et al. 2010; Hofstra et al. 2021).

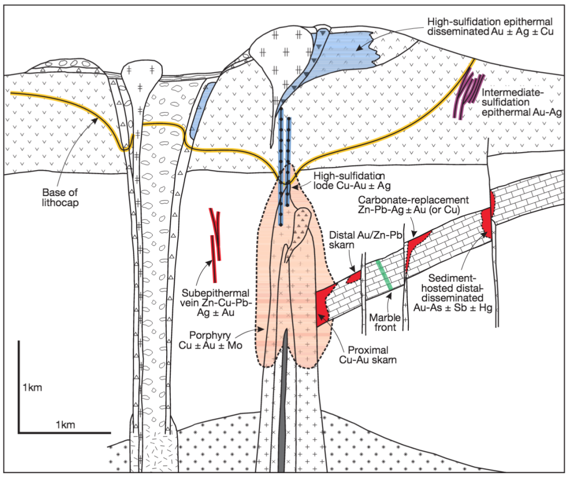

Figure 7. Anatomy of a Porphyry Cu-Mo-Au System showing the variety of ore deposit types that may develop within the system (Sillitoe 2010).

Acknowledgements

This project is funded by the individual project SIP-IPN (Secretaria de Investigación y Posgrado – Instituto Politécnico Nacional) no. 20221913. We thank Frank Tepley and Carlos Linares Lopez for their help with microprobes analysis. We also thank Alain Miron Velazquez, Nayeli Martinez Torres, Jorge Ivan Zuñiga Bautista and Jesús Guadarrama Garrido for field assistance.

References

Camprubí, A. (2009). Major metallogenic provinces and epochs of Mexico: SGA News, 25, 1-21.

Chiaradia, M. & Caricchi, L. (2022). Supergiant porphyry copper deposits are failed larged eruptions. Commun Earth Envioron 3, 107. https://doi.org/10.1038/s43247-022-00440-7

Damon, P., & Montesinos, E. (1978). Late Cenozoic volcanism and metallogenesis over an active Benioff zone in Chiapas, Mexico. AGS-Dig., 11, 155-168.

De Ignacio, C., Castiñeiras, P., Márquez, Á., Oyarzun, R., Lillo, J., & López, I. (2003). El Chichon volcano (Chiapas volcanic belt, Mexico) transitional calc-alkaline to adakitic-like magmatism: petrologic and tectonic implications. Int. Geol. Rev., 45(11), 1020-1028. https://doi.org/10.2747/0020-6814.45.11.1020

Espíndola, J.M., Macías, J.L., Tilling, R.I., Sheridan, M.F. (2000). Volcanic history of El Chichón Volcano (Chiapas, Mexico) during the Holocene, and its impact on human activity. Bull. Volcanol. 62, 90–104. https://doi.org/10.1007/s004459900064

Garcia-Palomo, A. G., Macıas, J. L., & Espındola, J. M. (2004). Strike-slip faults and K-alkaline volcanism at El Chichón volcano, southeastern Mexico. J. Volcanol. and Geotherm. Res., 136(3-4), 247-268. https://doi.org/10.1016/j.jvolgeores.2004.04.001

Hofstra, A., Lisitsin, V., Corriveau, L., Paradis, S., Peter, J., Lauzière, K., Lawley, C., Gadd, M., Pilote, J., Honsberger, I., Bastrakov, E., Champion, D., Czarnota, K., Doublier, M., Huston, D., Raymond, O., VanDerWielen, S., Emsbo, P., Granitto, M., and Kreiner, D. (2021). Deposit classification scheme for the Critical Minerals Mapping Initiative Global Geochemical Database: U.S. Geological Survey Open-File Report 2021–1049, 60 p., https://doi.org/10.3133/ofr20211049.

John, D.A., Ayuso, R.A., Barton, M.D., Blakely, R.J., Bodnar, R.J., Dilles, J.H., Gray, Floyd, Graybeal, F.T., Mars, J.C., McPhee, D.K., Seal, R.R., Taylor, R.D., and Vikre, P.G., (2010). Porphyry copper deposit model, chap. B of Mineral deposit models for resource assessment: U.S.G.S Sci. Investig. Rep. 5070–B, 169 p.

Layer, P. W., García-Palomo, A., Jones, D., Macías, J. L., Arce, J. L., & Mora, J. C. (2009). El Chichón volcanic complex, Chiapas, México: Stages of evolution based on field mapping and 40Ar/39Ar geochronology. Geophys. Int., 48(1), 33-54. https://doi.org/10.22201/igeof.00167169p.2009.48.1.98

Luhr, J. F. (2008). Primary igneous anhydrite: Progress since its recognition in the 1982 El Chichón trachyandesite. J. of Volcanol. and Geotherm. Res., 175(4), 394-407. https://doi.org/10.1016/j.jvolgeores.2008.02.016

Macías JL, Arce JL, Garduño-Monroy VH, Rouwet D, Taran Y, Layer P, Jiménez A, Álvarez R (2010): Estudio de prospección geotérmica para evaluar el potencial del volcán Chichonal, Chiapas. Unpublished Report no. 9400047770 IGF-UNAM-CFE

Mazot, A., Rouwet, D., Taran, Y., Inguaggiato, S. & Varley, N. (2011). CO2 and He degassing at El Chichón volcano, Chiapas, Mexico: gas flux, origin and relationship with local and regional tectonics. *B Volcanol* 73, 423–441. https://doi.org/10.1007/s00445-010-0443-y

Reed, M., Rusk, B. & Palandri, J. (2013). The Butte Magmatic-Hydrothermal System: One Fluid Yields All Alteration and Veins. *Econ Geol* 108, 1379–1396

Richards, J. P. (2011). High Sr/Y arc magmas and porphyry Cu ± Mo ± Au deposits: just add water. *Econ Geol* 106, 1075–1081.https://doii.org/10.2113/econgeo.106.7.1075

Sigurdsson, H., Carey, S. N., Espíndola J. M. (1984). The 1982 eruptions of El Chichón Volcano, Mexico (2): stratigraphy of pyroclastic deposits. J Volcanol. Geotherm. Res. 23. 11–37. https://doi.org/10.1016/0377-0273(84)90055-6

Sillitoe, R. H. (2010). Porphyry copper systems. Econ. Geol, 105(1), 3-41. https://doi.org/10.2113/gsecongeo.105.1.3

Tepley III, F. J., Davidson, J. P., Tilling, R. I., & Arth, J. G. (2000). Magma mixing, recharge and eruption histories recorded in plagioclase phenocrysts from El Chichon Volcano, Mexico. J. of Petrol., 41(9), 1397-1411. https://doi.org/10.1093/petrology/41.9.1397

Varekamp, J. C., Luhr, J. F., & Prestegaard, K. L. (1984). The 1982 eruptions of El Chichón Volcano (Chiapas, Mexico): character of the eruptions, ash-fall deposits, and gasphase. J Volcanol. Geotherm. Res. 23(1-2), 39-68. https://doi.org/10.1016/0377-0273(84)90056-8

Yogodzinski, G. M., Lees, J. M., Churikova, T. G., Dorendorf, F., Wöerner, G., & Volynets, O. N. (2001). Geochemical evidence for the melting of subducting oceanic lithosphere at plate edges. Nature, 409(6819), 500-504. https://doi.org/10.1038/35054039

Probing sulfur behavior in arc magmas with immiscible magmatic sulfides and apatite: Complementary data sets to assess ore-forming potential

Hervé Rezeau[1], Yannick Buret[2], Benjamin Z. Klein[3], Oliver Jagoutz[4], Shuhei Ono[4]
[1]*Department of Geosciences, University of Arizona, Tucson, USA*
[2]*Imaging and Analysis Centre, Natural History Museum, London, United Kingdom*
[3]*Institute of Earth Sciences, University of Lausanne, Bâtiment Géopolis, Lausanne, Switzerland*
[4]*Department of Earth, Atmospheric, and Planetary Sciences, Massachusetts Institute of Technology, Cambridge, USA*

Abstract. Sulfur is one of the most abundant volatiles in subduction zones. Sulfur displays a complex behavior in arc magmas arising from its ability to partition between various phases (solid, immiscible liquid, gas and dissolved ions) and from its redox-dependent speciation (S^{2-} to S^{6+}). As a result, sulfur plays a critical role in the mobilization and transport of economically essential chalcophile elements (e.g., Cu, Au) during melt differentiation and fluid saturation and exsolution.

Herein, we first present whole rock sulfur isotope data in two crustal arc sections - the Early–Middle Jurassic Talkeetna Arc in south-central Alaska, and the Late Cretaceous Bear Valley Intrusive Suite (BVIS) in southern Sierra Nevada. These results reveal that melt differentiation is characterized by a $\delta^{34}S$ increase in the Talkeetna Arc and a $\delta^{34}S$ decrease in the BVIS. These opposing trends are explained by the crystallization of immiscible magmatic sulfides, and possibly upper crustal magma degassing, in the presence of dissolved oxidized and reduced sulfur species, respectively. Then, we examine the distribution of sulfur concentrations in magmatic apatites using high-resolution laser ablation mapping in two ore-related upper crustal magmatic systems namely the Meghri-Ordubad pluton in southern Armenia and Bajo de la Alumbrera in Argentina. This approach reveals a variety of textures including primary sulfur zoning highlighting episodes of sulfur-rich rejuvenation and sulfur degassing.

Collectively, our results argue that sulfur is an insightful geochemical tracer of redox conditions and crustal processes, which should be considered to assess ore-forming potential of arc magmas.

1 Introduction

Porphyry copper systems are primarily associated with oxidized, sulfur-rich and hydrous arc magmas (Richards 2022). Oxygen fugacity (fO_2) strongly controls sulfur speciation (sulfide, S^{2-}; sulfate, S^{6+}), sulfur solubility, and hence the budget of chalcophile elements in arc magmas (Jugo et al. 2010). While Cu (and other economically important chalcophile elements) concentrations in melt may not represent a limiting factor for the formation of porphyry copper deposits, melt Cu concentrations certainly play a role to modulate the available mass of Cu that partition into the exsolving fluid phases and followed by Cu precipitation in porphyry copper systems (e.g., Rezeau and Jagoutz 2020). Thus, determining the evolution of sulfur speciation and sulfur concentrations during arc magmatic processes may help evaluate the ore-forming potential of arc magmas. While some studies have shown that sulfur isotope (expressed as $\delta^{34}S$) represent useful tracers of sulfur speciation in arc magmas and thus fO_2 (Sasaki and Ishihara 1979; de Moor et al. 2022), others have used sulfur concentrations in apatite - a common accessory mineral in arc magmas - to monitor the evolution of sulfur and fO_2 in arc magmas (Streck and DIlles 1998; Chelle-Michou and Chiaradia 2017). Here, we first present whole rock sulfur isotope data for two exposed crustal arc sections to track sulfur isotope compositions during transcrustal magmatic processes. Then, we examine the distribution of sulfur concentrations in magmatic apatites using high-resolution laser ablation mapping to evaluate the evolution of sulfur concentrations in upper crustal magmatic systems associated with porphyry copper systems.

Our results show that whole rock sulfur isotopes can accurately identify intrusions that crystallized under oxidized and reduced conditions, while sulfur concentration maps in apatite reveal primary igneous sulfur zoning allowing us to track episodes of sulfur-rich rejuvenation and sulfur degassing. Combined, these complementary data sets could help identifying these geochemical features, and hence may provide insightful tools to assess the ore-forming potential of arc igneous rocks.

2 Sulfur isotope fractionation during crystallization-differentiation processes

2.1 Study areas

Two well-studied exposed crustal arc sections are investigated to evaluate sulfur isotope systematics during crustal magmatic differentiation processes.

The Early–Middle Jurassic intra-oceanic Talkeetna Arc section exposed in the Chugach Mountains, south-central Alaska, represents a faulted crustal arc section (Burns 1985). It exposes ultramafic units formed at ~0.9-1.2 GPa (~30–35 km-depth), basal gabbros formed at ~0.5-1 GPa (~15–30 km-depth), middle to upper crustal mafic to felsic intrusions formed at ~0.2-0.5 GPa (~5–15 km-depth), and basalt to rhyolite volcanic rocks capping underlying intrusions (Burns 1985; Debari and Coleman 1989; Greene et al. 2006). Furthermore, the juvenile radiogenic isotopic compositions ($\varepsilon Nd_{(t)}$=6-7.8;$^{87}Sr/^{86}Sri$=0.703379-0.703951) argue for limited crustal assimilation (e.g., Greene et al 2006; Rioux et al. 2007).

The Late Cretaceous Bear Valley Intrusive Suite (BVIS) exposes a 30 km-depth continuous crustal arc section emplaced within 1.39 ± 0.06 Ma in the southern Sierra Nevada (Klein et al. 2021; Klein and Jagoutz 2021). The deepest portion of the BVIS exposes mafic igneous cumulates formed at ~0.8-0.9 GPa (~25–30 km-depth), whereas shallower units consist of tonalites formed between ~0.7 GPa and ~0.2 GPa (~5-20 km-depth). Isotopic studies indicate that these rocks are characterized by ~5-20% of crustal assimilation (Klein et al. 2021).

In Talkeetna and BVIS, petrogenetic models suggest that SiO_2-rich intrusions represent derivative melts from deep crustal crystallization-differentiation of a parental mafic melt (Greene et al. 2006; Klein and Jagoutz 2021; Rezeau et al. 2021, 2023). Importantly, both arc sections are characterized by ultramafic-mafic cumulates and felsic intrusions containing primary magmatic sulfides offering opportunities to track the evolution of sulfur isotopes ($\delta^{34}S$) during transcrustal magmatic processes.

2.2 Results and Interpretations

For each crustal section, we analyzed whole rock sulfur isotopes for samples representative of the entire compositional range and depths.

In Talkeetna, whole rock $\delta^{34}S$ values for 25 samples indicate a clear sulfur isotope fractionation during melt differentiation characterized by a $\delta^{34}S$ increase from -1.28 to +5.61‰ (Figure 1). Combined with a quantitative petrological model that constrains the liquid line of descent and sulfide saturation as a function of sulfur content, oxygen fugacity, pressure, and temperature, we demonstrate that saturation of immiscible magmatic sulfides is capable of generating such sulfur isotope fractionation in the presence of dissolved oxidized sulfur species (Rezeau et al 2023). The most positive $\delta^{34}S$ values observed for upper crustal felsic intrusions reflect enhanced sulfur fractionation due to fluid degassing. Therefore, we suggest that sulfide immiscibility and magma degassing are not mutually exclusive and represent complementary processes that combine to explain the observed range of positive $\delta^{34}S$ compositions in Talkeetna. Any influences by crustal assimilation of pre-existing oceanic crust containing seawater sulfate is unlikely.

In the BVIS, whole rock $\delta^{34}S$ for 21 samples range from -5.1 to -1.2 ‰, where $\delta^{34}S$ values for lower crustal mafic cumulates overlap with those of shallower tonalites (Figure 1). Additional whole rock $\delta^{34}S$ for six metasedimentary rock pendants reveal that deeper metasediments (~0.7-0.9 GPa) yield lighter $\delta^{34}S$ (-11.5 and -4.1‰) compared to shallower metasediments (~0.4-0.6 GPa) yielding heavier $\delta^{34}S$ (-0.7 to +6.4‰). The lack of correlation between $\delta^{34}S$ and the composition of mafic cumulates indicates heterogenous crustal assimilation (~5-20%) of deep metasediments in the lower crust. In contrast, whole rock $\delta^{34}S$ values for tonalites are negatively correlated with SiO_2 content or depths (Figure 1). This can be explained by saturation of immiscible magmatic sulfides and/or fluid degassing in the presence of dissolved reduced sulfur species, as opposed to crustal assimilation. In the BVIS, we suggest that primary arc melts ($\delta^{34}S$~0‰) assimilate graphite-bearing metasediments in the deep crust promoting reduced conditions and saturation of immiscible magmatic sulfides characterized by negative $\delta^{34}S$. Then, reduced derivative tonalitic melts are produced and ascend to shallower crustal levels, where melt differentiation is accompanied by saturation of immiscible magmatic sulfides and/or fluid saturation leading progressive negative $\delta^{34}S$.

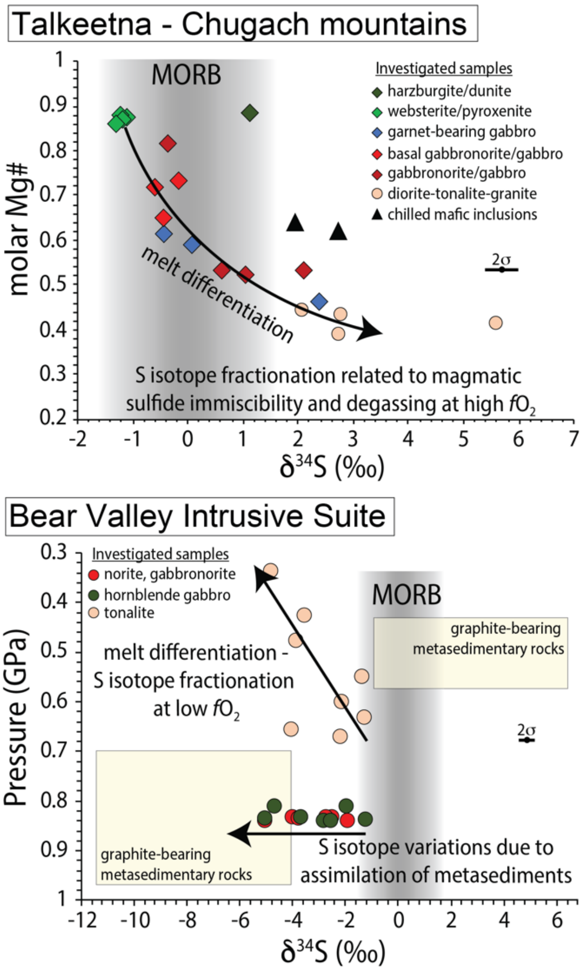

Figure 1. Evolution of sulfur isotope (expressed as $\delta^{34}S$) in rocks formed in the Talkeetna and Bear Valley Intrusion Suite arc sections. Top: whole rock S isotope compositions versus Mg# in Talkeetna rocks. Bottom: whole rock S isotope compositions versus pressure of crystallization in the Bear Valley Intrusive Suite rocks.

2.3 Implications for ore-forming potential

Our findings demonstrate that $\delta^{34}S$ is a faithful tracer of fO_2 during arc magma differentiation. For instance, both Talkeetna and BVIS consist of SiO_2-rich upper crustal intrusions characterized by similar whole rock geochemistry, yet they yield contrasting $\delta^{34}S$ values indicating different evolution of fO_2 during melt differentiation between the two locations.

Knowing that high fO_2 represent favourable conditions for the formation of porphyry copper systems (Richards 2021), upper crustal intrusions with positive $\delta^{34}S$ should represent better exploration targets higher with respect to those with negative $\delta^{34}S$.

While our results are consistent with the pioneering work of Sasaki and Shinohara (1979), we argue that positive $\delta^{34}S$ values in arc magmas are unlikely to reflect the mantle source region and may, instead, fingerprint the combination of early magmatic sulfide immiscibility and later magma degassing. Both processes may increase the ore-forming potential as immiscible sulfides represent temporary metal carriers that can be remobilized if melt reaches fluid saturation and degassing (e.g., Nadeau et al. 2010; Heinrich and Connolly 2022). Overall, sulfur isotope compositions in arc magmas should provide valuable information to evaluate the relative ore-forming potential between sets of intrusions in a given regional district.

3 High-resolution laser ablation mapping of sulfur concentration in apatite

3.1 Methodology

Traditionally, apatite is not analysed by laser ablation inductively coupled plasma mass spectrometry (LA-ICP-MS) due to high background levels from $^{16}O^{16}O$, $^{16}O^{17}O$ and $^{16}O^{18}O$ species. However, the ability to reduce these interferences using reaction gasses (O_2) has made it possible to measure the major sulfur isotope (^{32}S) as a reaction product ($^{32}S^{16}O$) therefore opening new avenues for sulfur analysis by ICP-MS (e.g., Nakano 2018). Furthermore, the new generation of laser ablation systems have ultra-fast signal washouts, permitting rapid elemental mapping at high repetition rates, thereby boosting sensitivity to permit smaller spot sizes. Here, we present LA-ICP-MS mapping of apatite crystals using the 193 nm Teledyne Iridia laser ablation system combined with an Agilent 8900 ICP-QQQ-MS. The full width of a single pulse at 10% of the maximum peak intensity was optimised at <5 ms in order to increase sensitivity and decrease imaging time. Individual maps (<100 x 100 µm to 300 x 100 µm) take between 1 and 5 minutes. Image processing and quantification was carried out using HDIP (v. 1.6). Routine analysis of Durango apatite reveals accuracy within the published range of sulfur concentrations. Our sulfur concentrations obtained from LA-ICP-MS maps are consistent with previously determined EMPA concentrations.

3.2 Results and interpretations

We use this approach to track the evolution of of sulfur concentrations in the formation of magmatic hosted porphyry copper deposits in two well-studied case study areas: Bajo de la Alumbrera in Argentina and the Meghri-Ordubad pluton in southern Armenia. High-resolution concentration maps of apatite grains reveal a variety of textures including primary igneous zoning, multi-phase growth, alteration and sulfide inclusions (Figure 2).

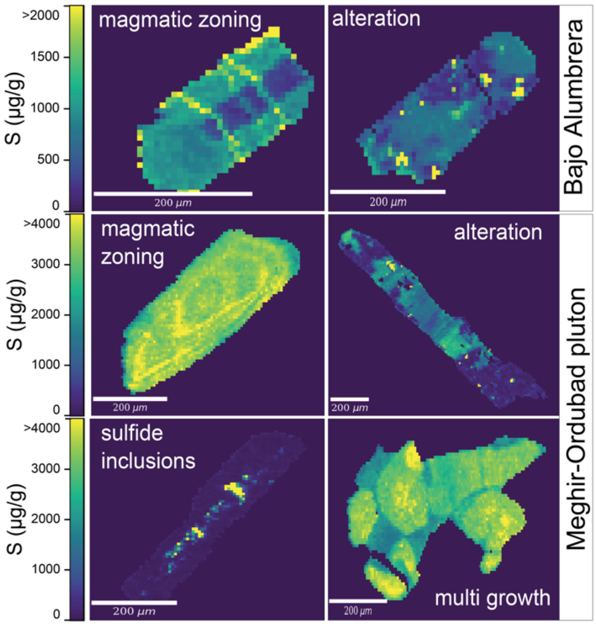

Figure 2. Representative high-resolution sulfur maps of apatite grains hosted in ore-related intrusions at Bajo de la Alumbrera and Meghri-Ordubad pluton.

In Bajo de la Alumbrera, apatite grains hosted in syn-mineralization altered intrusions reveal patchy sulfur zoning which show evidence for hydrothermal remobilization. In contrast, apatite from syn-mineralization volcanism display well-defined reverse sulfur zoning. These features are consistent with co-crystallizing plagioclase reverse zoning that is interpreted as rejuvenation of upper crustal reservoirs (Buret et al., 2017). In this case, it provides evidence for sulfur-rich mafic recharge.

In the Meghri-Ordubad pluton, we analyzed apatite grains hosted in shoshonitic intrusions that pre-date and that are contemporaneous to the formation of the large Kadjaran porphyry copper-molybdenum deposits (Rezeau et al 2016). Apatite grains hosted in syn-mineralization altered intrusions also reveal patchy sulfur zoning indicative of hydrothermal remobilization. In pre-mineralization intrusive rocks, primary sulfur zoning is interpreted as episodes of sulfur-rich mafic magma rejuvenation, whereas sulfur-poor zones may reflect sulfur degassing and/or saturation of co-existing magmatic anhydrite (Streck and Dilles 1998). The presence of sulfur-poor apatite with sulfide micro-inclusions suggests co-crystallization of apatite and magmatic sulfide at fairly reduced conditions where dissolved S^{2-} prevails with respect to S^{6+} in the melt. The multi-phase apatite growth is characterized by an early growth of euhedral sulfur-rich apatite grains that are cemented by late interstitial sulfur-poor anhedral apatite. While these textural features may either reflect two generations of magmatic apatites or an early generation of magmatic apatites that are resorbed during late deuteric or hydrothermal fluids, its origin remains elusive, and it requires further investigations.

3.3 Implications for ore-forming potential

We demonstrate the ability to generate fast and accurate high-resolution laser ablation mapping of sulfur concentration on apatite. This approach can reveal precious information on the sulfur distribution in apatite grains helping to monitor sulfur behavior during crustal magmatic processes. As sulfur-rich mafic rejuvenation of upper crustal felsic reservoirs is an important trigger for the formation of porphyry copper systems (Hattori and Keith 2001; Wilkinson 2013), revealing primary sulfur zoning in apatite would help identifying episodes of sulfur rejuvenation and degassing. As a result, this approach provides opportunities for the rapid assessment of sulfur concentrations in apatites and may provide insightful tools to evaluate the ore-forming potential of arc-related igneous rocks during mineral exploration.

Acknowledgements

This work was supported by the Swiss National Foundation postdoc mobility grant P400P2_194421 to Hervé Rezeau and by the National Science Foundation NSF EAR-1902179 and NSF EAR-1925863 to Oliver Jagoutz. The authors acknowledge Patrick Beaudry and Gareth Izon for collaboration on acquiring sulfur isotope data and for stimulating scientific discussions. Peter Kelemen is also acknowledged for sharing Talkeetna samples and key scientific inputs.

References

Buret, Y., Wotzlaw, J. F., Roozen, S., Guillong, M., von Quadt, A., & Heinrich, C. A. (2017): Zircon petrochronological evidence for a plutonic-volcanic connection in porphyry copper deposits; Geology, v. 45(7), p. 623-626.

Burns, L. E. (1985): The Border Ranges ultramafic and mafic complex, south-central Alaska: cumulate fractionates of island-arc volcanics; Canadian Journal of Earth Sciences, v. 22(7), p. 1020-1038.

Chelle-Michou, C., and Chiaradia, M. (2017): Amphibole and apatite insights into the evolution and mass balance of Cl and S in magmas associated with porphyry copper deposits; Contributions to Mineralogy and Petrology, v. 172(11-12), p. 105.

DeBari, S. M., and Coleman, R. G. (1989): Examination of the deep levels of an island arc: Evidence from the Tonsina ultramafic-mafic assemblage, Tonsina, Alaska; Journal of Geophysical Research: Solid Earth, v. 94, p.4373-4391.

De Hoog, J. C. M., Mason, P. R. D., and Van Bergen, M. J. M. (2001): Sulfur and chalcophile elements in subduction zones: constraints from a laser ablation ICP-MS study of melt inclusions from Galunggung Volcano, Indonesia; Geochimica et Cosmochimica Acta, v.65, p.3147-3164.

de Moor, J. M., Fischer, T. P., and Plank, T. (2022): Constraints on the sulfur subduction cycle in Central America from sulfur isotope compositions of volcanic gases; Chemical Geology, v. 588, 120627.

Greene, A. R., DeBari, S. M., Kelemen, P. B., Blusztajn, J., and Clift, P. D. (2006): A detailed geochemical study of island arc crust: the Talkeetna arc section, south–central Alaska; Journal of Petrology, v. 47(6), p. 1051-1093.

Hattori, K. H., and Keith, J. D. (2001): Contribution of mafic melt to porphyry copper mineralization: evidence from Mount Pinatubo, Philippines, and Bingham Canyon, Utah, USA; Mineralium Deposita, v. 36, p. 799-806.

Heinrich, C. A., and Connolly, J. A. (2022): Physical transport of magmatic sulfides promotes copper enrichment in hydrothermal ore fluids; Geology, v. 50(10), p. 1101-1105.

Jugo, P. J., Wilke, M., and Botcharnikov, R. E. (2010): Sulfur K-edge XANES analysis of natural and synthetic basaltic glasses: Implications for S speciation and S content as function of oxygen fugacity; *Geochimica et Cosmochimica Acta*, v. *74*(20), p. 5926-5938.

Klein, B. Z., and Jagoutz, O. (2021): Construction of a trans-crustal magma system: building the Bear Valley Intrusive Suite, southern Sierra Nevada, California; Earth and Planetary Science Letters, v. 553, 116624.

Klein, B. Z., Jagoutz, O., and Ramezani, J. (2021): High-precision geochronology requires that ultrafast mantle-derived magmatic fluxes built the transcrustal Bear Valley Intrusive Suite, Sierra Nevada, California, USA; Geology, v. 49(1), p.106-110.

Nadeau, O., Williams-Jones, A. E., and Stix, J. (2010): Sulphide magma as a source of metals in arc-related magmatic hydrothermal ore fluids; Nature Geoscience, v. 3(7), p.501-505.

Nakano, K., (2018): Agilent Application Note, 5991-3520EN

Rezeau, H., Jagoutz, O., Beaudry, P., Izon, G., Kelemen, P., and Ono, S. (2023): The role of immiscible sulfides for sulfur isotope fractionation in arc magmas: Insights from the Talkeetna Island arc crustal section, south-central Alaska; Chemical Geology, 121325.

Rezeau, H., Klein, B. Z., and Jagoutz, O. (2021): Mixing dry and wet magmas in the lower crust of a continental arc: new petrological insights from the Bear Valley Intrusive Suite, southern Sierra Nevada, California; Contributions to Mineralogy and Petrology, v. 176(9), 73.

Rezeau, H. and Jagoutz, O. (2020): The importance of H_2O in arc magmas for the formation of porphyry Cu deposits; Ore Geology Reviews 126, 103744.

Rezeau, H., Moritz, R., Wotzlaw, J. F., Tayan, R., Melkonyan, R., Ulianov, A., Selby, D., d'Abzac, F-X., and Stern, R. A. (2016): Temporal and genetic link between incremental pluton assembly and pulsed porphyry Cu-Mo formation in accretionary orogens; Geology, v. 44(8), p. 627-630.

Richards, J. P. (2022): Porphyry copper deposit formation in arcs: What are the odds?; *Geosphere*, v. *18*, p.130-155.

Rioux, M., Hacker, B., Mattinson, J., Kelemen, P., Blusztajn, J., and Gehrels, G. (2007): Magmatic development of an intra-oceanic arc: High-precision U-Pb zircon and whole-rock isotopic analyses from the accreted Talkeetna arc, south-central Alaska; Geological Society of America Bulletin, v. 119(9-10), p. 1168-1184.

Sasaki, A., and Ishihara, S. (1979): Sulfur isotopic composition of the magnetite-series and ilmenite-series granitoids in Japan; Contributions to Mineralogy and Petrology, v. 68, p. 107-115.

Streck, M. J., and Dilles, J. H. (1998): Sulfur evolution of oxidized arc magmas as recorded in apatite from a porphyry copper batholith; Geology, v. 26, p. 523-526.

Wilkinson, J. J. (2013): Triggers for the formation of porphyry ore deposits in magmatic arcs; *Nature Geoscience*, v. *6*(11), p. 917-925.

New experimental data on potassic vs. albitic alteration

Taraneh Roodpeyma[1]**, Thomas Driesner**[1]
[1]*Department of Earth Sciences, ETH University, Zurich, Switzerland*

Abstract. Porphyry copper deposits display different alteration types among which potassic alteration of plagioclase and amphiboles is the most prominent one as it typically overlaps with ore mineralization. However, in some Au-enriched porphyry deposits (e.g., Batu Hijau, Indonesia, and Bolcana, Romania), potassic feldspar alteration seems to be largely absent and albitic alteration is observed instead. K-Na exchange between fluid and alkali feldspars in reverse direction could be a plausible mechanism for albitic vs. potassic feldspar alteration but published experimental data seem to preclude this possibility of albitic alteration. As the published data bear significant problems we performed new experiments at 400 and 450°C and at different pressures over wide ranges of chloride concentrations. Results reveal that at low chloride concentrations and rather low pressures, cooling may potentially lead to albitic instead of potassic alteration. However, relationships are non-trivial if the full dependence on temperature, pressure and salinity is taken into account.

1 Introduction

Mapping of porphyry copper deposits revealed global similarities in terms of alteration patterns and vein sequences (e.g. Lowell and Guilbert 1970; Gustafson and Hunt 1975). Potassic alteration of plagioclase to K-feldspar and/or amphiboles to biotite has received particular interest as it is often correlated with the main ore zones (e.g., Seedorff et al. 2005). However, there are exceptions, the causes of which have remained elusive. For example, in some Au-enriched porphyry Cu deposits such as Batu Hijau, Indonesia (Schirra et al. 2022), and Bolcana, Romania (Blannin et al. 2019), potassic feldspar alteration is largely absent while biotite alteration of amphiboles is present and albitic feldspar alteration is observed instead. Although albitic alteration may simply reflect Ca-loss from plagioclase (e.g., Henley et al. 2022) or could belong to a post-potassic stage (e.g., Calder et al. 2023, and references therein), the question remains why no potassic feldspar alteration occurred.

The exchange reaction of K and Na between fluid and alkali feldpars:

$$albite + KCl_{aq} = K\text{-}feldspar + NaCl_{aq}$$

governs potassic feldspar alteration and implies a leading role of the fluid's K/Na concentration ratio for determining the direction of reaction, i.e., albite/sodic alteration may be possible by the reaction proceeding to the left. Previous experimental studies, however, are largely inconclusive whether sodic alteration of K-feldspar could be achieved: since the fluid's K/Na concentration ratio in equilibrium with albite and K-feldspar decreases with decreasing temperature (e.g. Orville 1963), heating of fluid would be required to achieve albitic alteration, or the fluid has to have a K/Na concentration ratio below the equilibrium value, which is difficult to realize as long as plagioclase is present in the host rock. Furthermore, an in-depth analysis (Roodpeyma and Driesner 2020) of the existing experimental data revealed that the most relevant study (Lagache and Weisbrod 1977) is based on data that were obtained in the two phase liquid+vapor fluid field, which obscured the derivation of the correct equilibrium values.

In order to obtain improved data on equilibrium K/Na exchange between alkali feldspars and hydrothermal fluids, we performed new experiments at 400°C and 450°C, both at pressures equivalent to pure water densities of about 0.3 and 0.5 g cm^{-3}, and for total aqueous concentrations ranging from 10^{-4} to 13 molal chloride. The comprehensive data set allows us to assess the effect of temperature, pressure, and total aqueous chloride molality at conditions relevant to porphyry deposit formation.

2 Experimental

The temperature, pressure, and chloride concentration range of the experiments were designed to close the existing gap of available data points (Roodpeyma et al. 2022). In order to be able to compare equilibrium K/Na molal ratios in the fluid, irrespective of the effect of (unknown) activity coefficients at finite concentrations, the experimental bulk concentration range starts from very dilute, close to infinite dilution, where the K/Na concentration ratio can be regarded as the equilibrium activity ratio (activity coefficients = 1). Following Lagache and Weisbrod (1977), we call the K/Na molal concentration ratio C, with C^{∞} denoting the value at infinite dilution. Figure 1 illustrates the measured C for all types of used initial aqueous solutions (pure KCl solution, pure NaCl solution, mixture) in reaction with alkali feldspars under various total chloride concentrations. The equilibrium state is confidently achieved through reversed experiments over all concentrated regions. Some deviating data points at high concentration reflect an inadequate choice of reactant ratios, i.e., lacking a sufficient mole amount of alkalis in solid or fluid phases, not allowing the reaction to proceed to completion.

3 Results

3.1 Temperature effect

Arguably the biggest deviation from the previous state of knowledge is that C^{∞} decreases with temperature at pressures equivalent to constant pure water density, at least for the studied temperature interval. At the given water density of 0.3 g cm^{-3}, the present study shows that C^{∞} value, depicted in Fig. 1, decreases from 0.056 to 0.04 as temperature increases from 400 to 450°C. At elevated concentrations, the C ratio is around 0.2 and shows little change from 400 to 450°C (Fig. 2A,C); if any, then a minor increase in C may occur with increasing temperature. C values at higher concentrations are typically higher than the ones reported by Lagache and Weisbrod (1977). A similar trend is seen for experimental results at pressures equivalent to 0.5 g cm^{-3} pure water density (Fig. 2B,D).

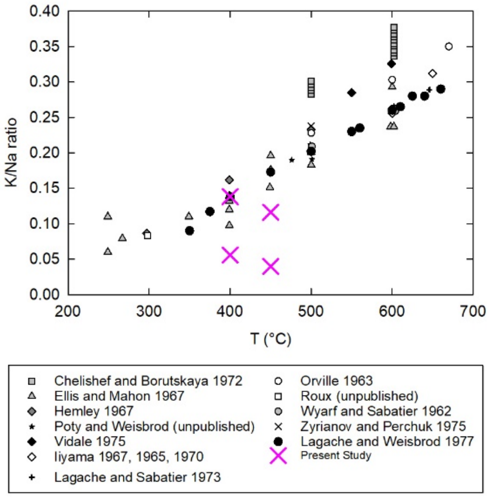

Figure 1. Effect of T on the K/Na molal ratio. New data compared to existing literature data

3.2 Pressure effect

At 400°C with increasing pressure equivalent to 0.3 g cm^{-3} (288 bar) to 0.5 g cm^{-3} (372 bar) pure water density, C_{∞} increases significantly from 0.056 to 0.138 (Fig. 2C). This finding is qualitatively consistent with the data points of C versus total chloride molalities plotted by Lagache and Weisbrod (1977).

While Lagache and Weisbrod (1977) showed a recognizable pressure dependence on C values at 500°C and low concentrations, this finding apparently did not enter their derivation of equilibrium constants and has largely been ignored in the literature. Our results at 400°C as well as the data at 450°C show a much more pronounced pressure effect than indicated by the plots of Lagache and Weisbrod (1977).

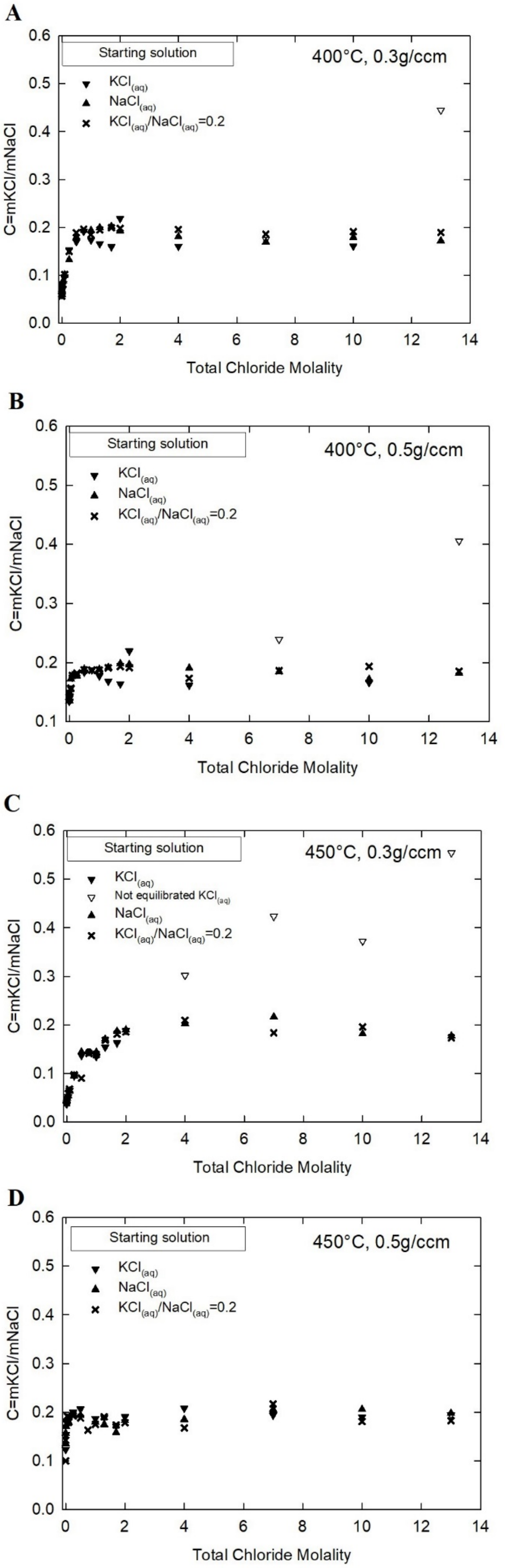

Figure 2. Experimental values of K/Na molal ratio at isotherms of 400 (A) and 450°C (C) and water density of 0.3 g cm-3 and at isotherms of 400 (B) and 450°C (D) and water density of 0.5 g cm-3

3.3 Concentration effect

C changes significantly as a function of concentration (Figures 2). However, it should be noted that all these C values represent equilibrium values at the given temperature and pressure and the concentration dependence is an expression of how activity coefficients for KCl and NaCl in the solution change differently with increasing concentration. There is evidence of liquid-vapor immiscibility at 450°C / 0.3 g cm^{-3} water density between ca. 0.1 and 2 m chloride concentration (however, with significant uncertainties).

4 Discussion

The new results imply that albitic instead of K-feldspar alteration may be possible for certain temperature-pressure-concentration paths of fluid in a porphyry-forming system. Namely – and contrary to previous thinking – a temperature decrease can induce albitic alteration, provided that the fluid is of low concentration and follows a temperature-pressure path of constant low or increasing density. This may be an explanation for its occurrence in gold-rich porphyries for which generally shallower depth of formation (and, therefore, lower pressure; Murakami et al. 2010) have been inferred.

(Near-)isothermal pressure decrease, on the contrary, would induce, at least at low concentrations, K-feldspar alteration. Our current data set does not yet allow to quantitatively assess which cooling paths and temperature-pressure-concentration window(s) would equally promote K-feldspar alteration. Given its widespread occurrence, however, such windows must be common in typical porphyry copper-forming systems.

The curved concentration dependence of the equilibrium K/Na ratio implies that mixing high- and low-concentration fluids may be an alternative way for inducing albitic alteration as the mixtures' C value would fall below the equilibrium curve in Figures 2. However, it is rather difficult to imagine how such fluids would follow independent flow paths prior to mixing.

5 Conclusion

Although the alteration pattern widely shows similarities among porphyry copper deposits, occasional sodic instead of potassic alteration of feldspar appears to violate the general sequence in some cases. As the role of cooling and depressurization during the fluid evolution paths has been widely emphasized, we presented new experimental data set studying the compositional state of the alkali feldspars-KCl-NaCl-H_2O system. Focusing on the K/Na molal ratio of fluid phase under influence of temperature, pressure, and concentration it is shown that temperature and pressure can have opposite effect on the equilibrated K/Na ratio, depending on the path. For example, decreasing temperature at a given density leads to the increase of K/Na ratio in the fluid phase, that is, the chemical reaction proceeds towards albitic precipitation while a decrease in pressure at a given temperature decreases the K/Na equilibrium ratio, which drives the reaction towards potassic alteration. Moreover, the curved trend of the equilibrium fluid K/Na molal ratio versus concentration shows the advent of new equilibrium K/Na implies that mixing of low- and high-salinity fluid phases leads to homogenization at K/Na concentration ratios below the equilibrium curve. We conclude that the new experimental insights contribute to further understanding of porphyry deposits through closing experimental and conceptual gaps that have led to potentially erroneous assumptions about potassic vs. sodic feldspar alteration.

6 References

Blannin R, Tusa L, Birtel S, Gutzmer J, Gilbricht S, Ivascanu P (2019) Metal deportment and ore variability of the Bolcana porphyry Au-Cu system (Apuseni Mts, Romania) - Implications for ore processing. 15th Biennial Meeting of the Society for Geology Applied to Mineral DepositsAt: Glasgow. https://www.researchgate.net/publication/349523731_Metal_deportment_and_ore_variability_of_the_Bolcana_porphyry_Au-Cu_system_Apuseni_Mts_Romania_-_Implications_for_ore_processing

Calder MF, Chang Z, Arribas A, Gaibor A, Dunkley P, Pastoral J, Kouzmanov K, Spandler C, Hedenquist JW (2022) High-Grade Copper and Gold Deposited During Postpotassic Chlorite-White Mica-Albite Stage in the Far Southeast Porphyry Deposit, Philippines. Economic Geology 117:1573-1596. https://doi.org/10.5382/econgeo.4940

Fekete S, Weis P, Driesner T, Bouvier A (2016) Contrasting hydrological processes of meteoric water incursion during magmatic–hydrothermal ore deposition: An oxygen isotope study by ion microprobe. Earth and Planetary Science Letters 451:263-271. https://doi.org/10.1016/j.epsl.2016.07.009

Gustafson LB, Hunt JP (1975) The porphyry copper deposit at El Salvador, Chile. Economic Geology 70:857–912.

Henley R, Mernagh T, Leys C, Troitzsch U, Bevitt J, Brink F, Gardner J, Knuefing L, Wheeler J, Limaye A, Turner M, Zhang Y (2022) Potassium silicate alteration in porphyry copper-gold deposits: a case study at the giant maar-diatreme hosted Grasberg deposit, Indonesia. Journal of Volcanology and Geothermal Research 432. https://doi.org/10.1016/j.jvolgeores.2022.107710

Lowell JD, Guilbert, JM (1970) Lateral and vertical alteration-mineralization zoning in porphyry ore deposits. Economic Geology 65:373–408.

Lagache M, Weisbrod A (1977) The System: Two Alkali Feldspars-KCl-NaCl-H_2O at Moderate to High Temperatures and Low Pressures. Contrib. Mineral. Petrol. 62:77-101.

Murakami H, Seo JH, Heinrich C (2010) The relation between Cu/Au ratio and formation depth of porphyry-style Cu–Au ± Mo deposits. Miner Deposita 45:11-21. https://doi.org/10.1007/s00126-009-0255-1

Orville PM (1963) ALKALI ION EXCHANGE BETWEEN VAPOR AND FELDSPAR PHASES. AMERICAN JOURNAL OF SCIENCE 261:201-237.

Parsons I (2012) Feldspars and their Reactions. Springer Dordrecht. https://doi.org/10.1007/978-94-011-1106-5

Roodpeyma T, Driesner T (2020) A re-assessment of the equilibrium constant and aqueous activity ratios for the Albite – K-Feldspar – $NaCl_{(aq)}$ – $KCl_{(aq)}$. 18th Swiss Geoscience Meeting. https://geoscience-meeting.ch/sgm2020/wp-content/uploads/abstracts/Roodpeyma_Taraneh_08-21-20-04-09-14.pdf

Roodpeyma T, Driesner T, Kost O (2022) Experimental study of thermodynamic behavior of NaCl-KCl electrolytes in reaction with alkali feldspars under supercritical condition of water. Goldschmidt Hawai'I 2022. https://conf.goldschmidt.info/goldschmidt/2022/meetingapp.cgi/Paper/10609

Schirra M, Laurent O, Zwyer T, Driesner T, Heinrich C (2022) Fluid Evolution at the Batu Hijau Porphyry Cu-Au Deposit, Indonesia: Hypogene Sulfide Precipitation from a Single-Phase Aqueous Magmatic Fluid During Chlorite–White-Mica Alteration. Economic Geology 117: 979-1012. https://doi.org/10.5382/econgeo.4921

Seedorff E, Dilles JH, Proffett JM, Einaudi MT (2005) Porphyry deposits: Characteristics and origin of hypogene features. In: Economic Geology, One Hundredth Anniversary Volume. pp 251-298. https://doi.org/10.5382/AV100.10

Evolution of the Skouries porphyry Cu-Au system by trace element variations

Alica Höss[1], Reiner Klemd[1], Manuel Keith[1], Karsten M. Haase[1], Vasilios Melfos[2], Lisa Gerlach[1], Fabian Pelloth[1], Jan Falkenberg[1], Panagiotis Voudouris[3]
[1]GeoZentrum Nordbayern, Friedrich-Alexander Universität (FAU) Erlangen-Nürnberg, 91054 Erlangen, Germany
[2]Aristotle University of Thessaloniki, Faculty of Geology, 54124 Thessaloniki, Greece
[3]National and Kapodistrian University of Athens, Faculty of Geology & Geoenvironment, 15784 Athens, Greece

Abstract. The Skouries deposit is a platinum-group element enriched Cu-Au porphyry system in NE Greece. The monzonite-syenite intrusions host a porphyry stockwork consisting of A- and B-type veins associated with potassic alteration, which is partly overprinted by C-type and D-type veins and related chlorite-sericite to sericitic alteration. The Cu-Au mineralization is dominated by pyrite, chalcopyrite, bornite, magnetite and additional native Au, telluride inclusions and platinum-group minerals. Incompatible trace element ratios of the host rocks (ICP-MS) were used to track the impact of alteration, while in-situ mineral chemistry (LA-ICP-MS) resolves changes in the fluid conditions. Trace element ratios of host rocks show that potassic alteration can change the composition of incompatible element ratios commonly used as tracers for magmatic signatures, such as $(La/Sm)_N$. Ti-in-quartz thermometry yields temperatures of 600°C ± 50° for the A-type veins, 610 ± 60°C for the early B-type veins and 545 ±45°C for late B-type veins. Furthermore, the pyrite mineralization is characterized by systematic variations in trace element contents (e.g., As, Ag, Au) and ratios (e.g., Sb/As, Ag/As) that trace temperature variations of the hydrothermal fluid and implicate phase separation. Phase separation is further suggested to cause the precipitation of native gold during potassic alteration.

1 Introduction

Magmatic fluids play a key role in the Cu-Au enrichment in porphyry intrusions which can form enormous ore deposits with relatively low-grade metal contents. Porphyry Cu-Au mineralization forms in vein stockworks hosted by pervasive alteration halos surrounding the porphyry intrusion.

The Serbo-Macedonian metallogenic belt extends from Serbia to northern Greece and is characterized by numerous porphyry deposits, either enriched in Cu, Cu-Au or Cu-Mo. The Skouries Cu-Au porphyry on the Chalkidiki peninsula contains ~289 Mt of ore at 0.43 % Cu and 0.58 g/t Au (Siron et al. 2018). The monzonite and syenite porphyry intrusions are of early Miocene age (20.56±0.48 Ma, Hahn 2014), and intruded into the Kerdilion and Vertiskos Unit (Siron et al. 2018). The Vertiskos Unit, which hosts the Skouries deposit, is mainly composed of schists, greenschist-facies gneisses, and a metamorphic sequence comprising thin interlayers of calcareous schist, marble and amphibolite (McFall et al. 2018). Additional micaceous schists of the Neoproterozoic to Ordovician age are present in close proximity to the Skouries porphyry (Siron et al. 2018).

The Skouries Cu-Au deposit expands over an area of ~200m in diameter and >900m in depth and is characterized by monzonitic to porphyritic syenite stocks and dykes with an associated porphyry stockwork (Figure 1). At least four intrusive stages, namely early monzonite, porphyritic syenite and melasyenite, and post-mineralization barren syenite were identified, which show extensive potassic and minor sericitic alteration (McFall et al. 2018). The Cu-Au mineralization is mainly hosted by pyrite, chalcopyrite, bornite, and accessories such as native gold, tellurides and PGE minerals in the vein system. The stockwork is dominated by A-type (qz+mt+cpy±bn), early B1- (reopening A-type veins, qz+mt+cp+py) and late B2-type (qz+cp+py±mt) veins. Late-stage massive pyrite-chalcopyrite veins (C-type and D-type) crosscut the main stage veining at depth, overprinting the potassic alteration with sericitic alteration (telescoping).

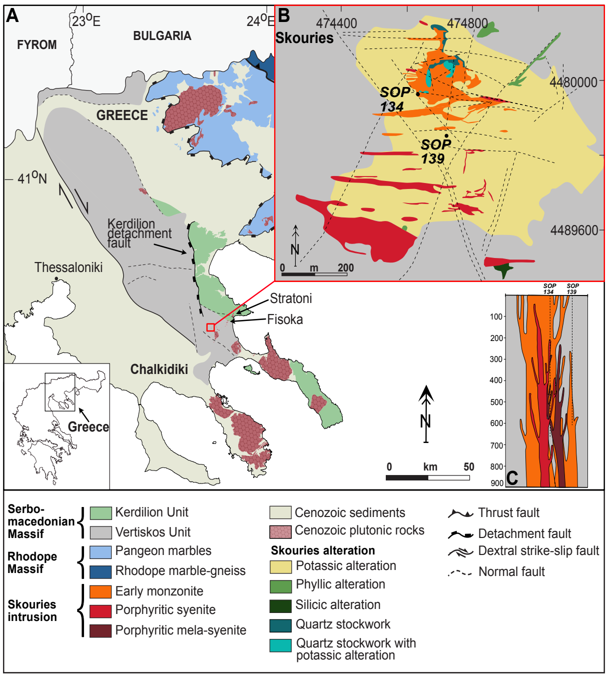

Figure 1. a) Geological map of the Greek part of the Serbo-Macedonian metallogenic belt (modified after Siron et al. 2018). **b)** Geological map the Skouries Porphyry and **c)** a schematic sketch of a section through the main ore body (modified after McFall et al. 2018).

2 Methodology

2.1 Micro-analytical techniques

The LA-ICP-MS study was conducted on sulfides and quartz with respect to the previously defined vein-types. A Teledyne Analyte Excite 193 nm laser coupled with an Agilent 7500c quadrupole ICP-MS, operating at a frequency of 20Hz, a fluence of 2.6 to 3.5 J/cm^3, a plasma power of 1270W and a beam size of 35 µm was used at the GeoZentrum Nordbayern. For the quartz measurements, the operating setting was changed to a frequency of 10Hz, plasma power of 1280W, a fluence of 8.59 J/cm^3 and a beam diameter of 65 µm.

2.2 Composition of the host rocks

The host rock samples were analyzed by XRD analyses on rock powder to quantify the type and degree of alteration due mineral abundances. The trace element measurements were performed by a Thermo Scientific X-Series 2 quadrupole ICP-MS at the GeoZentrum Nordbayern.

3 Results

3.1 Composition of the host rocks

The host rocks are dominated by potassic alteration, which is characterized by hydrothermal formation of orthoclase, biotite and magnetite, but can be overprinted by sericite and chlorite. The degree of alteration can therefore be quantified by the amount of orthoclase in each sample, determined by XRD and related whole rock major element data. The samples from the drill core SOP134 refer to the main ore body and vary considerably in their major and trace element composition, which refers to relatively minor and strong potassic alteration of monzonite and porphyry syenite. Trace element ratios of relatively fresh samples show (La/Sm)$_N$ of 4 to 5, no Eu anomaly and chondritic Nb/Ta values of 20. In contrast, altered samples contain decreasing (La/Sm)$_N$ between 5.8 and 7.6 with decreasing Yb, Eu/Eu* of 2 to 11, decreasing REE contents and Nb/Ta values (Figure 2). Altered samples with low Yb additionally have variable (La/Sm)$_N$ ratios. The trace element concentration of hydrothermally altered samples from Skouries show systematic differences from fresh magmatic rocks of the area even for elements that are commonly suggested to be immobile (Figure 2).

3.2 Trace element composition of quartz and sulfides

The trace element composition of quartz was only determined for A-and B-type veins due to the lack of quartz in the later vein types. Quartz from A-type and early B-type veins (B1) contains the highest Ti content (43-145; 24-183 ppm), followed by quartz from the late B-type veins (B2) (28-86 ppm). Aluminum (103-1840 ppm), Sb (<1.3 ppm) and As (<12 ppm) display similar concentrations in quartz irrespective of their vein type, while Ge (0.7-1.7 ppm) decreases in quartz from the A-type to the B-type veins.

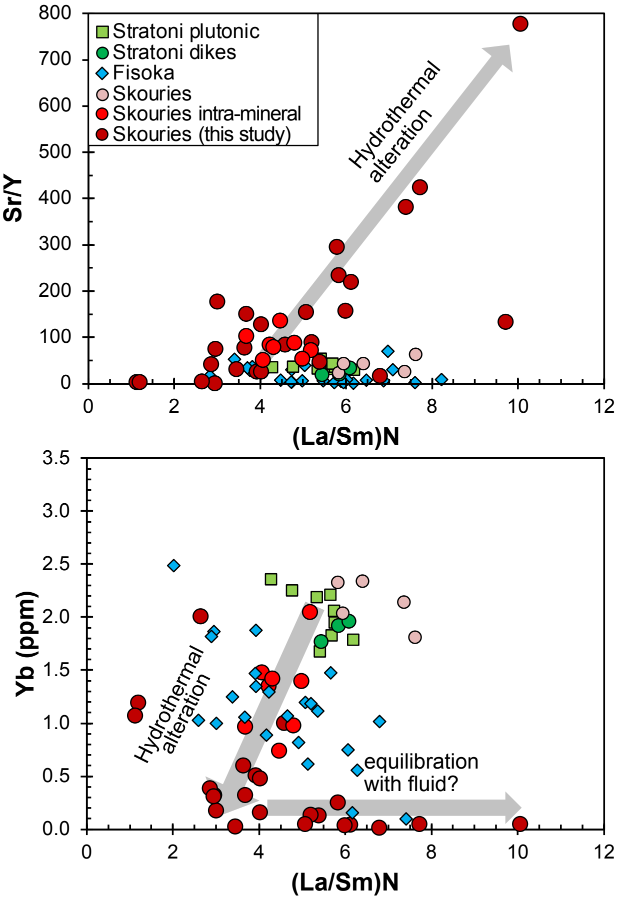

Figure 2. Trace element composition of host rocks (Drill core SOP134) from Skouries showing correlating Sr/Y and (La/Sm)$_N$ with increasing potassic alteration, as well as decreasing (La/Sm)$_N$ with decreasing Yb and increasing alteration. Literature data from Skouries and intrusions close to the deposit are added for comparison (Siron et al. 2018).

Bornite, chalcopyrite and pyrite were analyzed for their trace element content. Bornite is the major carrier of Te, Pb, Bi, Se, Ge and Ag, while Zn, Ga and In are highest in chalcopyrite and Co, Ni, As, Sb, Au and Tl are hosted by pyrite (Figure 3). Interestingly, bornite and chalcopyrite show relatively homogeneous trace element contents between different vein generations, while pyrite displays significant compositional variations.

Trace elements in pyrite vary systematically between the different vein generations and show increasing Sb, Au, Ag, Zn and Pb contents from the early B-type to the C-type veins, while As, Te are enriched in C-type veins. Furthermore, pyrite from D-type veins is generally depleted in most trace elements (e.g., Sb, Pb, Bi, Au, Ag, Zn) relative to the other vein types. Lastly, pyrite from early B-type veins is characterized by low trace element ratios (Sb/As < 0.01, Co/As < ~1), while later B-, C- and D-type veins show higher trace element ratios (Sb/As =0.01 to 1, Co/As = 0.1 to 100).

4 Fingerprinting hydrothermal processes on the deposit scale

4.1 Chemical alteration of the host rock

The replacement of plagioclase by K-feldspar and of pyroxene, amphibole and magmatic biotite by hydrothermal biotite is typical for the potassic alteration of monzonites and syenites in porphyry Cu-Au systems (Sillitoe 2010). The extreme REE and HFSE depletion and decreasing light REE relative to middle REE with increasing alteration, resulting in lower $(La/Sm)_N$ values, indicate the mobilization of light REE by a high temperature fluid capable of transporting such incompatible elements (Figure 2).

However, the rocks with strongest alteration have elevated $(La/Sm)_N$ and Eu anomalies, thus probably indicating the equilibration of the highly altered rocks with the fluids. Consequently, we suggest that the typical high Sr/Y and La/Yb ratios of the host rocks observed in other porphyry systems (Loucks 2014) may also result from alteration processes and not always preserve the primary magmatic signature.

4.2 Constraints on the fluid evolution

The Ti-in-Quartz thermometer was applied (Ti activity = 1, equilibrium with rutile, p_A=0.5kbar, $p_{B1,B2}$=0.4kbar to calculate the temperatures of quartz precipitation (Huang and Audétat 2012). Calculated temperatures yielded within error similar temperatures for A-type veins (600°C ±48°C) and early B-type veins (610 ±60°C) and lower temperatures for the late B-type veins (545 ±45°C) (Figure 3).

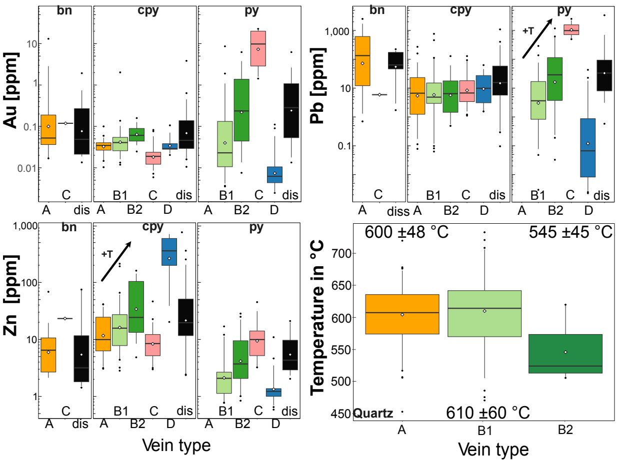

Figure 3. Boxplots of Au, Pb and Zn in bornite (bn), chalcopyrite (cpy) and pyrite (py) from the different vein generations and calculated temperatures for quartz from A-, B1-, and B2-type veins using the Ti-in-quartz thermometer (Huang and Audétat 2012).

Preliminary fluid inclusion results, which show a complex composition including NaCl and KCl, with minor $CaCl_2$, $FeCl_2$, and CO_2, are within range of quartz temperatures for A-type veins. Homogenization temperatures range from 516 to >600°C (salinities: 49-61 wt.% equiv. NaCl) for liquid-rich brine inclusions and from 523 to >600°C (salinities: 11-13 wt.% equiv. NaCl) for vapor-rich inclusions. B2-type veins show homogenization temperatures from 446 to 484°C for liquid-rich brine inclusions (salinities: 48-54 wt.% equiv. NaCl) and from 451 to 496°C (salinities: 7.3-6.9 wt.% equiv. NaCl) for vapor-rich inclusions.

Trace elements, such as Ag, Sb, Zn and Pb are enriched in pyrite that precipitated from lower temperature fluids (Franchini et al. 2015). Indeed, these elements increase from early B-type veins towards later C-type veins (Figure 3). Correspondingly, chalcopyrite displays decreasing Cd/Zn ratios from A-type to late B-type veins, which is also known as a temperature proxy (George et al. 2018). These trace element variations combined with the quartz thermometry and preliminary fluid inclusion results therefore indicate decreasing fluid temperatures between the vein generations.

In contrast to the temperature-dependent variations in the sulfide chemistry from A- to C-type veins, the pyrite in the D-type veins is depleted in most trace elements (e.g., Pb, Au, As). Phase separation forms a high-Cl liquid phase and a low-Cl vapor phase causing fractionation between volatile (e.g., As, Sb) and less-volatile (e.g., Pb) elements (Keith et al. 2022). Based on the temperature-independent low As/Sb and high Tl/Pb ratios of pyrite from D-type veins, we conclude that the D-type veins formed from a Cl-rich liquid after phase separation ("boiled liquid"), which lost its As content to the respective vapor, while Pb precipitated from the liquid phase (Figure 4). The low As/Sb and Co/As ratios in pyrite from early B-type veins may further imply repeated vapor fractionation of the early fluid. The coexistence of vapor- and liquid-rich inclusions observed in the preliminary fluid inclusion data supports phase separation.

5 Occurrence of Au in the Skouries deposit

The Skouries deposit is enriched in Au, which can either occur as native Au inclusions in the vein stockwork or precipitated in solid solution in sulfide minerals.

Micro-scale native gold inclusions, which are primary based on petrological observations, are mainly present in chalcopyrite from A- and early B-type veins. The Au-As ratio in pyrite further indicates nano-scale inclusions in pyrite from late B-type veins that could not be detected by LA-ICP-MS (Figure 4). Native gold usually precipitates from an Au-oversaturated fluid, which can be achieved by reducing the stability of Au complexes due to a change in temperature, pressure or availability of S. Gold saturation during potassic alteration is typically controlled by the sulfur budget rather than the temperature, and especially phase separation can effectively decrease the availability of S, which lowers the solubility of Au complexes (Pokrovski et al. 2014). Furthermore, Au in solid solution mainly occurs in pyrite related to B- and C-type veins while chalcopyrite in general and pyrite from the late-stage D-type veins are depleted in Au (Figure 3, 4). This suggests variable gold precipitation and enrichment processes during the different paragenetic stages.

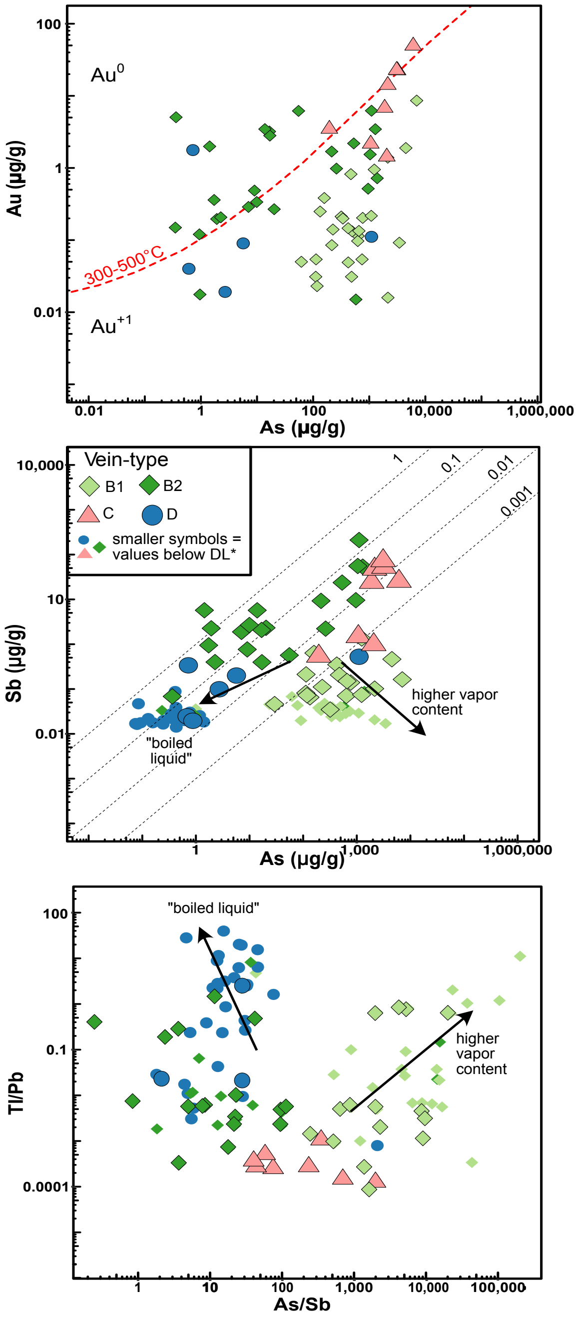

Figure 4. Trace elements and trace element ratios (As/Sb, Tl/Pb) in pyrite from different vein generations indicative for phase separation and the vapor content in the fluid. The As-Au ratio gives the occurrence of Au in solid solution and as native inclusions based on the solubility limit of Au (Deditius et al. 2014). Values below detection as DL/√2.

6 Conclusion

We conclude that hydrothermal alteration changes incompatible trace element ratios like La/Yb and Sr/Y, believed to be typical signatures of magmatic processes amongst others related to porphyry formation. Thus, host rocks need careful selection with respect to alteration before the interpretation of magmatic processes. The mineral composition suggests a decrease in temperature with the progressive evolution of the fluids and early phase separation observed in B-type vein sulfides. The fluid reached Au saturation during potassic alteration, probably caused by the early phase separation. This process effectively decreases the S availability in the fluid leading to Au oversaturation and hence precipitation of native gold and Au-rich sulfides. The residual liquid then precipitated sulfides with relatively low contents of As, Au and other trace elements in D-type veins.

Acknowledgements

Tim Baker is thanked for providing drill core samples and Helene Brätz for the support during the LA-ICP-MS analyses.

References

Deditius AP, Reich M, Kesler SE, et al (2014) The coupled geochemistry of Au and As in pyrite from hydrothermal ore deposits. Geochimica et Cosmochimica Acta 140:644–670.

Franchini M, McFarlane C, Maydagán L, et al (2015) Trace metals in pyrite and marcasite from the Agua Rica porphyry-high sulfidation epithermal deposit, Catamarca, Argentina: Textural features and metal zoning at the porphyry to epithermal transition. Ore Geology Reviews 66:366–387.

George LL, Cook NJ, Crowe BBP, Ciobanu CL (2018) Trace elements in hydrothermal chalcopyrite. Mineral mag 82:59–88.

Hahn A (2014) Nature, timing and geodynamic context of polymetallic mineralisation in the Kassandra mining district. Kingston University

Huang R, Audétat A (2012) The titanium-in-quartz (TitaniQ) thermobarometer: A critical examination and re-calibration. Geochimica et Cosmochimica Acta 84:75–89.

Keith M, Haase KM, Chivas AR, Klemd R (2022) Phase separation and fluid mixing revealed by trace element signatures in pyrite from porphyry systems. Geochimica et Cosmochimica Acta 329:185–205.

Loucks RR (2014) Distinctive composition of copper-ore-forming arcmagmas. Australian Journal of Earth Sciences 61:5–16.

McFall KA, Naden J, Roberts S, et al (2018) Platinum-group minerals in the Skouries Cu-Au (Pd, Pt, Te) porphyry deposit. Ore Geology Reviews 99:344–364.

Pokrovski GS, Akinfiev NN, Borisova AY, et al (2014) Gold speciation and transport in geological fluids: insights from experiments and physical-chemical modelling. SP 402:9–70.

Sillitoe RH (2010) Porphyry Copper System. Economic Geology 105:3-41

Siron CR, Rhys D, Thompson JFH, et al (2018) Structural Controls on Porphyry Au-Cu and Au-Rich Polymetallic Carbonate-Hosted Replacement Deposits of the Kassandra Mining District, Northern Greece. Economic Geology 113:309–345.

U-Pb ages and trace elements of zircons from Loei and Truong Son fold belts, northern Laos: Implication for porphyry deposit fertility

Peerapong Sritangsirikul[1], Sebastien Meffre[1], Khin Zaw[1], Ivan Belousov[1], Yi-Jen Lai[2], Alex Richards[3], Punya Charusiri[4]
[1]CODES Centre of Ore Deposit and Earth Sciences, University of Tasmania, Hobart, Tasmania 7001, Australia
[2] Macquarie GeoAnalytic, the Macquarie Analytical and Fabrication Facility (MAFF), Macquarie University, Sydney, New South Wales 2109, Australia
[3] Rio Tinto Exploration, Brisbane, Queensland 4001, Australia
[4] Morphology of Earth Surface and Advance Geohazards in Southeast Asia Research Unit (MESA RU), Department of Geology, Faculty of Science, Chulalongkorn University, Bangkok 10400, Thailand

Abstract. The Loei and Truong Son Fold Belts are well known as highly mineralized magmatic arc-related terranes in Southeast Asia. Zircon LA-ICP-MS studies provide U-Pb ages and magmatic fertility using trace elements of felsic to intermediate volcanic and plutonic rocks from ten prospects in the Loei and Truong Son fold belts, NW Laos region. The geochemical and geochronological analyses suggest at least three episodes of magmatism occurred in the region: Silurian-Devonian (434-411 Ma), Early to Middle Permian (299-277 Ma), and Late Permian to Middle Triassic (253-243 Ma). Key trace elements and ratios together with oxygen fugacity of magmas (e.g., Eu/Eu*, Dy/Yb, Ce/Nd, ΔFMQ) imply that the Phu Kham and the West of Vientiane area along the Mekong River are likely to be fertile for porphyry copper deposits. In contrast, the Pha Gnai and the other suites are less fertile. Therefore, zircon as a fertility indicator is a valuable tool to distinguish fertile magmatic suites from the barren suites in this area.

1 Introduction

The Loei (Loei-Phetchabun) Fold Belt (LFB) and the Truong Son Fold Belt (TSFB) are the most critical, highly mineralized volcano-magmatic arcs in mainland Southeast Asia. The NW-SE trending TSFB and the N-S trending LFB lies to the north of Khorat Plateau and the east of the Sukhothai Fold Belt and the Nan-Uttarradit Suture at the western margin of the Indochina terrane respectively (Figure 1A). The LFB consists of 1) Devonian-Carboniferous sedimentary rocks including claystones, shales, and sandstones with minor carbonates; 2) Carboniferous-Permian limestones and sandstones; 3) Triassic volcaniclastic rocks with minor claystones and limestones. 4) Late Paleozoic to Middle Triassic granitic rocks (Burrett et al. 2021; Khin Zaw et al. 2014; Shi et al. 2021). The TSFB consists of middle to upper Paleozoic volcano-sedimentary rocks along with late Paleozoic granitic rocks (Cromie et al. 2018; Zhang et al. 2020). Silurian granites and limestones also occur as the basement rocks in this terrane (Cromie et al. 2018).

The LFB hosts several major porphyry-related, copper-gold skarns and epithermal gold deposits such as Chatree deposit in Thailand (Salam et al. 2014). The porphyry-related skarn-type Cu-Au deposits (Puthep; PUT1 and PUT2, Phu Thap Fah, Phu Lon, French Mine) characterized by veins typically centered on dioritic to granodioritic intrusions (Kamvong et al. 2014; Khin Zaw et al. 2014). Recently orogenic gold deposits are recorded (e.g., Phabon gold deposit, Guo et al. 2019) and stratabound Cu–Pb–Ag deposits (e.g., Ban Kiouchep, Zhang et al. 2020) were also reported.

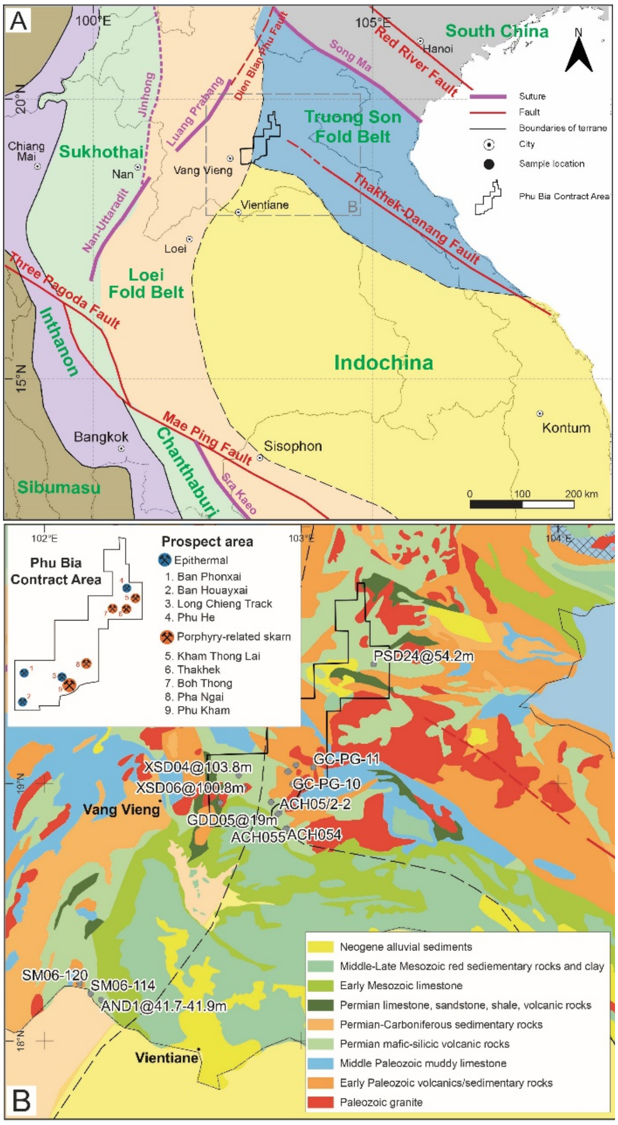

Figure 1. A Mainland Southeast Asia regional tectonic map **B** Simplified geological map of the Northwest Laos region.

Similar to the LFB, the TSFB contains major world-class porphyry-related skarn-type Cu-Au deposits (e.g., Phu Kham, Kamvong et al. 2014), epithermal Au deposits (e.g., Ban Houayxai, Manaka et al. 2014), sub-volcanic mesothermal Au deposits (e.g., Long Chieng Track, Leaman et al. 2019), sediment-hosted Au deposits (e.g., Sepon, Cromie et al. 2018) and orogenic gold deposits (Bounliyong et al. 2021). The geochemistry of zircons from volcanic and intrusive rocks using laser ablation inductively coupled plasma-mass spectrometry (LA-ICP-MS) has been used in mineralized fold belts worldwide to discriminate mineralized fertile magmas from pre-mineralization magmas and provides insights into complex petrogenesis that ended in a low-temperature, hydrous and oxidized fertile magma composition (e.g. Dilles et al. 2015; Leslie et al. 2022; Loucks et al. 2020; Lu et al. 2016). These techniques provide detailed geochemical information to investigate the petrogenesis of mineralized intrusive and volcanic rocks mainly in northern Laos by documenting the key trace element ratios (e.g., Eu/Eu*, (Ce/Nd)/Yb, Gd/Yb, and Hf) in zircons. These data are compared to discriminate the evolution of mineralized versus barren magmas highlighting the importance of zircon trace elements data and mineral fertility studies.

2 Methodology

2.1 Zircon LA-ICP-MS

The twenty-one selected zircon mounts are prepared from several Cu-Au and Au deposit and prospect sites in Laos (Figure 1B); 1) West of Vientiane along Mekong (porphyry skarn Cu ± Au), 2) Ang Noi intrusion-related Au Prospect, 3) Ban Nape intrusion-related Prospect, 4) Ban Houayxai epithermal Au-Ag Deposit, 5) Long Chieng Track (LCT) low-S epithermal Au-Ag-Cu Deposit, 6) Phu Kham porphyry-related skarn Cu (-Au) Deposit, 7) Ban Phonxai epithermal Au Deposit, 8) Nhon Nhang sediment-hosted Cu-Au Prospect, 9) Phu He low-S epithermal Au-Ag Prospect, and 10) Pha Gnai porphyry-related skarn Cu ± Au Prospect. The zircons were analyzed using an Agilent 7900 quadrupole ICPMS at CODES, the University of Tasmania, coupled to COMPex Pro 110 excimer laser operating at 193 nm wavelength and equipped with an ASI S155 laser ablation cell capable of holding 20 1-inch size grain mounts. The analysis was performed at least 1 hour after the ignition of the mass spectrometer to stabilize the machine. The primary and secondary standards zircons were analyzed at the beginning, at the end, and throughout the analytical run. The downhole fractionation, instrument drift, and mass bias correction factors for Pb/U ratios on zircons were calculated using analyses on the primary standard (91500) and checked on secondary standards (Temora), and Plešovice). The ^{207}Pb/^{206}Pb ratio was calibrated using analyses on NIST610. The zircons were analyzed with a laser beam at 29 µm spots at 5 Hz and approximately 2 J/cm^2 laser fluence. The 30-second gas blank was analyzed at the beginning of each measurement and followed by 30 seconds of ablation. The ablation was performed in He atmosphere flowing at 0.35 L/min and mixed with Ar straight after ablation flowing at 1.05 L/min. Each element was measured successively every 0.253 seconds and recorded for data reduction. Isotopic masses collected were ^{31}P, ^{49}Ti, ^{56}Fe, ^{89}Y, ^{91}Zr, ^{93}Nb, ^{139}La, ^{140}Ce, ^{141}Pr, ^{146}Nd, ^{147}Sm, ^{153}Eu, ^{157}Gd, ^{159}Tb, ^{163}Dy, ^{165}Ho, ^{166}Er, ^{169}Tm, ^{172}Yb, ^{175}Lu, ^{178}Hf, ^{181}Ta, ^{202}Hg, ^{204}Pb, ^{206}Pb, ^{207}Pb, ^{208}Pb, ^{232}Th, ^{235}U and ^{238}U. The U/Pb geochronology data reduction was conducted using the LADR software program. Cathodoluminescence (CL) imaging techniques were obtained and employed to document zircon grain structure at Central Science Laboratory at the University of Tasmania, using a FEI MLA650 scanning electron microscope (SEM). The CL images were the basis for locating and determining the options for LA-ICP-MS and Hf isotope analytical sites.

3 Zircon ages and trace elements

3.1 U-Pb ages

In Figure 2, U-Pb analyses from the zircons suggest that at least three episodes of magmatism occurred in the LFB and TSFB: Silurian-Devonian (434-411 Ma), Early to Middle Permian (299-277 Ma), and Late Permian to Middle Triassic (253-243 Ma). The Devonian-Carboniferous magmatic episode (ca 370-310 Ma) previously reported (Khin Zaw et al. 2014; Salam et al. 2014; Shi et al. 2021) was not observed in this study and probably occur in different locations. The results show that Early to Late Permian (299-250 Ma) magmatism is the dominant magmatic activity associated with epithermal and porphyry mineralization consistent with previous geochronology results (Khin Zaw et al., 2014; Kamvong et al., 2014; Shi et al., 2021).

3.2 Porphyry fertility

Zircon chondrite normalized REE shows light rare earth elements (LREE) depletion relative to the heavy rare earth elements (HREE) with positive Ce anomalies. This pattern is typical of zircons worldwide. Most analyzed zircons have similar REE patterns. However, samples from the Phu Kham porphyry-related skarn Cu (-Au) Deposits (GDD05@19m), Long Chieng Track (LCT) low-S epithermal Au-Ag-Cu Deposits (ACH067 and LSD9@50.9m), and West of Vientiane site (SM06-114) have anomalously high Ce with either a relatively small or no negative Eu anomaly. High oxidation state, magmatic water content, high S content, and a high degree of fractionation are key features of magmas fertile for porphyry Cu mineralization. The geochemistry of zircon is a robust, helpful tool for evaluating the mineralization

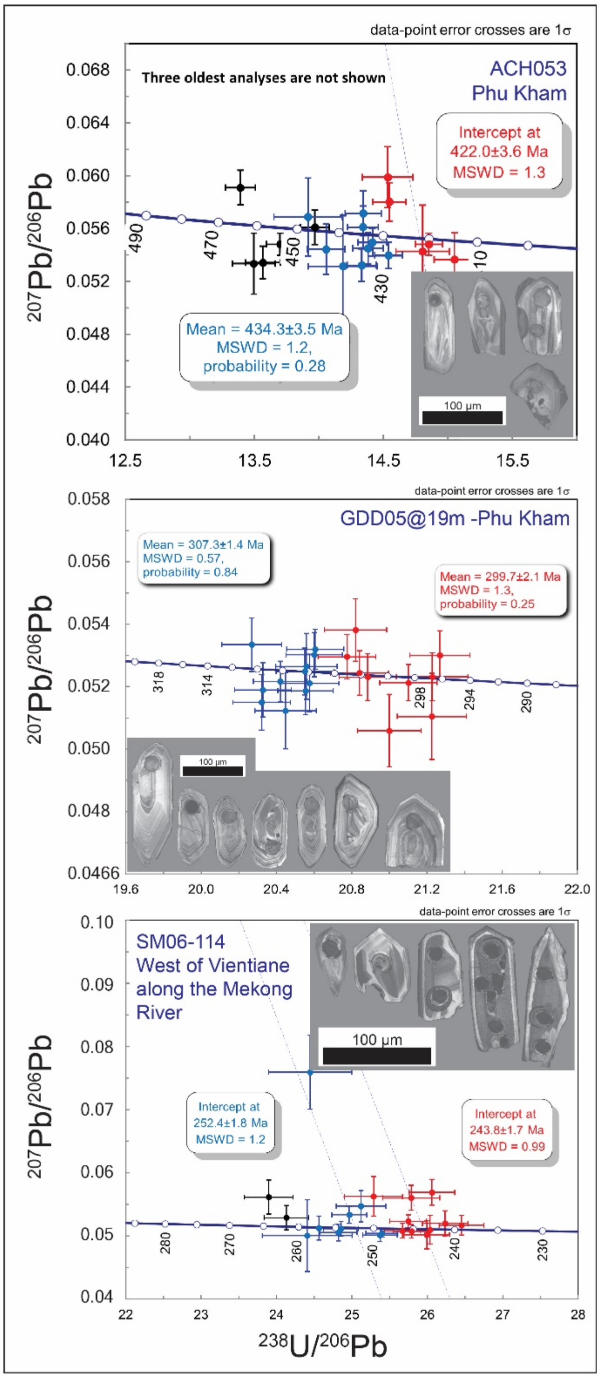

Figure 2. U-Pb Concordia isotopic age data for representative samples from the magmatic rocks along with their representative cathodoluminescence (CL) images from zircons.

potential in the porphyry environment (e.g., Lee et al., 2021; Loucks et al. 2020; Lu et al. 2016) and geochemical composition of zircon and ratios such as Eu/Eu*, (Ce/Nd)/Y, 104*(Eu/Eu*)/Y, Hf (ppm), Dy/Yb, have been widely used as fertility indicators to discriminate those fertile magmas from barren magmas (e.g., Lu et al. 2016). Chondrite-normalized rare earth element pattern of zircon from the dacite porphyry from Phu Kham (GDD05@19m) demonstrates typically low abundances of LREE and relatively high HREE with positive Ce and negative Eu anomalies that are consistent with the signature of oxidized and hydrous melts. Likewise, zircons from a quartz diorite from the West of Vientiane along the Mekong River (SM06-114), rhyolite porphyry (ACH067), and dacite (LSD09@50m) from the Long Chieng Track (LCT) also show large positive Ce anomaly with the small Eu anomaly that is typical of magmas fertile for porphyry Cu deposits. This contrasts with the other intrusive suites that display smaller positive Ce and more negative Eu anomalies. To further investigate the oxidation state of the magmas, the ΔFMQ values were calculated (fayalite-magnetite-quartz fO2 buffer: calculated using oxybarometer method using Ce, U, and Ti in zircon from Loucks et al. 2020). The data clusters in three distinct groups of analyses with Permian and Triassic zircons from Phu Kham and Triassic zircons from West of Vientiane are from strongly oxidized magmas and Silurian zircons from the Phu Kham and LCT are from strongly reduced magmas (Figure 3). Several different thresholds have been used to discriminate intrusions that are fertile and non-fertile for porphyry deposits, (e.g., Eu/Eu* >0.4, Ballard et al. 2002; Dilles et al. 2015; Eu/Eu* >0.3, 10,000*(Eu/Eu*)/Y >1, (Ce/Nd)/Y > 0.01 and lower Dy/Yb <0.3, Lu et al. 2016). The dacite porphyry from the Phu Kham and quartz diorite from the West of Vientiane have the high Eu/Eu* (> 0.5), and low Dy/Yb (<0.2) are typical of hydrous magmas characterized by early amphibole and clinopyroxene crystallization and suppression of plagioclase crystallization. In contrast, most of the zircons from other magmatic rocks in Laos have a lower Eu/Eu* (<0.5). Zircons from some of the Long Chieng Track and Pha Gnai samples also had high values of Eu/Eu* but show lower ΔFMQ values and are therefore considered less prospective. These analyses are also much more scattered on many of the trace element plots.

4 Conclusions

The Permo-Triassic magmatic suites from this study are identified to be more fertile than the Silurian-Devonian suites based on their zircon trace element compositions. The Phu Kham and the West of Vientiane area along the Mekong River are likely fertile for porphyry Cu deposits, whereas the Pha Gnai and the other suites are less fertile. Some of the Long Chieng Track samples are fertile, and further work is warranted in the area. This study suggests that zircon as a fertility indicator is a useful tool to distinguish fertile magmatic suites from the barren ones in this area.

Acknowledgments

This study has been financially supported by the Royal Thai Scholarship, Chulalongkorn University, Department of Mineral Resources (DMR), and Rio Tinto Exploration for the analytical costs.

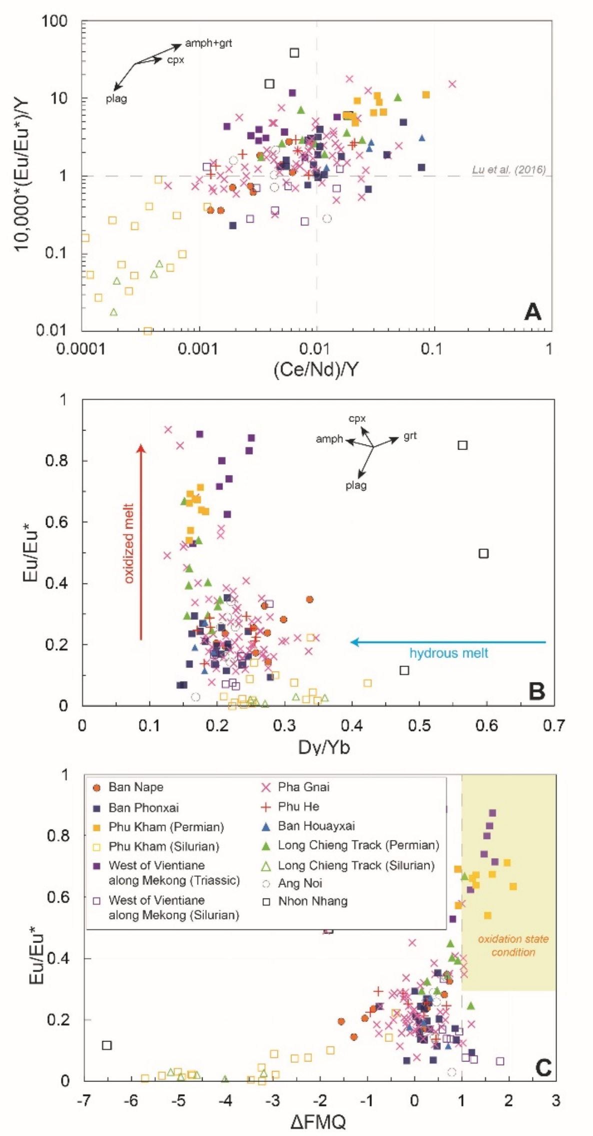

Figure 3. Zircon trace elements **A** 10,000*(Eu/Eu*)/Y vs (Ce/Nd)/Y **B** Eu/Eu* vs Dy/Yb **C** Eu/Eu* vs ΔFMQ, differentiated based on trace element compositions in zircon related to oxidation and hydrous conditions.

References

Bounliyong, P, Arribas, A, Watanabe, Y, Echigo, T, Wong, H, and Gold, K (2021). A new orogenic gold belt in Southeast Asia: Geology, mineralogy and genesis of the Vangtat gold deposit, Southeastern Laos. Resource Geology, 72(1),

Burrett, C, Udchachon, M, and Thassanapak, H (2021). The Truong Son, Loei-Phetchabun, and Kontum Terranes in Indochina: Provenance, Rifting, and Collisions. Frontiers in Earth Science, 9, 289.

Cromie, PW, Makoundi, C, Zaw Khin, Cooke, DR, White, N, and Ryan, C (2018). Geochemistry of Au-bearing pyrite from the Sepon Mineral District, Laos DPR, Southeast Asia: Implications for ore genesis. Journal of Asian Earth Sciences, 164, p. 194–218.

Dilles, JH, Kent, AJR, Wooden, JL, Tosdal, RM, Koleszar, A, Lee, RG, and Farmer, LP (2015). Zircon compositional evidence for sulfur-degassing from ore-forming arc magmas. Economic Geology, 110(1), p. 241–251.

Guo, L, Liu, S, Hou, L, Wang, J, Shi, M, Zhang, Q, Nie, F, Yang, Y, and Peng, Z (2019). Fluid Inclusion and H-O Isotope Geochemistry of the Phapon Gold Deposit, NW Laos: Implications for Fluid Source and Ore Genesis. Journal of Earth Science 2019 30:1, 30(1), p. 80–94.

Kamvong, T., Khin Zaw, Meffre, S, Maas, R, Stein, H, and Lai, CK (2014). Adakites in the Truong Son and Loei fold belts, Thailand and Laos: Genesis and implications for geodynamics and metallogeny. Gondwana Research, 26(1), p. 165–184.

Khin Zaw, Meffre, S, Lai, CK, Burrett, C., Santosh, M., Graham, I., Manaka, T., Salam, A., Kamvong, T., and Cromie, P (2014). Tectonics and metallogeny of mainland Southeast Asia — A review and contribution. Gondwana Research, 26(1), p. 5–30.

Leaman, P, Manaka, T, Jarical, K, Villar, M, and Libao, JB (2019). The geology and mineralization of the Long Chieng Track (LCT) subvolcanic Au-Ag-Cu-Pb-Zn deposit, Lao PDR. Ore Geology Reviews, 106, p. 387–402.

Lee, RG, Byrne, K, D'Angelo, M, Hart, CJR, Hollings, P, Gleeson, SA, and Alfaro, M (2021). Using zircon trace element composition to assess porphyry copper potential of the Guichon Creek batholith and Highland Valley Copper deposit, south-central British Columbia. Mineralium Deposita, 56(2), p. 215–238.

Leslie, C, Meffre, S, Cooke, DR, Thompson, J, Howard, N, and Barker, A (2021). Complex Petrogenesis of Porphyry-Related Magmas in the Cowal District, Australia: Insights from LA ICP-MS Zircon Imaging. In Tectonomagmatic Influences on Metallogeny and Hydrothermal Ore Deposits: A Tribute to Jeremy P. Richards v.2, p. 159–180.

Loucks, RR, Fiorentini, ML, and Henriquez, GJ (2020). New magmatic oxybarometer using trace elements in zircon. Journal of Petrology, 61(3).

Lu, YJ, Loucks, RR, Fiorentini, M, Campbell MT, Evans, NJ, Yang, ZM, Hou, ZQ, Kirkland, CL, Parra-Avila, LA, and Kobussen, A (2016). Zircon Compositions as a Pathfinder for Porphyry Cu ± Mo ± Au Deposits*. Society of Economic Geologists, 19 (February 2019), p. 329–347.

Manaka, T, Khin Zaw, Meffre, S, Vasconcelos, PM, and Golding, SD (2014). The Ban Houayxai epithermal Au-Ag deposit in the Northern Lao PDR: Mineralization related to the Early Permian arc magmatism of the Truong Son Fold Belt. Gondwana Research, 26(1), p. 185–197.

Salam, A, Khin Zaw, Meffre, S, McPhie, J, and Lai, CK (2014). Geochemistry and geochronology of the Chatree epithermal gold–silver deposit: Implications for the tectonic setting of the Loei Fold Belt, central Thailand. Gondwana Research, 26(1), p. 198–217.

Shi, M, Khin Zaw, Liu, S, Xu, B, Meffre, S, Cong, F, Nie, F, Peng, Z, and Wu, Z (2021). Geochronology and petrogenesis of Carboniferous and Triassic volcanic rocks in NW Laos: Implications for the tectonic evolution of the Loei Fold Belt. Journal of Asian Earth Sciences, 208, 104661.

Zhang, Z, Shu, Q, Wu, C, Zaw, Khin, Cromie, P, Von Dollen, M, Xu, J, and Li, X (2020). The endogenetic metallogeny of northern Laos and its relation to the intermediate-felsic magmatism at different stages of the Paleotethyan tectonics: A review and synthesis. Ore Geology Reviews, 123p,

The apparent decoupling of magmatic and hydrothermal activities in the Chuquicamata District

Adrianna L. Virmond[1], **David Selby**[2], **Dawid Szymanowski**[1], **Jörn-Frederik Wotzlaw**[1], **Cyril Chelle-Michou**[1]
[1]*Department of Earth Sciences, ETH Zurich*
[2]*Department of Earth Sciences, Durham University*

Abstract. Understanding the primary controls on the formation of mineral deposits is fundamental to assist exploration geologists in finding more resources in an ever growing high-demand world. Even though Porphyry Copper Systems have been extensively researched, the primary controls on the tonnage of deposits are still poorly quantified. Recent studies suggest the timescales and physical parameters involved in the formation of such deposits might be the missing key control. Here we investigate the behemothian deposits of the Chuquicamata District in northern Chile and show that prolonged magmatic and hydrothermal activities were involved in their formation. Our high precision geochronology results point to the occurrence of multiple magmatic-hydrothermal events, separated in space and time. An unexposed intrusion could explain the temporal gap between hydrothermal and magmatic activities in the Chuquicamata District. A long lived magmatic history with pulsed hydrothermal events in the same area seem to favour the formation of oversized deposits without triggering eruptions.

1 Introduction

The development of new technologies and consequent pursuit of alternative greener sources of energy will increase significantly the demand for metals in the coming decades. Porphyry copper deposits are the main source of copper and other base metals that will continue to play a key role in future. Thus, these systems have been thoroughly studied and many important ore-forming processes are well understood. However, one remaining question regarding porphyry copper systems (PCS) addresses the size distribution of such deposits, which varies over 5 orders of magnitude (Singer et al. 2008).

Since some of the processes involved are common to those that occur in most magmas in arc settings, it has been suggested that giant PCS are simply the result of the “perfect alignment” of processes and conditions (Richards 2013). Recent studies applied numerical simulations and suggested physical parameters could be the primary controls on the size of the deposits (e.g. Chelle-Michou et al. 2017; Chiaradia & Caricchi 2022). Such simulations show that the volume and duration of magmatic activity have a key control over the total endowment of a deposit and that magma volumes necessary to generate some of the largest deposits are comparable to those required to produce super eruptions (Chelle-Michou et al. 2017; Chelle-Michou & Rottier 2021; Chiaradia & Caricchi 2022). The relative timing of hydrothermal and magmatic activities in the Chuquicamata porphyry system, a behemothian deposit located in northern Chile, is investigated here.

2 Geological Background

The Eocene-Oligocene metallogenic belt of northern Chile hosts many of the country’s most important copper deposits, including the behemothian Chuquicamata, one of the biggest deposits in the world, with more than 100 Mt of copper and a mining history of over a century (Ossandón et al. 2001; Rivera et al. 2012; Figure 1).

The Chuquicamata Intrusive Complex (CIC; Tomlinson et al. 2018) comprises the intrusive rocks associated with the Cu-Mo mineralization at the Chuquicamata and Radomiro Tomic deposits. It occurs as a NNE 14 km-long, 0.7–2 km-wide west-dipping subvertical dike that outcrops mostly within the mines, extending from Chuquicamata to north of the Radomiro Tomic mine (Rivera et al. 2012). In Chuquicamata, the unit presents, to the east, both intrusive and fault contacts with the Triassic East and Elena Granodiorites and Jurassic metasedimentary rocks of the Caracoles Group (Tomlinson et al. 2018). To the west, it is truncated by the West Fissure, which juxtaposes the complex against the Eocene Fortuna Complex (Ossandón et al. 2001; Rivera et al. 2012; Tomlinson et al. 2018). Towards the north, within the Radomiro Tomic mine, the complex presents intrusive contacts with the Elena Granodiorite to the east and to the west (Rivera et al. 2012).

The CIC is composed of three main units. The Este porphyry is the most abundant lithology, comprising most of the CIC. It is a granodiorite with “crowded” texture, abundant phenocrysts (plagioclase, biotite, deformed quartz, titanite and hornblende) in a fine- to coarse- groundmass composed of quartz and K-feldspar (Ossandón et al. 2001; Arnot 2003). Smaller bodies of texturally different porphyries intrude the Este porphyry: (1) the Banco porphyry, with bimodal size distribution of plagioclase phenocrysts, aphanitic groundmass (Arnott, 2003), often described as “more porphyritic” than Este porphyry (Ossandón et al. 2001; Rivera et al. 2012, Tomlinson et al. 2018); and (2) the Oeste porphyry, which presents a finer, aplitic groundmass, and lower crystallinity (Ossandón et al. 2001, Arnot 2003, Rivera et al 2012). A fourth variety of porphyry, the Fino porphyry, is reported only in the Radomiro Tomic mine. It differs from the Este porphyry mainly by presenting smaller biotite in the groundmass (Cabrera 2011; Tomlinson et al. 2018).

Previous work in the CIC reported that sharp intrusive contacts are observed only between Este and Banco porphyries, whereas the contact between Oeste and Este is diffuse and often gradational (Ossandón et al. 2001). The Fino porphyry is intruded by the Oeste Porphyry in the Radomiro Tomic mine (Tomlinson et al. 2018).

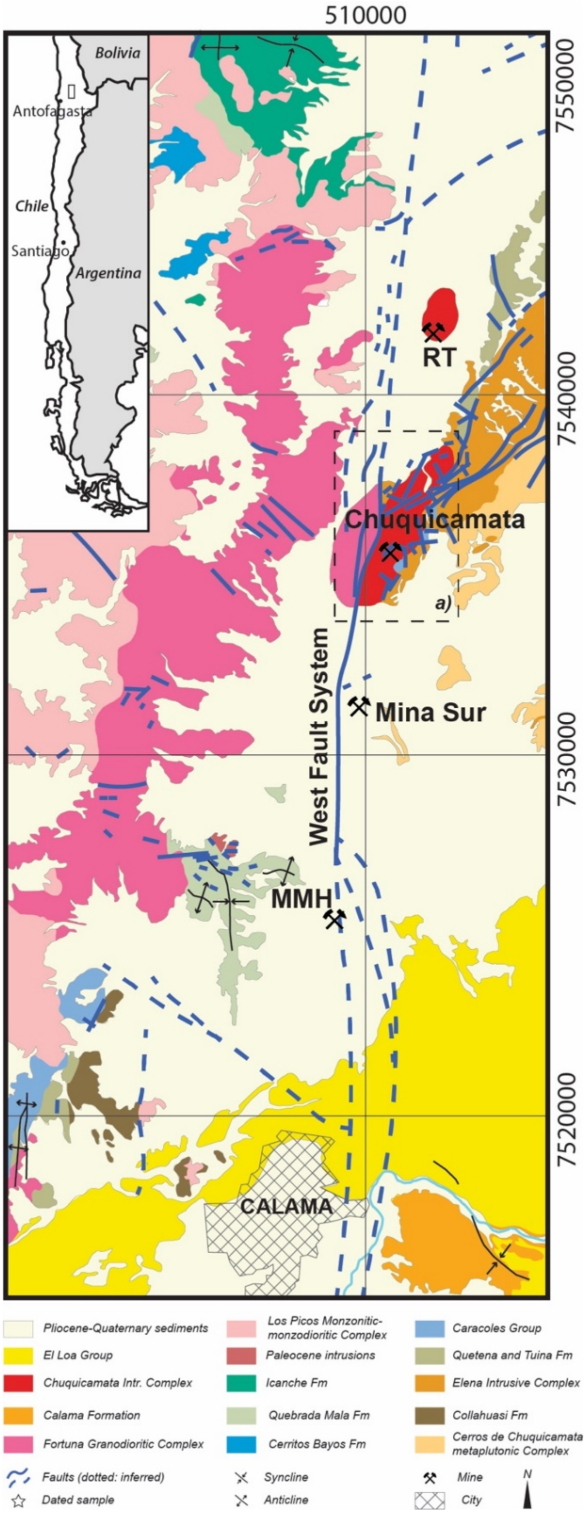

Figure 7 – Simplified geological map of the Chuquicamata District, modified after Rivera et al 2012.

Previous geochronological studies on the Chuquicamata District identified two ages of porphyry intrusion. The Este Porphyry yields zircon U-Pb SHRIMP age of 35.2 ± 0.4 Ma (Ballard et al. 2001; Campbell et al. 2006) whereas the Oeste and Banco Porphyries yield younger and identical crystallization ages (34.0 ± 0.3 and 34.1 ± 0.3 Ma, respectively, Ballard et al. 2001; Campbell et al. 2006). Recent Re-Os molybdenite dates for the Chuquicamata mine, constrain the mineralization between 32.9 ± 0.2 and 31.9 ± 0.2 Ma (Barra et al. 2013). The long-lived protracted magmatic-hydrothermal history of Chuquicamata led authors to suggest superimposed events that ultimately produced the giant deposit (e.g. Ballard et al. 2001).

3 Materials and methods

3.1 Sample summary

Our geochronological investigation covers all lithologies found in the CIC, including a north - south spatial coverage of Este porphyry, the most abundant unit. Molybdenite occurring both in sheeted “blue veins” and small B-type veins were sampled.

3.2 Zircon U-Pb Geochronology

Zircon separates were obtained by conventional techniques (crushing, panning, sieving and density separation using a heavy liquid). After picking, the grains were annealed (900°C furnace for 48-60 h) and mounted in epoxy mounts. Preliminary U-Pb dating and trace element compositions of the outer rims of the crystals were obtained using LA-ICP-MS, in order to characterize the last magma from which the zircons crystallized. Afterwards, the grains are polished and cathodoluminescence (CL) images are obtained for textural characterization. A second LA-ICP-MS session was conducted on the cores and rims of the same grains to obtain dates and trace element compositions.

After data reduction, around 10 to 15 zircon crystals from each sample were selected for high precision geochronology using Chemical Abrasion Isotope Dilution Thermal Ionization Mass Spectrometry (CA-ID-TIMS). Grains were selected based on absence of inclusions and inheritance and homogeneity of the grain.

All LA-ICP-MS work was conducted in the Institute of Geochemistry and Petrology at ETH Zurich, using a 193-nm Resolution (S155) ArF excimer laser coupled to an Element SF-ICP-MS. CA-ID-TIMS analyses were conducted in the same institute and the samples were measured with a TRITON Plus thermal ionization mass spectrometer using protocols modified from von Quadt et al. (2016) and Wotzlaw et al. (2017).

3.3 Molybdenite Re-Os Geochronology

Molybdenite separates were prepared by handpicking under a binocular from samples that underwent crushing in the hydraulic press, dry sieving (fraction <300µm and >63µm), magnetic separation and density concentration by heavy liquid. Some samples were handpicked from fractions prepared following the HF dissolution protocol of Lawley and Selby (2012), more suitable for fine-grained molybdenite enclosed in quartz. Re-Os analyses were performed in the Source Rock and Sulphide Geochronology and Geochemistry Laboratory in Durham University.

4 Relative timing of magmatic and hydrothermal activities in Chuquicamata

Zircon U-Pb high precision geochronology shows the porphyry units present broad distribution of ages, lasting up to 1 Myr at the hand-sample scale. Within the Este porphyry, individual zircon dates tend to be older in the northern part of the CIC. Towards south, the zircon distribution tends to be much narrower (Figure 2).

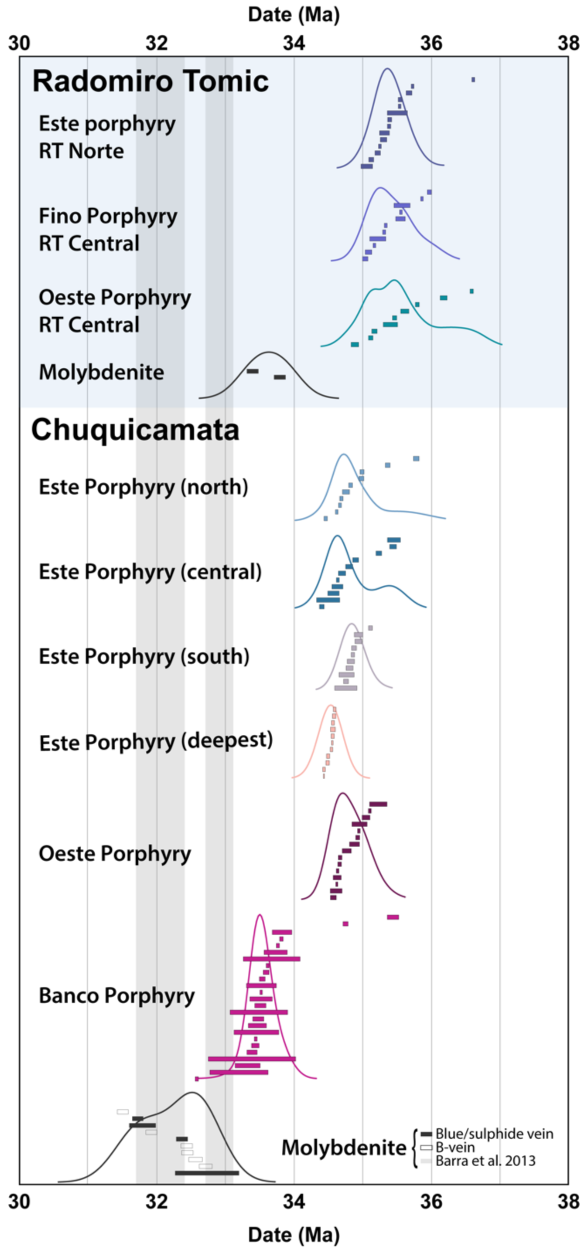

Figure 8 – Geochronological summary of the Chuquicamata Intrusive Complex. Each bar is an individual date with its associated 2σ and the curves represent KDE for each sample. For the porphyries, the zircon U-Pb TIMS date is presented while for molybdenite, the Re-Os date is shown.

We interpret the youngest zircon dates as the emplacement ages for each sample. In Radomiro Tomic, emplacement ages are very similar between different porphyries, and up to 500 kyr older than in Chuquicamata. The Oeste porphyry in Radomiro Tomic has a slightly younger emplacement age, consistent with crosscutting relationships (e.g. Cabrera 2011).

In the Chuquicamata mine, the Este porphyry mostly presents similar emplacement ages (within uncertainty) regardless of spatial location. The Oeste porphyry presents indistinguishable zircon date distribution compared to the Este porphyry. Despite being considered up to 1 Myr younger (e.g. Ballard et al 2001; Campbell et al. 2006) our preliminary data suggest the Oeste porphyry is closely associated with Este porphyry and possibly reflects a local textural variant of the same unit. High precision zircon dating of the Banco porphyry confirm it is a younger intrusion in the system, emplaced up to 2 Myrs after the Este Porphyry.

The preferential occurrence of older zircon grains only in the northern part of the CIC (including Radomiro Tomic and the north of Chuquicamata) is coincident with samples topographically higher. This suggests older parts of the underlying magma reservoir are preferentially sampled in the northern part of the deposit, which appears to be further away from the feeding zone. The southernmost samples also come from deeper parts of the deposit (Figure 3), where the more homogeneous distribution of zircon dates occur. This could suggest either that this zone is fed by a more homogeneous section in the underlying pluton, or potentially that it's closer the feeder zone of the megadyke.

Molybdenite Re-Os geochronology results suggest a pulsed behaviour on hydrothermal activity in the CIC (Figure 2) and a clear correlation between vein type and molybdenite age. The oldest molybdenite ages are obtained in the Radomiro Tomic deposit, separated by a few ten of thousands of years from the hydrothermal activity within the Chuquicamata mine. There, molybdenite crystallized for over 1 Myr and the obtained dates suggest one continuous long-lived hydrothermal event. Alternatively, our data reflect a pulsed behaviour for molybdenite crystallization within the Chuquicamata mine that was unresolvable with high-precision Re-Os geochronology. In Chuquicamata the older set of molybdenite dates only marginally overlap with the Banco porphyry and may in fact be younger.

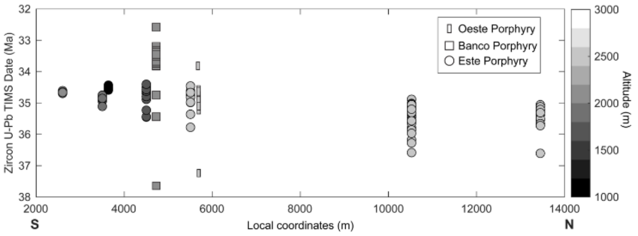

Figure 9 – Spatial distribution of zircon U-Pb dates for the CIC. Samples are color-coded according to the altitude they were taken from (true depth calculated with dip of drill cores).

5 Preliminary conclusions

We investigated the timescales of magmatic and hydrothermal activity in the Chuquicamata Intrusive Complex (CIC) using zircon and molybdenite high precision geochronology. Preliminary results suggest complex spatial distribution of dates, suggesting different parts of the underlying magma reservoir were preferentially sampled in different moments of time or crystallized zircons at different moments.

The apparent age gap between the emplacement of the porphyries and the hydrothermal activity observed in the Chuquicamata deposit raises an alert to assuming that the mineralized porphyries are necessarily genetically linked to the mineralization. In the CIC, it seems that the volumetrically minor Banco porphyry is the most temporally associated with the mineralization. However, the youngest molybdenite dates suggest there's potentially another unexposed intrusion, deep in the system and responsible for the mineralization, as previously suggested based on younger Ar-Ar and K-Ar dates obtained for the district (e.g. Ballard et al 2001; Rivera et al 2012).

Long lived magmatic systems with multiple episodes of intrusion and hydrothermal activity are also observed in other giant deposits, such as El Teniente (Spencer et al. 2015) and they seem to be favorable to forming behemothian deposits such as the Chuquicamata District.

Acknowledgements

We would like to acknowledge the help and support of the geologists from Codelco (distrito Norte), in special Elizabeth Demané, Rodrigo Rojas, Giorgio Realini and their teams.

References

Arnot, A.M. (2003): Evolution of the Hydrothermal Alteration at the Chuquicamata Porphyry Copper System, Northern Chile, PhD thesis, Dalhousie University, 450 p.

Ballard, J.R., Palin, J.M., Williams, I.S., Campbell, I.H., and Faunes A., A. (2001): Two ages of porphyry intrusion resolved for the super-giant Chuquicamata copper deposit of northern Chile by ELA-ICP-MS and SHRIMP: Geology, v. 29, no. 5, p. 383–386.

Barra, F., Alcota, H., Rivera, S., Valencia, V., Munizaga, F., and Maksaev, V. (2013): Timing and formation of porphyry Cu-Mo mineralization in the Chuquicamata district, northern Chile: New constraints from the Toki cluster: Mineralium Deposita, v. 48, doi:10.1007/s00126-012-0452-1.

Cabrera, J.B. (2011): Estudio petrografico y petrologico de los porfidos alimentadores del distrito mina Radomiro Tomic, II Region, Chile Memoria para optar al titulo de geologo: Universidad de Concepcion, 179 p.

Campbell, I.H., Ballard, J.R., Palin, J.M., Allen, C., and Faunes, A. (2006): U-Pb Zircon Geochronology of Granitic Rocks from the Chuquicamata-El Abra Porphyry Copper Belt of Northern Chile: Excimer Laser Ablation ICP-MS Analysis: Economic Geology, v. 101, no. 7, p. 1327–1344, doi:10.2113/gsecongeo.101.7.1327

Chelle-Michou, C., Rottier, B., Caricchi, L., and Simpson, G. (2017): Tempo of magma degassing and the genesis of porphyry copper deposits: Scientific Reports, v. 7, no. 1, p. 40,566, doi:10.1038/srep40566

Chelle-Michou, C., Rottier,B. (2021): Transcrustal magmatic controls on the size of porphyry Cu systems: State of knowledge and open questions, Society of Economic Geologists, p. 87–100, doi: 10.5382/SP.24.06

Chiaradia, M., Caricchi, L. (2022): Supergiant porphyry copper deposits are failed large eruptions. Commun Earth Environ 3, 107. https://doi.org/10.1038/s43247-022-00440-7

Krogh, T. E. (1973): A low-contamination method for hydrothermal decomposition of zircon and extraction of U and Pb for isotopic age determinations, Geochemica et Cosmochimica Acta, v.37, pp 485–494.

Lawley, C.J.M., and Selby, D. (2012): Re-Os Geochronology of Quartz-enclosed ultrafine molybdenite: Implications for Ore Geochronology: Economic Geology, v. 107, no. 7, p. 1499–1505, doi:10.2113/econgeo.107.7.1499.

Ossandón, G., Fréraut C, R., Gustafson, L.B., Lindsay, D.D., and Zentilli, M. (2001): Geology of the Chuquicamata mine: A progress report: Economic Geology, v. 96, no. 2, p. 249–270, doi:10.2113/gsecongeo.96.2.249.

Richards, J.P. (2013): Giant ore deposits formed by optimal alignments and combinations of geological processes: Nature Geoscience, v. 6, no. 11, p. 911–916, doi:10.1038/ngeo1920.

Rivera, S.L., Alcota, H., Proffett, J., Díaz, J., Leiva, G., and Vergara, M. (2012): Update of the Geologic Setting and Porphyry Cu-Mo Deposits of the Chuquicamata District, Northern Chile, in Geology and genesis of major copper deposits and districts of the world: Society of Economic Geologists, p. 19–54, doi:10.5382/SP.16.02.

Singer, D., Berger, V., and Moring, B. (2008): Porphyry copper deposits of the world: Database and grade and tonnage models: Open File Report.

Spencer, E. T., Wilkinson, J. J., Creaser, R. A., Seguel, J. (2015): The Distribution and Timing of Molybdenite Mineralization at the El Teniente Cu-Mo Porphyry Deposit, Chile: Economic Geology, v. 110, p. 387-421.

Tomlinson, A., Blanco, N., Dilles, J., Maksaev, V., and Ladino, M. (2018): Carta Calama, región de Antofagasta, in Carta Geológica de Chile, Serie Geologia Básica, v. No.199: Servicio Nacional de Geologia y Minería, p. 199

von Quadt, A., Wotzlaw, J.F., Buret, Y., Large, S.J., Peytcheva, I., and Trinquier, A. (2016): High-precision zircon U/Pb geochronology by ID-TIMS using new 1013 ohm resistors: Journal of Analytical Atomic Spectrometry, v. 31, no. 3, p. 658–665, doi:10.1039/c5ja00457h.

Wotzlaw, J.F., Buret, Y., Large, S.J., Szymanowski, D., and von Quadt, A. (2017): ID-TIMS U-Pb geochronology at the 0.1‰ level using 1013 W resistors and simultaneous U and 18O/16O isotope ratio determination for accurate UO2 interference correction: Journal of Analytical Atomic Spectrometry, v. 32, no. 3, p. 579–586, doi:10.1039/c6ja00278a

Sulfide resorption contributes to porphyry deposit formation in collisional settings

Wen-jie Xia[1], **Rui Wang**[1†], **and Frances Jenner**[2]
[1]*State Key Laboratory of Geological Processes and Mineral Resources, and Institute of Earth Sciences, China University of Geosciences, Beijing 100083, China.*
[2]*School of Environment, Earth and Ecosystem Sciences, The Open University, Walton Hall, Milton Keynes, Buckinghamshire MK7 6AA, UK.*

Abstract. Production of Cu-rich melts via melting of sulfide-bearing lower crustal cumulates is thought to contribute to porphyry Cu formation at the post-collisional Gangdese belt (Tibet). We present new whole rock platinum group elements (PGE) data for ore-causative granites (OCG), ore-related granites (ORG) and barren granites (BG) from the Gangdese belt. The OCG, ORG and BG show indistinguishable PGE and Cu/Ag at a given MgO during differentiation down to ~2 wt.% MgO. These systematics, together with the occurrence of sulfides, indicate that the propensity for some Gangdese magmas to be ore-associated is unrelated to the magma source or the magmatic evolution. The behavior of PGE and Cu during differentiation of the OCG, ORG and BG diverges when melts evolve past 2 wt.% MgO. The OCG and ORG rapidly reached fluid saturation and released their metals to the hydrothermal fluids or silicate melts as a result of sulfide resorption. In contrast, BG show the sharp decrease in Cu until ~1 wt. % MgO. Because the OCG are cogenetic with the ORG granitoids and contain textural evidence for focused fluid exsolution, we suggest that metals in the magma reservoir have been efficiently extracted when the magma body reach fluid saturation.

1 Introduction

A series of post-collisional (Miocene; 22-12Ma) porphyry copper deposits (PCDs) with Cu reserves of over 45 Mt have been discovered in the Gangdese magmatic belt in southern Tibet (Hou et al. 2009, 2015a; Yang and Cooke 2019). The ore-forming magmas are generally characterized by felsic composition, high-K calc-alkaline signature, high-Sr/Y and La/Yb ratios and are regarded as the products of melting of lower crustal mafic cumulates (Hou et al. 2015b; Wang et al. 2015, 2018). Previous studies have suggested that the ore-related magmas are more Cu-rich than the barren magmas because of melting of sulfides in the lower crust (Hou et al. 2015b) and/or secondary sulfides formed during hydrous metasomatism of the subcontinental lithospheric mantle (SCLM) (Zheng et al. 2019). However, numerous geochemical studies have suggested that magmas that are enriched in economic metals (e.g., Cu and Au) are not a requirement for porphyry Cu mineralization (Halter et al. 2005; Zhang and Audétat 2017; Du and Audétat 2020; Hao et al. 2021). Instead, several magmatic processes occurring in the upper to middle crust are regarded as contributing factors for the formation of PCDs, such as: (1) magmatic-sulfide fractionation happening before or after volatile exsolution (Jenner et al. 2010; Wilkinson 2013; Hao et al. 2019; Park et al. 2019); (2) cannibalization of pre-existing magmatic sulfides in upper crustal magmatic mush systems (Halter et al. 2005; Nadeau et al. 2010); (3) the volume of magma with "normal" Cu concentrations; and (4) the timescales of magmatic activity (Chelle-Michou et al. 2017; Chiaradia and Caricchi 2017; Chelle-Michou and Rottier 2021).

In this study, we selected a series of Gangdese belt post-collisional granitoids from ore-causative (source porphyry stocks for porphyry mineralization), ore-related (precursor pluton or mafic dykes emplaced penecontemporaneously with porphyry stocks) and barren magmatic systems and use a combination of petrology, geochemistry and literature data to track the role of magmatic sulfides during ascent, differentiation, and degassing of Gangdese magmas.

2 Geological Settings

The Gangdese belt in southern Tibet preserves a continuous magmatic record from the Late Triassic to the middle Miocene, which includes Neo-Tethyan oceanic slab subduction from 210-60 Ma and the India-Asia collision from 60-55 Ma (Zhu et al. 2011; van Hinsbergen et al. 2012; Wang et al. 2018). The Miocene post-collisional extension-related magmatism is characterized by predominantly potassic-ultrapotassic (trachytic) volcanism west of ~89°E and by granitoids with high-Sr/Y ratios (also named high-Sr/Y granitoids) east of ~89°E (Wang et al., 2018). There are also sparse Oligocene high-Sr/Y granitoids at Zedang and Miocene diorite porphyries at Xigaze and in the ore fields (Fig. 1). Many of the Oligocene to Miocene granitic intrusions contain mafic magmatic enclaves (MME), which have been attributed to mixing between the high-Sr/Y granitic magmas and more mafic mantle-derived ultra-potassic magmas (Zheng et al. 2012; Lu et al. 2015). Alternatively, others attribute the occurrence of MME at other settings (e.g., Nisyros volcano, Aegean arc, Greece) to entrainment of clasts of mafic material (e.g., sulfide-bearing cumulates) from the lower crustal magmatic mush zones that lie beneath intrusions and volcanoes (e.g., hot crustal mush zones, see Annen et al. 2006) by melts that are filtering upwards through the mush zones (Georgatou et al. 2022 and references therein). Indeed, the MME associated with the Gangdese Miocene Qulong porphyry magmas (Yang 2008) show a range in Cu from 130 to 1287 ppm, which are consistent with the high Cu concentrations expected for sulfide-bearing mushes (e.g., Chen et al. 2020; Guo et al. 2020).

Most of the porphyry Cu-Mo deposits in the Gangdese belt, including two giant deposits (Qulong, 2200 Mt @ 0.5% Cu; Jiama, 1055 Mt @ 0.44% Cu; Yang and Cooke 2019) and several smaller deposits, were formed in the Miocene, in response to rapid uplift and erosion of the Gangdese arc batholiths (Yang et al. 2009). These porphyry Cu(-Mo) systems are centered around granitic porphyritic stocks which intruded into and/or through composite precursor batholiths. The ore-causative stocks and other ore-bearing pre-mineralization and post-mineralization intrusions are commonly high-Sr/Y granitoids emplaced at 30-12 Ma. At some deposits the ore-causative stocks are associated with post-mineralization high-Mg diorites or lamprophyre dykes (Yang and Cooke, 2019). This study focuses on: (1) the ore-causative granitoids (OCG); (2) pre- and post-mineralization high-Sr/Y ore-related granitoids (ORG); and (3) high and low Sr/Y granitoids that are unrelated to any deposits, which are referred to here as barren granitoids (BG).

3 Results

3.1 Major and trace elements

On the total alkalis (Na_2O+K_2O) verses silica (TAS) diagram, the Gangdese samples show a range in compositions from monzodiorite to granite, with SiO_2 concentrations ranging from 50.2 wt. % to 75.5 wt. %. The OCG samples span to higher SiO_2 concentrations than the ORG and BG samples, whereas the BG samples span to lower SiO_2 concentrations compared to the other samples. All samples show a decrease in FeO_T with decreasing MgO. The least fractionated primitive (highest MgO) ORG samples are offset to lower FeO_T at a given MgO compared to the BG samples. However, all three groups of samples with ~2 wt.% MgO show an overlapping range in FeO_T. Collectively, the Gangdese samples show an initial increase in P_2O_5 with decreasing MgO and an inflection in the trend at ~3-5 wt.% MgO.

3.2 Chalcophile elements

The majority of the Gangdese samples analyzed for this study show a decrease in Cu concentrations with decreasing MgO from 361 ppm Cu in the most primitive MgO-rich sample, down to 15.2 ppm Cu in the most fractionated MgO-poor sample. The OCG, ORG and BG samples show an overlapping and very narrow range in Cu until at ~2wt.% MgO, then the OCG and ORG samples decrease of an order of magnitude. Exceptions include most of altered samples and two of the OCG samples and one of the ORG samples, which Cu contents are two orders of magnitude greater than the fresh OCG and ORG samples with the similar MgO concentrations. With the exceptions of one high Ag and Au BG sample, the altered samples also have relatively higher Ag and Au contents than the fresh ones (Fig. 1). In contrast, the altered samples are indistinguishable from the other samples on plots of MgO versus FeO_T, P_2O_5, Sr, Y and Sr/Y, Pd, Pt, Ir and Ru (Fig. 1). When compared to literature data for samples from the Gangdese with <2 wt.% MgO, it is notable that many other OCG and ORG samples also have extremely variable Cu at a given MgO compared to literature BG data. The BG samples show a moderate decrease in Cu with decreasing MgO and an inflection in the trend at ~1 wt.% MgO.

4 Chalcophile and siderophile element systematics of the Gangdese magmas

With the exception of three high Cu samples and altered samples, the majority of the sample analyses presented here show an overlapping and extremely narrow range in Cu concentrations. Notably, these Cu trends are defined by Gangdese samples from a range of different localities but mostly from Qulong. Similarly, with the exception for Pt, the other PGE, Au and Ag contents of ORG and OCG samples also are indistinguishable from the BG samples until ~2 wt.% MgO (Fig 1). Hence, the propensity for Gangdese magmas to fuel the formation of ore-deposits in the region appears to be unrelated to the initial Cu of the parental melt or the initial behavior of Cu during magma differentiation down to ~2 wt.% MgO. Hence, melting of lower-crustal sulfide-bearing cumulates (Hou et al. 2015b; Zheng et al. 2019) as a model to explain why only some of the magmas are ore-causative appears to be inconsistent with the chalcophile elements systematics of the Gangdese magmas. In particular, the <2 wt.% MgO samples that were analyzed for this study, together with literature data for <2 wt.% MgO samples (Fig. 1) show an extremely large range in chalcophile elements at a given MgO compared to samples with >2 wt.% MgO. Thus, it is important to assess the potential cause (s) of the inflection of these chalcophile elements trends and the difference between the ore-associated samples and barren ones.

The PGE and Cu show extremely various after ~2 wt.% MgO. Several previous studies (Nadeau et al., 2010; Reekie et al. 2019; Wieser et al. 2020; Georgatou et al., 2022) all show that the chalcophile elements contents have an instant change after sulfide resorption. Together with the texture evidence of fluid exsolution (e.g., miarolitic cavities and UST quartz) found in OCG porphyries (Yang et al. 2009), we suggest that the sulfides in magma reservoir may be resorbed after fluid exsolution.

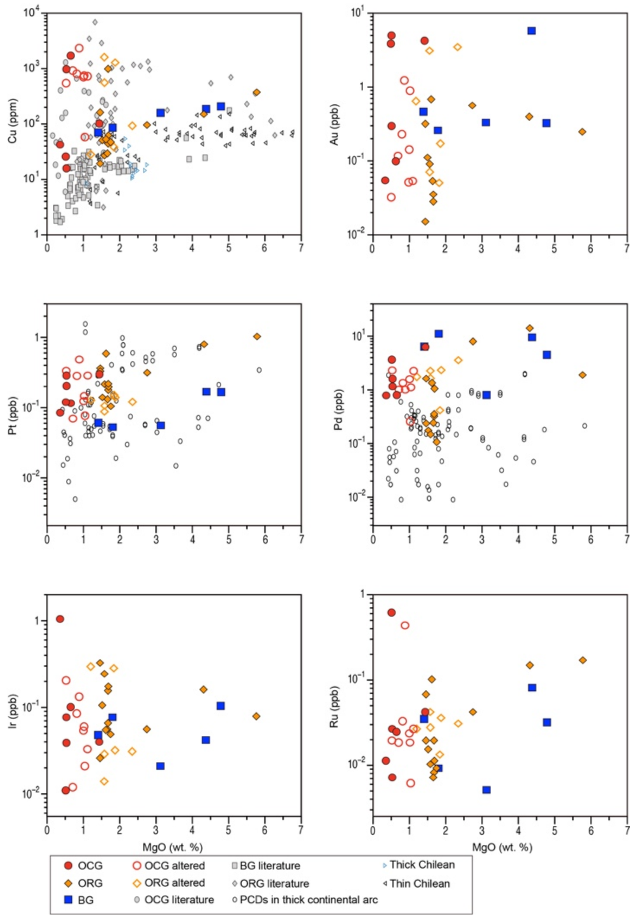

Figure 1. Plots of Cu, Au, Pt, Pd, Ir and Ru versus MgO for samples analyzed for this study, local previous study, and intrusions associated with porphyry deposits located in regions of thick (≥55km) Chilean crust.

Acknowledgements

This research was financially supported by the Chinese National Natural Science Foundation (42121002, 41973037 and 92162104) and the 111 Project (B18048). We thank Dr. Jian-feng Gao for support with analysis of PGEs.

References

Annen C, Blundy JD, Sparks RSJ (2006) The Genesis of Intermediate and Silicic Magmas in Deep Crustal Hot Zones. Journal of Petrology 47:505–539. https://doi.org/10.1093/petrology/egi084

Chelle-Michou C, Rottier B (2021) Transcrustal Magmatic Controls on the Size of Porphyry Cu Systems: State of Knowledge and Open Questions. In: Tectonomagmatic Influences on Metallogeny and Hydrothermal Ore Deposits: A Tribute to Jeremy P. Richards (Volume I). Society of Economic Geologists, pp 87–100

Chelle-Michou C, Rottier B, Caricchi L, Simpson G (2017) Tempo of magma degassing and the genesis of porphyry copper deposits. Sci Rep 7:40566. https://doi.org/10.1038/srep40566

Chen K, Tang M, Lee C-TA, et al (2020) Sulfide-bearing cumulates in deep continental arcs: The missing copper reservoir. Earth and Planetary Science Letters 531:115971. https://doi.org/10.1016/j.epsl.2019.115971

Chiaradia M, Caricchi L (2017) Stochastic modelling of deep magmatic controls on porphyry copper deposit endowment. Sci Rep 7:44523. https://doi.org/10.1038/srep44523

Du J, Audétat A (2020) Early sulfide saturation is not detrimental to porphyry Cu-Au formation. Geology 48:519–524. https://doi.org/10.1130/G47169.1

Georgatou A, Chiaradia M, Klaver M (2022) Deep to Shallow Sulfide Saturation at Nisyros Active Volcano. Geochem Geophys Geosyst 23:. https://doi.org/10.1029/2021GC010161

Guo L, Jagoutz O, Shinevar WJ, Zhang H-F (2020) Formation and composition of the Late Cretaceous Gangdese arc lower crust in southern Tibet. Contrib Mineral Petrol 175:58. https://doi.org/10.1007/s00410-020-01696-y

Halter WE, Heinrich CA, Pettke T (2005) Magma evolution and the formation of porphyry Cu-Au ore fluids: evidence from silicate and sulfide melt inclusions. Miner Deposita 39:845–863. https://doi.org/10.1007/s00126-004-0457-5

Hao H, Campbell IH, Cooke DR, et al (2021) Geochronology, Petrogenesis and Oxidation State of the Northparkes Igneous Suite, New South Wales, Australia: Implications for Magma Fertility. Economic Geology 116:1161–1187. https://doi.org/10.5382/econgeo.4825

Hao H, Campbell IH, Richards JP, et al (2019) Platinum-Group Element Geochemistry of the Escondida Igneous Suites, Northern Chile: Implications for Ore Formation. Journal of Petrology 60:487–514. https://doi.org/10.1093/petrology/egz004

Hou Z, Duan L, Lu Y, et al (2015a) Lithospheric Architecture of the Lhasa Terrane and Its Control on Ore Deposits in the Himalayan-Tibetan Orogen. Economic Geology 110:1541–1575. https://doi.org/10.2113/econgeo.110.6.1541

Hou Z, Yang Z, Lu Y, et al (2015b) A genetic linkage between subduction- and collision-related porphyry Cu deposits in continental collision zones. Geology 43:247–250. https://doi.org/10.1130/G36362.1

Hou Z, Yang Z, Qu X, et al (2009) The Miocene Gangdese porphyry copper belt generated during post-collisional extension in the Tibetan Orogen. Ore Geology Reviews 36:25–51. https://doi.org/10.1016/j.oregeorev.2008.09.006

Jenner FE, O'Neill HSTC, Arculus RJ, Mavrogenes JA (2010) The Magnetite Crisis in the Evolution of Arc-related Magmas and the Initial Concentration of Au, Ag and Cu. Journal of Petrology 51:2445–2464. https://doi.org/10.1093/petrology/egq063

Lu Y-J, Loucks RR, Fiorentini ML, et al (2015) Fluid flux melting generated postcollisional high Sr/Y copper ore–forming water-rich magmas in Tibet. Geology 43:583–586. https://doi.org/10.1130/G36734.1

Nadeau O, Williams-Jones AE, Stix J (2010) Sulphide magma as a source of metals in arc-related magmatic hydrothermal ore fluids. Nature Geosci 3:501–505. https://doi.org/10.1038/ngeo899

Park J-W, Campbell IH, Malaviarachchi SPK, et al (2019) Chalcophile element fertility and the formation of porphyry Cu ± Au deposits. Miner Deposita 54:657–670. https://doi.org/10.1007/s00126-018-0834-0

Reekie CDJ, Jenner FE, Smythe DJ, et al (2019) Sulfide resorption during crustal ascent and degassing of oceanic plateau basalts. Nat Commun 10:82. https://doi.org/10.1038/s41467-018-08001-3

van Hinsbergen DJJ, Lippert PC, Dupont-Nivet G, et al (2012) Greater India Basin hypothesis and a two-stage Cenozoic collision between India and Asia. Proc Natl Acad Sci USA 109:7659–7664. https://doi.org/10.1073/pnas.1117262109

Wang R, Richards JP, Zhou L, et al (2015) The role of Indian and Tibetan lithosphere in spatial distribution of Cenozoic magmatism and porphyry Cu–Mo deposits in the Gangdese belt, southern Tibet. Earth-Science Reviews 150:68–94. https://doi.org/10.1016/j.earscirev.2015.07.003

Wang R, Weinberg RF, Collins WJ, et al (2018) Origin of postcollisional magmas and formation of porphyry Cu deposits in southern Tibet. Earth-Science Reviews 181:122–143. https://doi.org/10.1016/j.earscirev.2018.02.019

Wieser PE, Jenner F, Edmonds M, et al (2020) Chalcophile elements track the fate of sulfur at Kīlauea Volcano, Hawai'i. Geochimica et Cosmochimica Acta 282:245–275. https://doi.org/10.1016/j.gca.2020.05.018

Wilkinson JJ (2013) Triggers for the formation of porphyry ore deposits in magmatic arcs. Nature Geosci 6:917–925. https://doi.org/10.1038/ngeo1940

Yang Z, Cooke DR (2019) Porphyry copper deposits in China. Society of Economic Geologists Special Publication 22: 133–1876

Yang Z, Hou Z, White NC, et al (2009) Geology of the post-collisional porphyry copper–molybdenum deposit at Qulong, Tibet. Ore Geology Reviews 36:133–159. https://doi.org/10.1016/j.oregeorev.2009.03.003

Zhang D, Audétat A (2017) What Caused the Formation of the Giant Bingham Canyon Porphyry Cu-Mo-Au Deposit? Insights from Melt Inclusions and Magmatic Sulfides. Economic Geology 112:221–244. https://doi.org/10.2113/econgeo.112.2.221

Zheng Y-C, Hou Z-Q, Li W, et al (2012) Petrogenesis and Geological Implications of the Oligocene Chongmuda-Mingze Adakite-Like Intrusions and Their Mafic Enclaves, Southern Tibet. The Journal of Geology 120:647–669. https://doi.org/10.1086/667812

Zheng Y-C, Liu S-A, Wu C-D, et al (2019) Cu isotopes reveal initial Cu enrichment in sources of giant porphyry deposits in a collisional setting. Geology 47:135–138. https://doi.org/10.1130/G45362.1

Zhu D-C, Zhao Z-D, Niu Y, et al (2011) The Lhasa Terrane: Record of a microcontinent and its histories of drift and growth. Earth and Planetary Science Letters 301:241–255. https://doi.org/10.1016/j.epsl.2010.11.005

Can post-subduction porphyry Cu magmas form by partial melting of typical lower crustal amphibole-rich cumulates?

Jingbo Zhang[1,2], Jia Chang[2], Rui Wang[1], Andreas Audétat[2]
[1]*China University of Geosciences, Beijing, China*
[2]*University of Bayreuth, Bayreuth, Germany*

Abstract. Lower crustal cumulates are considered a likely source for porphyry Cu-forming magmas in post-subduction settings. However, it remains controversial whether post-subduction porphyry Cu magmas can be produced by partial melting of lower crustal arc cumulates. Here we performed detailed petrographic and geochemical studies on exhumed lower to middle crustal cumulates from the Gangdese and Kohistan arc sections, and then conducted partial melting experiments at 1.5 GPa and 800-1150 °C using a piston cylinder press. Both the Gangdese and the Kohistan arc-root samples formed as cumulates in the lower to middle crust, but the Kohistan samples were subsequently brought into the garnet stability field during the India–Eurasia continental collision. Most of the Gangdese samples contain relatively high abundances of magmatic sulfides preserved in the form of monosulfide solid solution (MSS). In contrast, most of the Kohistan samples contain very low abundances of Cu-rich sulfides, probably due to metamorphic dehydration and up to 2 wt.% partial melting. Furthermore, the experimental partial melts contain much less K_2O, MgO, Cl and ±S than typical post-subduction porphyry Cu-forming magmas. Hence, we conclude that the role of sulfide-rich arc cumulates in the formation of post-subduction porphyry Cu magmas has been severely overestimated.

1 Introduction

Porphyry Cu deposits are typically formed in subduction zones (Richards 2003; Sillitoe 2010). These subduction-related porphyry Cu magmas were produced by fractionation of mafic magmas derived from metasomatized asthenospheric mantle wedge, which provides the major source of metals (e.g., Cu and Au) and volatiles (e.g., H_2O, S and Cl) for the ore formation (Richards 2003, 2015b; Audétat and Simon 2012). However, large porphyry Cu deposits that are generally related to more potassium-rich magmas have been discovered in post-subduction settings (Hou et al. 2004; Richards 2009), particularly in the Alpine-Himalayan Tethyan orogen (Richards 2015a). Due to the absence of oceanic slab subduction during the formation of these deposits, the origin of the associated magmas has been a matter of debate. The most popular model proposes that post-subduction porphyry Cu magmas were produced by partial melting of lower crustal, amphibole-rich cumulates that were formed by earlier subduction-related magmatism, with or without minor contributions from lithospheric mantle-derived potassic to ultrapotassic mafic magmas (Hou et al. 2004; Yang et al. 2015; Wang et al. 2018). The lower crustal partial melting model suggests that dissolution of magmatic sulfides from amphibole-rich arc cumulates may have provided abundant Cu, Au and S for post-subduction porphyry Cu magmas (Richards 2009; Hou et al. 2017; Chang and Audétat 2018; Hou and Wang 2019).

In this study, we first performed a detailed petrographic and geochemical study on two sets of exhumed amphibole (± garnet)-bearing lithologies at Lilong in the Tibetan Gangdese arc (SW China) and at Jijal in the Kohistan arc (NE Pakistan). Subsequently we conducted 14 piston-cylinder partial melting experiments on sulfide-rich hornblendite and gabbronorite from Gangdese at 1.5 GPa and 800-1150 °C. The results were used to reveal the petrogenesis of the Kohistan garnet-bearing lithologies and the behavior of magmatic sulfides during metamorphic and partial melting processes. Furthermore, the role of sulfide-rich, hydrous arc cumulates in the formation of post-subduction porphyry Cu magmas is discussed.

2 Results

2.1 Sulfide petrography and geochemistry

All the Gangdese arc-root samples contain magmatic sulfides in the form of sulfide inclusions within other minerals and in the form of interstitial sulfides. Well-preserved sulfide inclusions, consisting of pyrrhotite plus minor amounts of chalcopyrite and pentlandite (Figure 1a, b), are rather common in hornblende of hornblendite samples. The hornblendites contain the most abundant magmatic sulfides (~0.4 vol.%). Sulfide inclusions in gabbroic rocks are hosted by both hornblende and plagioclase. Many sulfides (particularly the interstitial ones) are partially to completely altered to Fe oxide assemblages, in which tiny residual sulfides (pyrite or chalcopyrite) are often visible (Figure 1c). The sulfide inclusions consist dominantly of FeS, with 1.2-8.3 wt.% Cu, 0.1-1.5 wt.% Ni, and 0.2-0.4 wt.% Co.

In contrast, the Kohistan arc-root samples are generally very poor in magmatic sulfides. The olivine- and hornblende-clinopyroxenite samples contain very rare sulfides that consist of pyrrhotite, pentlandite and chalcopyrite. No sulfides were found in the Kohistan garnet granulites. The modal abundance of sulfides in the garnet-bearing ultramafic samples (including the decomposed equivalents that can be identified) is highly variable from virtually none to ~1 vol.%. Hornblende or clinopyroxene in some samples contain a few well-preserved sulfide inclusions, all of which are composed of pyrrhotite plus minor chalcopyrite ± pentlandite/pyrite (Figure 1d). Garnets in some garnetites samples contain very Cu-rich sulfide inclusions that consist of either bornite plus chalcopyrite, pyrite ± digenite (Figure 1e), or of chalcocite and digenite (Figure 1f). However, most sulfide inclusions and all intergranular sulfides in the garnet-bearing ultramafic samples were transformed into an intergrowth of greenschist-facies minerals (epidote + actinolite ± albite ± diopside), Cu-rich sulfides (chalcopyrite ± bornite ± digenite) and fine-grained hematite (Figure 1g, h). The Kohistan sulfide inclusions hosted in hornblende and clinopyroxene have similar compositions to the Gangdese MSS inclusions, but sulfide inclusions hosted in garnet show extremely variable Cu contents ranging from 12 to 80 wt.%.

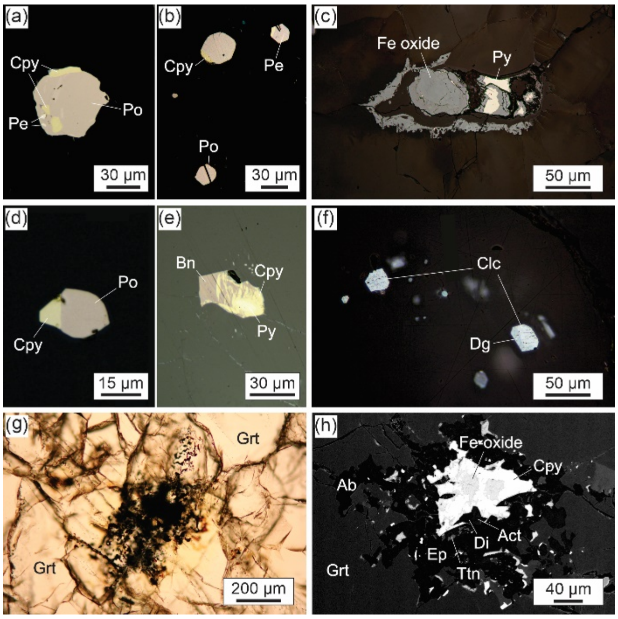

Figure 1 Photomicrographs and BSE image of sulfides from the Gangdese arc root (**a-c**) and the Kohistan arc root (**d-h**). Abbreviations: Bn – bornite; Cpy – chalcopyrite; Dg – digenite; Di – diopside; Pe – pentlandite; Po – pyrrhotite; Ab – albite; Act – actinolite; Ep – epidote; Grt – garnet; Ttn – titanite.

2.2 Experimental melt compositions

In the three runs using hornblendite as starting material, the partial melts show basaltic compositions (38-41 wt.% SiO_2 normalized dry). By contrast, the partial melts in the other runs using gabbronorite or the 1:1 mixture of gabbronorite and hornblendite as starting material show andesitic to rhyolitic compositions (56-73 wt.% SiO_2 normalized dry). In the latter runs, the SiO_2 contents of melts increase with the decrease of temperature, while the Al_2O_3, MgO, FeO^T, CaO, and TiO_2 contents decrease with the decrease of temperature. The Na_2O contents of the melts vary from 1.5 to 5.6 wt.%, but most are in the range of 4.0-6.0 wt.%. Notably, all experimental melts show very low K_2O contents of ≤1.4 wt.% (Figure 2b).

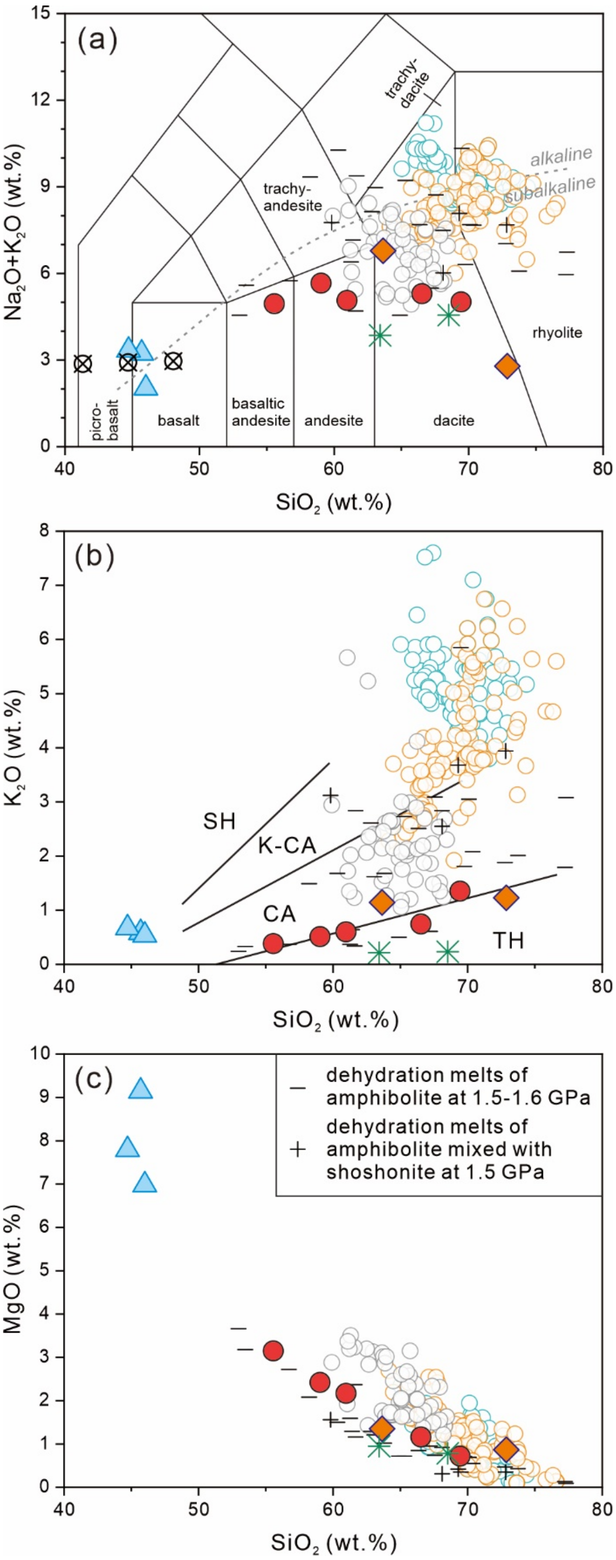

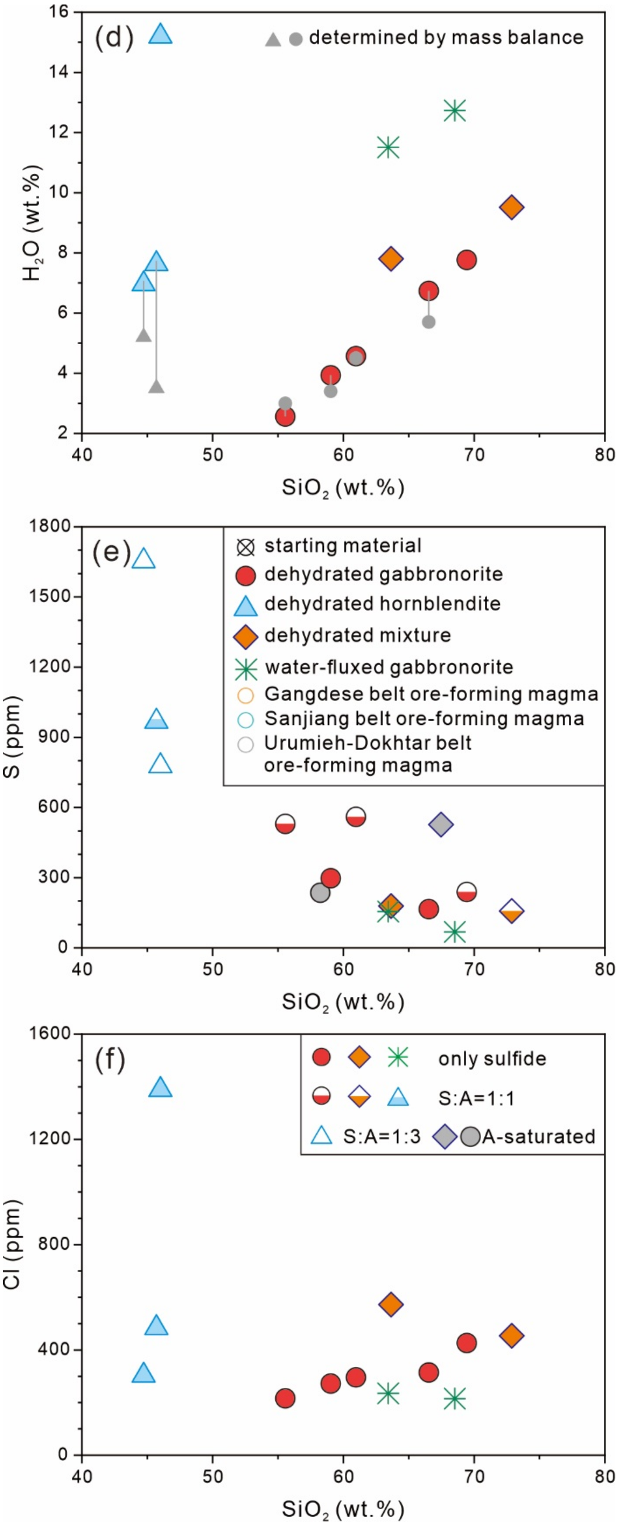

Figure 2 Diagrams showing the major and volatile element compositions of experimental melts produced in the present study (colored symbols) and in previous studies (minus and plus symbols), compared with the whole-rock compositions of post-subduction ore-forming magmas in the Tethyan Alpine-Himalaya orogenic belt. Abbreviations: CA – calc-alkaline series; K-CA – high-K calc-alkaline series; SH – shoshonite series; TH – tholeiite series; S – sulfide; A – anhydrite.

Water contents of partial melts were estimated by the difference of the EPMA totals to 100 wt.% and applying a correction based on the analysis of glasses with known H_2O contents (glasses #7, #13, #35 and #36 of Botcharnikov et al. 2011). For the runs that hornblende dehydration is the dominant reaction, the melt water content can be independently calculated by mass balance using an assumed 2 wt.% water in hornblende, and the EPMA-determined melt water contents are in good match with the results of mass balance calculations. For silicic melts (SiO_2 > 65 wt.%), the water content is greater than 6 wt.%. The melt water contents of the two water-fluxed runs are around 12 wt.%. Mafic melts of the hornblendite melting experiments show relatively high S concentrations (779-1205 ppm by weight), whereas intermediate to felsic melts of all the other experiments contain ≤600 ppm S, even though two of the latter experiments were anhydrite-saturated. Both sulfide and anhydrite are stable, suggesting an oxygen fugacity between ΔFMQ+1.5 and ΔFMQ+2.5 (Parat et al. 2011). The intermediate to felsic melts also contain rather low Cl concentrations (≤600 ppm).

3 Implications for post-subduction porphyry Cu deposits

In contrast to "normal" porphyry Cu deposits, post-subduction porphyry Cu deposits formed when there was no ongoing subduction of oceanic slabs. The magmas associated with the latter type of ore deposits are characterized by relatively high potassium contents (≥3.0 wt.% K_2O; Figure 2b), high volatile contents (H_2O, S and Cl), and high oxidation state (Richard 2011, 2015b; Wang et al. 2018). In many studies it was proposed that these magmas were derived from re-melting of sulfide-bearing arc cumulates in the lower crust (e.g., Hou et al. 2017; Wang et al. 2018).

Consistent with several previous studies (Lee et al. 2012, Chiaradia 2014; Chang and Audétat 2018; Du and Audétat 2020), our study of arc-root samples suggests that sulfides indeed tend to be precipitated at the base of magmatic arcs, but abundant sulfides could have been removed by metamorphic dehydration prior to partial melting in the course of crustal thickening.

The presence of garnet in our partial melting experiments can lead to the generation of melts with high La/Yb and Sr/Y ratios, which are characteristic features of post-subduction porphyry magmas (e.g., Hou et al. 2004; Wang et al. 2019). However, both dehydration and water-fluxing partial melting experiments in our and most previous studies contain too little potassium (<3.0 wt.% K_2O including some runs with relatively high K_2O content in the starting materials; our experimental melts contain only 0.2-1.4 wt.% due to the relatively low K_2O content of the starting materials; Figure 2b). This is in strong contrast with the ≥3.0 wt.% K_2O of ore-forming magmas in the Gangdese and Sanjiang belts (Figure 2b). In addition, MgO contents of partial melts in our and previous experiments are generally lower than those of the ore-forming magmas, particularly in the Urumieh-Dokhtar belt (Figure 2c).

High magmatic H_2O content is thought to be favorable for the formation of porphyry Cu deposits (Richards 2003), but the H_2O content of porphyry Cu magmas is poorly constrained. Our dehydration experiments show that the H_2O content of silicic partial melts (SiO_2 >65 wt.%) is more than 6 wt.% (Figure 2d), suggesting that breakdown of hornblende generates melts that may be hydrous enough to produce porphyry Cu deposits (Richards 2009). However, Lu et al. (2015) proposed that ore-forming magmas in post-subduction settings probably contained >10 wt.% H_2O. Apparently, more studies are needed to better understand the H_2O content of ore-forming magmas.

Two other volatile elements (S and Cl) are also crucial as ligands for the transportation and deposition of Cu (Richards 2003). Ore-forming magmas in subduction settings were estimated to contain up to 2500 ppm S (Grondahl and Zajacz 2022). The presence of abundant magmatic anhydrite in some subduction-related mineralizing porphyries suggests that the ore-forming magmas are relatively sulfur-rich (e.g., Audétat et al. 2004). Magmatic anhydrite was also found in the Qulong and Yulong post-subduction porphyry Cu deposits, suggesting that post-subduction porphyry Cu magmas may be also sulfur-rich. High sulfur contents of the Gangdese mineralizing magmas seem to be supported by high S contents of magmatic apatite (Tang et al. 2020). However, our experimental intermediate to felsic partial melts contain only 68-560 ppm S (Figure 2e). Typical intermediate to felsic arc magmas contain 500-2500 ppm Cl (Wallace 2005). The post-subduction porphyry Cu magmas at Bingham Canyon contain 1000-3000 ppm Cl (Grondahl and Zajacz 2017). However, Cl concentrations in our experimental intermediate to felsic partial melts are extremely low (210-570 ppm Cl; Figure 2f).

In summary, dehydration- or H_2O-fluxed partial melting of sulfide-rich, hydrous lower crustal arc cumulates does not produce magmas that match the relatively high K_2O, MgO, Cl and ±S contents of post-subduction porphyry Cu magmas.

References

Audétat A, Pettke T, Dolejš D (2004). Magmatic anhydrite and calcite in the ore-forming quartz-monzodiorite magma at Santa Rita, New Mexico (USA): genetic constraints on porphyry-Cu mineralization. Lithos 72:147-161

Audétat A, Simon AC (2012). Magmatic controls on porphyry Cu genesis. Society of Economic Geologists, Special Publications 16:553-572

Botcharnikov RE, Linnen RL, Wilke M, Holtz F, Jugo PJ, Berndt J (2011). High gold concentrations in sulphide-bearing magma under oxidizing conditions. Nature Geoscience 4:112-115

Chang J, Audétat A (2018). Petrogenesis and metal content of hornblende-rich xenoliths from two Laramide-age magma systems in southwestern USA: Insights into the metal budget of arc magmas. Journal of Petrology 59:1869-1898

Chiaradia M (2014). Copper enrichment in arc magmas controlled by overriding plate thickness. Nature Geoscience 7:43-46

Du J, Audétat A (2020). Early sulfide saturation is not detrimental to porphyry Cu-Au formation. Geology 48:519-524

Grondahl C, Zajacz Z (2017). Magmatic controls on the genesis of porphyry Cu-Mo-Au deposits: The Bingham Canyon example. Earth and Planetary Science Letters 480:53-65

Grondahl C, Zajacz Z (2022). Sulfur and chlorine budgets control the ore fertility of arc magmas. Nature Communations 13:4218

Hou ZQ, Gao YF, Qu XM, Rui ZY, Mo XX (2004). Origin of adakitic intrusives generated during mid-Miocene east-west extension in southern Tibet. Earth and Planetary Science Letters 220:139-155

Hou ZQ, Wang R (2019). Fingerprinting metal transfer from mantle. Nature Communications 10:3150

Hou ZQ, Zhou Y, Wang R, Zheng Y, He W, Zhao M, Evans NJ, Weinberg RF (2017). Recycling of metal-fertilized lower continental crust: Origin of non-arc Au-rich porphyry deposits at cratonic edges. Geology 45:563-566

Lee CTA, Luffi P, Chin EJ, Bouchet R, Dasgupta R, Morton DM, Le Roux V, Yin QZ, Jin D (2012). Copper systematics in arc magmas and implications for crust-mantle differentiation. Science 336:64-68

Lu YJ, Loucks RR, Fiorentini ML, Yang ZM, Hou ZQ (2015). Fluid flux melting generated postcollisional high Sr/Y copper ore-forming water-rich magmas in Tibet. Geology 43:583-586

Parat F, Holtz F, Streck MJ (2011). Sulfur-bearing magmatic accessory minerals. Reviews in Mineralogy & Geochemistry 73:285-314

Richards JP (2003). Tectono-magmatic precursors for porphyry Cu-(Mo-Au) deposit formation. Economic Geology 98:1515-1533

Richards JP (2009). Postsubduction porphyry Cu-Au and epithermal Au deposits: Products of remelting of subduction-modified lithosphere. Geology 37:247-250

Richards JP (2011). Magmatic to hydrothermal metal fluxes in convergent and collided margins. Ore Geology Reviews 40:1-26

Richards JP (2015a). Tectonic, magmatic, and metallogenic evolution of the Tethyan orogen: From subduction to collision. Ore Geology Reviews 70:323-345

Richards JP (2015b). The oxidation state, and sulfur and Cu contents of arc magmas: implication for metallogeny. Lithos 233:27-45

Sillitoe RH (2010). Porphyry copper system. Economic Geology 105:3-41

Tang M, Lee CTA, Ji WQ, Wang R, Costin G (2020). Crustal thickening and endogenic oxidation of magmatic sulfur. Science Advances 6

Wallace PJ (2005). Volatiles in subduction zone magmas: concentrations and fluxes based on melt inclusion and volcanic gas data. Journal of Volcanology and Geothermal Research 140:217-240

Wang R, Weinberg RF, Collins WJ, Richards JP, Zhu DC (2018). Origin of postcollisional magmas and formation of porphyry Cu deposits in southern Tibet. Earth-Science Reviews 181:122-143

Wang X, Zhang JF, Rushmer T, Adam J, Turner S, Xu WC (2019). Adakite-like potassic magmatism and crust-mantle interaction in a postcollisional setting: An experimental study of melting beneath the Tibetan Plateau. Journal of Geophysical Research: Solid Earth 124:782-798

Yang ZM, Lu YJ, Hou ZQ, Chang ZS (2015). High-Mg diorite from Qulong in southern Tibet: implications for the genesis of adakite-like intrusions and associated porphyry Cu deposits in collisional orogens. Journal of Petrology 56:227-254